

NANOCOMPOSITE STRATEGIES FOR LIMITING MEDICAL AND MARINE
BIOFOULING

By

SCOTT PATRICK COOPER

A DISSERTATION PRESENTED TO THE GRADUATE SCHOOL
OF THE UNIVERSITY OF FLORIDA IN PARTIAL FULFILLMENT
OF THE REQUIREMENTS FOR THE DEGREE OF
DOCTOR OF PHILOSOPHY

UNIVERSITY OF FLORIDA

2011

© 2011 Scott Patrick Cooper

For my loving wife, Jessica

ACKNOWLEDGMENTS

First I must thank the chair of my committee, Dr. Anthony Brennan. He balances a demand for scientific rigor while also providing genuine support and care for his students. His philosophy of requiring students formulate their own ideas has taught me a tremendous amount about the challenges of research. I would also like to thank the other members of my committee for their insight on this project: Dr. Chris Batich, Dr. Laurie Gower, Dr. A.E. “Buddy” Clark, and Dr. Tommy Angelini. I also thank Dr. Jim Farese for the time he spent on my committee and the clinical perspective he brought to our discussions. I would also like to thank Dr. David Greenspan, who provided technical and career guidance. I must also express my sincere gratitude to Dr. Larry Hench, who sparked my interest in bioactive glasses in my senior year at the University of Arizona and who helped guide me to the University of Florida.

I thank my fellow students and postdocs for their assistance and companionship. This includes members of the Brennan Research Group past and present: Dr. Leslie Hoipkemeyer-Wilson, Dr. Cliff Wilson, Dr. Jim Schumacher, Dr. Michelle Carman, Ken Chung, Jim Seliga, Dr. Chris Long, Dr. Chelsea Magin, Dr. David Jackson, Dr. Julian Sheats, Jiun-Jeng “Jack” Chen, Joe Decker, Adwoa Baah-Dwomoh, Angel Ejiasi, Dr. Canan Kizilkaya, and Dr. Medhat Khedr. I also would like to thank Dr. Douglas Rodriguez for his steadfast friendship.

This work would not have been possible without the help of numerous undergraduate students. These students (and the chapters they contributed to) include: Nick Sexson (chapter 4), Miranda So (chapter 5), Kristi Lim (chapter 5), Sean Royston (chapter 6), Melissa Goude (chapter 7), and Scott Brown (chapter 7). Working with

these students has been a two-way learning experience. I look forward to the bright futures that await them.

Much of this work was performed at the Major Analytical Instrumentation Center (MAIC), Nanoscale Research Facility (NRF), Interdisciplinary Center for Biotechnology Research (ICBR), and the Particle Engineering Research Center (PERC). I would like to acknowledge the staff at these facilities for their training and technical support. I would also like to thank the labs of Dr. Pat Antonelli, Dr. Josephine Allen, and Dr. Jim Farese for assisting with cell studies.

I must also express my sincere gratitude to our collaborators Jim and Maureen Callow, John Finlay, and Gemma Cone at the University of Birmingham (UK). They were critical for the work presented chapter 6. They are outstanding biologists and true academicians. It has been a pleasure collaborating with their group.

I would like to acknowledge the funding sources for this work, which include: the National Science Foundation Graduate Research Fellowship, the Office of Naval Research contract numbers N00014-10-1-0579 and N00014-02-1-0325, the UF Alumni Fellowship, and the Margaret A. Ross Professorship.

I would also like to thank my mother and father for instilling the value of education in me. My brother, Ryan, must also be thanked for his support and good humor. Finally, I would like to express my sincere gratitude to my wife, Jessica, for her unwavering support and encouragement throughout this process.

TABLE OF CONTENTS

| | <u>page</u> |
|--|-------------|
| ACKNOWLEDGMENTS..... | 4 |
| LIST OF TABLES..... | 10 |
| LIST OF FIGURES..... | 11 |
| LIST OF ABBREVIATIONS..... | 16 |
| ABSTRACT..... | 18 |
| CHAPTER | |
| 1 INTRODUCTION..... | 21 |
| Biofouling on Medical and Marine Surfaces..... | 21 |
| Biofilm Mitigation and Prevention..... | 22 |
| Scope of Research..... | 23 |
| Specific Aim 1: Identify the synthesis parameters that affect the size, morphology, and stability of microspheres containing bioactive glass and water-soluble polymers. | 23 |
| Specific Aim 2: Demonstrate that vancomycin maintains its effectiveness against <i>Staphylococcus aureus</i> and is released from glass microspheres for at least 1 week <i>in vitro</i> | 24 |
| Specific Aim 3: Determine if the density of zoospores of <i>Ulva</i> is lower on micropatterned PDMS _e versus smooth PDMS _e over a 4-hr period. | 24 |
| 2 BACKGROUND..... | 26 |
| Introductory Remarks..... | 26 |
| The Process of Biofouling..... | 26 |
| Properties of Biofilms..... | 28 |
| Instances of Biofouling..... | 29 |
| Marine biofouling..... | 30 |
| Medical biofouling..... | 33 |
| Approaches to Limit Biofouling..... | 35 |
| Lethal Approaches..... | 35 |
| Non-specific Compounds..... | 36 |
| Semi-Specific Compounds..... | 37 |
| Non-Lethal Approaches..... | 39 |
| Chemical Cues..... | 39 |
| Physical Cues..... | 42 |
| Nanocomposite Materials..... | 44 |
| Sol-gel Chemistry..... | 46 |
| Examples of Nanocomposites in Non-Fouling Applications..... | 49 |

| | | |
|---|---|-----|
| | Antifouling/Fouling-Release Nanocomposites | 49 |
| | Drug-Eluting Nanocomposites | 52 |
| | Summary | 53 |
| 3 | NANOCOMPOSITE BIOACTIVE GLASS MICROSPHERES CREATED BY A BASE-CATALYZED WATER-IN-OIL EMULSION..... | 54 |
| | Introductory Remarks..... | 54 |
| | Materials and Methods..... | 59 |
| | Emulsion Formation | 60 |
| | Microsphere Isolation | 60 |
| | Scanning Electron Microscopy / Energy Dispersive Spectroscopy (SEM/EDS)..... | 60 |
| | Thermal Analysis | 61 |
| | Microsphere immersion | 61 |
| | X-ray Diffraction (XRD)..... | 62 |
| | Atomic Emission Spectroscopy | 62 |
| | Results..... | 62 |
| | Discussion | 74 |
| | Summary | 80 |
| 4 | PARAMETERS AFFECTING THE SIZE AND MORPHOLOGY OF ACID- CATALYZED BIOACTIVE GLASS MICROSPHERES | 81 |
| | Introductory Remarks..... | 81 |
| | Acid-Catalyzed Microspheres..... | 81 |
| | Compositional Effects on Size and Morphology | 82 |
| | Materials and Methods..... | 85 |
| | Aqueous Phase Preparation..... | 85 |
| | Initial acid catalysis study..... | 85 |
| | Size and Morphology study..... | 86 |
| | Microsphere Synthesis | 86 |
| | Rheology | 87 |
| | Laser Light Scattering..... | 87 |
| | SEM/EDS | 88 |
| | Thermal Analysis | 89 |
| | Microsphere Immersion and XRD | 89 |
| | Osteoblast Viability | 89 |
| | Results..... | 90 |
| | Initial Acid-Catalyzed Microsphere Study | 90 |
| | Microsphere Size..... | 94 |
| | Microsphere Morphology | 98 |
| | Cell Viability | 101 |
| | Discussion | 102 |
| | Initial Acid-Catalyzed Microsphere Study | 102 |
| | Microsphere Size..... | 104 |

| | | |
|----------|--|-----|
| | Microsphere Morphology | 106 |
| | Summary | 109 |
| 5 | <i>IN VITRO</i> DRUG RELEASE FROM BIOACTIVE GLASS MICROSPHERES | 111 |
| | Introductory Remarks..... | 111 |
| | Materials and Methods..... | 115 |
| | Microsphere Synthesis | 115 |
| | UV Absorption | 116 |
| | Thermal Analysis | 116 |
| | SEM..... | 116 |
| | Drug Release Study | 117 |
| | Bacterial Inhibition Study | 117 |
| | Results..... | 118 |
| | Microsphere Synthesis | 118 |
| | Vancomycin Release Study..... | 122 |
| | Bacterial Inhibition Study | 126 |
| | Discussion | 129 |
| | Summary | 131 |
| 6 | KINETIC ANALYSIS OF THE ATTACHMENT OF ZOOSPORES OF THE GREEN AGLA <i>ULVA</i> TO SILICONE ELASTOMERS | 133 |
| | Introductory Remarks..... | 133 |
| | Materials and Methods..... | 136 |
| | Sample Preparation..... | 136 |
| | Attachment Assay for Zoospores | 136 |
| | Zoospore Mapping and Grouping Distribution | 138 |
| | Statistical Analysis..... | 139 |
| | Results..... | 139 |
| | Kinetic Attachment Assays | 139 |
| | Mapping Spore Attachment | 140 |
| | Spore Grouping | 143 |
| | Discussion | 146 |
| 7 | CONCLUSIONS AND FUTURE WORK | 153 |
| | Introductory Remarks..... | 153 |
| | Composite Bioactive Glass Microspheres | 153 |
| | Antifouling Topographies on Elastomeric Films..... | 155 |
| | Amphiphilic, Nanocomposite Hydrogels as Fouling-Release Coatings | 156 |
| APPENDIX | | |
| A | CALCULATION OF CRITICAL MOLECULAR WEIGHT OF ENTANGLEMENT FOR PVP IN SOLUTION | 163 |

| | | |
|---|---|-----|
| B | REAGENTS USED IN SIZE AND MORPHOLOGY STUDY OF ACID-CATALYZED MICROSPHERES..... | 166 |
| C | VISCOSITIES AND WEBER NUMBERS OF ACID-CATALYZED EMULSIONS .. | 168 |
| D | IMAGES OF EXTERNAL AND INTERNAL MORPHOLOGY OF BIOACTIVE GLASS MICROSPHERES..... | 169 |
| E | PROCESS FOR CREATING NANOCOMPOSITE HYDROGELS | 184 |
| | LIST OF REFERENCES | 186 |
| | BIOGRAPHICAL SKETCH..... | 203 |

LIST OF TABLES

| <u>Table</u> | <u>page</u> |
|---|-------------|
| 3-1 SEM micrographs with corresponding EDS spectra of microspheres as a function of PVP concentration. | 64 |
| 3-2 SEM micrographs and EDS spectra of microspheres with various concentrations of PEG..... | 65 |
| 3-3 SEM micrographs and EDS spectra of microspheres with various concentrations of gelatin..... | 66 |
| 3-4 Composition of base-catalyzed microspheres as determined by EDS and TG/DTA. | 67 |
| 4-1 Sol-gel glass compositions tested in this study..... | 86 |
| 5-1 Molar ratio of components (relative to TEOS) used to make vancomycin-loaded microspheres. | 115 |
| 5-2 Physical properties of vancomycin-loaded microspheres. | 120 |
| 5-3 Drug release properties of vancomycin-loaded microspheres..... | 124 |
| 6-1 Parameters A_e and β generated by the least squares fit of Equation (6-1)..... | 150 |
| 7-1 Swelling ratio of nanocomposite hydrogels after 48 hrs in DI water. | 158 |
| B-1 Moles of reagents used in synthesizing acid-catalyzed microspheres for size/morphology study in chapter 4. | 166 |
| B-2 Relative moles of reagents (to TEOS) used in synthesizing acid-catalyzed microspheres for size/morphology study in chapter 4..... | 167 |
| C-1 Viscosity, diameter, and Weber number of acid-catalyzed microspheres..... | 168 |
| E-1 Concentrations of reagents (M) used in making multi-functional silica nanoparticles. | 184 |

LIST OF FIGURES

| <u>Figure</u> | <u>page</u> |
|---|-------------|
| 2-1 Schematic of the biofouling process..... | 27 |
| 2-2 Example of macroscopic fouling on marine surfaces..... | 32 |
| 2-3 Common fouling organisms in the marine and biomedical environment..... | 34 |
| 2-4 Chemical structures of lethal compounds used to inhibit biofouling..... | 36 |
| 2-5 The “Baier curve,” established a relationship between retention of fouling organisms and critical surface energy | 40 |
| 2-6 Scanning electron micrographs of the skin of a spinner shark and Sharklet topography..... | 43 |
| 2-7 Chemical reactions that form silica from TEOS | 46 |
| 2-8 Polymerization of silica under various solution conditions | 48 |
| 3-1 Chemical structures of common analgesics and antibiotics..... | 56 |
| 3-2 Mass loss versus temperature for PVP/bioactive glass microspheres..... | 68 |
| 3-3 Mass loss versus temperature for PEG/bioactive glass microspheres. | 69 |
| 3-4 Mass versus temperature for gelatin/bioactive glass microspheres..... | 70 |
| 3-5 First derivative of sample mass versus time (DTG) and thermal differential (DTA) signals for 6 wt% PVP nanocomposite microspheres. | 70 |
| 3-6 SEM micrograph of 10wt% PVP bioactive glass microspheres after heating to 800 °C. | 71 |
| 3-7 Dissolution of 10 wt% PVP microspheres..... | 71 |
| 3-8 Electron micrographs bioactive glass particles prior to and after immersion in SBF for 7 days..... | 72 |
| 3-9 XRD spectra of base-catalyzed bioactive glass microspheres after immersion in SBF for 1 week. | 73 |
| 3-10 Elemental composition of SBF containing various compositions of bioactive glasses as measured by ICP-AES..... | 74 |
| 3-11 Phase behavior in the calcium nitrate tetrahydrate (CNT)-PEG-TEOS system. | 76 |

| | | |
|------|--|-----|
| 3-12 | Proposed structure of PVP and gelatin nanocomposite microspheres produced by base catalysis. | 79 |
| 4-1 | “Grace curve” relationship describing droplet breakup in an emulsion. | 84 |
| 4-2 | SEM images of acid-catalyzed bioactive glass microspheres made with 6 wt% PVP in the aqueous phase | 91 |
| 4-3 | SEM images of acid-catalyzed bioactive glass microspheres made with 6 wt% gelatin in the aqueous phase. | 92 |
| 4-4 | SEM images of acid-catalyzed bioactive glass microspheres made with without any polymer in the aqueous phase | 93 |
| 4-5 | Thermogravimetic analysis of acid-catalyzed bioactive glass microspheres. | 94 |
| 4-6 | XRD spectra of acid-catalyzed bioactive glass microspheres after immersion in SBF for 1 week. | 95 |
| 4-7 | 6 wt% gelatin microspheres remain intact after one week in SBF | 96 |
| 4-8 | Viscosity versus shear rate for the oil phase and 77S; 1,000 kg/mol; 10 wt% aqueous phase | 97 |
| 4-9 | Relationship between Weber number and viscosity ratio | 97 |
| 4-10 | Ternary phase diagrams summarizing the observed morphologies of PVP-nanocomposite microspheres prepared by acid catalysis..... | 98 |
| 4-11 | Microsphere made with 2 wt% of 1,000 kg/mol PVP in the aqueous phase at a nominal glass composition of 77S. | 99 |
| 4-12 | Microsphere made with 10 wt% of 1,000 kg/mol PVP in the aqueous phase at a nominal glass composition of 77S. | 100 |
| 4-13 | Microspheres made with 10 wt% of 10 kg/mol PVP in the aqueous phase at a nominal glass composition of 77S. | 101 |
| 4-14 | Results of MTT assay of human osteoblasts exposed to 77S; 1,000 kg/mol; 10 wt% PVP microspheres | 102 |
| 4-15 | Critical Weber number versus viscosity ratio for droplet breakup in different types of laminar flow | 105 |
| 4-16 | Proposed mechanism of microsphere formation by acid catalysis. | 107 |
| 4-17 | SEM images of microspheres with wrinkled surfaces | 109 |
| 5-1 | SEM images of vancomycin-loaded microspheres prior to soaking in SBF | 119 |

| | | |
|-----|---|-----|
| 5-2 | Thermogravimetric analysis of vancomycin-loaded microspheres..... | 121 |
| 5-3 | Absorbance of SBF solutions containing various compounds. | 122 |
| 5-4 | Calibration curve for vancomycin in Tris-buffered SBF..... | 123 |
| 5-5 | Vancomycin release from various microsphere compositions measured by absorbance at 280 nm. | 124 |
| 5-6 | Cumulative vancomycin release from composite bioactive glass microspheres..... | 125 |
| 5-7 | SEM images of vancomycin-loaded microspheres after 7 days in SBF..... | 126 |
| 5-8 | Zone of inhibition for <i>S. aureus</i> measured around paper disks containing the SBF drawn from a solution of vancomycin-encapsulated microspheres..... | 127 |
| 5-9 | Vancomycin release in the bacterial inhibition study. | 128 |
| 6-1 | Schematic of sample arrangements on 2.54 cm x 7.62 cm glass slides..... | 135 |
| 6-2 | Kinetic response of zoospore of <i>Ulva</i> to smooth and Sharklet PDMS _e surfaces..... | 140 |
| 6-3 | Reduction in attachment of zoospores on Sharklet microtopography versus smooth PDMS _e (6.5 cm ² areas)..... | 141 |
| 6-4 | Maps of all zoospores attached to the Sharklet topography during the kinetic study..... | 142 |
| 6-5 | Settlement maps of individual spores on the Sharklet topography. | 143 |
| 6-6 | Settlement maps of spores in groups of 2 on the Sharklet topography. | 144 |
| 6-7 | Settlement maps of spores in groups of 3 on the Sharklet topography. | 145 |
| 6-8 | Settlement maps of spores in groups of more than 3 on the Sharklet topography..... | 146 |
| 6-9 | Distribution of zoospores in groups of 1, 2, 3, or more than 3. | 147 |
| 7-1 | Dynamic swelling of PEGMA gels containing various concentrations of functionalized SiO ₂ nanoparticles..... | 159 |
| 7-2 | Contact angle on nanocomposite gels..... | 160 |
| 7-3 | SEM/EDS analysis of gels containing 25 wt% NHF/MAP-SiO ₂ particles. | 161 |
| A-1 | Spherical pervaded volume of a polymer chain (V_{sp})..... | 163 |

| | | |
|------|--|-----|
| A-2 | The condition of entanglement, in which two chains are present in the pervaded volume of a single chain (N=2). | 164 |
| D-1 | Example of ternary phase diagram that is used as a guide throughout this appendix..... | 169 |
| D-2 | 10 kg/mol, 77S, 2 wt% bioactive glass microspheres external morphology and in cross-section..... | 170 |
| D-3 | 10 kg/mol, 77S, 6 wt% bioactive glass microspheres external morphology and in cross-section..... | 170 |
| D-4 | 10 kg/mol, 77S, 10 wt% bioactive glass microspheres external morphology and in cross-section..... | 171 |
| D-5 | 10 kg/mol, 86S, 2 wt% bioactive glass microspheres external morphology and in cross-section..... | 171 |
| D-6 | 10 kg/mol, 86S, 6 wt% bioactive glass microspheres external morphology and in cross-section..... | 172 |
| D-7 | 10 kg/mol, 86S, 10 wt% bioactive glass microspheres external morphology and in cross-section..... | 172 |
| D-8 | 10 kg/mol, 100S, 2 wt% bioactive glass microspheres external morphology and in cross-section..... | 173 |
| D-9 | 10 kg/mol, 100S, 6 wt% bioactive glass microspheres external morphology and in cross-section..... | 173 |
| D-10 | 10 kg/mol, 100S, 10 wt% bioactive glass microspheres external morphology and in cross-section..... | 174 |
| D-11 | 40 kg/mol, 77S, 2 wt% bioactive glass microspheres external morphology and in cross-section..... | 174 |
| D-12 | 40 kg/mol, 77S, 6 wt% bioactive glass microspheres external morphology and in cross-section..... | 175 |
| D-13 | 40 kg/mol, 77S, 10 wt% bioactive glass microspheres external morphology and in cross-section..... | 175 |
| D-14 | 40 kg/mol, 86S, 2 wt% bioactive glass microspheres external morphology and in cross-section..... | 176 |
| D-15 | 40 kg/mol, 86S, 6 wt% bioactive glass microspheres external morphology and in cross-section..... | 176 |

| | | |
|------|---|-----|
| D-16 | 40 kg/mol, 86S, 10 wt% bioactive glass microspheres external morphology and in cross-section..... | 177 |
| D-17 | 40 kg/mol, 100S, 2 wt% bioactive glass microspheres external morphology and in cross-section..... | 177 |
| D-18 | 40 kg/mol, 100S, 6 wt% bioactive glass microspheres external morphology and in cross-section..... | 178 |
| D-19 | 40 kg/mol, 100S, 10 wt% bioactive glass microspheres external morphology and in cross-section..... | 178 |
| D-20 | 1,000 kg/mol, 77S, 2 wt% bioactive glass microspheres external morphology and in cross-section..... | 179 |
| D-21 | 1,000 kg/mol, 77S, 6 wt% bioactive glass microspheres external morphology and in cross-section..... | 179 |
| D-22 | 1,000 kg/mol, 77S, 10 wt% bioactive glass microspheres external morphology and in cross-section..... | 180 |
| D-23 | 1,000 kg/mol, 86S, 2 wt% bioactive glass microspheres external morphology and in cross-section..... | 180 |
| D-24 | 1,000 kg/mol, 86S, 6 wt% bioactive glass microspheres external morphology and in cross-section..... | 181 |
| D-25 | 1,000 kg/mol, 86S, 10 wt% bioactive glass microspheres external morphology and in cross-section..... | 181 |
| D-26 | 1,000 kg/mol, 100S, 2 wt% bioactive glass microspheres external morphology and in cross-section..... | 182 |
| D-27 | 1,000 kg/mol, 100S, 6 wt% bioactive glass microspheres external morphology and in cross-section..... | 182 |
| D-28 | 1,000 kg/mol, 100S, 10 wt% bioactive glass microspheres external morphology and in cross-section..... | 183 |
| E-1 | Mold assembly for polymerizing nanocomposite hydrogels..... | 185 |

LIST OF ABBREVIATIONS

| | |
|-------------------|--|
| 45S5 | Melt-derived glass: 46 SiO ₂ – 24 Na ₂ O – 27 CaO – 3 P ₂ O ₅ (mole %) |
| 100S | Sol-gel derived glass: 96 SiO ₂ – 0 CaO – 4 P ₂ O ₅ (mole %) |
| 86S | Sol-gel derived glass: 90 SiO ₂ – 6 CaO – 4 P ₂ O ₅ (mole %) |
| 77S | Sol-gel derived glass: 80 SiO ₂ – 16 CaO – 4 P ₂ O ₅ (mole %) |
| AF | Antifouling |
| CNT | Calcium nitrate tetrahydrate |
| CPC | Calcium phosphate cement |
| EDS | Energy dispersive spectroscopy |
| EPS | Exopolysaccharide |
| ERI | Engineered roughness index |
| FR | Fouling-release |
| HA | Hydroxyapatite |
| ICP-AES | Inductively coupled plasma-atomic emission spectroscopy |
| MAP | 3-methacryloxypropyltriethoxysilane |
| MIC | Minimum inhibitory concentration |
| MRSA | Methicillin-resistant <i>Staphylococcus aureus</i> |
| NHF | Nonahexylfluorotriethoxysilane |
| PDMS _e | Poly(dimethylsiloxane) elastomer |
| PEG | Poly(ethylene glycol) |
| PEGMA | Poly(ethylene glycol) methacrylate |
| PVP | Poly(n-vinylpyrrolidone) |
| QAC | Quaternary ammonium compound |
| R | Molar ratio of water:TEOS |
| SBF | Simulated body fluid |

| | |
|----------------|--|
| TBT | Tributyltin |
| TEOS | Tetraethylorthosilicate |
| TEP | Triethylphosphate |
| Tris | Tris(hydroxymethyl)aminomethane |
| W/O | Water-in-oil |
| XRD | X-ray diffraction |
| γ_c | Critical surface energy |
| γ_{int} | Interfacial energy between two liquids |
| η_c | Viscosity of the continuous phase of an emulsion |
| η_d | Viscosity of the dispersed phase of an emulsion |

Abstract of Dissertation Presented to the Graduate School
of the University of Florida in Partial Fulfillment of the
Requirements for the Degree of Doctor of Philosophy

NANOCOMPOSITE STRATEGIES FOR LIMITING MEDICAL AND MARINE
BIOFOULING

By

Scott Patrick Cooper

December 2011

Chair: Anthony Brennan

Major: Materials Science and Engineering

Microorganisms affect many aspects of human life. When microorganisms colonize a surface, the resulting microbial community is called a biofilm. Biofilms can negatively affect human health and productivity. Osteomyelitis is caused by biofilms of bacteria attached to the bone. These biofilms pose a threat to human life and lead to the loss of healthy tissue. Biofilms attached to marine vessels decrease the fuel economy of ships, resulting in a significant economic cost. There is a need to develop new materials which eradicate and prevent biofouling. Nanocomposites and mixed-phase organic/inorganic materials are presented in various embodiments as a means to limit biofouling.

Antibiotic-filled microspheres are created to improve the treatment of osteomyelitis. These microspheres consist of bioactive glass and poly(n-vinylpyrrolidone) (PVP) or gelatin. Bioactive glasses have historically been shown to promote the regeneration of bone. Sol-gel chemistry is used to make the bioactive glass component, in this case a calcium silicate. The low temperature of the reaction allows organic molecules such as drugs and polymers to be blended with the glass.

The catalyst used during the sol-gel reaction affects the structure and composition of the microspheres. Base catalysis leads to microspheres that exhibit behavior indicative of a nanocomposite structure. Acid catalysis produces microspheres that appear to exist as more as a mixed phase between silica and PVP. These structures directly affect the stability of the microspheres in simulated body fluid (SBF): base-catalyzed microspheres degrade within the first day in SBF, while acid-catalyzed microspheres are stable for at least one week.

The morphology of acid-catalyzed microspheres is directly affected by the following compositional parameters: molecular weight of PVP, concentration of PVP, and concentration of calcium. Solid, hollow, and core/shell morphologies are produced by adjusting these parameters. These morphologies are likely caused by various rates of silicate hydrolysis, condensation, and hydrogen bonding to PVP. Viscosity of the sol plays little role in determining the diameter of the dried microspheres.

An antibiotic, vancomycin, is successfully incorporated into these hybrid microspheres. Vancomycin is released for 5-7 days as measured by UV absorption. An *in vitro* assay against cultures of *Staphylococcus aureus* demonstrates that the drug remains effective for 4 days.

Marine biofouling is addressed by imparting topography onto silica-reinforced poly(dimethylsiloxane) elastomeric (PDMS_e) films. Swimming zoospores from the green alga *Ulva* are used as a model fouling organism. A bio-inspired topography deterred attachment of the zoospores by 70-80% over a 4-hr assay. Image analysis of the zoospores suggests that the topography may inhibit biofilm formation by disrupting the early-stage aggregation of spores on the surface. The attachment kinetics fit, with

high correlation, equations used to describe that adsorption of bacteria to surfaces. This suggests the same physical phenomena drives the attachment of bacteria and swimming algal zoospores to solid surfaces.

CHAPTER 1 INTRODUCTION

Biofouling on Medical and Marine Surfaces

The earliest form of life to appear on earth was cyanobacteria, also known as blue-green algae. These organisms thrived approximately 3.5 billion years ago and produced the oxygen that later allowed animal and human life to flourish. The only record of these early microorganisms is found in the oldest known fossils, stromatolites. These fossils have a multi-layered structure which is caused by calcified mats or “biofilms” of bacteria.¹ It is likely that the cyanobacteria aggregated into biofilms as a defense mechanism from the harsh environment of the early Earth. Approximately 3.5 billion years later, biofilms are still one of the most predominant forms of life on earth.

“Biofouling” is the process by which microscopic organisms colonize a surface. These organisms are bound together with a layer of extracellular polysaccharide (EPS) to form a dynamic community called a biofilm. The EPS protects the organisms and allows life to exist in extreme environments. For example, the bacteria found in superheated hydrothermal vents or freezing polar ice are nearly always exist as biofilms.² Biofilms also offer other advantages beyond protection from the environment. Individual cells within the biofilm can perform specific tasks, allowing the microbial community to behave like a higher, complex organism. This allows biofilms to exist ubiquitously in diverse environments that would otherwise be uninhabitable for individual cells.

Coexisting with microorganisms often comes at a cost to human health and productivity. Biomedical infections are one example. Human tissue would be an ideal surface for biofouling to occur if not for the body’s immune system that constantly

eliminates foreign organisms. When the immune system is compromised, however, biofilms can proliferate in human tissue, resulting in an infection. If left unchecked, the infection poses a serious risk for sepsis (systemic infection) and death. Patients are often hospitalized at the first sign of an infection and given extensive antibiotic therapy. This can be costly and dangerous, especially if numerous surgical procedures are required to clear the infection.

Biofouling negatively impacts productivity in other sectors as well. The marine environment is full of organisms such as algae, barnacles, and tubeworms which form biofilms as part of their life cycle³. Marine vessels that become coated with these organisms suffer a significant loss in efficiency⁴. Fouling on ship hulls places an economic burden on international commerce and can compromise naval defense capability⁵. Marine fouling is also harmful to the environment because it serves a mechanism by which invasive species spread into new ecosystems⁶.

Biofilm Mitigation and Prevention

There are three general strategies that are used to control biofilms today. The first is to use lethal compounds that kill the fouling organisms. Some compounds such as antibiotics are lethal to a narrow range of organisms, while compounds such as copper are toxic to many organisms. Another approach is to create a material that forms a very weak bond with the early biofilm. The idea is that only a small mechanical force is required to slough off weakly attached organisms. These “fouling-release” (FR) coatings are gaining popularity in the marine industry, but have limited use in biomedical applications. Finally, “antifouling” (AF) technologies prevent biofouling by avoiding the initial attachment altogether. One approach is to use the topography, or roughness, of a surface to deter the initial attachment of marine and biomedical organisms.³

Scope of Research

This research uses organic/inorganic materials to eradicate or limit biofouling utilizing the various strategies listed above. The materials presented herein all contain silica as an inorganic phase. Silica is one of the most ubiquitous minerals on earth and has found numerous uses in composite materials.

This work targets two applications in which biofouling poses a significant problem. The first application is osteomyelitis, which is an infection of bacterial biofilms on bone tissue. There is currently a need for a material that delivers drugs, degrades in the body, and regenerates natural tissue. Bioactive glass has historically been shown to slowly degrade and regenerate bone⁷ and is therefore used in this work to improve osteomyelitis treatment. Low temperature processing is used to form the bioactive glass, which allows organic molecules such as antibiotics to be incorporated.

The second application is marine biofouling. The Brennan Research Group has found that a topography inspired by shark skin is particularly effective at inhibiting the attachment of marine organisms. This topography, called Sharklet, is formed by patterning the surface of silica-filled poly(dimethylsiloxane) elastomer (PDMS_e). These nanocomposite materials are attractive for marine applications because of their toughness and low surface energy. The ability of PDMS_e topographies to inhibit fouling of algae spores is evaluated in an extended laboratory assay.

Specific Aim 1: Identify the synthesis parameters that affect the size, morphology, and stability of microspheres containing bioactive glass and water-soluble polymers.

A process for forming organic/inorganic microspheres is presented. Microspheres are formed by sol-gel synthesis in a water-in-oil (W/O) emulsion. Polymers are dissolved in the aqueous droplets to act as a binder for the calcium silicate glass. This

results in a hybrid organic/inorganic microsphere. Poly(n-vinylpyrrolidone) (PVP), poly(ethylene glycol) (PEG), and gelatin are tested for their ability to form microspheres. The effects of pH are examined with respect to the organic/inorganic ratio of the final microspheres. PVP molecular weight, PVP concentration, and calcium concentration are varied to identify the parameters that influence the diameter and morphology of the resulting microspheres. Since the microspheres are derived from droplets in an emulsion, the hypothesis is that the diameter of the microspheres will vary logarithmically with the viscosity of the aqueous droplets according to a relationship described in the literature.

Specific Aim 2: Demonstrate that vancomycin maintains its effectiveness against *Staphylococcus aureus* and is released from glass microspheres for at least 1 week *in vitro*.

Vancomycin is loaded into the microspheres and released into simulated body fluid (SBF). Drug release kinetics are measured by UV absorption. The efficacy of the released vancomycin is tested against cultures of *S. aureus*. The hypothesis is that microspheres will release a statistically significant concentration of vancomycin for at least 1 week as determined by 1-tailed t-test ($\alpha = 0.05$).

Specific Aim 3: Determine if the density of zoospores of *Ulva* is lower on micropatterned PDMS_e versus smooth PDMS_e over a 4-hr period.

Zoospores of the green algae *Ulva* are used as a model marine fouling organism. The kinetics of fouling are measured on smooth and micropatterned PDMS_e. The percent inhibition is compared between the two surfaces for up to 4 hrs. A 4 hr assay is chosen because it is believed that zoospores become less selective at periods longer than 1 hr. Previous results show that the Sharklet topography inhibits attachment by approximately 80% over smooth surfaces. The hypothesis is that the fouling on PDMS_e

with the Sharklet microtopography will remain consistently lower (~ 80 %) lower than smooth PDMS_e for up to 4 hrs, as determined by an ANOVA test ($\alpha = 0.05$)

CHAPTER 2 BACKGROUND

Introductory Remarks

The term “biofouling” refers to the undesirable process by which a surface becomes coated with biological substances. These substances include living organisms that can come from various kingdoms of life such as *Bacteria*, *Animalia*, *Plantae*, and *Fungi*. Biomolecules produced by these organisms (including proteins, polysaccharides, lipids, and nucleic acids) are critical components because they mediate adhesion to the surface. The resulting encrustation creates a coating called a biofilm. Biofilms are dynamic communities that can respond to environmental stimuli and interaction with other organisms.

Biofilms can negatively affect human health, the environment, and the performance of engineered devices. Therefore, eradication and prevention of biofilms is desirable in many applications. Eliminating a biofilm that is already established typically requires careful selection of chemical compounds that will kill the problematic organisms. Preventing biofilms altogether poses a significant engineering challenge due to the diversity of fouling species. This typically involves intervention at the early stages of the fouling process.

The Process of Biofouling

Biofouling is a dynamic process that spans many length scales (Figure 2-1). When a synthetic material is placed in an aqueous environment, ions from the liquid adsorb to the surface within fractions of a second. An electric double layer is established in this manner, the properties of which are dictated by the surface charge and ion concentration in solution. Larger molecules such as polypeptides interact with

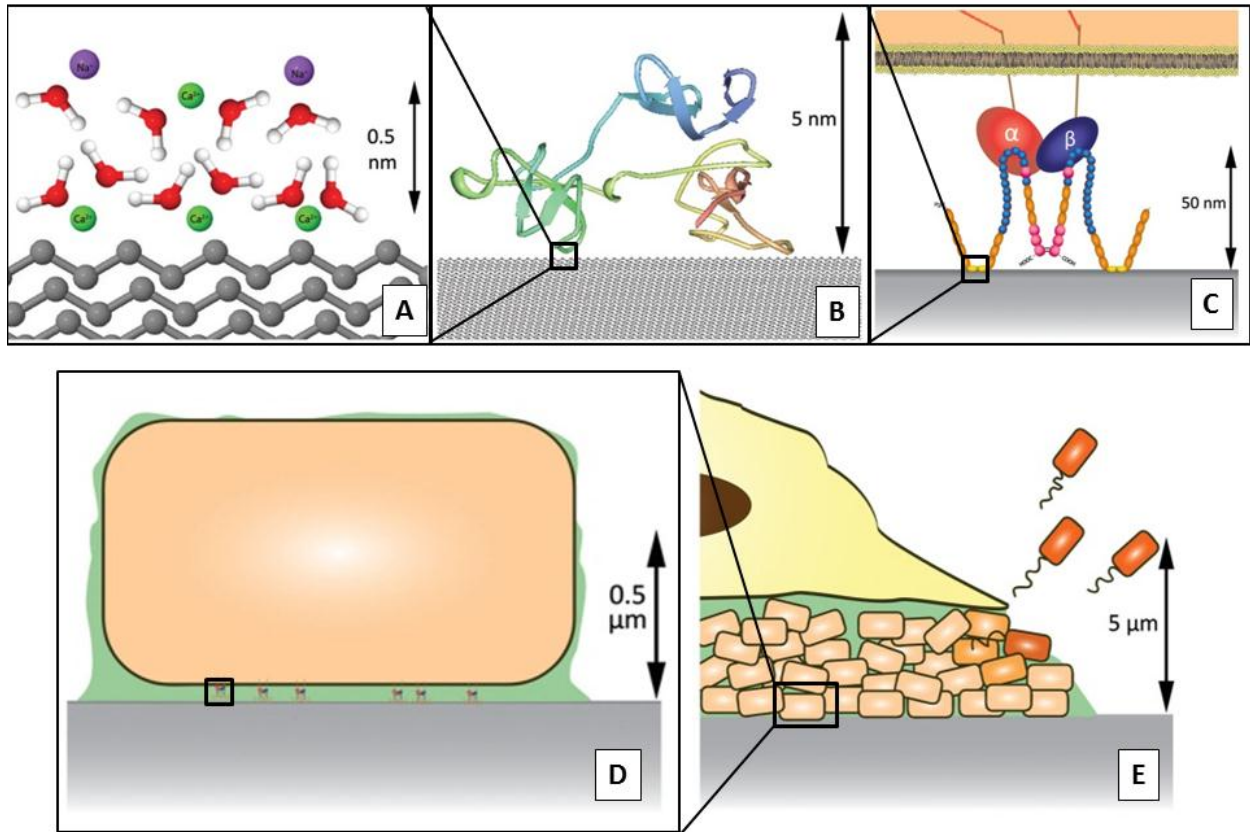


Figure 2-1. Schematic of the biofouling process. Note that the time and length scales increase from (A) to (E). Adapted from Magin, et al.³ with permission. (A) Ions adsorb from solution to form an electric double layer on a surface, in this case a linear polymer. (B) This electric layer mediates the interaction of larger molecules, such as peptide sequences (in this case Type II subunits of fibronectin). (C) The protein assumes a low energy conformation, which may expose certain parts of the protein to the microorganisms (in this case, fibronectin is shown interacting with α and β integrins of a larger cell). (D) Small organisms such as bacteria and secrete extracellular polysaccharide (EPS) which provides protection from the environment and increase adhesion to the substrate. (E) After a period of several days, a bacterial biofilm community is established which is covered by the EPS. Cells within the biofilm will differentiate to perform different functions, such as swarmer cells that seek out new surfaces (shown in red). Larger cells (such as white blood cells) may interact with this initial biofilm.

the surface through the electric double layer. These large molecules can be attracted to the surface by van der Waals forces, electrostatic, and hydrophobic interactions. This occurs within a range of seconds to minutes. If the polypeptide is part of a protein, the

lowest energy conformation of the protein may expose certain domains to binding by microorganisms. Small organisms such as bacteria will come in close contact with the surface via van der Waals forces. Strong bonds are then established via specific interactions between the organism and the proteins.

The small organisms then begin establish a biofilm by secreting the EPS, which increases adhesion to the substrate and offers protection from the environment. As a result, bacteria in biofilms are more resistant to antiseptic⁸ and antibiotic⁹ treatments than free floating (planktonic) cells. Bacteria undergo phenotypic changes as the biofilm grows. Cells deep in the biofilm become less metabolically active while cells near the surface of the biofilm can differentiate into motile cells which can leave the biofilm and colonize new surfaces.

Large cells or other organisms may subsequently interact with this initial biofilm. In the body, these may be white blood cells which attempt to eliminate the biofilm. In the marine environment, it may be unicellular organisms such as zoospores of algae or multicellular species such as tubeworms or barnacles. The result is a dynamic microbial community that can contain a multitude of species. The species within this community are continually interacting and competing with one another to survive on the surface.

Properties of Biofilms

Biofilms possess unique properties which set them apart from planktonic cells. Bacteria in biofilms tend to be more resistant to attack from chemicals and biological organisms.¹⁰ This is attributed to the EPS, which is a complex polysaccharide network that contains lipids, surfactants and DNA. Biofilms of *Bacillus subtilis*, a bacteria found in soil, have recently been shown to be resistant to solutions containing 70% alcohol

(which is commonly used to sterilize surfaces).⁸ This demonstrates how difficult it may be to kill biofilms by chemical methods alone. The variety species that are often found within a biofilm also makes chemical treatments challenging. Dental plaque, for example, is known to consist of many species that co-aggregate to form complex biofilm structures.¹¹ Since bacteria have different susceptibilities to chemical treatments, identifying a single compound that can eradicate a diverse community can prove especially challenging.

Instances of Biofouling

Biofouling has negative consequences in numerous applications. One example is tooth decay. Tooth decay is caused by biofilms of acid-producing bacteria such as *Streptococcus mutans* and *Lactobacillus* which lower the local pH until the tooth dissolves.¹¹ It has been shown that 92% of adults in the US will have a tooth decay by age 64¹² and that the necessary treatment (dental restorations) costs \$46 billion per year in the US.¹³ Biofouling has a dramatic impact on other industries as well.

Biofilm growth on heat exchangers causes a loss in efficiency of up to 10%.⁹ The critical nature of heat exchangers in power plants and industrial processes makes fouling on these devices extremely costly. A 1985 estimate of the total cost of fouling on heat exchangers was in the range of \$3-10 billion dollars per year – a number that has certainly grown along with the demand for energy.¹⁴

Two applications in which biofouling has a significant impact are marine biofouling and persistent infections. These two applications are the focus of this research and are explained in greater detail below.

Marine biofouling

Fouling on ship hulls has been recognized as a significant problem since ancient times. The first-century Greek historian Plutarch wrote:¹⁵

When weeds, ooze, and filth stick upon its sides, the stroke of the ship is more obtuse and weak; and the water, coming upon this clammy matter, doth not so easily part from it; and this is the reason why they usually scrape the sides of their ships.

Ancient shipbuilders used tar, pitch, sulfur, and sheets of lead to prevent fouling on their hulls. Copper was later discovered as a compound that is highly effective at preventing fouling. By the mid-1700s, ship bottoms were covered with copper plates or made entirely out of copper.

The drawback of copper plates was that they corroded when placed in contact with iron or steel. This was a significant problem because the nails used to attach the copper sheets to wooden ships were made of iron. While performing galvanic protection experiments on copper surfaces in the early 1800s, Sir Humphry Davy noted that copper's ability to prevent fouling was related to its ability to slightly dissolve in seawater. He was the first to establish a correlation between copper leaching from a surface and its ability to prevent biofilms. The use of copper plates became more challenging in the 19th century as more ships were built from iron.¹⁶ Copper continues to be used in marine paints even today, although in the form of an oxide. Despite the effectiveness of copper-based coatings, marine biofouling still occurs and comes at a significant cost.

There are many factors that contribute to the economic impact of marine biofouling. A detailed analysis by Schultz, et al.⁵ estimated that biofouling on the mid-size US Navy destroyer class of ships (*Arleigh Burke* class, DDG-51) costs \$56 million

per year and up to \$1 billion over 15 years. This analysis showed that increased fuel consumption due to drag is the primary expense, with dry docking, repainting, and hull cleaning also contributing to the cost. The cost of biofouling to all marine activity (naval as well as commercial) is much higher. The \$56 million/year estimate accounts for only 1/5th (approximately 60 ships) of the US Navy fleet.¹⁷ The number of cargo ships currently active in the world exceeds 50,000¹⁸. Although cargo ships have different service lives than Navy vessels, a conservative extension of Schultz's estimate puts the total cost of marine fouling on the order of tens of billions of dollars per year.

Beyond the economic penalties of marine biofouling, there are also troubling environmental consequences. Hull fouling acts as a transport mechanism for the spread of invasive species. A study by Hewitt, et al.⁶ revealed that hull fouling was the primary mechanism for the delivery of invasive species at four ports around the world. Hull fouling is responsible for the spread of nonindigenous species over thousands of miles via intercontinental cargo ships. Species can also be spread between nearby freshwater lakes by overland transport of small, recreational boats.¹⁹ Small boats have been attributed to the spread of the zebra mussel in North America, for example.²⁰ Evaluating the cost of damages caused by invasive species is difficult due to the complex interactions of with the new ecosystem. Colautti, et al.²¹ have estimated that six invasive, aquatic species in Canada are responsible for damages of \$343 million/year.

Algae are one of the most common types of marine fouling organisms. Algae are commonly referred to as “soft foulers” or “slime” (Figure 2-2B). This is in contrast to barnacles, tubeworms, and mussels which are described as “hard foulers” (Figure

2-2A). Hard foulers create calcified structures that can be centimeters in length, generating a very rough surface that dramatically increases drag.⁴ Algae, however, are more ubiquitously observed on ship hulls than hard foulers, partially because algae are more resistant to copper-based coatings.²² Soft foulers have been found to be the predominant type found on US Navy vessels.⁵ It is therefore necessary to have a model organism to study soft fouling.



Figure 2-2. Example of macroscopic fouling on marine surfaces (A) Hard fouling of organisms such as barnacles and mussels encrust the bow of a ship. Image courtesy of Jacksonville Shipyards. (B) The soft fouling algae *Ulva* covers the surface of a submarine. Reprinted with permission from Nature Publishing Group (<http://www.nature.com/ncomms/index.html>): Nat Commun. 2:244, copyright 2011.

Ulva (formerly called *Enteromorpha*) is one of the most common types of algae found on ships. Algae from this genus are widespread, tolerant to various types of salinity, and are commonly found on copper-based coatings.²² *Ulva* plants release zoospores as part of their reproductive cycle. These zoospores are 5-7 μm in diameter, have flagella, and can swim up to 100 $\mu\text{m}/\text{second}$.²³ Zoospores of *Ulva* will probe a surface to find a suitable site for attachment and can respond to light, chemical species,

and texture. The zoospores spin on the surface to secrete their EPS and subsequently start the process of growing into a plant (Figure 2-3A).^{24,25}

Medical biofouling

The first recorded observations of medically-relevant biofilms were made by the inventor of the microscope, Antonie van Leeuwenhoek. In 1684, van Leeuwenhoek scraped the plaque of his teeth and observed a number of swimming organisms which he termed “animalcules.”²⁶ Yet the link between human healthcare and bacterial growth in an attached (sessile) state was not recognized until much later.

A major breakthrough came in the mid-1800s when the German bacteriologist Robert Koch postulated that diseases were caused by single types of bacteria that could be isolated, grown in pure culture, and would cause disease when inoculated into a healthy organism. Koch made significant contributions to establishing the methods of bacterial culture and to correlating infection with disease.²⁷ However, his postulates could not explain diseases, particularly those that involved a community of organisms or bacteria that cannot be grown in a culture plate. The concept of bacteria flourishing on a surface was not introduced until the early 1900s when Henrici²⁸ and ZoBell²⁹ noted that aquatic bacteria preferred to grow on surface, rather than free-floating in suspension.

Biofilms were not recognized as a predominant mode of existence for disease-causing bacteria until the 1970s.³⁰ It is now recognized that biofilms are responsible for afflictions such as tooth decay, periodontal disease, cystic fibrosis, pneumonia, urinary tract infections, and chronic wounds.^{10,31} The Center for Disease Control estimates that approximately 65% of all human infections involve biofilms.³² Patients often acquire such infections while in the hospital being treated for a separate condition. There were

1.7 million hospital-acquired infections in 2002, which resulted in nearly 100,000 deaths.³³ The financial costs associated with hospital-acquired infections include longer hospital stays, more laboratory diagnoses, and extensive antibiotic therapy. These costs amount to an annual total of ~\$4.5 billion (1995 estimate).³⁴

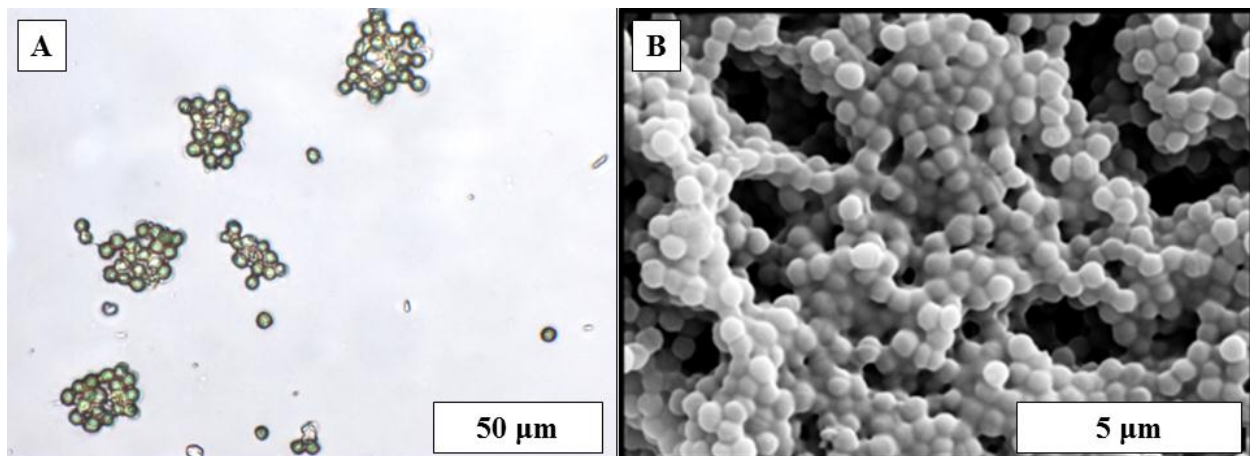


Figure 2-3. Common fouling organisms in the marine and biomedical environment. (A) Transmitted light micrograph of zoospores of *Ulva* attached to smooth PDMS after 240 mins of exposure. Image taken by John Finlay, University of Birmingham. (B) Scanning electron micrograph of a biofilm of *S. aureus* grown in culture. Image taken from *Biofilms: The Hypertextbook*, Montana State University with permission.²⁶ Although the biofilms appear similar, note that the images are taken at different magnifications. The zoospores (~5 μm diameter) are actually larger than the bacteria cells (<1 μm diameter).

Chronic infections are examples of biofilms that persist on human tissue.³⁵ These wounds typically originate in soft tissues, but cause significant complications when they proliferate into hard tissue such as bone. One example is periodontal disease that originates from the plaque in the mouth but spreads to infect the cementum of the tooth or the alveolar bone. Another example is diabetic ulcers. A lack of blood supply in the ulcerated region allows bacteria to proliferate until they spread to bone. The condition of infected bone is called osteomyelitis. Osteomyelitis is caused by *Staphylococcus aureus* in more than half of all cases.^{36,37} *S. aureus* is a bacterial species that is

commonly found as a biofilm (Figure 2-3B). Bacterial biofilms produce acid as a byproduct of their metabolism, lowering the pH of the local environment.³⁸

Hydroxyapatite, the crystalline component of bone, dissolves below a pH of approximately 5.8.¹¹ Therefore, bone is dissolved in cases of chronic osteomyelitis, leaving the patient with a serious defect region that requires restoration.

Approaches to Limit Biofouling

There are many ways to limit biofouling. The traditional method has been to eradicate the biofilm by using a lethal compound. The toxicity of the compounds can operate by any number of mechanisms including: lysis of cell membrane, inhibition of cell wall synthesis, or induction of apoptosis. Historically, lethal methods have been widely used in marine and biomedical industries and are effective at removing biofilms that have already established. Current trends, however, have been to move away from lethal approaches due to long-range environmental and health concerns surrounding these compounds.

Many non-lethal approaches focus on weakening the protein interaction with the surface, allowing the organisms and biomolecules to easily slough off. Other approaches use the physical structure of a surface to deter attachment. The long-term efficacy of these non-lethal approaches are still being evaluated.

Lethal Approaches

One of the most widely used methods to eliminate or prevent biofouling is the use of compounds that kill fouling organisms. Many marine and biomedical approaches still rely on lethal compounds to prevent or remove biofilms from surfaces. The specificity of these compounds varies widely, which makes them effective in different scenarios.

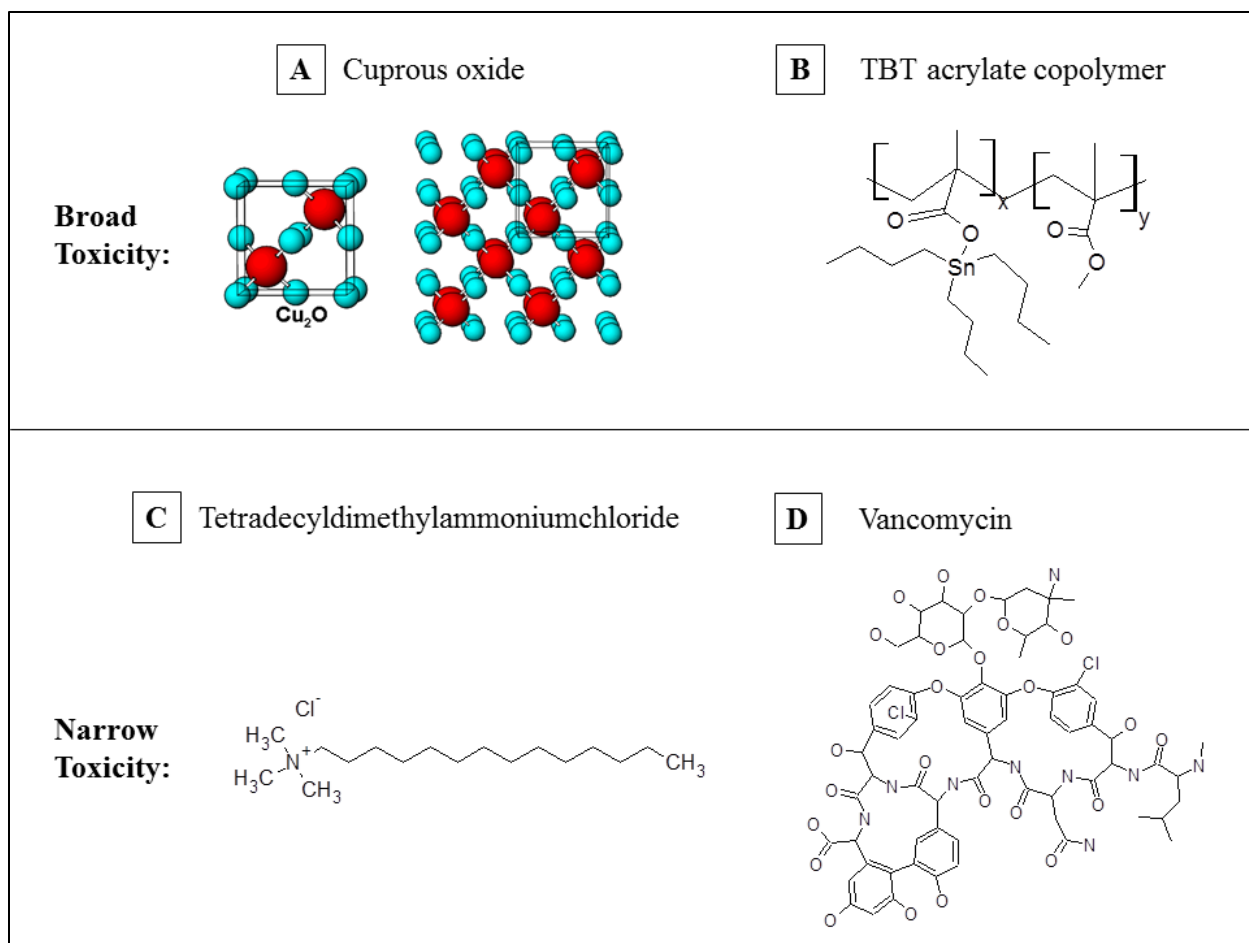


Figure 2-4. Chemical structures of lethal compounds used to inhibit biofouling. (A) Cuprous oxide, typically dispersed as a powder in acrylate paints. Image provided by North Carolina State University under Creative Commons license. (B) Tributyltin (TBT) copolymerized with methyl methacrylate form self-polishing coatings that have been used in the marine industry.³⁹ (C) Tetradecyldimethylammoniumchloride is one example of a quaternary ammonium compound (QAC) that lyses cells on contact. The specificity of these compounds is often related to the alkyl chain length. (D) Vancomycin, a glycopeptide antibiotic, inhibits cell wall synthesis of gram positive bacteria.

Non-specific Compounds

Copper is one of the oldest broad-spectrum, lethal compounds to be used in antifouling (AF) coatings. Modern AF paints typically contain copper in the form of cuprous oxide (Cu_2O), rather than the metallic form used by ancient shipbuilders. Such paints are often red in color and can be commonly seen on commercial shipping

vessels as the paint used below the waterline. Cuprous oxide is blended with film-forming vinyl or acrylic polymers with rosin added to slightly increase the solubility of the film in sea water. Once dissolved in the sea water, the copper oxidizes to form the cupric (Cu^{2+}) ion, which is toxic to nearly all forms of marine life.^{40,41} Some species of algae, including *Ulva*, have demonstrated resistance to copper. Therefore, other broad-spectrum toxic compounds are typically used to increase the performance against algae. The incorporation of tributyltin (TBT) into marine paints was based on this principle.

The development of coatings containing TBT was a landmark in the development of AF paints because it significantly extended the lifetime of the coatings. TBT is typically polymerized into the backbone of an acrylate polymer via carboxylate ester groups.³⁹ The dissolution of these coatings is based on the hydrolysis of the TBT molecule and occurs at only the outermost molecular layer. These coatings are called self-polishing because the top layer slowly erodes, keeping the surface hydrodynamically smooth. This is environmentally problematic because the carboxylic acid of tributyltin is soluble in seawater and highly toxic to marine life. TBT has been indicated in the impotence of bivalves and has the ability to bioaccumulate in organisms higher in the food chain. The International Maritime Organization banned use of TBT in paints in 2008 due to environmental concerns^{40,41}. However, the US Navy still uses TBT for critical underwater components such as sonar domes.

Semi-Specific Compounds

The environmental and health concerns over metals like copper and tin have led to an increased interest in biocides with a narrower range of toxicity, such as quaternary ammonium compounds (QACs). QACs are typically formulated as salts containing a

positively charged quaternary ammonium with one or two long alkyl chains.

Electrostatic and hydrophobic interactions cause the molecule to insert itself into the membrane. This increases permeability of the membrane, causing cell lysis and death.⁴²

The sensitivity of bacteria to various formulations of QACs differs from one organism to another. For example, QACs have limited effectiveness against gram-negative bacteria such as *Pseudomonas aeruginosa*, which have an additional lipopolysaccharide layer with limited permeability.⁴³ On the other hand, QACs dispersed in solution are typically effective against gram positive bacteria such as *Staphylococcus* and are commonly used in disinfectants such as hand soap. A relatively new strategy to limit biofouling is to covalently bind QACs into polymers or onto surfaces to kill the cells on contact.⁴⁴ This strategy has been shown effective against both marine and biomedical organisms.^{44,45}

Other lethal compounds with semi-specific toxicity are antibiotics. Antibiotics such as penicillin and vancomycin kill bacteria by binding to the peptidoglycans on the surface of the cell wall, arresting assembly of the cell wall and causing autolysis.⁴⁶ Since eukaryotic cells do not have cell walls, these types of antibiotics can be safely used to kill bacteria infecting a larger organism. One serious disadvantage to using antibiotics is the ability of bacteria to develop resistance to these compounds. Approximately half of hospital isolates of *Staphylococcus aureus* are methicillin-resistant *S. aureus* (MRSA), which indicates a resistance to the β -lactam class of antibiotics (such as penicillin). Recent reports have also indicated cases of *S. aureus* resistant to

vancomycin, commonly viewed as the last line-of-defense against antibiotic resistant bacteria.⁴⁷

Antibiotics present a dilemma in that they are currently the only defense against serious infections such as osteomyelitis, yet their use leads to the creation of drug-resistant strains of bacteria. There are currently no other alternatives to removing established biofilms from underlying tissue except for amputation. The best practice for using antibiotics is to characterize the infecting species and to deliver a high antibiotic dose over an extended period of time. Doing so gives the best chance that no bacteria will survive to develop drug resistance.

Non-Lethal Approaches

Concerns over the environmental effects of broad-spectrum toxins (such as copper and organotin) as well as antibiotic resistance have led to an increased interest in non-lethal strategies. Weakening the initial adhesion of the biofilm to the surface is typically the approach that these strategies utilize. These concepts hold promise for both marine and biomedical applications.

Chemical Cues

One of the earliest attempts to correlate surface chemistry with the degree of biofouling was made by Baier in the 1960s. This empirical relationship identified the regions of high and low fouling retention (Figure 2-5)⁴⁸ based on the critical surface tensions (γ_c) of the substrate as determined by the method described by Zisman.⁴⁹ The Baier curve shows a minima in fouling retention in the range of $\gamma_c = 20-25$ mN/m. This critical surface tension corresponds to the dispersive component of the surface tension of water. This energy corresponds to the lowest thermodynamic “cost” for water to re-wet a surface after removing proteins or cells.^{3,48}

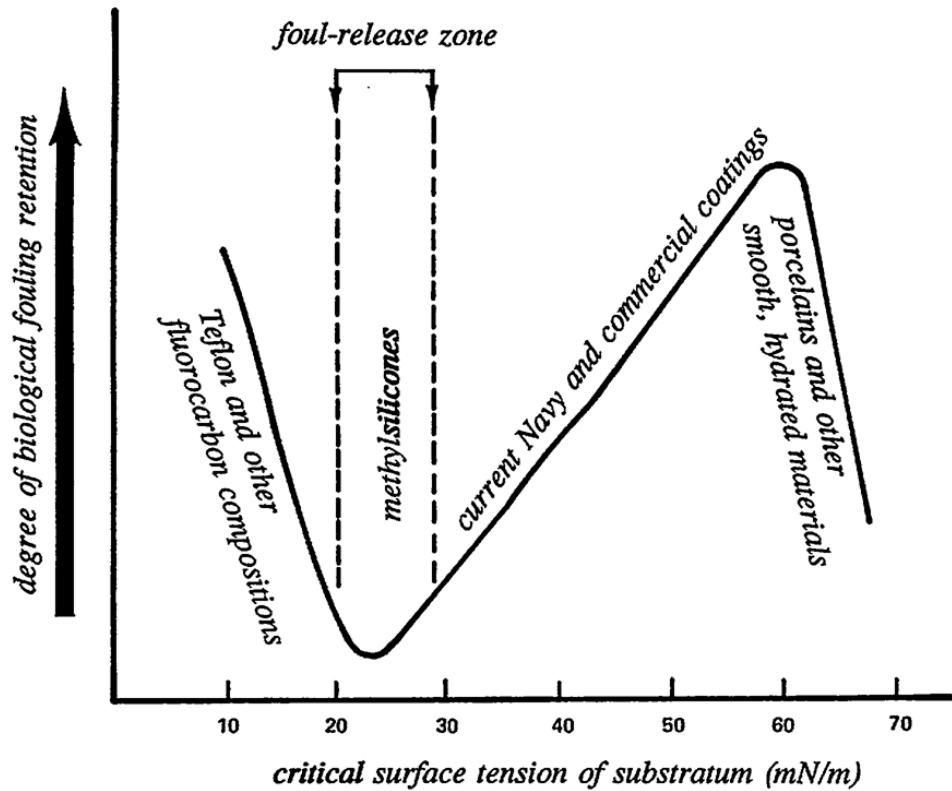


Figure 2-5. The “Baier curve,” established a relationship between retention of fouling organisms and critical surface energy. Image taken from Baier⁴⁸ with permission.

Coatings in this range of surface energy are called “fouling release” (FR) and are typically made of silicones such as PDMS. Organisms may attach to FR coatings, but only require a small shear force to remove them from the surface. Hard fouling organisms such as barnacles are removed more easily from surfaces because their bodies are larger and more rigid than soft foulers. As a result, hard foulers experience a greater shear force over the length of their body than soft foulers.⁴⁰

The Baier curve presented in Figure 2-5 also recognizes a low level of biofouling for highly hydrated surfaces with $\gamma_c > 60$ mN/m. One of the most ubiquitous hydrated materials used for AF applications is poly(ethylene glycol) (PEG). PEG molecules have repeatedly demonstrated a resistance to non-specific protein adsorption, regardless of

whether the polymer is chemically bound or physically adsorbed onto a surface.⁵⁰ Jeon and de Gennes proposed that the antifouling nature of PEG is due to the high affinity of water for the PEG molecule.⁵¹ Energy is required to displace water from the polymer chain, resulting in an enthalpic energy barrier. The polymer chain must also undergo a conformation change upon dehydration, which is entropically unfavorable. The result is a polymer that binds water so strongly that biological molecules often cannot overcome the high energy barrier to adsorb onto the surface. Jeon and de Gennes predicted that the greatest resistance to protein adsorption would be caused by high molecular weight PEG. Szleifer modified this analysis to show that low molecular weight PEG at a high density could achieve the same effect.⁵²

PEG can be implemented as an AF surface in many ways. Self-assembled monolayers (SAMs) with only a few ethylene glycol units have been shown to prevent protein adsorption^{53,54} as well as attachment of larger organisms such as zoospores of *Ulva*.^{55,56} Another approach is to create cross-linked hydrogels from PEG. These gels swell in water and present a surface that is nearly 100% water, making protein adsorption very difficult. Such gels can be made by methacrylate⁵⁷ or thiol-ene⁵⁸ chemistry and have proven effective at lowering the attachment of marine bacteria and algae zoospores.

Recent efforts have focused on creating “amphiphilic” surfaces in which both high and low surface energy groups are dispersed on the nanoscale. Several amphiphilic coatings are based on fluorocarbon ($\gamma_c \approx 18$ mN/m) and PEG ($\gamma_c \approx 70$ mN/m) groups.⁵⁹ Ober’s research group created a variety of polystyrene copolymers with pendant side chains of consisting of PEG and fluoropolymer blocks.⁶⁰ These PEG-fluoropolymer

coatings have higher removal of *Ulva* spores and diatoms than PDMS. The authors proposed a dynamic nature of these surfaces, such that either PEG or fluoropolymer can be presented at the surface depending on the environment. Similar work by Wooley's group have shown that hyperbranched fluoropolymers copolymerized with PEG display nanoscale phase separation.⁶¹ These cross-linked materials have demonstrated resistance to protein adsorption as well as low settlement and high removal of *Ulva* zoospores and sporelings⁶². Similar chemistries are currently being used in the Intersleek series of paints (International Paint), which is one of the most commercially successful FR coatings.⁴⁰

Physical Cues

New approaches to create non-lethal AF coatings focus on using the physical, rather than chemical, attributes of a surface to prevent adhesion. Nature serves as an inspiration for some of these physical attributes, since many marine organisms such as sharks do not foul. The reason why living organisms do not foul while synthetic materials quickly become encrusted with biofilms is still an unanswered question. Recent studies indicate that both physical and chemical mechanisms are responsible.⁶³ The topography, or roughness, of a surface is a crucial feature that can dictate how an organism attaches to the surface. A wide range of marine organisms including mussels, crabs, oysters, sea stars, porpoises, and sharks all have defined topographies on their surfaces, typically on the micron scale. Some of these organisms are also reported to have surface energies in the range associated with minimum fouling (20-30 mN/m) as well as unique topographies.⁶⁴

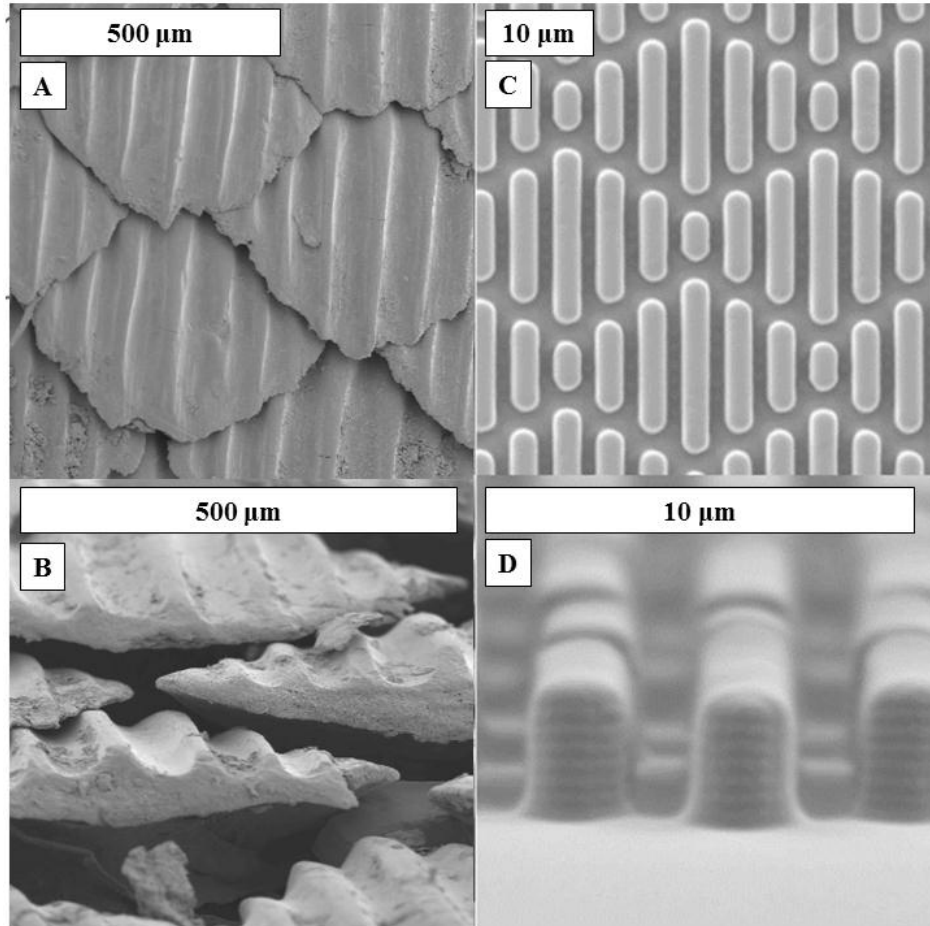


Figure 2-6. Scanning electron micrographs of the skin of a spinner shark and Sharklet topography. The skin is covered with denticles, which are tooth-like scales with a regular series of ridges. (A) Top-down (B) and side-on view of denticles from a spinner shark. A PDMS film with the bio-inspired topography Sharklet is shown from top-down (C) and side-on (D). The Sharklet topography has a repeating diamond pattern of ridges, although they are smaller than those of the shark and are not offset at different heights.

Previous work has shown that a topographic pattern inspired by shark skin, called Sharklet (Figure 2-6), is effective at deterring attachment of a variety of organisms. Reductions in attachment density were 86% for zoospores of *Ulva*⁶⁵, 97% for cyprids of the barnacle *Balanus amphitrite*⁶⁶, and up to 99% for cells of the marine bacteria *Cobetia marina*.⁵⁷ The Sharklet topography has also been effective at slowing the

biofilm growth of biomedically-relevant bacteria. Chung, et al.⁶⁷ showed that the Sharklet topography reduced the growth of biofilms of *S. aureus* for up to 3 weeks.

The mechanism behind AF topographies such as Sharklet deter settlement has not been clearly identified, but some trends have been observed. Topographies that have spacing narrower than the size of the fouling organism reduce attachment, while spaces wider than the organism may increase the attachment (compared to smooth surfaces).^{25,68} Scardino, et al.⁶⁹ proposed a model correlating the attachment strength of diatoms to the number of attachment points the organism makes with the surface. The number of attachment points in this model serve as a proxy to the attachment area that the organism makes with the surface. Schumacher et al. used areal terms which are typically used to describe wetting behavior [Wenzel's roughness, (r) and depressed area fraction, (f_d)] to correlate surface topography with fouling behavior.⁶⁸ This model produces a unitless number called the "Engineered Roughness Index" (ERI), which correlates to settlement reduction. The ERI model has since been extended to include the Reynolds number of the particular organism moving through the fluid above the surface. The resulting ERI model describes, with good correlation ($r^2 = 0.77$), the fouling behavior of a variety of organisms on textured surfaces.⁵⁷

Nanocomposite Materials

A composite is a blend of two different materials which exist in separate domains (or phases). The reason for creating a composite is typically to achieve a desired property that could not be achieved by either material individually. Composites often take the form of one material dispersed within a matrix as a second material. This can be in the form of particles, whiskers, or fibers. Fiberglass composites are one example. These composites have high strength and toughness that allows them to be used in

applications which would otherwise not be suitable for either the glass or polymer materials alone. The term “nanocomposite” refers to the case when the dispersed phase is on the order of hundreds of nanometers or less in size. The high interfacial area between components in a nanocomposite can offer desirable properties, but may pose challenges such as effective dispersion on the discontinuous phase.

Bone is one example of a nanocomposite commonly found in nature that has outstanding properties. Bone is composed of approximately 65% hydroxyapatite $[\text{Ca}_{10}(\text{PO}_4)_6(\text{OH})_2]$, 30% proteins, and 5% water by weight.⁷⁰ The majority of the protein in bone is Type I collagen, a protein that forms a rod-shaped triple helix with a molecular weight of approximately 300,000 g/mol.⁷¹ These triple helices self-assemble into fibrils with narrow gaps that allow for the intercalation of hydroxyapatite plates that are approximately 25 nm wide and 2-3 nm thick. The dispersion of hydroxyapatite within the collagen fibril and the layering of these nanocomposite fibrils within the bone imparts considerable strength, toughness, and elongation to failure.⁷²

Nanocomposites have unique structural, optical, and biological properties and are thus desirable to create synthetically. There are various methods to create organic/inorganic nanocomposites.⁷³ Hybrid materials can be created by polymerizing organic molecules in the presence of inorganic particles. Inorganic particles can also be formed in situ within a polymer.⁷⁴ The result in either case is often a network with elastomeric properties. The organic and inorganic phases can be polymerized simultaneously to create an interpenetrating network with unique mechanical and optical properties.⁷⁵ Sol-gel chemistry is the method typically used to create the inorganic phase and therefore necessitates further discussion.

Sol-gel Chemistry

Sol-gel chemistry⁷⁶ is a solution-based method of making oxide ceramics. The most common precursors for these ceramics are metal alkoxides with the general formula $M^{n+}(OR)_n$ in which R is an alkyl group. Alkoxysilanes, $Si(OR)_4$, are used to create silica, which is one of the most ubiquitous ceramic phases used in nanocomposites.

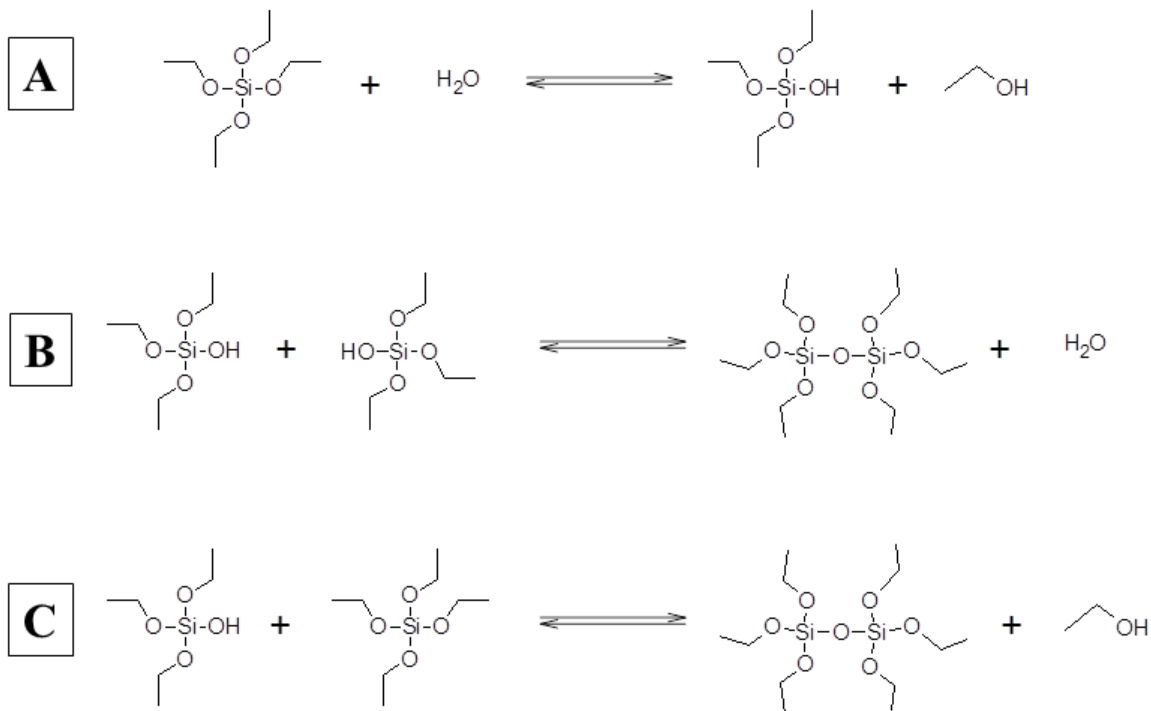


Figure 2-7. Chemical reactions that form silica from TEOS. (A) Hydrolysis of TEOS occurs by nucleophilic attack (S_N mechanism) of water at the silicon atom. (B) Condensation can occur between two silanol groups, producing water or (C) between a silanol and alkoxy group, producing ethanol. Reaction arrows are shown as bidirectional, however all reactions (A-C) heavily favor the product side.

Tetraethylorthosilicate (TEOS), which has $R = CH_2CH_3$, is one of the most common alkoxysilanes used in sol-gel chemistry. TEOS will hydrolyze in the presence of water, creating a silanol group (Figure 2-7A). Siloxane (Si-O-Si) bonds are formed by

condensation of a silanol group with either another silanol (Figure 2-7B) or an alkoxy group (Figure 2-7C).

A sol is created as the hydrolysis and condensation reactions produce a colloidal suspension of silica. The molecular weight of silica increases as the colloidal particles begin to condense together. The silica polymer has infinite molecular weight at the point of gelation. The resulting gel is porous, with water or alcohol occupying the pores. When dried, the solid material is called a “xerogel” and typically has a very high surface area. There are numerous factors that influence the structure of gels prepared by sol-gel chemistry.

One of the most critical parameters that affect gel morphology is pH. Under acidic conditions, the hydrolysis reaction occurs very quickly, while condensation occurs more slowly. The result is that gels polymerized under acidic conditions tend to form branched chains, much like organic polymers. These chains cross-link to form a network structure. Under basic conditions, hydrolysis is the rate-limiting step, while condensation occurs readily. Therefore sols created at high pH tend to be more particulate in nature and gelation occurs as these particles aggregate.

At high pH, sols tend to be very stable and the colloidal particles can remain in solution for months. This is because the surface of silica has a significant negative charge at high pH and the electrostatic repulsion between particles allows the solution to be stable. Salts will cause the sol to gel as well as lowering the pH of the solution. At the $\text{pH} \approx 2$, sols are metastable. This pH corresponds to the isoelectric point of silica, where particle growth is very slow due to low solubility of silica.

Another crucial parameter is the molar ratio water to alkoxysilane (R ratio). Technically, $R = 2$ is sufficient to fully hydrolyze an alkoxysilane. However, hydrolysis is rarely complete, leaving a mixture of silanol and alkoxy groups on the silica surface. Generally, higher R ratios result in a greater degree of hydrolysis. Low R ratios ($R < 4$) create polymeric sols that can be spun into fibers while higher R ratios ($R \gg 4$) encourage more of a particulate morphology (similar to the track B shown in Figure 2-8).

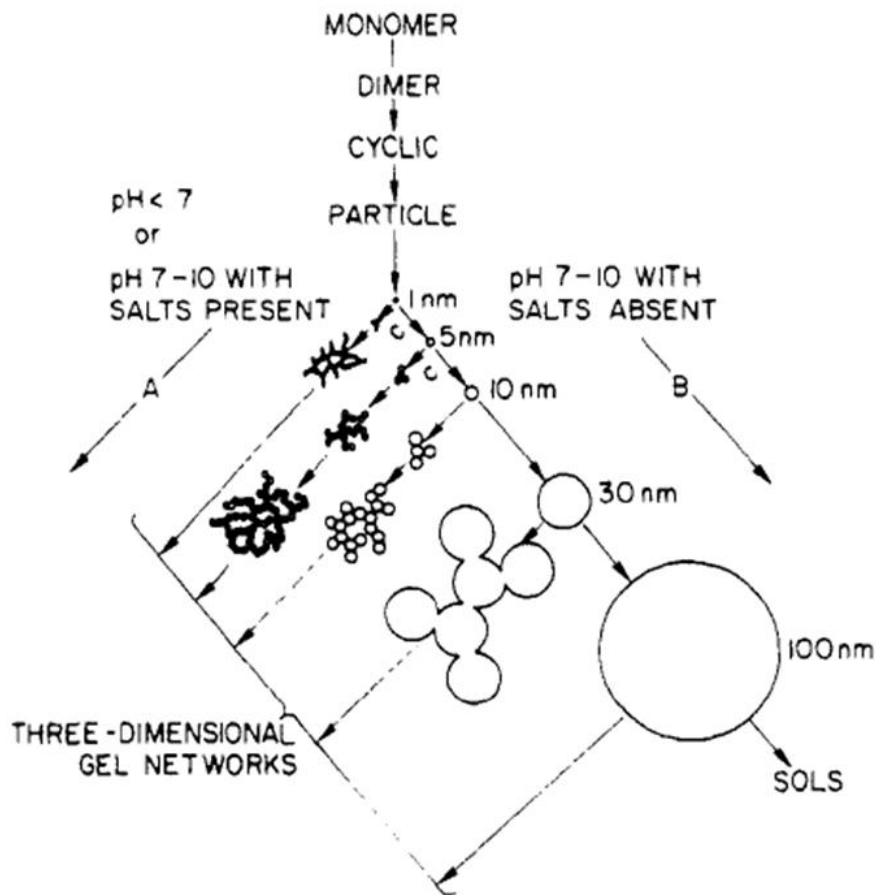


Figure 2-8. Polymerization of silica under various solution conditions. (A) Acid catalysis produces polymer-like network structures. (B) Base catalysis encourages particle formation. Image from Iler⁷⁷, with permission from John Wiley and Sons.

Silane coupling agents can be used to bring organic functionality into the inorganic network. These compounds have the general formula $R'-Si-(OR)_3$ in which R' may be a

polymer, oligomer, or functional group capable of bonding with organic species.

Covalently binding the organic and inorganic phases typically enhances the mechanical properties of the nanocomposite.

Examples of Nanocomposites in Non-Fouling Applications

Sol-gel chemistry can be utilized to create hybrid materials with unique properties such as low surface energy and controlled drug release. Often, these materials are phase separated in a nanocomposite structure. Below are examples of mixed phase hybrid materials and nanocomposites aimed at preventing fouling in the marine and medical environments.

Antifouling/Fouling-Release Nanocomposites

PDMS_e has historically been one of the most widely used nanocomposite materials for AF/FR applications. The surface energy of PDMS_e is typically ~22 mN/m, in the “fouling release” zone shown previously. Cross-linked PDMS is soft and gum-like. Silica fillers are commonly added to increase the modulus and strength of the material. The strength can increase by a factor of 40, with a dramatic increase for particles less than 100 nm in diameter.⁷⁸

Silica-filled PDMS_e is an attractive material for marine coating applications because it has a low surface energy and high toughness. However, the retention of fouling organisms changes with modulus. One study has shown that pseudobarnacle adhesion increases with the concentration of silica filler⁷⁹. Brady used a fracture analysis model to predict that higher modulus materials would retain more fouling organisms.⁸⁰ This was later experimentally demonstrated with silicones by Chaudhury, et al.⁸¹ Schumacher, et al.⁸² attempted to overcome fouling on silica-filled PDMS_e by patterning the surface with a heterogeneous microtopography. The idea behind these

surfaces was that deflection of adjacent, dissimilar features imparts a force gradient of ~100s nN on the organism. These gradients represent the mismatch in the force required to uniformly deform two adjacent features with different lengths. Indeed, the force gradients appeared to loosely correlate to the lowest settlement of zoospores of *Ulva*.

More recent work has been focused on blending other chemistries with silica. Specifically, hybrid xerogels have been examined as AF/FR coatings. Xerogels containing alkyl, fluoroalkyl, and aminoalkyl groups performed better than glass at releasing of zoospores of *Ulva* (up to 65%) and preventing settlement barnacle cyprids (as low as 10%). Coatings with a critical surface tension (γ_c) of approximately 20 mN/m had the highest release of *Ulva* sporelings and lowest settlement of barnacle cyprids.⁸³ A later study supported this result by demonstrating a distinct Baier curve behavior for the adhesion of protein-coated AFM tips to xerogel surfaces. This work showed that barnacle cyprid settlement decreased with γ_c , although the release of diatoms showed the opposite behavior.⁸⁴ Most of these hybrid materials appear to be a single, mixed phase. However, a later study identified xerogels with phase separation on the nanoscale. These materials contained a blend of n-octane and n-octadecane groups with a critical surface tension of $\gamma_c = 21-23$ mN/m. These phase segregated materials had higher release of zoospores of *Ulva* (up to 90 %) and lower settlement of barnacle cyprids (<10%) than previous hybrid xerogels.⁸⁵

Because nanocomposites allow the incorporation of many different chemical species, it is possible to vary the surface energy over a wide range. This has allowed detailed studies on the particular components of surface energy (γ) that contribute to AF

or FR behavior. Liu, et al⁸⁶ plated 316 L stainless steel surfaces with various compositions of Ni-P-TiO₂-polytetrafluoroethylene (PTFE) from a solution containing colloidal TiO₂, an emulsion of PTFE, and salts of Ni and P. The coatings ranged in surface energy from 20-45 mN/m. The adhesion of *Pseudomonas fluorescens*, *Cobetia marina*, and *Vibrio alginolyticus* bacteria was directly proportional ($r^2 = 0.82-0.92$) to the ratio $\gamma_2^{LW} / \gamma_2^-$. γ_2^{LW} and γ_2^- are components of surface energy representing nonpolar and electron-donor interactions, respectively. This analysis supports the results by Bennett, et al.⁸⁷ which established a strong ($r^2 = 0.94$) relationship between the attachment density of zoospores of *Ulva* and the percent of the surface energy contributed by polar interactions of xerogel surfaces. While these two studies used different theories to calculate surface energies, they both arrived at the same conclusion: lower biological attachment is achieved by increasing the polar contribution to the surface energy.

Sol-gel chemistry has the advantage of being a low temperature process. This allows sensitive organic molecules such as enzymes to be encapsulated in the material. Proteolytic enzymes, which digest the proteins that organisms use to adhere to surfaces, are promising non-toxic compounds that are gaining interests as components of AF coatings⁸⁸. Luckarift, et al.⁸⁹ used silica and titania xerogels to encapsulate lysozyme. The lysozyme containing-gels maintained 70-100% of their ability to lyse *Micrococcus lysodeikticus* and had better resistance to heat treatment than the free molecule. Kim, et al.⁹⁰ covalently bound α -chymotrypsin into silicate gels and found that it could digest human serum albumin. An extensive review on the subject states that polymers and oligomers can be incorporated into xerogels to protect the enzyme from

being denatured. These studies show that while some enzyme activity may be lost in the process of encapsulating enzymes in a nanocomposite, the activity is generally more resistant to aging and environmental degradation.⁹¹

Drug-Eluting Nanocomposites

Sol-gel chemistry is also conducive to encapsulating drugs. Aughenbaugh, et al.⁹² demonstrated that vancomycin can be incorporated into silica xerogels. Vancomycin release rate was directly proportional to the R ratio (moles H₂O:moles alkoxy silane) in the range of R = 4-10. The extent of vancomycin released from the material was also proportional to R ratio, with R = 10 gels releasing 90% of the initial amount of vancomycin. Radin, et al.⁹³ continued this work and showed that higher vancomycin loading produced a longer extent of first-order release kinetics. Vancomycin released from these xerogels was effective against *S. aureus* for up to 21 days. These silica xerogels were made into microspheres (100-700 μm) in a later study by Radin, et al.⁹⁴ by emulsifying the gel containing vancomycin in vegetable oil. But microspheres prepared by this method had slower release and less cumulative release of vancomycin than ground xerogel. It should be noted that these studies investigated vancomycin in silica xerogels without the addition of any polymer or salts.

Blending polymers with xerogels has the ability to change the release rate of encapsulated drugs. Costache, et al.⁹⁵ demonstrated that zero-order release rates for anesthetic drugs could be obtained by blending silica xerogels with poly(ether carbonate)-PEG block copolymers. Similar results were obtained by Ahola, et al.⁹⁶ who demonstrated that adding PEG to a silica xerogel slowed the release of an anti-cancer drug. The authors cite dissolution of the PEG/silica matrix as the reason for the observed first-order release kinetics. However, this group also found that the same

drug had a higher release rate from poly(ϵ -caprolactone-co-DL-lactide) when it was encapsulated into a silica xerogel.⁹⁷ This indicates that drug release from nanocomposites is dependent on complex interactions between the components (drug, polymer, inorganic phase) as well as the method by which the material is made.

Summary

Biofouling is a complex process that involves a wide variety of biomolecules and living organisms. Once a biofilm establishes on a surface, it is often difficult to remove due to the defense mechanism inherent in the biofilm phenotype. Therefore, there is significant interest in creating AF coatings that prevent the initial adhesion event from taking place. This has been effective in some instances; however due to the long working life of these coatings and the diversity of fouling species, attachment does still occur. FR surfaces that require a low amount of energy to release any attached organisms are also of great interest for this reason. Recent efforts have focused on developing materials that have limited toxicity. However, in some cases, such as a life-threatening infection, the use of toxic antibiotics is necessary.

Nanocomposites are a class of materials that combine the benefits of polymers and ceramics. There are a wide range of chemistries that can be created by using nanocomposites due to the flexible nature of sol-gel processing. Nanocomposites created by sol-gel processing have shown promising results as both AF and FR materials in the marine environment. Drugs have also been successfully encapsulated in nanocomposites to treat biofilms present in wounds or infected tissue.

CHAPTER 3 NANOCOMPOSITE BIOACTIVE GLASS MICROSPHERES CREATED BY A BASE- CATALYZED WATER-IN-OIL EMULSION

Introductory Remarks

Osteomyelitis is the infection of bone caused by biofilms of bacteria. These biofilms lower the local pH and destroy the underlying tissue. The current treatment is to administer antibiotics locally over several weeks to achieve a high, sustained dosage.^{37,98} Poly(methyl methacrylate) (PMMA) beads have been used in as the drug delivery material for osteomyelitis treatment for decades.^{99,100} However, there are several drawbacks to using PMMA. First, the material tends to exhibit rapid, burst-release kinetics.¹⁰¹ Second, PMMA is not bioresorbable and a second surgery must be performed to prevent fibrous encapsulation. Finally, PMMA does not stimulate regeneration of bone tissue that has been lost due to the infection. Bioceramics have been proposed as drug carriers because they can remain at the site and would encourage bone growth.¹⁰²

Bioceramics such as the bioactive glasses in the $\text{SiO}_2 - \text{Na}_2\text{O} - \text{CaO} - \text{P}_2\text{O}_5$ system are promising candidates for this application because they are well tolerated in the body.⁷ One reason why these glasses are tolerated so well is that they slowly dissolve into ionic byproducts such as Ca^{2+} , PO_4^{3-} , and $\text{Si}(\text{OH})_4$. These small molecules are easily metabolized. These ions also allow the glass to physically bond to the bone tissue. This occurs through a series of surface-mediated reactions in which Ca^{2+} and PO_4^{3-} precipitate as an amorphous solid on the glass.¹⁰³ The amorphous calcium phosphate subsequently crystallizes into an apatite by incorporating OH^- , CO_3^{2-} , or F^- ions from solution. Bioactive glasses and their dissolution products have been shown to increase the proliferation¹⁰⁴ and collagen production¹⁰⁵ of the bone precursor cells. This

produces a mineralized interface that forms a strong bond between the glass and the surrounding tissue.

Melt-derived bioactive glasses have been proposed as drug delivery materials.¹⁰⁶ However, drugs cannot be encapsulated into the glass matrix due to the high temperature processing. Instead, drugs must be adsorbed onto the surface of the material. Silanol groups on the surface of silicate materials offer sites for hydrogen bonding to occur with the drug. However, this leads to the adsorption of a monolayer of drug at the surface. The low surface area and of melt-derived glasses does not allow for an appreciable amount of drugs to be adsorbed. However, mesoporous silicates have very high surface areas and have attracted attention as drug-release materials.

Mesoporous silicates are created by sol-gel processing. Micelles of a surfactant are used as templates to create the pores in the final silicate. An alkoxy silane is polymerized around the micelles, which typically have spherical or tube-like morphology. The micelles are removed by either heating to ~500 °C or by acid treatment. The result is a xerogel with pores ~5-15 nm in diameter with extremely high surface area (~1,000 m²/g). Drugs are typically physically adsorbed from solution into the pores of the gel.¹⁰⁷

The drug release rate depends on numerous factors including: the size of the drug relative to the pores, interaction between the drug and silica surface, and the tortuosity of the pores. The first drug release study with mesoporous silica showed that ibuprofen (~1 nm molecule) was released over a period of 3 days when the average pore size was ~4 nm¹⁰⁸. Mesoporous silicates with larger pores (~12 nm mean size) exhibited a complete release of ibuprofen within 1 day.¹⁰⁹ Arcos, et al.¹¹⁰ demonstrated that

calcium can be incorporated mesoporous silicates and that these could be spray dried into 0.2-1 μm microspheres. These microspheres released triclosan, an antibiotic, over a period of ~ 12 hrs. Most studies show that untreated mesoporous silica releases drugs throughout a period of hours to a few days.

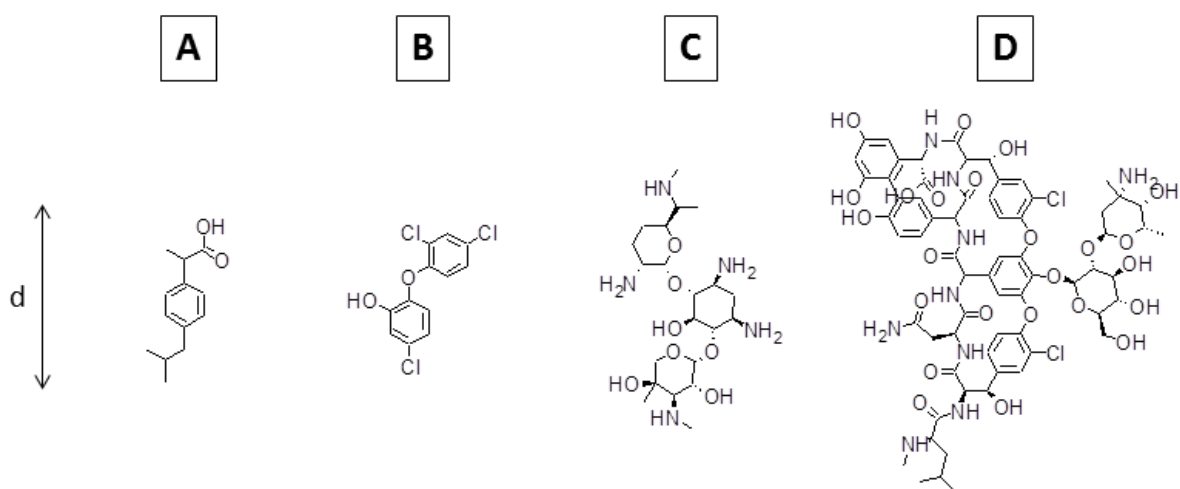


Figure 3-1. Chemical structures of common analgesics and antibiotics. Approximate size of the drug molecules were estimated by measuring the molecule along the axis indicated by “d” with the software Jmol. (A) Ibuprofen, ~ 0.8 nm. (B) Triclosan, ~ 0.7 nm. (C) Gentamycin, ~ 1.2 nm. (D) Vancomycin, ~ 1.7 nm.

Another approach to encapsulate a drug within a xerogel is to polymerize the silicate in a solution containing the drug. Unsintered xerogels have porosity on the range of 1-20 nm, depending on the catalyst and processing conditions.⁷⁶ Ducheyne’s group has demonstrated the effectiveness of this technique in numerous publications. One study found that vancomycin could be trapped within an acid catalyzed, 100% silica xerogel that produce transparent monoliths when dried.⁹³ The release rate of vancomycin directly correlated to the molar ratio H_2O :alkoxysilane ratio and the concentration of vancomycin in the gel.⁹²

A later study showed that microspheres (100-700 μm) encapsulating vancomycin could be produced by emulsifying these sols in vegetable oil. However, emulsifying the sol diminished the release rate and cumulative release of vancomycin. This may have been due to vancomycin dissolving into the oil phase, because the average pore size (~ 2.5 nm) was the same xerogels regardless of whether it was emulsified. The release kinetics fit a model for diffusion-limited release from spherical bodies. This model indicates that diffusion, rather than matrix dissolution, was responsible for driving the release of vancomycin (~ 1.7 nm molecule) from the porous xerogel.⁹⁴

Polymers have been blended with ceramics to change the nature of the drug release. Xia, et al.¹¹¹ demonstrated that two different drugs could be released from mesoporous silica depending on the pH of the surrounding media. This was accomplished by coating the mesoporous silica with pH-responsive micelles of poly(γ -benzyl-L-glutamate)-block-poly(ethylene glycol). Ahola, et al.⁹⁶ showed that release of an anti-cancer drug from xerogels was slower when poly(ethylene glycol) (PEG) was incorporated into the acid-catalyzed, silica sol.

Most studies to date on drug-releasing ceramics have been performed on xerogels that did not contain polymers. Although some studies (mentioned above) have shown that polymers have the ability to slow the release kinetics. Polymer-bioactive glass blends have been created in various morphologies. Hatcher, et al.¹¹² created poly(*n*-vinylpyrrolidone) (PVP) bioactive glass nanocomposites that could be sprayed or spun into fibers. Costa, et al.¹¹³ produced macroporous foams of a bioactive glass-poly(vinyl alcohol) hybrid material. Incorporating CaO and P₂O₅ generally increases the dissolution rate of xerogel materials.¹¹⁴ However, in the presence of polymers, the

interaction between ions and the polymerizing silicate becomes more complex. Arcos, et al.¹¹⁰ reported that Ca^{2+} decreases the ordering of pores within mesoporous silica formed in the presence of PEO-PPO-PEO block copolymer.

The goal of this study is to characterize the morphology of hybrid microspheres made by a water-in-oil (W/O) emulsion process. This work is an extension of a publication by Park, et al.^{115,116} who created PVP/silica and PEG/silica microspheres by W/O emulsion. The droplets of the emulsion serve as precursors to the microspheres in this method. Tetraethylorthosilicate (TEOS) is added to the emulsion and hydrolyzes at the oil/water interface to become water soluble. Polymers dissolved in the aqueous droplets to slow the diffusion of hydrolyzed silica. This study showed that the microspheres have a hollow structure after heating to 600 °C.¹¹⁵ This work differs from that by Park, et al. in that microspheres will be made with the 77S composition¹¹⁴ of bioactive glass (80 SiO_2 – 16 CaO – 4 P_2O_5 , mole %).

Three polymers are used in this study for the organic phase of the microsphere: PVP, PEG, and gelatin. PVP is commonly used as a binder in pharmaceutical applications and is generally well tolerated by the body.¹¹⁷ PEG is a water-soluble polymer that is widely used as an excipient in drug formulations. Gelatin is a naturally occurring polyamide found in skin and bone. It is commonly used in drug-delivery applications and is generally inexpensive.¹¹⁸ Furthermore, gelatin has been shown to significantly increase the early-stage bonding strength of apatite-wollastonite bioactive glass to bone.¹¹⁹ For these reasons, gelatin is a suitable polymer filler for drug delivery using bioactive glass.

Materials and Methods

A process was adapted from the method shown by Park, et al¹¹⁵ to create microspheres by a W/O emulsion. The oil phase consisted of 1-octanol with 3% (wt/wt) Span 80 (an oil-soluble emulsifier) and 1.4% (wt/wt) hydroxypropylcellulose (a rheological modifier). This was prepared by heating the 1-octanol to 80 ± 5 °C before slowly adding the hydroxypropylcellulose over a 5 min period while stirring. The solution was stirred for an additional 4 hrs at this temperature and subsequently cooled to 40 ± 5 °C before adding the Span 80.

To prepare the aqueous phase, a 2.7 M solution of $\text{Ca}(\text{NO}_3)_2$ was prepared with DI water (>17 M Ω ·cm resistivity). The catalyst, ammonia, was added in the form of a strong ammonium hydroxide solution which titration revealed $[\text{NH}_3] = 10.6$ M. The ammonium hydroxide was added to the 2.7 M $\text{Ca}(\text{NO}_3)_2$ solution until pH = 10.5 as measured by a Thermo Orion 2-Star Benchtop pH meter.

Polymers were added to the aqueous solutions at concentrations of 2%, 6%, and 10% (wt/wt) of the pH-adjusted 2.7 M $\text{Ca}(\text{NO}_3)_2$ solution. The polymers tested in this study were: PVP (molar mass $\sim 1,000$ kg/mol, Polysciences #06067), PEG (molar mass ~ 20 kg/mol, Alfa Aesar #A17925), and gelatin type B (molar mass ~ 50 kg/mol, Sigma #G-939). The appropriate amounts of polymer were added to each sample and stirred until a transparent, homogenous mixture was achieved. Because gelatin is more soluble at higher temperatures, the aqueous solution was heated to 70 ± 3 °C for 40 mins to allow the gelatin to dissolve. The gelatin solutions then were cooled to ambient; i.e., below 30 °C, prior to adding it to the oil phase.

Emulsion Formation

The oil phase was added by weight ($46 \pm 2\text{g}$) to a 250 ml glass beaker. A Caframo mechanical mixer was used to mix the emulsion at 500 rpm with a propeller-type blade. 6.1 ml of the aqueous solution was added dropwise with a pipette to the continuously stirring oil phase. This corresponds to an emulsion with a volume ratio of approximately 9:1 (oil:water). The emulsion was stirred for 30 mins. 18.8 ml of TEOS was added directly to the emulsion immediately followed by 1.4 ml of triethylphosphate (TEP). These reagent concentrations correspond to a 77S composition of bioactive glass ($80 \text{ SiO}_2 - 16 \text{ CaO} - 4 \text{ P}_2\text{O}_5$, mole %) with a $\text{H}_2\text{O}:\text{TEOS}$ molar ratio of 4. The molar ratio of sol-gel reactants $\text{H}_2\text{O}:\text{TEOS}:\text{Ca}(\text{NO}_3)_2:\text{TEP}:\text{NH}_3$ was 4:1:0.18:0.01:0.02. The emulsion was stirred for 24 ± 1 hrs at 21 ± 3 °C.

Microsphere Isolation

The microspheres were washed three times by centrifugation at 2,000 rpm and were rinsed with ~20 ml of 200 proof ethanol after each centrifugation. A vortex mixer was used to re-disperse the microspheres after each rinsing. The microspheres were dried by placing them in a vacuum oven at 45 ± 10 °C and placing them under vacuum. The microspheres were dried until ethanol was no longer visible, typically 2-4 hrs.

Scanning Electron Microscopy / Energy Dispersive Spectroscopy (SEM/EDS)

All samples were mounted on aluminum stubs with double-sided tape for SEM/EDS analysis. A layer of gold-palladium was sputter coated on a Denton Desk II at 38 mA for 60 seconds. SEM/EDS analysis was performed on a JEOL 6400. All images were taken in secondary electron mode with 15 mm working distance and 15 kV accelerating voltage. Elemental content was determined by EDS at the following x-ray

energies: C $K\alpha_1$ = 0.2675 keV, Si $K\alpha_1$ = 1.7475 keV, Ca $K\alpha_1$ = 3.7075 keV, P $K\alpha_1$ = 2.0075 keV. EDS spectra were taken on spots are indicated on the micrographs.

Thermal Analysis

Thermogravimetric and differential thermal analysis (TG/DTA) was performed on a Seiko TG/DTA 320. Each sample had a mass of 9-11 mg. The samples were purged with air at a flow rate of 100 ml/min. Heating was performed between 30-800 °C at a rate of 2 °C/min. For DTA analysis, the reference material was 14 mg of Al_2O_3 powder. DTA curves have been baseline corrected against an empty sample pan.

Microsphere immersion

Microspheres were immersed in simulated body fluid (SBF) to determine if hydroxyapatite would precipitate at the surface. The SBF was prepared as described by Kokubo, et al.¹²⁰ and contained the following ions (in mM): 142.7 Na^+ , 5.0 K^+ , 1.5 Mg^{2+} , 2.6 Ca^{2+} , 187.8 Cl^- , 4.2 HCO_3^- , 1.0 HPO_4^{2-} , 0.5 SO_4^{2-} . The solution and was buffered to pH = 7.40 using tris(hydroxymethyl)aminomethane.¹²⁰ Samples were immersed in a shaker bath at 37 °C for up to 7 days. The concentration of microspheres to SBF was fixed at 0.001 g/ml. Melt melt-derived, 45S5 bioactive glass⁷ granules were included in these experiments (46 SiO_2 – 24 Na_2O – 27 CaO – 3 P_2O_5 , mole %). The granules were prepared by Mo Sci Corp (donated by Dr. Larry Hench) and had a particle size of 200-300 μm .

45S5 particles were collected for XRD analysis by filtration with 0.45 μm cellulose paper. The particles were rinsed three times with ~10 ml DI water. The samples were then dried at room temperature in a desiccator. Because SBF containing microspheres filtered very slowly, these samples were collected by centrifugation at 1500 rpm. The

pellet was rinsed with 50 mL of DI water. This process was repeated three times before drying as described above.

The SBF was analyzed by ICP-AES to determine composition changes induced by dissolution of the particles. SBF was collected by filtration through 0.45 μm cellulose filter paper and collected in centrifuge tubes. These solutions analyzed without any further modification.

X-ray Diffraction (XRD)

X-ray diffraction (XRD) was used to determine whether crystalline hydroxyapatite forms at the surface of microspheres after immersion in SBF. The analysis was performed on a Philips 3720 with $\text{CuK}\alpha$ source with $\lambda_{\text{avg}} = 0.154 \text{ nm}$. Scans were performed with a step size of 0.02° and time per step of 0.5 seconds. Powdered samples were mounted onto a piece of glass slides with double sided tape.

Atomic Emission Spectroscopy

Inductively coupled plasma atomic emission spectroscopy (ICP-AES) was used to monitor the presence of Ca, Si, and P in SBF as a function of time. ICP-AES analysis was performed on a Perkin-Elmer Optima 3200. A 100 ppm standard of each element was serially diluted in DI water ($18.2 \text{ M}\Omega\text{-cm}$) to give standards of 10 and 1 ppm. A calibration curve was established using for each element using a non-linear fit to an r^2 value of 0.9999 or greater. Each sample was measured 5 times and correlated to the calibration curve using a peak area algorithm. The wavelengths used for reporting concentrations were $\lambda_{\text{Ca}} = 317.933 \text{ nm}$, $\lambda_{\text{Si}} = 212.412 \text{ nm}$, and $\lambda_{\text{P}} = 214.914 \text{ nm}$.

Results

Aqueous droplets which contained PVP (Table 3-1) at concentrations of 6 wt% and 10 wt%. The microspheres made with 6 wt% PVP had diameters of approximately

5-20 μm , while microspheres made with 10 wt% PVP were slightly larger with diameters of approximately 10-40 μm . The 2 wt% PVP composition produced few microspheres. The material instead appeared largely as a film.

Table 3-1. SEM micrographs with corresponding EDS spectra of microspheres as a function of PVP concentration.

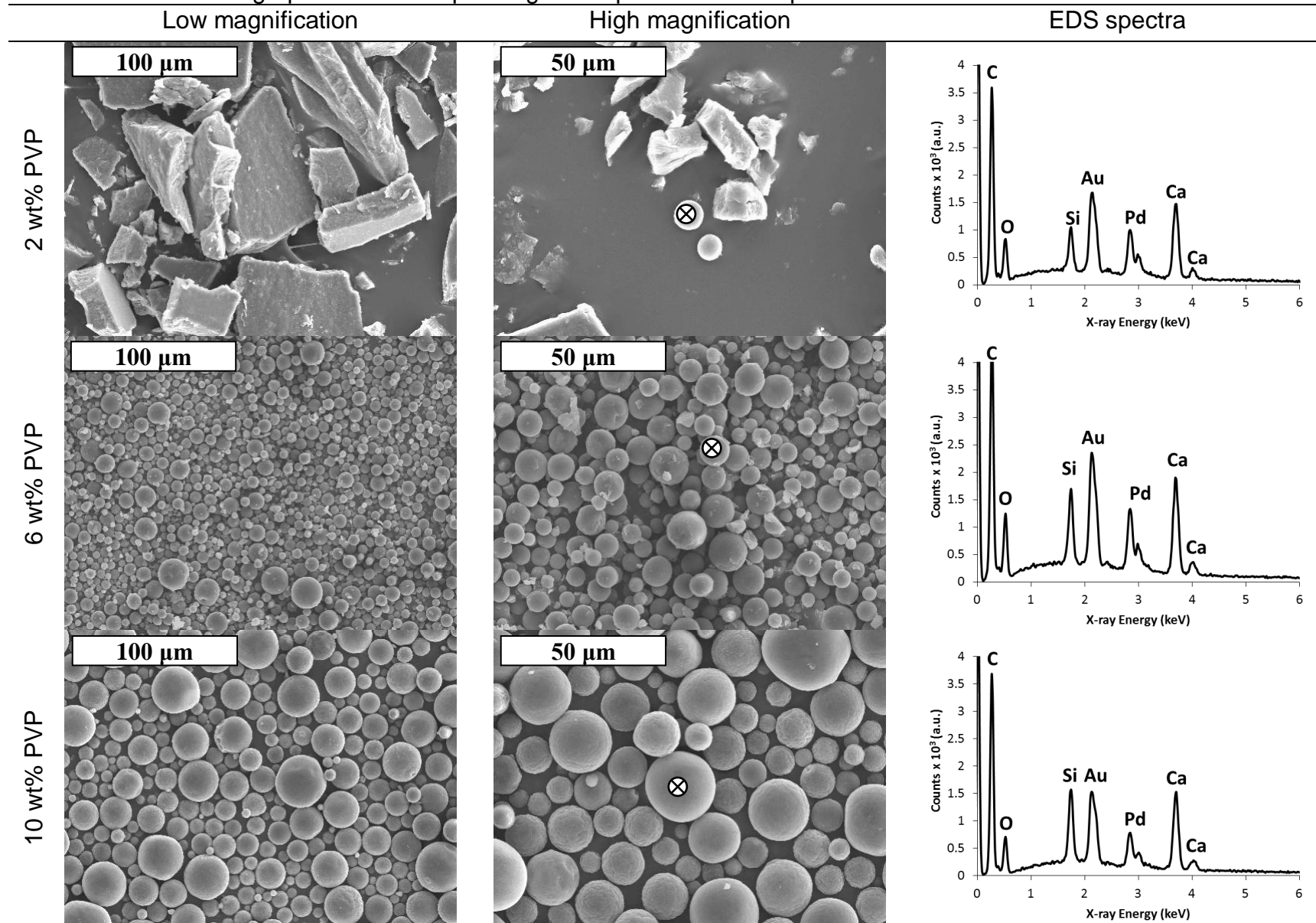


Table 3-2. SEM micrographs and EDS spectra of microspheres with various concentrations of PEG.

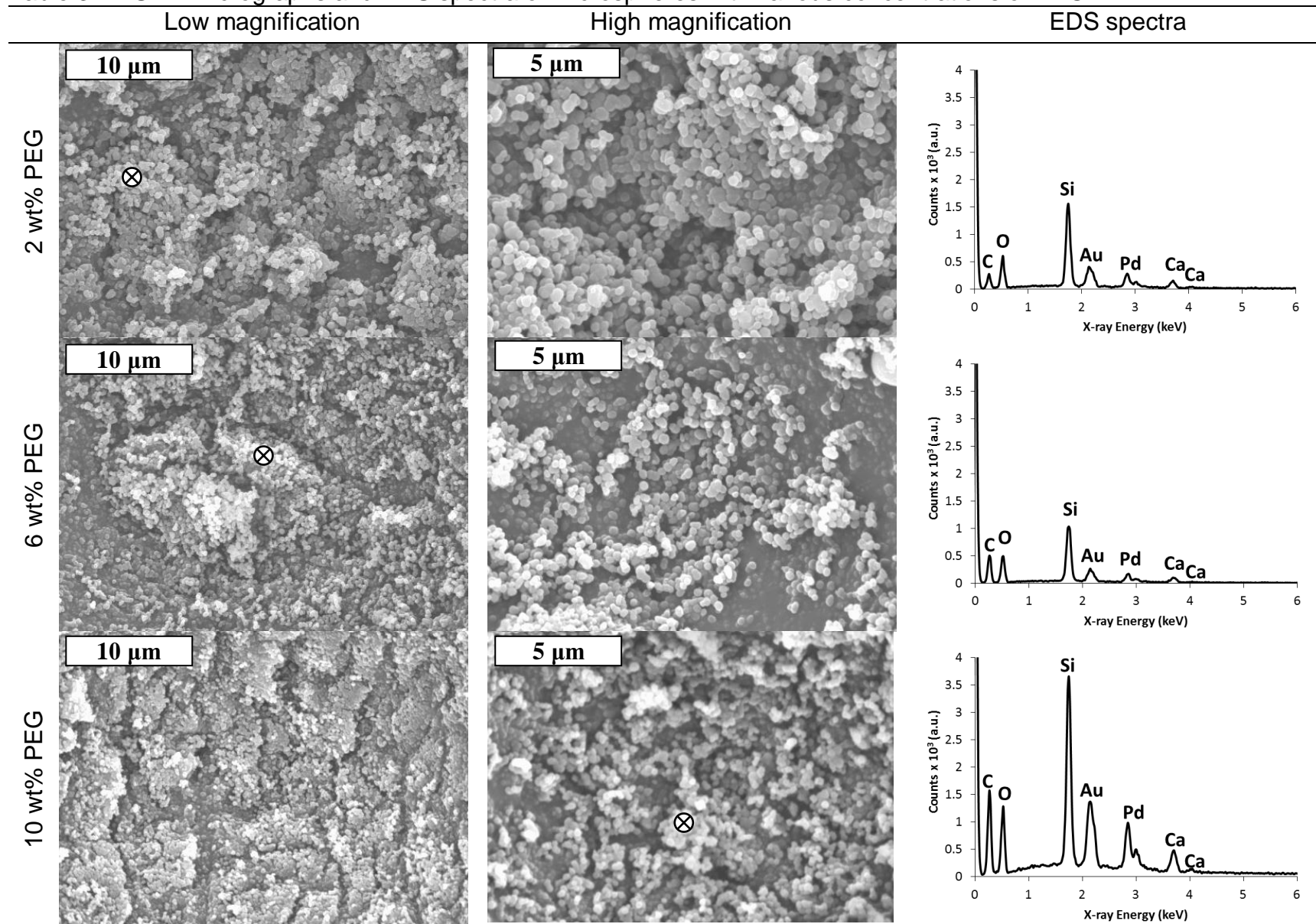
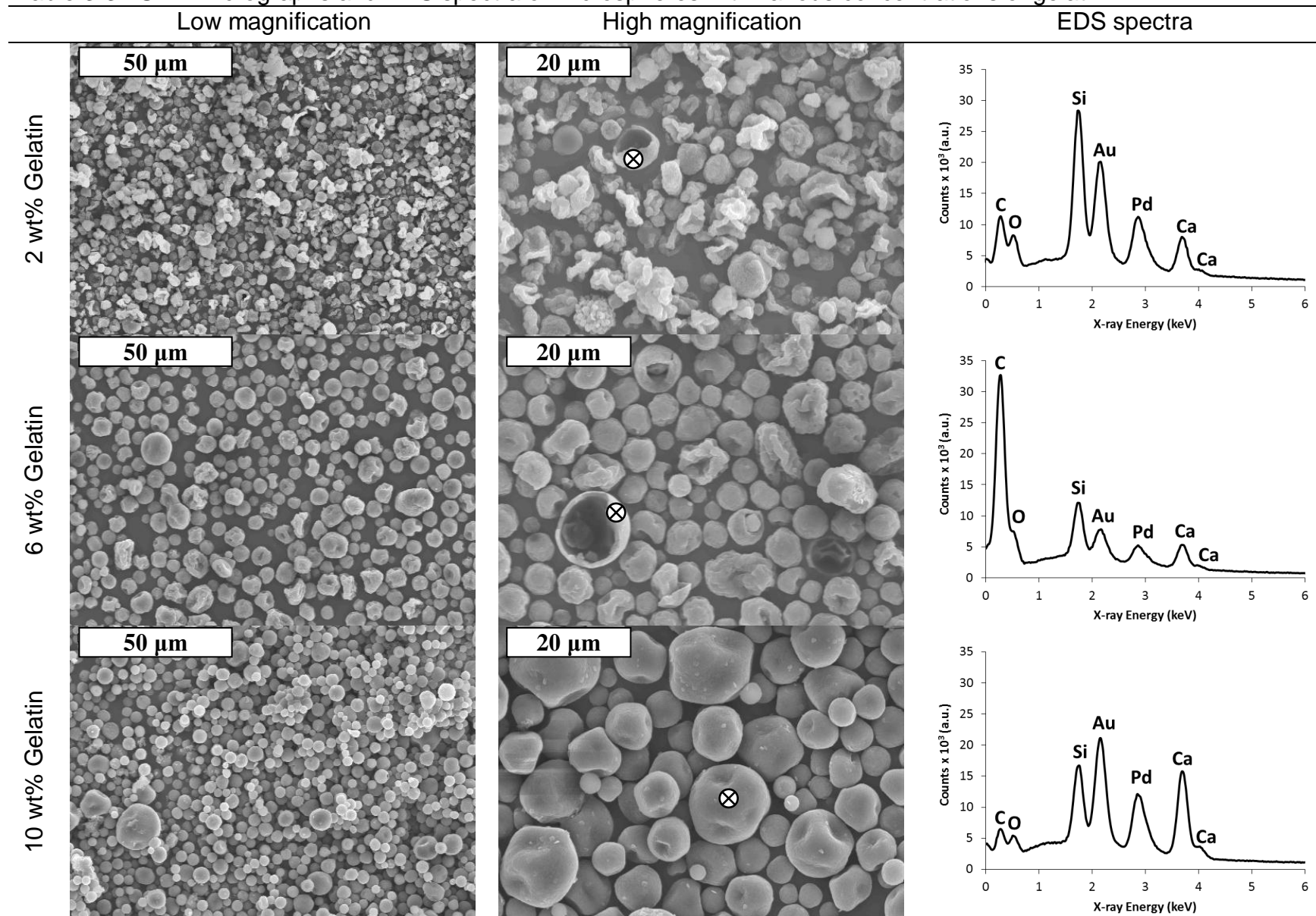


Table 3-3. SEM micrographs and EDS spectra of microspheres with various concentrations of gelatin.



Microspheres made with PEG were significantly smaller, i.e., 0.2-1 μm , at all concentrations tested. Microspheres made with gelatin appeared to be 1-20 μm in diameter by visual inspection of the micrographs (Table 3-3). The concentration of gelatin appears to affect the morphology of the microspheres. Some microspheres prepared with 2-6 wt% gelatin appeared hollow, despite never having been fired. Many of these microspheres also appeared collapsed. However, microspheres prepared with 10 wt% gelatin concentration appear more spherical and less “deflated.”

Table 3-4. Composition of base-catalyzed microspheres as determined by EDS and TG/DTA. Ca:Si ratios with error values indicate the average and standard deviation of 2 measurements. Numbers without error are a single measurement.

| Polymer | Polymer concentration (% wt/wt) | Ca:Si ratio | C:Si ratio | Mass loss between 150-800 °C (%) |
|---------|---------------------------------|---------------|---------------|----------------------------------|
| PVP | 2 | 0.8 \pm 0.9 | 1.8 \pm 2.3 | 68 |
| | 6 | 0.8 \pm 0.4 | 3.2 \pm 0.7 | 84 |
| | 10 | 1.1 \pm 0.1 | 2.7 \pm 0.4 | 85 |
| PEG | 2 | 0.1 \pm 0.0 | 0.1 \pm 0.1 | 28 |
| | 6 | 0.1 \pm 0.0 | 0.3 \pm 0.3 | 26 |
| | 10 | 0.1 \pm 0.0 | 0.3 \pm 0.2 | 29 |
| Gelatin | 2 | 0.3 \pm 0.0 | 0.4 \pm 0.0 | 65 |
| | 6 | 0.9 \pm 0.6 | 2.0 \pm 1.0 | 75 |
| | 10 | 0.9 | 0.4 | 81 |

Calcium concentration in the final microspheres was dependent upon the type of polymer in the aqueous phase. Silicon was used as an internal reference for comparing EDS signals between samples. The ratio of Ca:Si was approximately 10 times lower for samples containing PEG than samples containing PVP or gelatin (Table 3-4). The amount of carbon relative to silicon was also lower in samples containing PEG than other polymers.

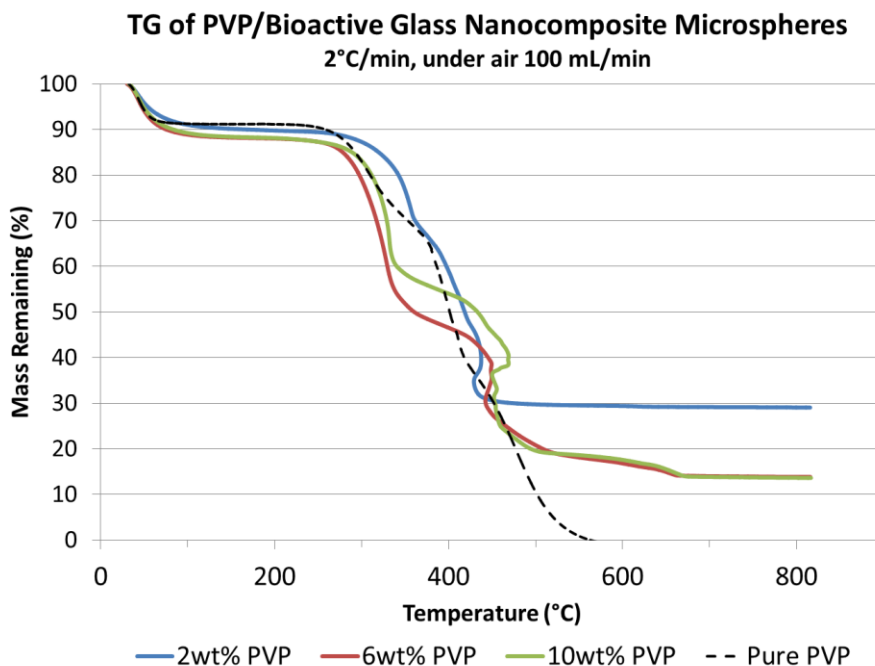


Figure 3-2. Mass loss versus temperature for PVP/bioactive glass microspheres.

TG/DTA analysis was used to determine the approximate ratio of organic and inorganic components in the microspheres. All samples lost approximately 10% of their initial mass upon heating to 150 °C. This mass loss is largely associated with residual water or ethanol being driven out of the microspheres. However, completion of the sol-gel reaction by condensation of residual silanol or alkoxide groups will also produce a mass loss in this region. Mass loss between 150-800 °C is attributed to the removal of the organic polymer. Therefore, the percent mass loss in this range (Table 3-4) is assumed to be the weight percent polymer in the microspheres.

Compositions prepared with 2 wt% PVP (Figure 3-2) lost approximately 68% of its original mass between 150-800 °C. Microspheres prepared with 6 and 10 wt% PVP lost approximately 85% of their mass. This indicates that microspheres prepared with 6 and 10 wt% PVP had essentially the same ratio of organic to inorganic components. All nanocomposites made with PEG lost between 26-29% of their original weight. There

was no correlation between PEG concentration and mass loss (Figure 3-3).

Microspheres prepared with gelatin lost between 65-81% of its mass between 150-800 °C. The mass loss directly correlated to the concentration of gelatin (Figure 3-4).

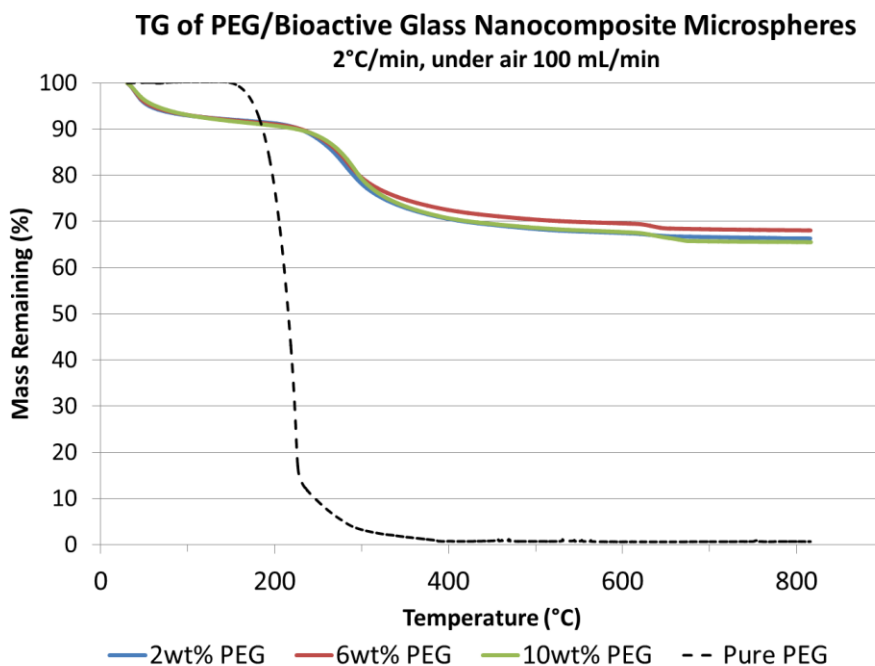


Figure 3-3. Mass loss versus temperature for PEG/bioactive glass microspheres.

The mass loss curves for the PVP microspheres showed unusual backwards loops at ~450 °C. This is caused by a rapid mass loss followed by a significant exothermic event (Figure 3-5). The slight delay (approximately 1 min) between mass loss and temperature increase creates an artifact that appears as “loops” when sample mass is plotted versus temperature. This delay may have been caused by the heat capacity of the sample holders. The artifact was more pronounced at faster heating rates.

Samples containing gelatin also displayed this behavior when heated at 10 °C/min. The PEG microspheres did not display this behavior at heating rates between 2-10 °C/min.

This sharp exothermic event may correspond to microspheres that ruptured during heating. SEM analysis of the remnants of the TG/DTA heat treatment reveals hollow

spheres, many of which had ruptured. These hollow spheres appear similar to that reported by Park, et al.¹¹⁵

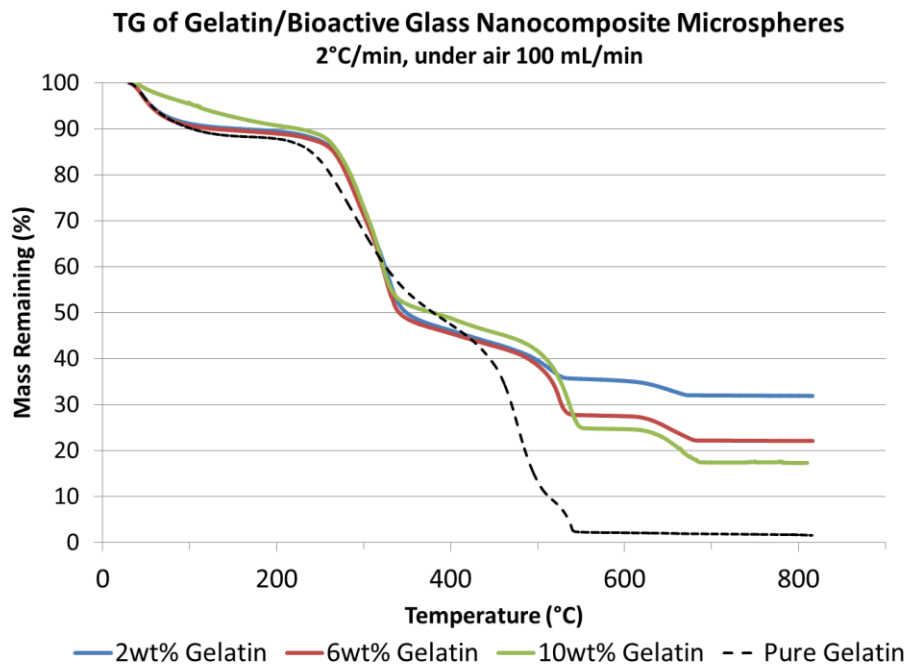


Figure 3-4. Mass versus temperature for gelatin/bioactive glass microspheres.

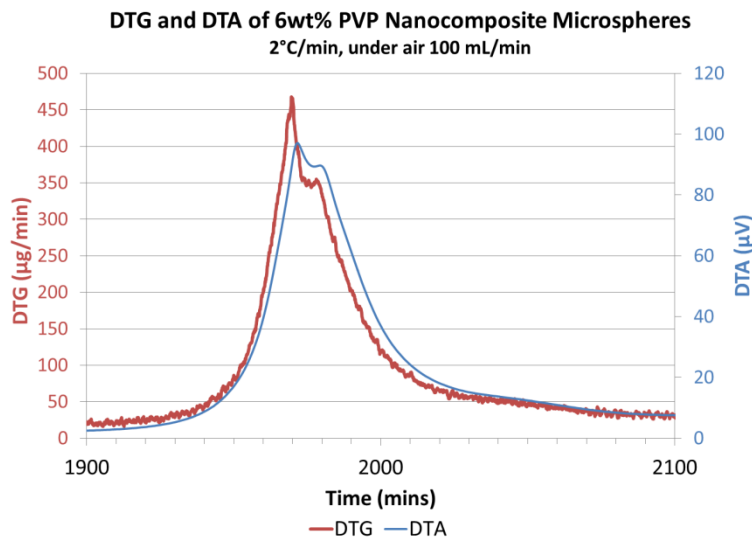


Figure 3-5. First derivative of sample mass versus time (DTG) and thermal differential (DTA) signals for 6 wt% PVP nanocomposite microspheres.

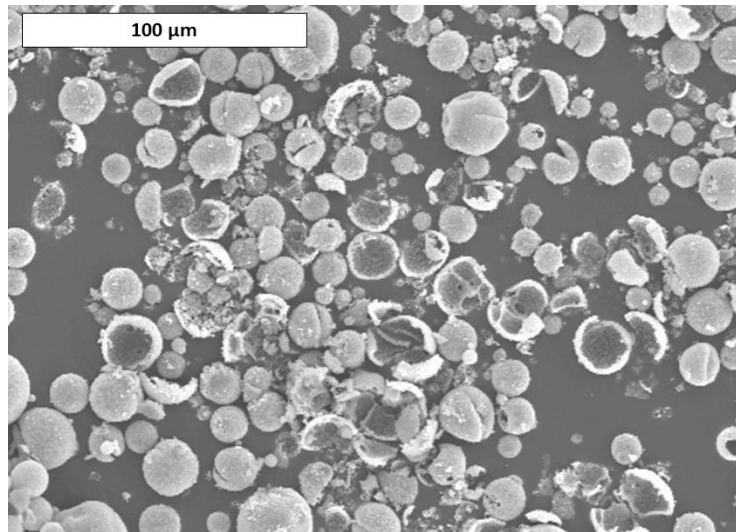


Figure 3-6. SEM micrograph of 10wt% PVP bioactive glass microspheres after heating to 800 °C.

Microspheres containing PVP and gelatin dissolved within 1 day of immersion in SBF. There were no spherical particles 10s μm in diameter observed by SEM at this time (Figure 3-7). The material that remained predominantly consisted of calcium and phosphorous at a 1.4:1 ratio as measured by EDS (Figure 3-8). Silicon was detected in the remnants of the gelatin microspheres. The remnants of the PVP microspheres had a weak silicon signal.

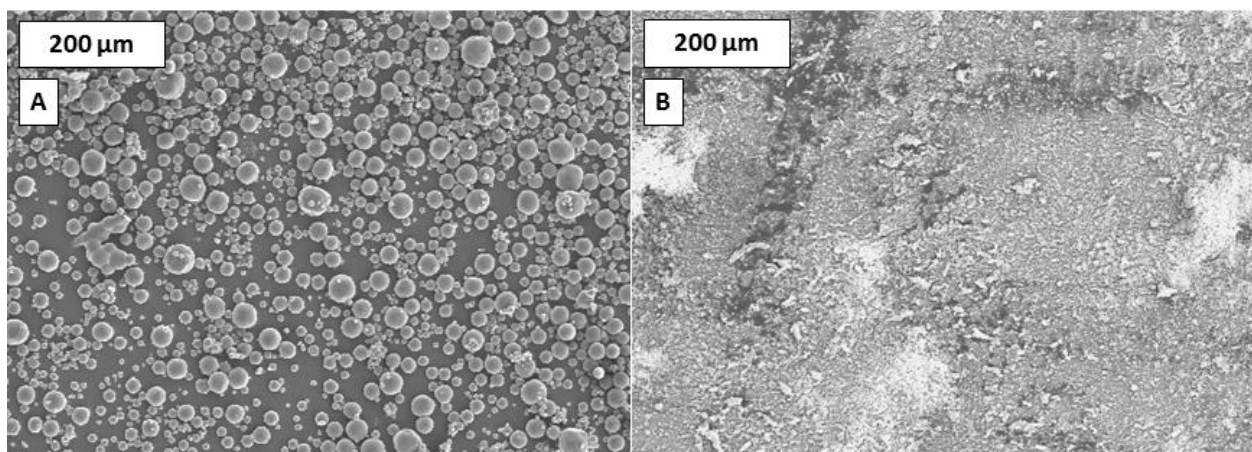


Figure 3-7. Dissolution of 10 wt% PVP microspheres. Microspheres (A) prior to immersion and (B) after 1 day in SBF.

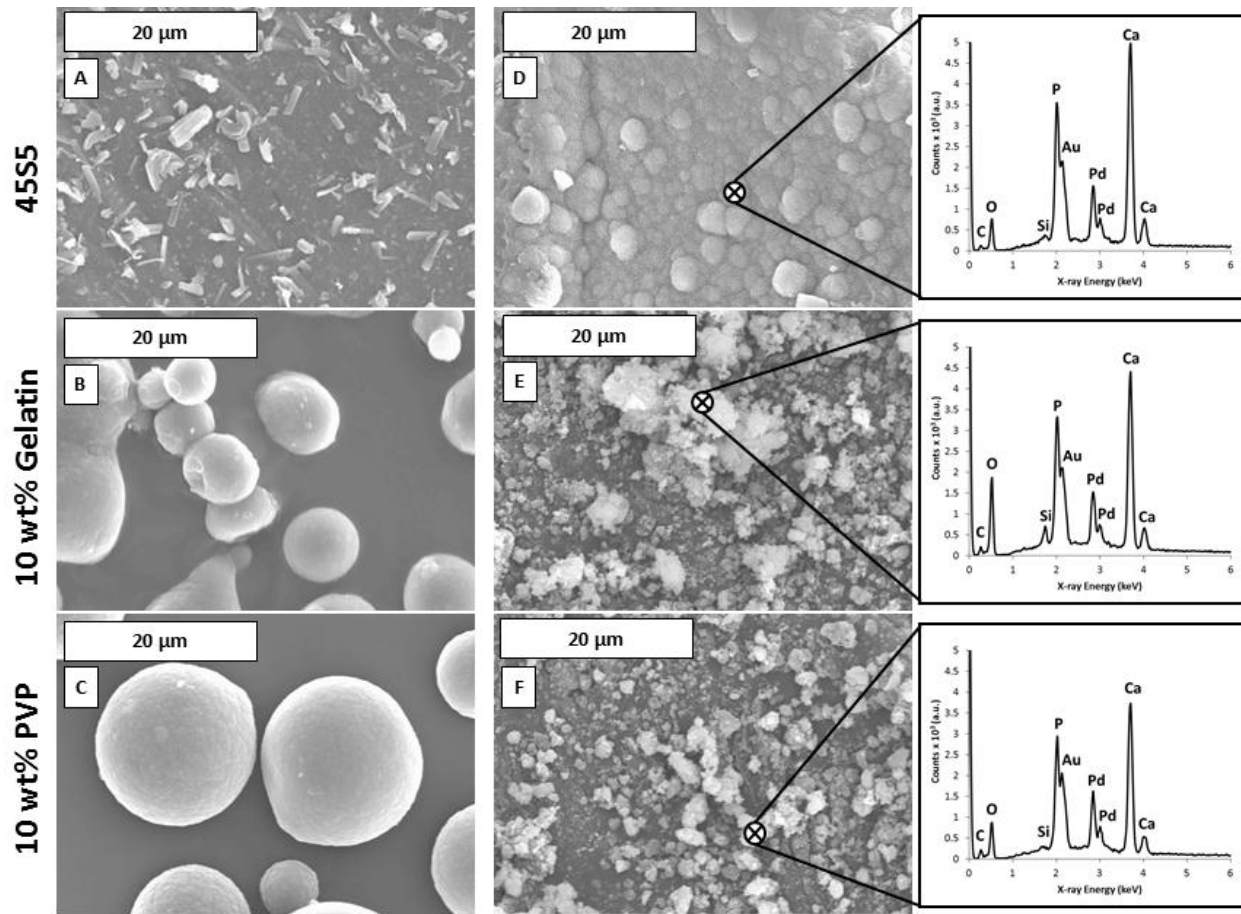


Figure 3-8. Electron micrographs bioactive glass particles prior to and after immersion in SBF for 7 days. (A-C) Prior to immersion in SBF. (D-F) Material remaining after 7 days immersion in SBF with corresponding EDS spectra.

The surface of the 45S5 particles drastically changed after 7 days in SBF (Figure 3-8D). The surface appeared coated with a material that had a coral-like morphology. This morphology is commonly associated with hydroxyapatite nucleated on bioactive glass surfaces hydroxyapatite^{7,110,120-122}. This coating was also rich in calcium in phosphorous, with a Ca:P ratio of 1.4.

XRD analysis was performed to examine the crystallinity of the calcium phosphate compounds observed after immersion in SBF (Figure 3-9). All samples showed a weak peak around $2\theta = 31.8^\circ$, which is the (211) reflection and strongest peak for

hydroxyapatite. The peaks were broad, which indicates a small crystal size. No other characteristic peaks of hydroxyapatite were observed.

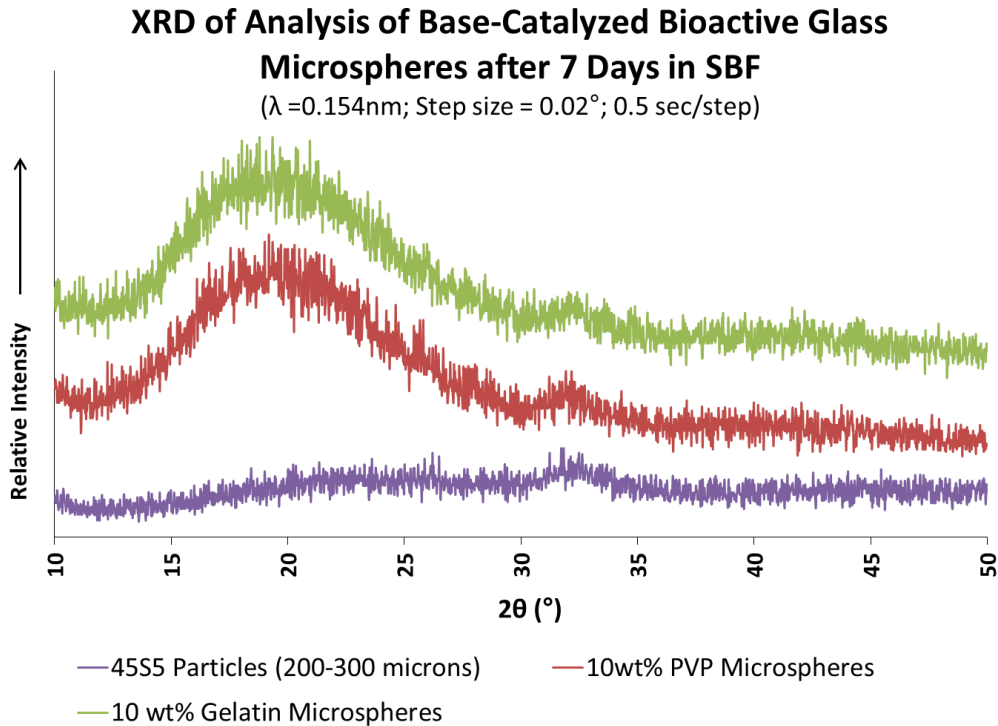


Figure 3-9. XRD spectra of base-catalyzed bioactive glass microspheres after immersion in SBF for 1 week.

Nucleation of hydroxyapatite occurs by reacting with ions in SBF, which was monitored by ICP-AES. Hydroxyapatite formation is indicated by a decrease in phosphorous concentration. This occurred for all samples, although more rapidly for SBF containing microspheres (Figure 3-10 B and C) than SBF containing 45S5 particles (Figure 3-10A). Microspheres produced a higher calcium concentration after 1 day which subsequently decreased at days 3 and 7. The calcium concentration decreased more slowly in SBF containing for 45S5 particles. All of the samples released silicon (likely in the form of $\text{Si}(\text{OH})_4$). The concentration of Si was highest for the 6 wt% gelatin composition, which reached a value of ~ 30 ppm after the first day of immersion.

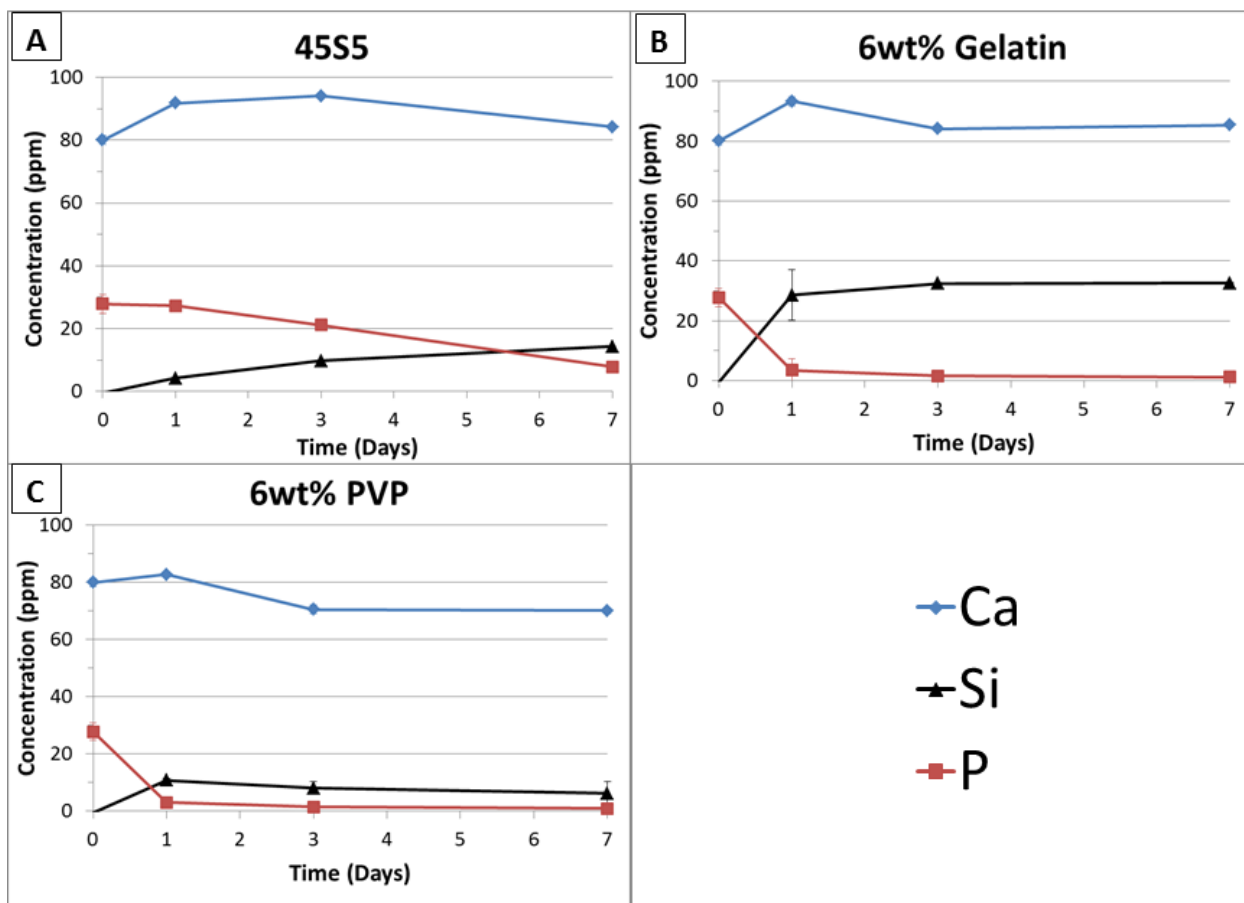


Figure 3-10. Elemental composition of SBF containing various compositions of bioactive glasses as measured by ICP-AES. The elemental composition at day 0 is the composition of SBF for all samples. Error bars indicate 95% confidence intervals. A) SBF containing 45S5 glass particles. B) SBF containing 6 wt% gelatin nanocomposite microspheres. C) SBF containing 6 wt% PVP nanocomposite microspheres.

Discussion

This study demonstrates, as a proof-of-concept, that microspheres consisting of calcium silicate and water-soluble polymers can be made by a water-in-oil process. Solutions containing PVP (6 and 10 wt%) and gelatin (2, 6 and 10 wt%) produced microspheres ~10s μm in diameter. This particle size corresponds to the size of the droplets in the initial emulsion as shown by Park, et al.¹¹⁵ Calcium was detected by

EDS in these microspheres at a ratio of ~1:1 with silicon. The inorganic content was 15-32% and was consistent for microspheres over this composition range.

However, the substitution of PVP or gelatin with PEG caused a significant change in morphology and composition. First, the particles were too small (<1 μm) to be associated with the initial droplets of the emulsion. EDS revealed that these particles contain less calcium than microspheres made with PVP or gelatin. The PEG particles contained much more inorganic material (~63%) than those made with PVP or gelatin. Therefore, it is likely that a different phenomenon is responsible for the morphology of the PEG-silicate material.

The incorporation of organic polymers into inorganic sol-gel systems can be described in terms of classical polymer-polymer mixing. The silicate phase is assumed to be a polymeric species which has a molecular weight that is increasing with time. Phase separation can occur depending on the compatibility of the two polymeric components. This behavior can be described by the Flory-Huggins equation for a two-component polymer mixture:^{123,124}

$$\Delta G \propto RT \left[\left(\frac{\varphi_1}{P_1} \right) \ln(\varphi_1) + \left(\frac{\varphi_2}{P_2} \right) \ln(\varphi_2) + \chi_{12} \varphi_1 \varphi_2 \right]$$

in which ΔG is the free energy of mixing, R is the gas constant, T is temperature, φ_i is the volume fraction of component i , P_i is the degree of polymerization of component i , and χ_{12} is the interaction parameter between the two components.

PEG-silica gels have been shown to undergo phase separation to produce structures ranging from macroporous, bi-continuous structures to aggregated particles. Nakanishi, et al.¹²⁵ reported that PEG-SiO₂ phase separated gels consist of 22-32 wt%

organic material. This correlates well to the polymeric content of the PEG-silicate particles measured in this study (26-29 wt%).

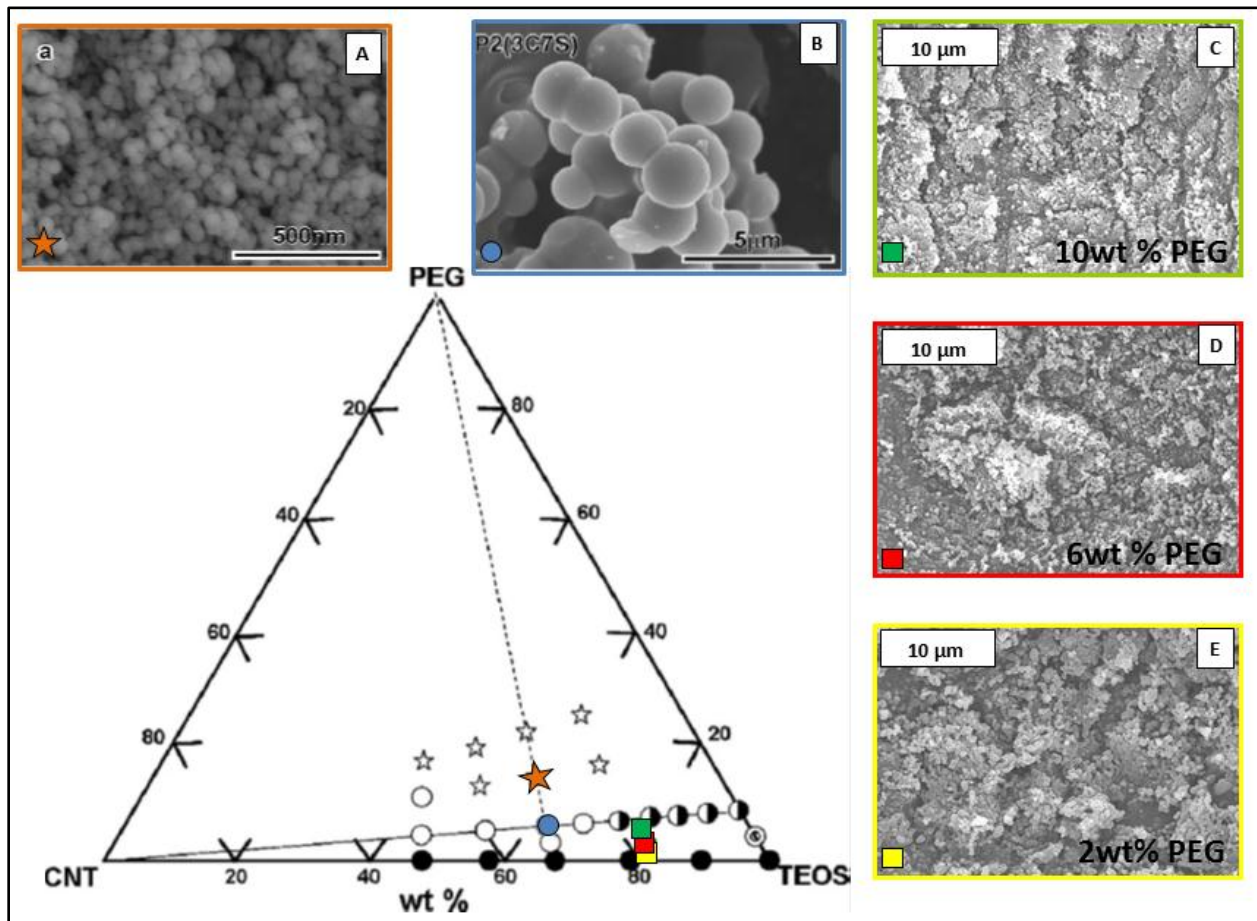


Figure 3-11. Phase behavior in the calcium nitrate tetrahydrate (CNT)-PEG-TEOS system. (A-B) Particulate structures observed by Kim, et al.¹²⁶ are indicated by circle and star shapes. (C-E) Compositions produced in this study, which also produced submicron particulate morphology. Phase diagram and images reproduced from Kim, et al. with permission.

Kim, et al.¹²⁶ demonstrated that the $\text{Ca}(\text{NO}_3)_2$ -PEG-TEOS system is capable of producing a range of morphologies by phase separation (Figure 3-11). Aggregated microparticles (Figure 3-11 A-B) were observed when PEG was present in the sol. The primary particle size was inversely correlated to the concentration of PEG. These aggregated particles were observed in a similar region of the phase diagram to the

compositions tested in this study (Figure 3-11 C-E). Although the PEG-silicate particles in this chapter appear smaller than would be predicted by the phase diagram established by Kim, et al. This is likely due to the catalyst that was used in this study (basic) compared that used by Kim, et al. (acidic). Base-catalyzed systems encourage silicates to form a particulate morphology. It is worth noting that despite using different catalysts, similar structures were observed in both studies.

Kim et al.¹²⁶ also showed that the Ca:Si ratio in PEG-silicate gels (as measured by EDS) is approximately 1/3 the molar ratio Ca:Si of the initial sol. A similar observation was made in this study; the PEG-silicate particles had a Ca:Si ratio of $\sim\frac{1}{2}$ that of the initial sol. Both studies demonstrate that calcium is not completely incorporated into the silicate. The slightly higher Ca:Si ratio in this study can be attributed to pH. The water surrounding calcium ion is more hydrolyzed at high pH.⁷⁶ This produces hydroxyl groups which can condense with the silicate or undergo hydrogen bonding with PEG.

Elemental analysis of SBF showed an increase in the concentration of silicon and calcium within the first day for all compositions. Calcium and silicon indicate that the glass is dissolving. The concentration of phosphorous decreased more rapidly in SBF containing microspheres than 45S5 particles. These results are consistent with those of Saravanapavan, et al.¹²⁷, which showed that sol-gel derived glasses react more rapidly with the ions in SBF than melt derived, 45S5 glass. The rapid loss of phosphorous indicates that the microspheres precipitate hydroxyapatite more quickly than the 45S5 particles. The rapid degradation of the microspheres likely caused a burst-release of calcium, which saturated the solution and drove calcium phosphate precipitation. The

burst release of calcium was observed by ICP-AES on the first day of immersion (Figure 3-18).

The PVP and gelatin microspheres did not retain their initial shape upon immersion in SBF. Rather, they appear dissolve or “fall apart,” leaving behind hydroxyapatite and a small amount of submicron silica particles. Heating the microspheres to 800 °C led to ruptured, hollow silica shells. These results point to a nanocomposite morphology (Figure 3-12) in which the organic polymer is the matrix that binds silicate nanoparticles at the edge of the microsphere. The submicron silica particles are generated by the base-catalyzed condensation of silicate species at the edge of the droplet. The interior of the particle remains largely organic.

The interaction between the polymer and silica surface dictates the stability of the nanocomposite. Microspheres made with PVP or gelatin are stable, indicating a strong preference of these polymers for the silica surface. Hydrogen bonding of the carbonyl group of PVP to silanol groups on ammonia-catalyzed silica has been demonstrated in the literature by NMR spectroscopy¹²⁸. Gun'ko, et al. observed hydrogen bonding between PVP and fumed silica by FTIR¹²⁹. It is likely that gelatin forms a similar hydrogen bond to the silanol groups due to the structural similarities between gelatin and the amide-like bond in the PVP ring. The free energy of the PVP-silanol hydrogen bond has been calculated by density functional theory as -25 kJ/mol in the presence of water¹²⁹. This is greater than the free energy of binding polyethylene oxide to silica surface, which has been estimated to be -5.9 kJ/mol in the presence of water¹³⁰.

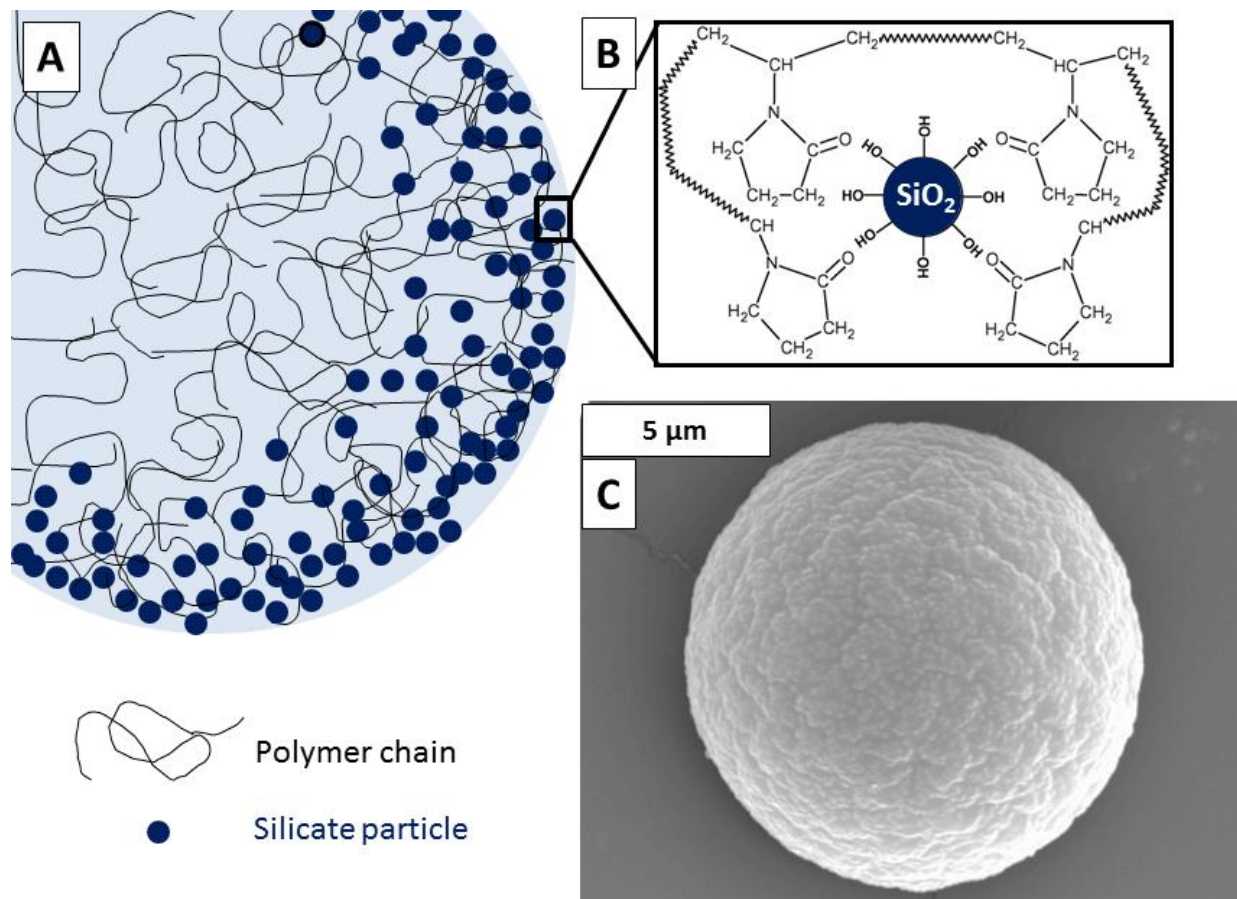


Figure 3-12. Proposed structure of PVP and gelatin nanocomposite microspheres produced by base catalysis. (A) Silica nanoparticles form at the surface of the droplet and are bound together by the polymer. (B) Hydrogen bonding between the silanol groups and the carbonyl of PVP binds the organic and inorganic phases together. Image adapted from Xu, et al.¹²⁸ with permission. (C) High magnification SEM image of 10 wt% PVP microsphere, which exhibits a surface texture indicative of the structure shown in (A).

The nanocomposite structure proposed in Figure 3-12 can be disrupted by water. Dissolution of the organic matrix leaves behind submicron silica particles. Silicate material was observed in the remnants of the gelatin microspheres (Figure 3-8). Future experiments should use small angle X-ray scattering (SAXS) and transmission electron microscopy (TEM) to confirm the nanocomposite structure of the microspheres.

Summary

Three water-soluble polymers (PEG, PVP, and gelatin) were tested for their ability to form microspheres with sol-gel derived bioactive glasses. PVP and gelatin produced microspheres 1-40 μm in diameter as dictated by the droplets of the initial emulsion. These microspheres contained a significant amount of calcium and dissolve within 1 day in SBF. Compositions made with PEG produced 0.2-1 μm aggregated silicate particles with low concentration of calcium and polymer concentration. Phase separation appeared to be driving the formation of these PEG-silicate particles. Microspheres made with PVP or gelatin appear to have a nanocomposite structure in which the polymer acts as a matrix and binder for silicate nanoparticles. Future work attempting to encapsulate drugs in bioactive glass microspheres should use PVP or gelatin because they produce more stable particles. The dissolution rate of the microspheres should be slower if they are to be used as extended drug release materials.

CHAPTER 4 PARAMETERS AFFECTING THE SIZE AND MORPHOLOGY OF ACID-CATALYZED BIOACTIVE GLASS MICROSPHERES

Introductory Remarks

Microspheres comprising calcium silicate glass and various water soluble polymers were made by a W/O emulsion in the previous chapter. The organic polymer was the largest component of these microspheres by weight. The polymer component seemed to act as the matrix in a nanocomposite structure, which caused the microspheres to rapidly degrade in SBF. The ideal material for treating osteomyelitis should fight the disease and regenerate tissue lost from the infection. The microspheres described in chapter 3 degraded within one day in SBF. Microspheres should hold their shape over a period of at least one week to effectively stabilize a wound. Increasing the glass content in the nanocomposite may slow the degradation of the particles. It may be possible to do this by making microspheres at a lower pH.

Acid-Catalyzed Microspheres

One of the most important factors dictating the structure of sol-gel derived materials is the pH of the sol. TEOS hydrolyzes more readily in acidic solutions than in basic solutions. Hydrolysis is restricted to the oil/water interface in this procedure. This produces silicate species which become more soluble in the aqueous phase as the degree of hydrolysis increases. Once drawn into the droplet, the silicate species can subsequently interact with PVP and/or undergo condensation. Because hydrolysis is more rapid at low pH, droplets containing an acid catalyst should generate more hydrolyzed silica, resulting in microspheres with more inorganic material. This may also change the structure of the microsphere from discrete, silica particles dispersed in an organic coating to a more cross-linked and interconnected network. The first goal of

this chapter is to identify the differences between microspheres presented in chapter 3 (base catalyst) with those made with an acid catalyst.

An initial study was performed to evaluate the effects of acid-catalysis on microsphere formation and composition. Three compositions of microspheres were made for this study: compositions containing PVP (molar mass ~1,000 kg/mol), gelatin (molar mass ~50 kg/mol), and one composition without any polymer present in the aqueous phase. SEM/EDS and thermogravimetric analysis was performed to examine the general structure and composition of these acid-catalyzed microspheres.

Compositional Effects on Size and Morphology

The second goal of this chapter is to identify how the initial sol composition affects the final microsphere size and morphology. Size and morphology are important factors that can affect the release rate of drugs and attachment of cells. Therefore, it is important to understand how the composition affects the size and shape of the final microsphere.

The relationship between sol composition and microsphere size is examined in the context of droplet formation. The emulsion is crucial in this procedure because the droplets act as templates for the final microspheres. An emulsion is a mixture of two immiscible liquids consisting of a discontinuous phase dispersed in a continuous phase. Stirring the emulsion leads to the formation of droplets of the discontinuous phase. The work required for forming droplets is given by:

$$W = \Delta A \times \gamma_{int}$$

where ΔA is the change in interfacial area between the two liquids and γ_{int} is the interfacial tension. Smaller droplets can be created by adding more work into the system (such as stirring the emulsion faster). Lowering the interfacial tension also

produces smaller droplets for a fixed amount of work. One of the most common methods for lowering interfacial tension is through the use of a surfactant.

Surfactants are molecules that contain both hydrophilic and hydrophobic groups. These molecules selectively partition at the interface between two immiscible liquids. This reduces the thermodynamic “penalty” of creating an interface between the two liquids, resulting in a lower interfacial tension. The surfactant molecule may have more of a hydrophilic or hydrophobic character, depending on the chemistry. The HLB number (hydrophilic/lipophilic balance) is a semi-quantitative measure of this character. Surfactants with HLB <10 tend to be oil-soluble, while HLB >10 are water soluble. Surfactants are most successfully employed when they are soluble in the continuous phase of the emulsion. Span 80, the non-ionic surfactant used in these experiments, has HLB ~4, which makes it suitable for use in the oil phase, 1-octanol.

Emulsions are thermodynamically unstable systems. In the absence of stirring there is a constant driving for droplets to coalesce and reduce the interfacial area between the two liquids. Polymers dissolved in the continuous phase slow the process of coalesce by limiting the diffusion of droplets. Thickeners, such as hydroxypropylcellulose used in this system, are commonly added to stabilize the emulsion. However, increasing the viscosity of the continuous phase means that more work must be added to stir the system.

This balance between viscous forces and interfacial forces is characterized by a dimensionless number called the Weber number (We). The Weber number for an emulsion is given as:

$$We = \frac{\text{viscous forces}}{\text{interfacial forces}} = \frac{d\dot{\eta}_c}{2\gamma_{int}}$$

in which d is the diameter of the droplet, $\dot{\epsilon}$ is the shear rate, and η_c is the viscosity of the continuous phase. The droplet will rupture when the Weber number exceeds a critical value (We_{cr}). A relationship between We_{cr} and the ratio of dispersed and continuous phase viscosities was identified in 1982 and is commonly referred to as the “Grace curve.”¹³¹ The Grace curve predicts that, under simple shear flow, the droplet size can vary over several orders of magnitude by changing the viscosity of the dispersed phase (Figure 4-1). Polymers dissolved in the aqueous phase can alter the viscosity of the dispersed phase in this system. This establishes a connection between solution composition and size of the final microspheres, which is one of the goals of this chapter.

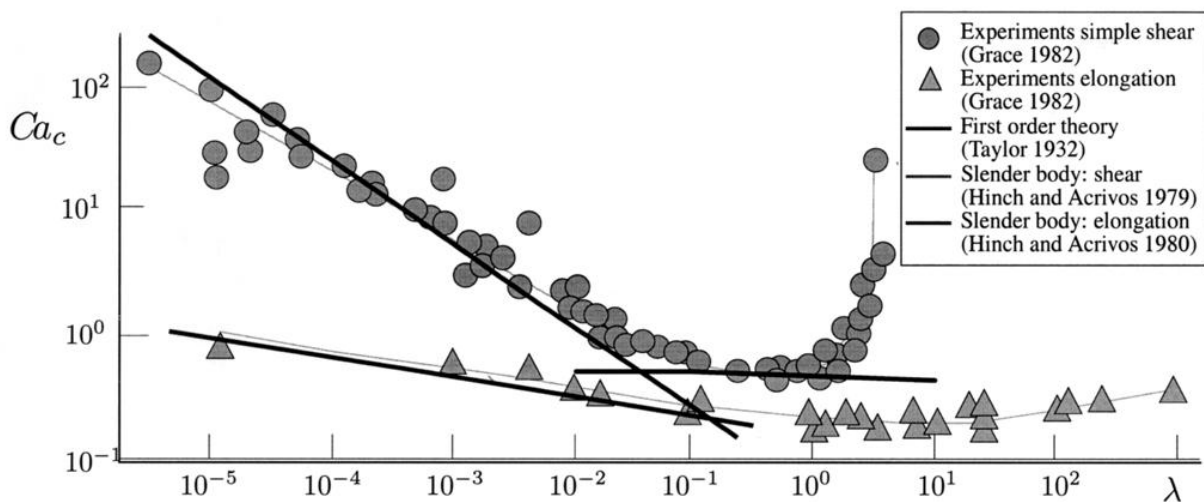


Figure 4-1. “Grace curve” relationship describing droplet breakup in an emulsion. Droplets undergoing breakup in simple shear are follow the relationship of the upper curve. Droplets undergoing breakup under elongational flow are shown by the bottom curve. Note that the ordinate (critical capillary number, Ca_c) is equivalent the critical Weber number (We_{cr}). Image from Stegeman¹³², with permission from John Wiley and Sons.

This chapter examines whether the size of the microspheres follow the behavior described by Grace¹³¹. PVP is chosen to perform this study. PVP made distinct microspheres in chapter 3 and is soluble over at a wide range of concentrations and

molecular weights. The variables tested in this study are: PVP molecular weight (10, 40, and 1,000 kg/mol), concentration of PVP (2, 6, and 10 wt% of the aqueous phase), and calcium concentration (Table 4-1). The PVP molecular weights tested in this study are predicted to be above the critical molecular weight for entanglement for PVP in water, which is calculated to be approximately 8 kg/mol (Appendix A).

The morphology of the microspheres should also be affected by the composition. This was observed in chapter 3, most notably for the gelatin microspheres. Ternary phase diagrams are used in this chapter to map out the observed morphologies of the various PVP microspheres. This is done with the aim of correlating composition to the final microsphere structure.

Finally, if the microspheres presented in this chapter are to be used for treating osteomyelitis, it is important to test whether they are toxic to bone cells. Residual ethanol or alkoxy groups can impart a toxic effect to sol-gel derived ceramics. An MTT assay is performed to evaluate the viability of osteoblasts exposed to the microspheres made in the size and morphology study. This assay relies on enzymes in the mitochondria of viable cells to reduce methylthiazolyldiphenyl-tetrazoliumbromide (MTT, a yellow compound) to a purple formazan. The formazan precipitates as crystals, which are then dissolved and measured by absorbance.

Materials and Methods

Aqueous Phase Preparation

Initial acid catalysis study

Microspheres were made with PVP (molar mass ~1,000 kg/mol, Polysciences #06067), gelatin (molar mass ~50 kg/mol, Sigma #G-939), and one without any polymer. Aqueous solutions were made by dissolving 6 wt% of polymer in a 2.8 M

solution of $\text{Ca}(\text{NO}_3)_2$. This corresponds to a 77S composition with molar $\text{H}_2\text{O}:\text{TEOS}$ ratio of 4, similar to the conditions in chapter 3. Nitric acid (1 M) was added to reach $\text{pH} = 1$ as measured by a digital pH meter. The volume of nitric acid added to each solution was less than 10% (vol/vol) for all solutions.

Size and Morphology study

Solutions of $\text{Ca}(\text{NO}_3)_2$ and nitric acid were prepared in 100 ml volumes for each glass composition (Table 4-1). PVP was dissolved in 10 ml of the appropriate salt solution at concentrations of 2, 6, or 10 wt%. PVP powders were dried at $125\text{ }^\circ\text{C}$ for 1 hr prior to adding to the solution. The aqueous solutions were covered and stirred overnight at room temperature with a magnetic stir bar to allow for complete dissolution. PVP was tested at three molecular weights (weight-averaged): 10 kg/mol (Polysciences #03315); 40 kg/mol (Polysciences #01051); and 1,000 kg/mol (Polysciences #06067). The molar ratio of reactants for each composition is listed in Appendix B.

Table 4-1. Sol-gel glass compositions tested in this study. The calcium concentration in the glass was controlled by the amount of CaNO_3 dissolved in the aqueous phase of the emulsion.

| Abbreviation ¹¹⁴ | Initial glass composition (% mole) | $\text{Ca}(\text{NO}_3)_2$ (M) | HNO_3 (M) |
|-----------------------------|--|--------------------------------|--------------------|
| 100S | 100 $\text{SiO}_2 - 0 \text{ CaO} - 0 \text{ P}_2\text{O}_5$ | 0 | 0.02 |
| 86S | 90 $\text{SiO}_2 - 6 \text{ CaO} - 4 \text{ P}_2\text{O}_5$ | 0.9 | 0.02 |
| 77S | 80 $\text{SiO}_2 - 16 \text{ CaO} - 4 \text{ P}_2\text{O}_5$ | 2.8 | 0.02 |

Microsphere Synthesis

The same oil phase was used in all studies. The oil phase was prepared as described in chapter 3 and consisted of 1-octanol with 1.4% (wt/wt) hydroxypropylcellulose and 3% (wt/wt) Span 80.

The emulsion was formed by the same method described in chapter 3. Briefly, 45 g of the oil phase was added to a 250 ml glass beaker. The oil phase was stirred at 500

rpm with a Caframo overhead laboratory mixer equipped with a pitched blade impellor. As the oil phase was being stirred, 6.1 ml of the aqueous phase was added dropwise with a pipette. The emulsion was stirred for 30 mins before adding 18.7 ml of tetraethylorthosilicate (TEOS) and triethylphosphate (TEP) (0, 1.3, and 1.4 ml for glass compositions 100S, 86S, and 77S, respectively). This mixture was stirred constantly for 24 hrs at room temperature.

The resulting slurries were poured into 50ml centrifuge tubes and centrifuged at 1,500 rpm for 15 mins to isolate the microspheres. The supernatant was poured out and 30 ml of 200 proof ethanol was added to each centrifuge tube. The samples were vortexed and centrifuged again at 1,000 rpm. This process was repeated twice. The samples were then dried under vacuum until the ethanol had evaporated by visual inspection. Samples were stored in a bell jar with desiccant.

Rheology

Rheological measurements were made on the oil and aqueous phases using a Brookfield cone and plate viscometer. A circulating water bath was used to maintain a constant temperature of 25 °C during all measurements. The calibration of the viscometer was checked against PDMS standards prior to taking measurements.

Laser Light Scattering

Particle size distributions were measured using light scattering with a Coulter LS13320. Samples were analyzed using the Universal Liquid Module by suspending the particles in 200 proof ethanol. The optical model used for calculating particle size assumed completely spherical particles of silica suspended in ethanol. This optical model assumes: fluid refractive index = 1.359, real refractive index of the sample = 1.46, and imaginary refractive index of the sample = 0.01.

SEM/EDS

Upon drying, the microspheres typically produced a single, agglomerated pellet. Agglomerates were broken up by placing them between two pieces of wax paper and lightly grinding them on a flat glass surface with a ceramic pestle. The resulting powder was spread onto double sided tape and blown with nitrogen gas at 10 psi to remove any weakly attached particles. The double sided tape was then placed on aluminum SEM stubs and sputter coated as described in chapter 3.

Cross-sectional views of the microspheres were made by embedding the particles in epoxy and fracturing the resulting composite. Microspheres were first treated with a silane coupling agent to improve the bonding with the epoxy matrix. Approximately 0.2 ml of microsphere powder was added to a 2 % (vol/vol) solution of 3-aminopropyltrimethoxysilane in 190 proof ethanol. This solution was vortexed for 2 mins and then centrifuged for 5 mins at 1500 rpm. Microspheres were washed twice with 5 ml of 190 proof ethanol. The powder was dried on a watch glass at 100 °C for 15 mins in a convection oven.

The two-part epoxy consisted of Epon 826 (Hexion) and Jeffamine D230 (Huntsman) in a 1:0.33 weight ratio. The epoxy components were first mixed before adding the silane-treated microspheres. The mixture was cast into a silicone mold and degassed for 30 mins under vacuum. Samples were cured at room temperature for 24 hrs, then at 60 °C for 2 hrs. The epoxy was fractured by hand and mounted onto aluminum SEM stubs with double-sided tape. Samples were then sputter coated with gold-palladium as described in chapter 3.

Thermal Analysis

Thermogravimetric analysis was performed on a Seiko 320. Samples were heated at 2 °C/min under air at a flow rate of 100 ml/min. The initial sample masses were 7-12 mg.

Microsphere Immersion and XRD

SBF was prepared as described in chapter 3. Microspheres were immersed in SBF at a fixed ratio of 0.001 g/ml. 45S5 bioactive glass (US Biomaterials) powder with a particle size of ~5 µm particles was included as a standard material. Microspheres were removed from SBF by filtration at through a 0.45 µm filter, dried with acetone, and stored overnight in a desiccator. XRD analysis was performed as described in chapter 3.

Osteoblast Viability

The assay was performed using human osteoblasts (NHOst, Lonza). Cells were grown in a T75 flask to 75% confluence in growth in media containing 10% fetal bovine serum, 0.1% ascorbic acid, and 1000 units of gentamicin/amphotericin A. Cells were trypsinized with a solution of 0.25% trypsin and 1 mM ethylenediaminetetraacetic acid and counted using a hemocytometer. Cells were plated into 96 well plates at a density of 5,000 cells/cm² and incubated for 2 hours at 37 °C and 5% CO₂ prior to adding microspheres.

Microspheres (77S; 1,000 kg/mol PVP; 10 wt% composition) were prepared for cell culture by washing three times with 200 proof ethanol. This was performed by vortexing 15 mg of microspheres with 10 mL of ethanol followed by centrifugation for 5 minutes. The supernatant was removed by pipette. The microspheres were then dried by placing them in an oven at 150 °C for 16 hrs. The microspheres were pre-treated by

soaking in 3.8 ml of media for 15 mins. This solution was centrifuged and the media replaced prior to seeding the microspheres. Cells were allowed to attach to the wells for 2 hrs before adding microspheres. The microspheres were suspended by repeated pipetting before adding them to the plate. Microspheres were seeded at a density of 1 mg/cm² which corresponded appeared to cover half of the well by microscopic evaluation.

The MTT assay was performed in accordance to the instructions provided in the kit (Caymen Chemical Cat No. 10009365). After incubating the cells for 24 hrs with the microspheres, 10 µL of the MTT reagent was added to each well. The plate was incubated again for 4 hrs. The wells were then completely aspirated and 100 µL of the crystal dissolving solution was added to each well. The plate was gently mixed by hand for 5 mins prior to reading absorbance on a plate reader at 570 nm.

Six replicates were tested for each condition. Cells grown in the polystyrene well served as the positive control. Cells grown in media containing 0.05% Triton X-100 served as negative control. Wells containing particles and cells were used as an optical blank to correct for any absorbance that may have been caused by the particles.

Results

Initial Acid-Catalyzed Microsphere Study

One of the goals of this chapter was to understand the differences between acid and base catalysis on the resulting microsphere composition. Microspheres were made with either 6 wt% PVP, 6 wt% gelatin, or no polymer in the aqueous solution at pH = 1. All of the resulting microspheres were approximately 5-40 µm in diameter (Figures 4-2 through Figure 4-4), similar to the PVP and gelatin microspheres made by base catalysis in chapter 3.

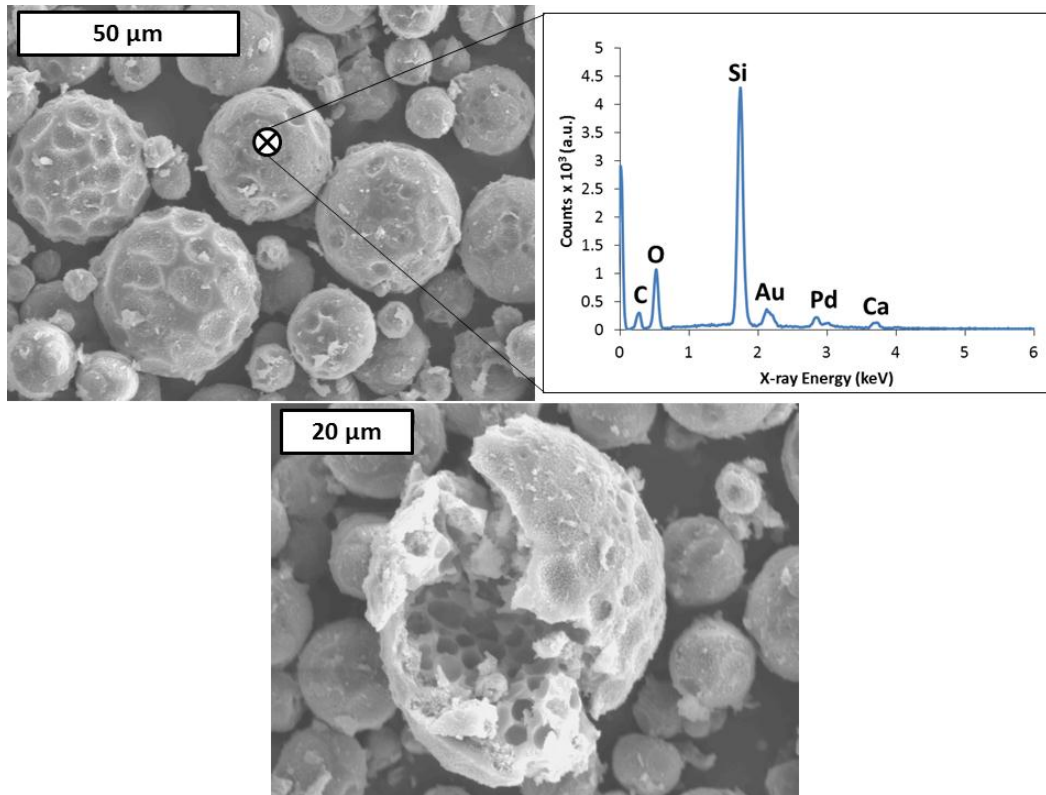


Figure 4-2. SEM images of acid-catalyzed bioactive glass microspheres made with 6 wt% PVP in the aqueous phase. EDS spectrum was taken on the spot indicated in the image. Secondary electron image, 15 keV accelerating voltage, 16 mm working distance.

Microspheres made with PVP were not completely smooth and appeared to have dimples on their surface. A few microspheres were fractured and appeared to have an interior structure that contained many voids (Figure 4-2). Microspheres made with PVP appeared larger by examination of the micrographs (up to ~40 μm) than those made with gelatin (up to ~20 μm). Gelatin microspheres did not appear to have dimples or voids such as those made with PVP (Figure 4-3).

It was possible to form microspheres without any polymer dissolved in the aqueous droplets. These microspheres were also dimpled, although not to the extent as compositions made with PVP (Figure 4-4). This composition had a much higher proportion of fractured particles than compositions containing PVP or gelatin. The

contents of the fractured particles appeared to be a fine, particulate material. This indicates these microspheres may have been mechanically weaker than those containing PVP or gelatin.

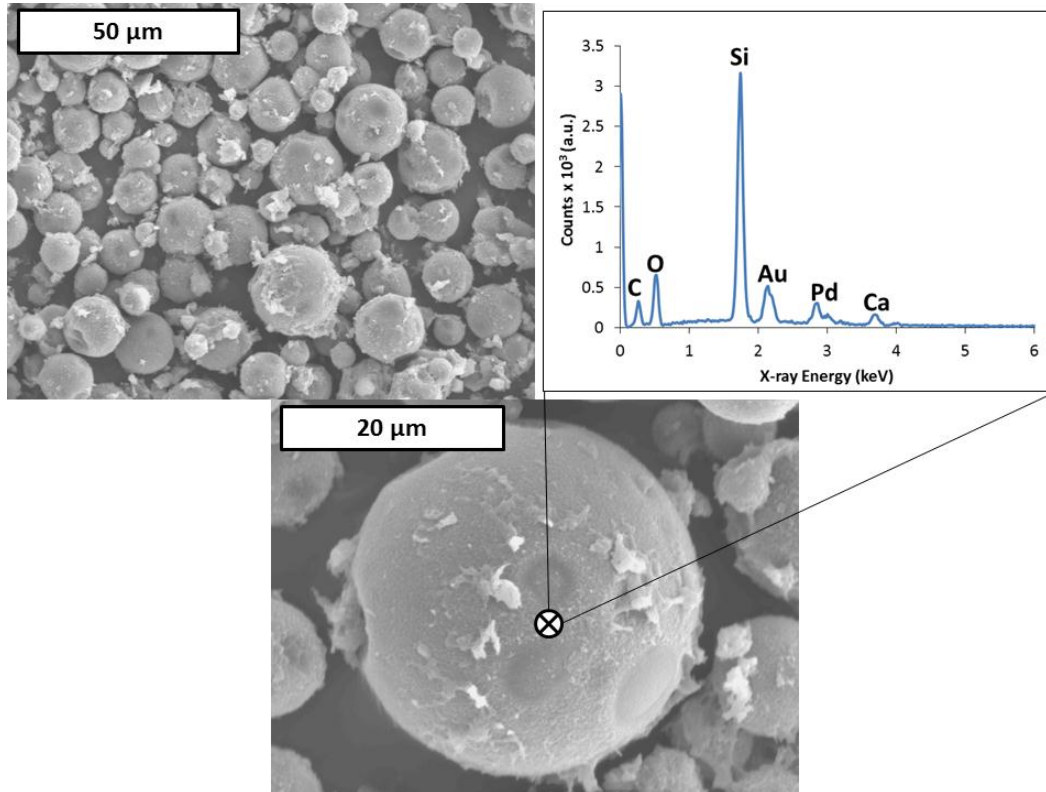


Figure 4-3. SEM images of acid-catalyzed bioactive glass microspheres made with 6 wt% gelatin in the aqueous phase. EDS spectrum was taken on the spot indicated in the image. Secondary electron image, 15 keV accelerating voltage, 16 mm working distance.

All compositions had EDS peaks indicative of silicon, oxygen, and carbon (Figure 4-2 through Figure 4-4). Microspheres made with PVP and gelatin showed peaks for calcium, although they were very weak. The Ca:Si peak ratio was 3×10^{-2} and 5×10^{-2} , for PVP and gelatin samples, respectively. This is much lower than the Ca:Si ratio of approximately 1 for samples made by base catalysis (chapter 3). Microspheres made without any polymer in the droplets did not have a detectable calcium peak.

Thermogravimetric analysis revealed that acid-catalyzed microspheres contained mostly inorganic by weight (Figure 4-5). The mass loss between 150-800 °C was 48%, 38%, and 21% for microspheres made with PVP, gelatin, and no polymer, respectively. The mass loss for equivalent compositions made by base catalysis were much higher: 84% for PVP and 75% for gelatin. Furthermore, the mass loss curves for acid catalyzed microspheres did not show the unusual “loops” that were observed in chapter 3.

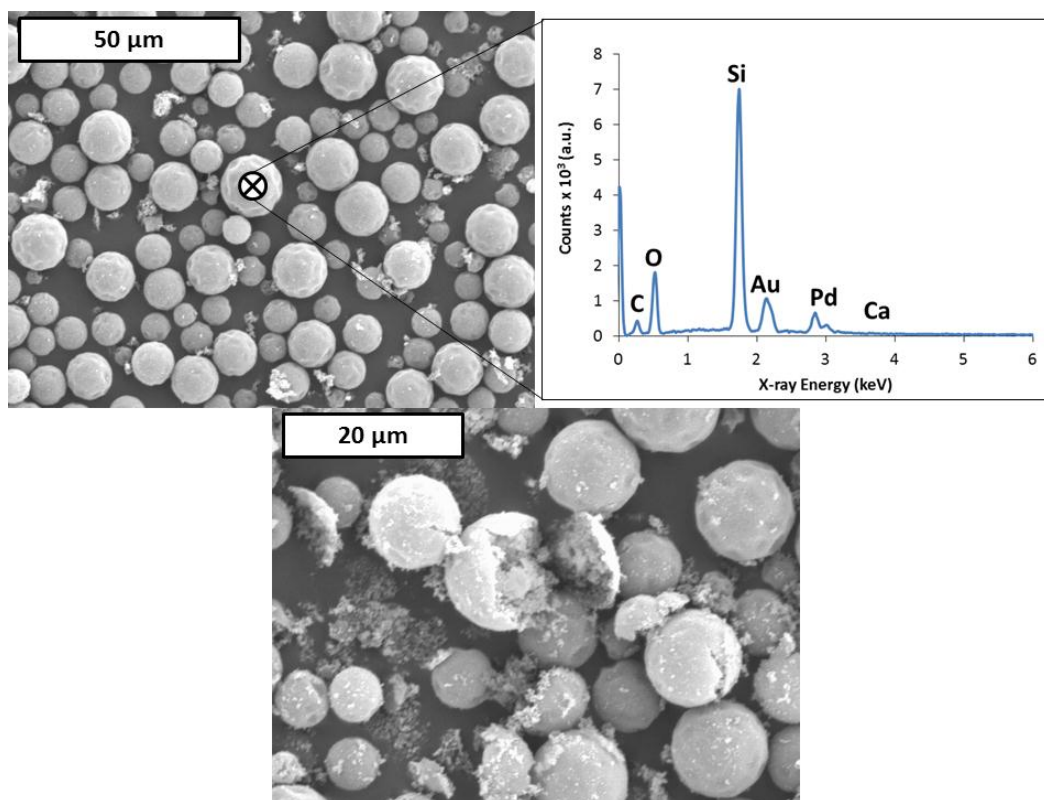


Figure 4-4. SEM images of acid-catalyzed bioactive glass microspheres made with without any polymer in the aqueous phase. EDS spectrum was taken on the spot indicated in the image. Secondary electron image, 15 keV accelerating voltage, 10 mm working distance.

XRD showed peaks characteristic of hydroxyapatite after soaking the microspheres in SBF for one week (Figure 4-6). The (211) reflection at 31.8°, which is the strongest peak for hydroxyapatite, was observed on all samples, although it was

weak for 6 wt% gelatin and no polymer microspheres. The (002) reflection at 25.9° was detected on the 45S5 particles and possibly the 6 wt% PVP sample.

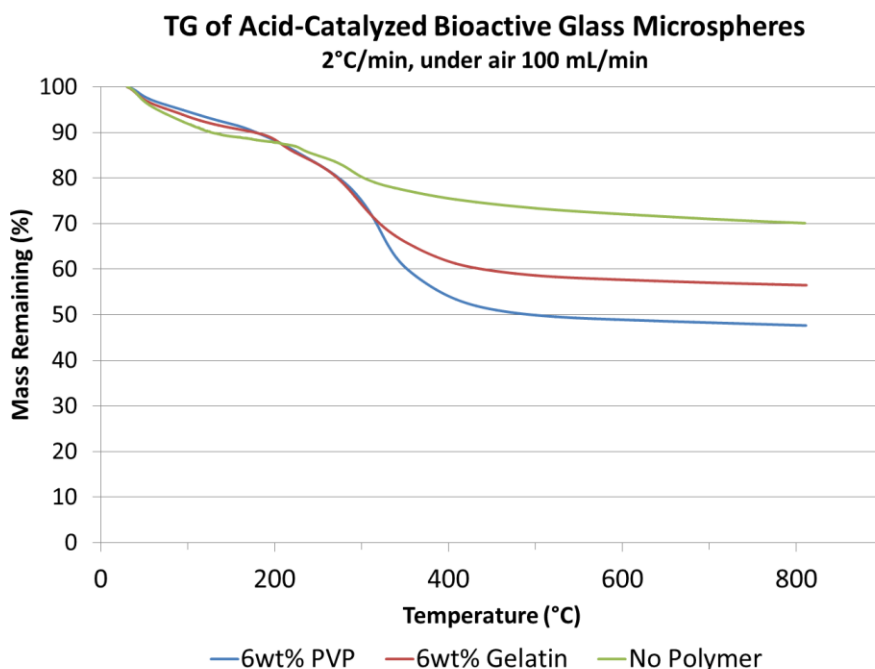


Figure 4-5. Thermogravimetric analysis of acid-catalyzed bioactive glass microspheres.

Microscopic evaluation of the immersed samples revealed globules growing off of the microspheres (Figure 4-7A). These globules are rich in calcium and phosphorous (Figure 4-7B) and have a coral-like morphology (Figure 4-7C) that has been associated with hydroxyapatite^{7,110,120,121}. This material occasionally appeared as a coating in which the underlying microspheres had dissolved or delaminated from the calcium phosphate (Figure 4-7D). Yet the microspheres made in this study appeared to maintain their shape after soaking in SBF. They did not dissolve into submicron, particles such as the microspheres in chapter 3.

Microsphere Size

Emulsion droplets act as templates for the microspheres made by this process. Particle sizes were measured in an effort to correlate size with aqueous phase viscosity.

A Weber number was calculated for each microsphere composition. The diameter was assumed to be the median (volume-weighted) particle size measured by laser light scattering. This metric of particle size appeared to correlate best with SEM observations. The interfacial tension in all instances was assumed to be 4 mN/m, which was the value Xu, et al.¹³³ measured for deionized water and 2 wt% span 80 in n-octanol. The shear rate was estimated as 83 s⁻¹. This value is 1/6 of the stirring speed (rpm) and was the recommended estimate of the shear rate given by the manufacturer of the stirrers (Caframo). The oil phase of the emulsion showed strong shear thinning behavior (Figure 4-8). The viscosity of the oil phase was estimated at a shear rate of 83 s⁻¹ by fitting the viscosity versus shear rate to a power function. This resulted in a viscosity 557 cP. The aqueous phases exhibited no shear thinning behavior (Figure 4-8).

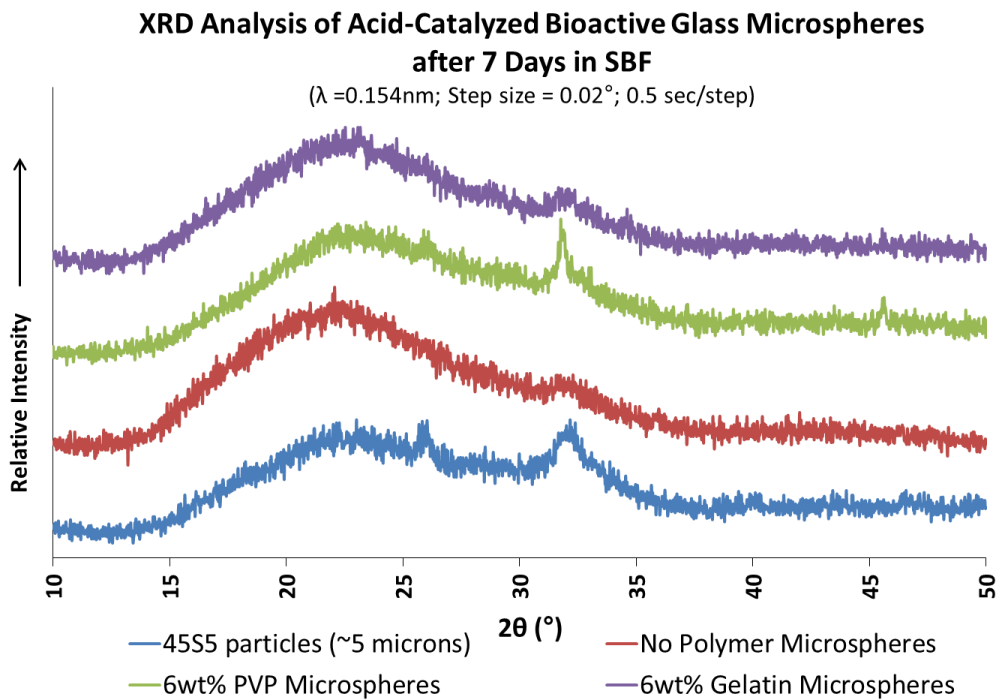


Figure 4-6. XRD spectra of acid-catalyzed bioactive glass microspheres after immersion in SBF for 1 week.

The values for dispersed phase viscosity to continuous phase viscosity (η_d/η_c) spanned nearly three orders of magnitude. The median particle sizes measured by light scattering ranged between 6-31 μm (Appendix C). These values were used to calculate the Weber number, which shows no slope on a log-log plot versus viscosity ratio (Figure 4-9). This means that changing the viscosity of the dispersed phase alone has little effect on the final particle size. The calculated Weber numbers are also lower than the predicted values for droplet breakup in simple shear.

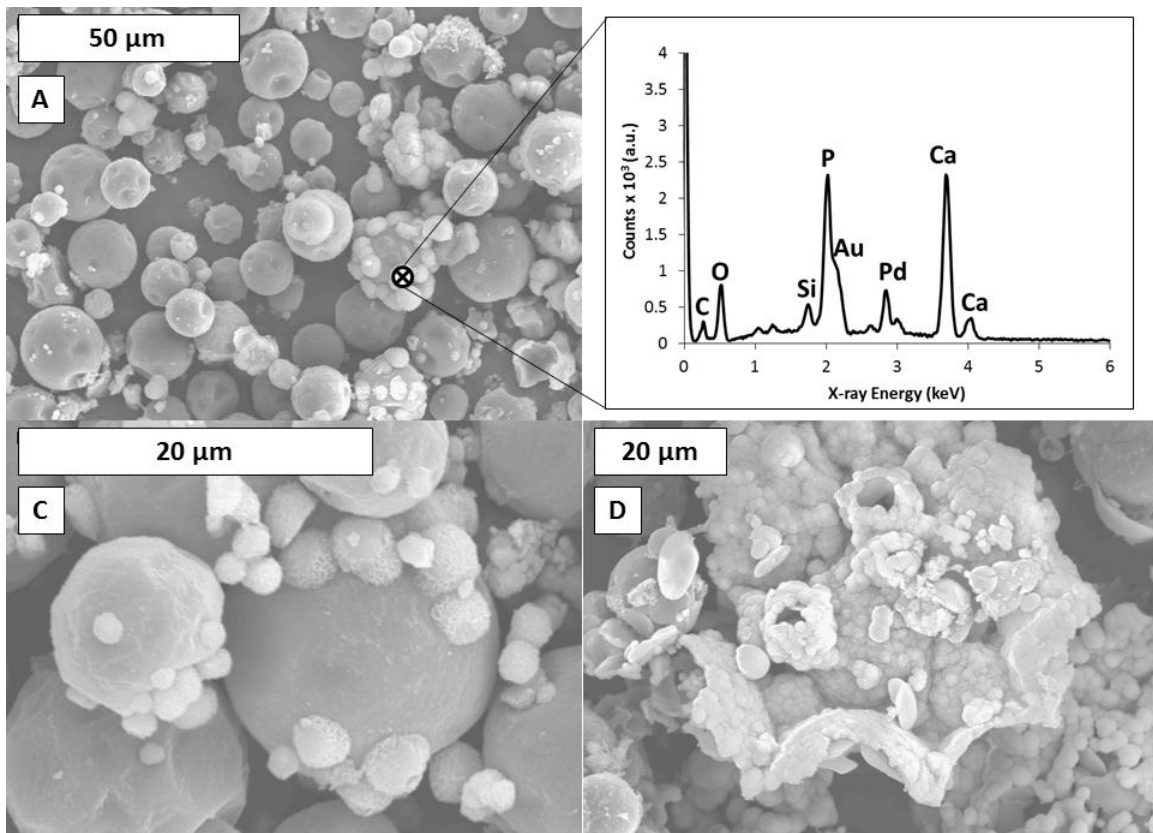


Figure 4-7. 6 wt% gelatin microspheres remain intact after one week in SBF. (A) The surface of these spheres appears to have nodules that are rich in calcium and phosphorous (B). Higher magnification of these nodules (C) shows that they appear to have a coral-like morphology, which is indicative of hydroxyapatite. (D) A calcium phosphate-rich structure that appears to have delaminated from the surface of microspheres with made from a 6 wt% PVP solution.

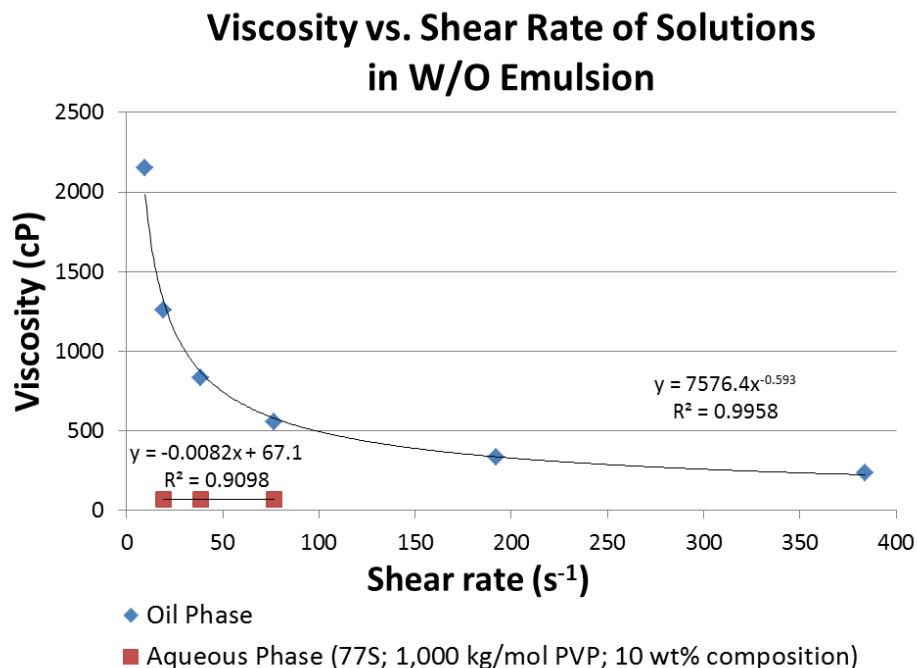


Figure 4-8. Viscosity versus shear rate for the oil phase and 77S; 1,000 kg/mol; 10 wt% aqueous phase. The power function fitted to the oil phase was used to calculate the viscosity during emulsification (557 cP at a shear rate of 83 s⁻¹).

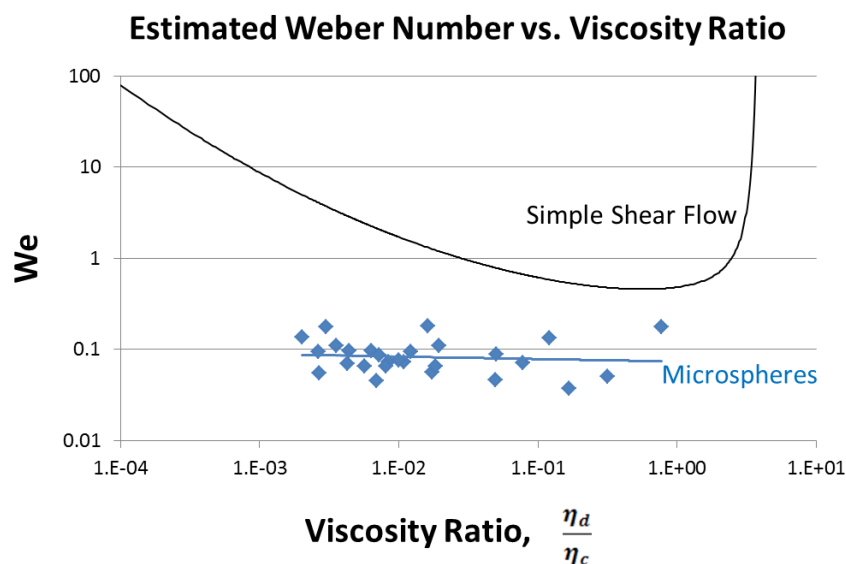


Figure 4-9. Relationship between Weber number and viscosity ratio. Calculated values for microspheres are shown in blue. The theoretical value for simple shear flow (i.e. the “Grace curve”) is shown in black and was calculated by the equation given by de Bruijn¹³⁴.

Microsphere Morphology

Several different morphologies were observed in this study. Top-down and cross-sectional images of all the compositions prepared in this study can be found in Appendix D. Mapping these morphologies on ternary phase diagrams reveals trends that hold between the three different molecular weights tested (Figure 4-10). The 100S compositions generally appeared to have a “folded” or “wavy” morphology on the surface. This was observed at all molecular weights of PVP. The “wavy characteristic” appeared to diminish with increasing concentration of PVP.

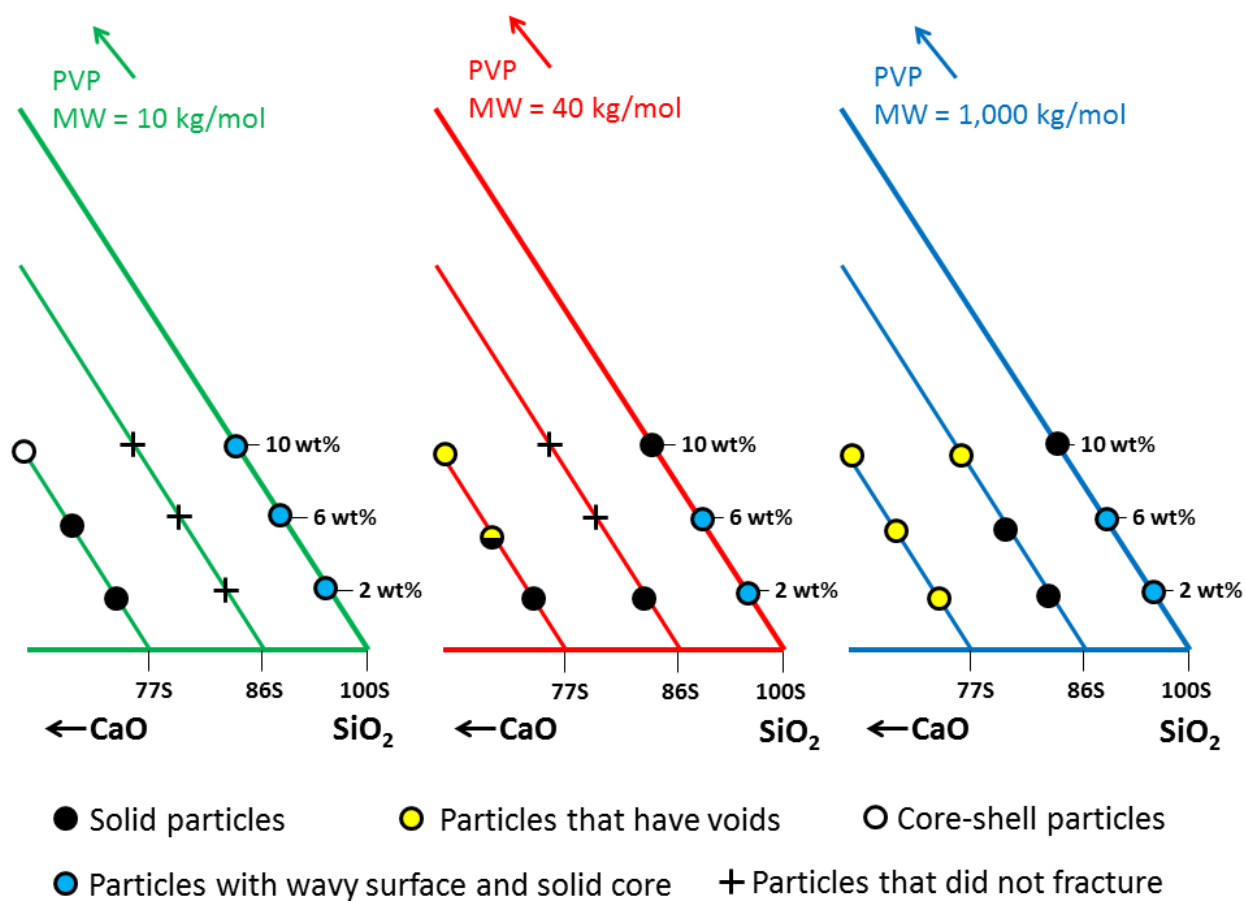


Figure 4-10. Ternary phase diagrams summarizing the observed morphologies of PVP-nanocomposite microspheres prepared by acid catalysis.

Many of the microspheres with the 86S composition did not fracture, particularly those made with 10 and 40 kg/mol PVP. A second attempt was made to embed the microspheres in epoxy using a slightly higher concentration of silane coupling agent. This yielded the same results. However, 86S microspheres prepared with 1,000 kg/mol PVP did fracture when embedded in epoxy. Compositions made with 2 and 6 wt% PVP appeared topologically uniform in cross-section. However the contrast of the backscattered electron signal appeared to be higher near the edge of the microsphere and darker towards the inside of the microsphere. When the PVP concentration was increased to 10 wt%, voids were observed on the inside of the particles.

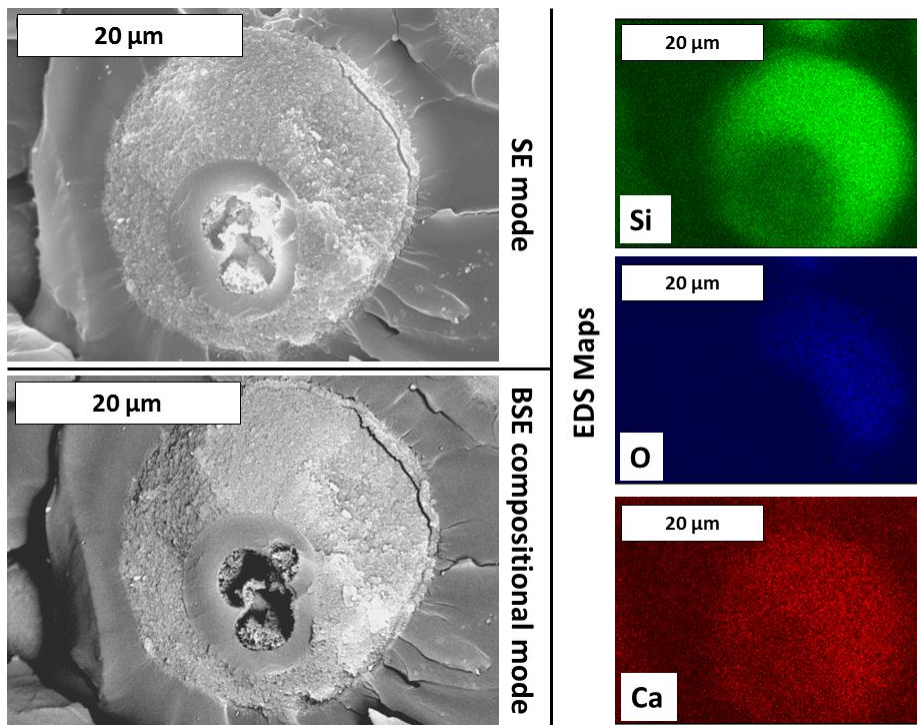


Figure 4-11. Microsphere made with 2 wt% of 1,000 kg/mol PVP in the aqueous phase at a nominal glass composition of 77S. Micrographs on the left were taken in secondary electron (SE) and backscattered electron (BSE) modes.

These voids were also observed in microspheres prepared with the highest concentration of calcium, 77S. However, voids were only observed when the molecular

weight of PVP was 40 or 1,000 kg/mol. Voids were typically surrounded by a region that appeared smooth and had low backscattered electron signal (Figure 4-11). This smooth region was surrounded by another region that appeared “rough” and had stronger backscatter electron signal. EDS mapping revealed that the outer, rough layer contains silicon, oxygen, and calcium. The inner, smooth region does not contain these elements. The relative size of the inner, smooth region appeared to be directly correlated to the concentration of PVP.

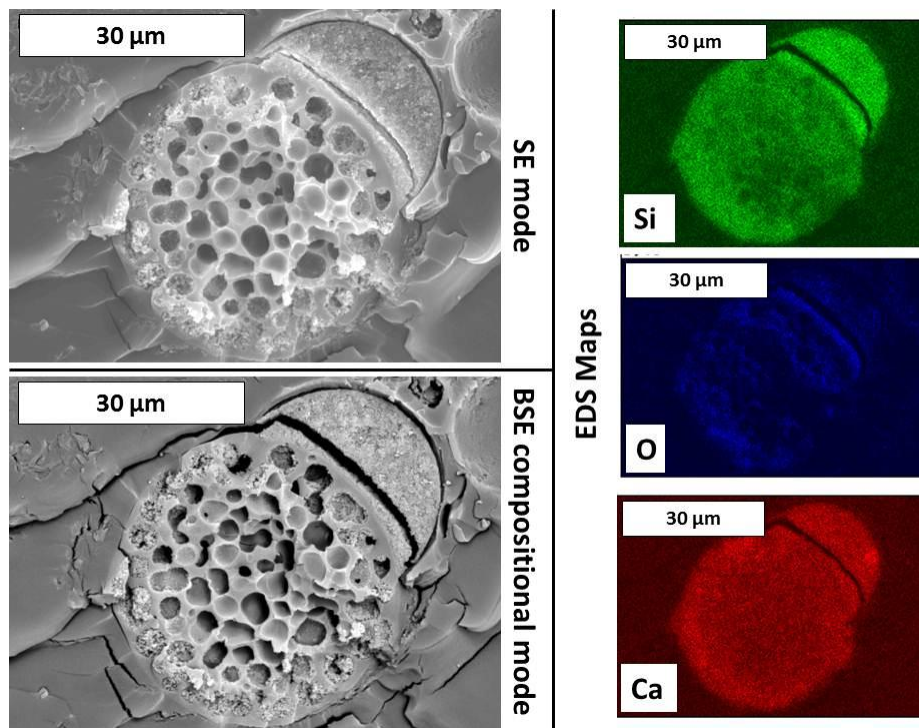


Figure 4-12. Microsphere made with 10 wt% of 1,000 kg/mol PVP in the aqueous phase at a nominal glass composition of 77S. Micrographs on the left were taken in secondary electron (SE) and backscattered electron (BSE) modes.

77S microspheres made with the highest molecular weight (1,000 kg/mol) and concentration (10 wt%) of PVP consisted almost entirely of voids (Figure 4-12). Many microspheres with this composition had a dense bulge that appeared to be growing off the primary particle. EDS mapping shows that these regions are rich in silicon.

77S microspheres made with low molecular weight PVP (10 kg/mol) showed similar behavior to 40 kg/mol particles at 2-6 wt% PVP. However, at 10 wt% PVP, the microspheres had a very unusual morphology. The particles appeared to have a solid “core” nested inside of a “shell” (Figure 4-13). EDS mapping showed that both the “core” and “shell” components contain the elements of the inorganic phase: silicon, calcium, and oxygen. This was the only composition that produced “core/shell” morphology.

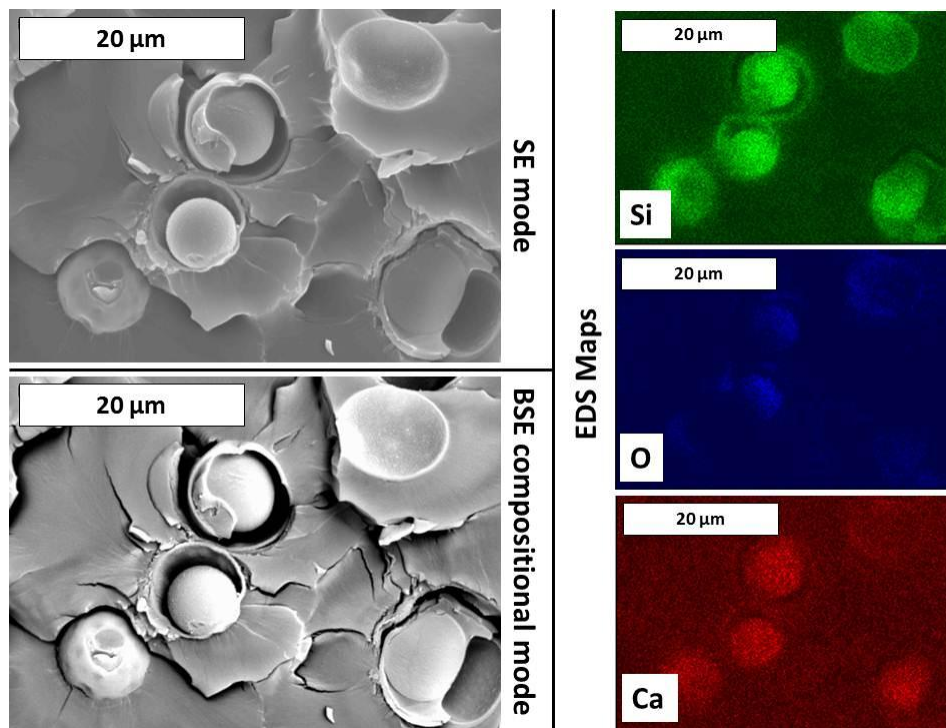


Figure 4-13. Microspheres made with 10 wt% of 10 kg/mol PVP in the aqueous phase at a nominal glass composition of 77S. Micrographs on the left were taken in secondary electron (SE) and backscattered electron (BSE) modes.

Cell Viability

Osteoblasts grown in the presence of microspheres showed a two-fold increase in absorbance over the cells grown on the polystyrene dish (positive control, Figure 4-14). This indicates that the microspheres are not only non-toxic, but they also encourage the

proliferation of osteoblasts. No absorbance was observed for cells treated with Triton X-100, as anticipated.

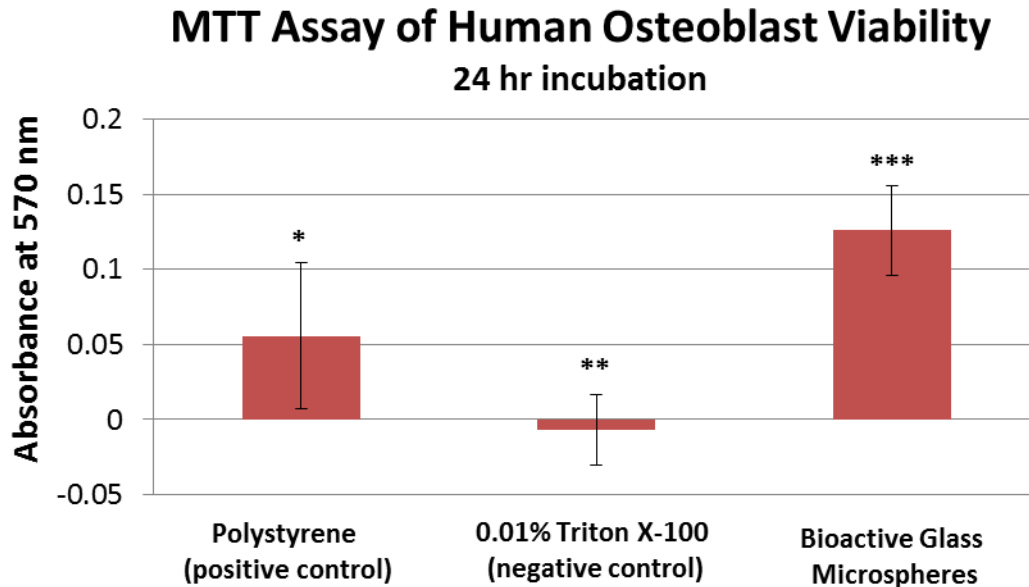


Figure 4-14. Results of MTT assay of human osteoblasts exposed to 77S; 1,000 kg/mol; 10 wt% PVP microspheres. Each condition was statically different according to an ANOVA ($\alpha = 0.05$) with Tukey's multiple comparisons test ($\alpha = 0.05$). Error bars indicate 95% confidence intervals.

Discussion

Initial Acid-Catalyzed Microsphere Study

The goal of the first study in this chapter was to identify the differences between acid and base catalyzed microspheres. Acid-catalyzed microspheres have a similar diameter to base catalyzed microspheres (~5-30 μm) which corresponds to the initial droplets of the emulsion. This indicates that the emulsion is stable over pH = 2-10.

These microspheres contained were more than 50 wt% inorganic. This is attributed to the faster hydrolysis of TEOS under acidic conditions. Efficient hydrolysis should allow more silicate species to be drawn into the aqueous phase. These hydrolyzed silicate species condense in the droplet to form the inorganic silica. Higher

silica content is one explanation for why acid-catalyzed microspheres do not dissolve as readily in SBF as those made by base catalysis.

The structure of the silicate may have also increased the stability of the microspheres. Acid catalysis tends to produce cross-linked, polymeric gels of silica, rather than particles of silica. Cross-sectional images did not indicate the nanocomposite structure suggested in chapter 3. Rather, most of the microspheres appeared as a mixed phase of PVP and silica with some exhibiting domains that were rich in either the organic or inorganic components.

Calcium was not incorporated efficiently into microspheres created by acid catalysis. This may be caused by a number of factors. First, calcium ions are far less likely to be hydrolyzed at low pH. This reduces the chance for direct condensation with silica. Second, the polymers present in the aqueous phase are capable of associating with calcium. The polymers are more likely to be protonated at low pH, limiting the ability of the polymer to bind positively charged calcium ions. Although this is less likely since the pyrrolidone group is a very weak base with a pKa around -0.2 (pKa of n-methylpyrrolidone)¹³⁵.

Phosphorous was not detected by EDS in microspheres made by either catalyst. While it may be surprising that the microspheres deficient in calcium and phosphorous form hydroxyapatite, these results are consistent with the literature. P_2O_5 has been shown to have little effect on the precipitation of hydroxyapatite onto xerogels.¹²⁷ Other studies have demonstrated that hydroxyapatite can form on silica gels that contain no calcium.¹³⁶ The high surface area may be responsible for the high reactivity of xerogels with SBF. It is commonly believed that the formation silica gel precedes the nucleation

of calcium phosphate on melt-derived glass.^{103,127} Glasses made by sol-gel chemistry exhibit this porous, gel-like surface, which is one explanation for why they have been observed to form hydroxyapatite more quickly than melt-derived glasses.¹¹⁴

The hydroxyapatite peaks appeared more distinct for acid-catalyzed microspheres than base-catalyzed microspheres. Acid-catalyzed microspheres did not dissolve as readily in SBF, which meant that more material could be recovered from the SBF. This meant that a greater quantity of powder was analyzed for these samples. The 45S5 particles also showed more distinct hydroxyapatite peaks than those presented in chapter 3. This is likely due to the difference in size of the 45S5 particles tested in this chapter (~5 μm) versus the previous chapter (200-300 μm), accounting for 50 times more surface area. This higher surface area may cause more hydroxyapatite to precipitate from SBF.

Microsphere Size

The critical Weber number analysis (Figure 4-9) demonstrated that particles do not follow the behavior attributed to simple shear flow. However, the Grace curve for simple shear is not applicable to all types of mixing. A number of assumptions are made in this model. First, both the dispersed and continuous fluids are assumed to be Newtonian fluids. Second, shear is assumed to be applied slowly to the droplets in a stepwise equilibrium manner. Finally, the flow is assumed to be simple shear.¹³⁷ These conditions cause the droplet undergoes rotation. The viscosity of the dispersed phase is responsible for translating the external shear stress into rotation. Rotation causes the droplet to elongate and fracture into two separate drops. These smaller drops undergo fracture until the critical Weber number is reached. Viscous coupling between the

dispersed and continuous phase is critical to determining droplet size by this mechanism ($\alpha = 0$, Figure 4-15).

However, the conditions mentioned above are rarely applicable in practical mixing operations. Stegeman, et al.¹³² have noted that in most industrial mixing operations, droplet breakup occurs under elongational flow. This type of flow arises from non-Newtonian behavior, sudden exposure to high shear stress, or from inhomogeneous flow. Elongational flow causes droplets extend into long threads. The Rayleigh instability of the elongated droplet causes spontaneous break up into numerous small drops. The viscosity of the droplet plays little role in this case ($\alpha = 1$, Figure 4-15).

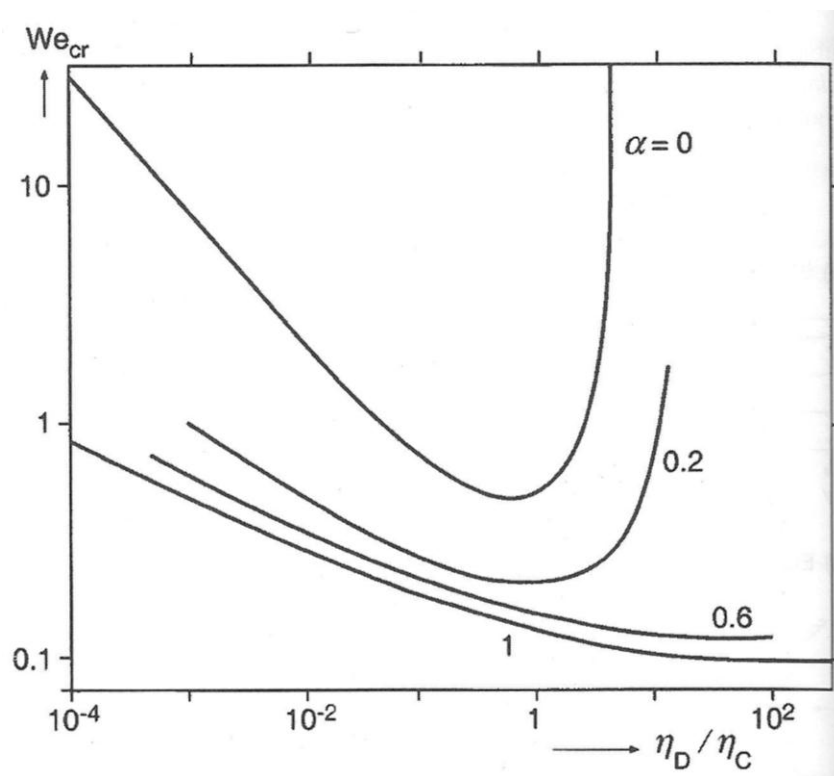


Figure 4-15. Critical Weber number versus viscosity ratio for droplet breakup in different types of laminar flow. The amount of elongation a droplet undergoes is given by α . The Grace curve, which assumes simple shear is described by the $\alpha = 0$ curve. Two-dimensional, purely planar flow is described by the curve at $\alpha = 1$. Image reproduced from Walstra with permission from Taylor and Francis, copyright 2002.¹³⁸

The critical Weber number analysis shows that microspheres formed from droplets created by elongational flow. The experimental conditions are appropriate for elongational flow and the continuous phase is clearly non-Newtonian (Figure 4-8). Sudden shear stress was imparted on the aqueous phase by adding to the oil phase under stirring. Finally, the mixing apparatus used in these experiments likely imparts a two-dimensional, rotational shear, rather than simple shear. A more effective means to controlling droplet size in this system would be to change the shear stress (i.e. stirring speed) during emulsion formation.

The critical Weber number analysis assumed that the microspheres did not shrink during drying. The 100S microspheres did appear to undergo more shrinkage than other compositions (as discussed below). The effect of this shrinkage is a lower calculated Weber number. Since the 100S solutions typically had lower viscosity than other compositions, this may have contributed to the lack of slope in Figure 4-9.

Microsphere Morphology

Systematically varying the composition of the particles allowed phase diagrams to be constructed which showed distinct regions of similar morphologies (Figure 4-10). The phase behavior of particles can be explained in terms of the sol-gel reactions that form the microspheres. Hydrolysis of the TEOS molecule occurs at the interface of the water droplet (Figure 4-16A). This occurs readily under the acidic conditions. This allows the orthosilicate to become more water-soluble. Silanol groups hydrogen bond with the carbonyl groups of PVP^{128,139} as the molecule enters the water droplet. Unbound silanol or alkoxy groups can undergo condensation. The condensation reaction is more rapid in the presence of calcium salts.

Compositions with high calcium and PVP concentrations form a gel before the silicate has a chance to completely diffuse into the droplet. This creates a silica-rich shell surrounding a core of PVP (Figure 4-16B). This phenomena explains why at 77S microspheres with high concentrations of PVP (40 and 1,000 kg/mol), appears to have “voids” in the particles (Figure 4-10, yellow circles). The “voids” are likely caused by the evaporation of water from the hydrated PVP at the core of the particle. EDS mapping has shown that the core of these particles contain very little inorganic material (Figure 4-11).

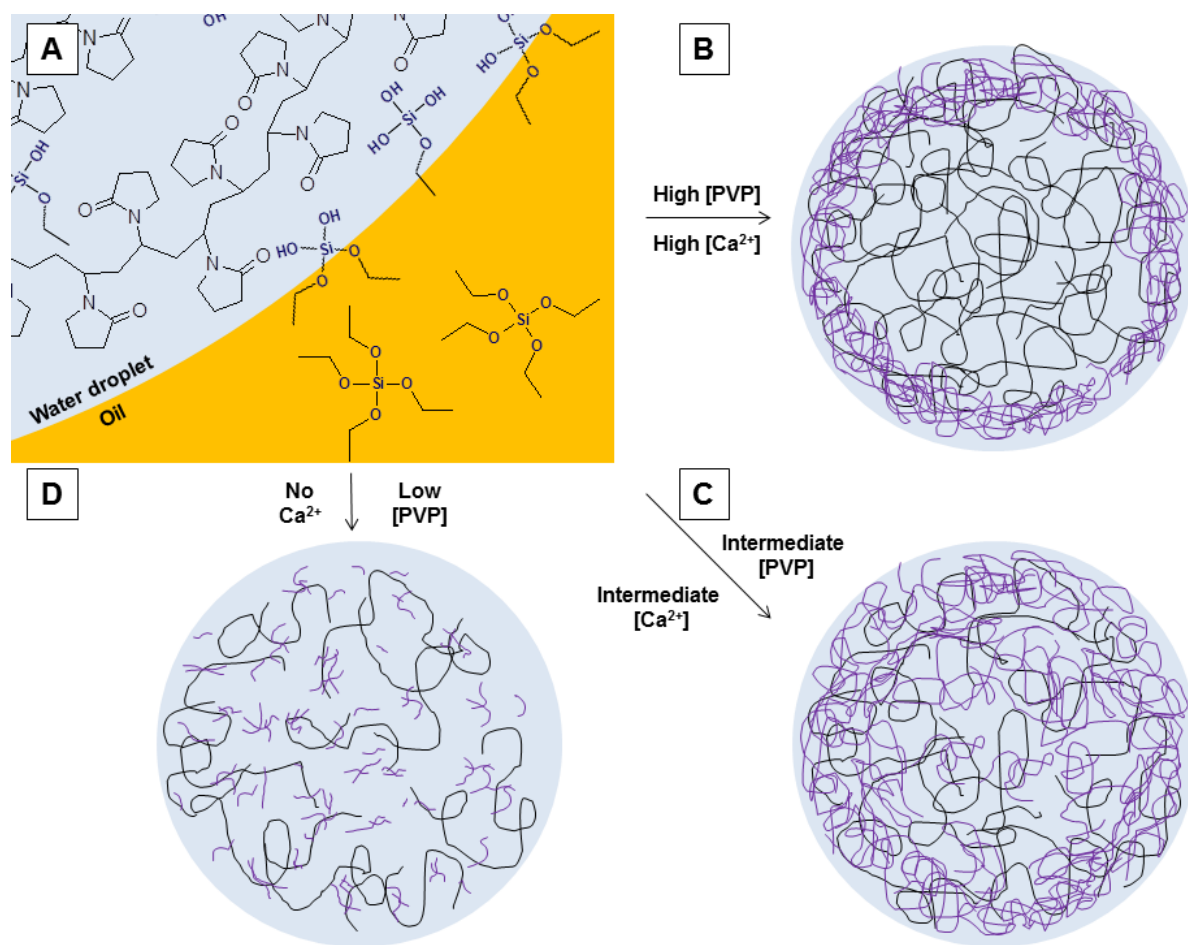


Figure 4-16. Proposed mechanism of microsphere formation by acid catalysis. All drawings are highly schematic, do not show the surfactant, and are not drawn to scale. PVP networks are indicated by black lines. Silicate networks are indicated by purple lines.

Condensation does not occur as rapidly at lower concentrations of calcium. This allows the hydrolyzed silicate species to diffuse more thoroughly into the droplet, creating a particle that appears homogeneous (Figure 4-10, black circles). The PVP may slow the diffusion of hydrated silica into the center of the droplet (Figure 4-16C). This accounts for why some of the solid particles appeared to have a middle region with lower backscattered electron contrast than the outer region. This contrast is indicative of a difference in the average atomic number of the material caused by regions rich in PVP or silica (Appendix D).

Microspheres made without calcium (100S compositions) displayed a very unusual “rippled” or “folded” morphology on their surface. While this morphology appears similar to phase separation by spinodal decomposition, this structure is not maintained throughout the cross-section of the particle. It is possible that very little condensation has occurred in these compositions prior to washing the particles. A limited number of branched silicates would create a fluid droplet with relatively low density (Figure 4-16D). The droplet may still be fluid at the time that the reaction is stopped. Drying the microspheres at this stage would cause the microspheres to collapse. Zhao, et al.¹⁴⁰ observed this phenomenon for polystyrene microspheres that were cross-linked in the presence of solvent. Drying the microspheres caused a wrinkled surface (Figure 4-17).

Latex particles with a binary polymer composition have displayed similar morphologies to those observed in this chapter. This includes core-shell structures, particles with inclusions, and particles with lobes.^{141,142} Latex particles are also formed in an emulsion, although the polymerization mechanism is different. Instead of acting as a template for the final particle, the droplets of the emulsion (10s μm) serve as

reservoirs for the monomer. Latex particles are produced in micelles (~100s nm) outside of the monomer droplets. Despite the different mechanism, it is worth noting that the similar morphologies can be created in both processes.

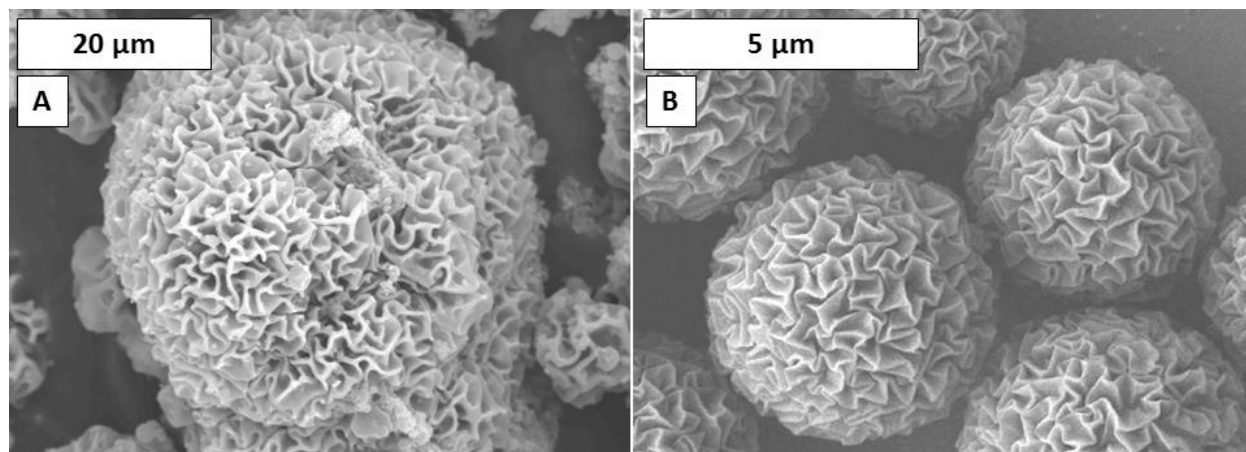


Figure 4-17. SEM images of microspheres with wrinkled surfaces. (A) 100S; 1,000 kg/mol PVP; 2 wt% bioactive glass composite microsphere produced in this chapter. (B) Microspheres produced by Zhao, et al.¹⁴⁰ by drying cross-linked polystyrene microspheres that were previously swollen with toluene. Reprinted with permission from the American Chemical Society. Copyright 2011.

Summary

Acid catalysis produced composite microspheres that contain more inorganic material and less calcium. These microspheres were less soluble in SBF and formed hydroxyapatite on their surface within 7 days. The viscosity of the aqueous droplets had little effect on the final particle size due to elongational flow in the emulsion. However, viscosity and calcium concentration affected the morphology of the final microspheres. These morphologies were potentially caused by differences in the rate of diffusion and gelation of silicate species inside the droplets. Microspheres approximately doubled the proliferation of osteoblasts, indicating that they are a suitable material to treat bone infections. Acid-catalyzed microspheres should be used for

encapsulating drugs because they are more stable than microspheres made by base catalysis.

CHAPTER 5
IN VITRO DRUG RELEASE FROM BIOACTIVE GLASS MICROSPHERES

Introductory Remarks

Osteomyelitis is a localized infection of bone that destroys tissue, causes severe pain, and can lead to loss of limb. Osteomyelitis affects approximately one in 5,000 people¹⁴³ and costs approximately \$10,000 per patient to treat.³⁶ The infection is typically caused by biofilms of Staphylococci, Streptococci, and Pseudomonas bacteria.^{36,37,98,143} The Gram-positive bacterium *Staphylococcus aureus* (*S. aureus*) causes approximately 50% of all cases.³⁷ One study reported that 53% of the *S. aureus* isolates from osteomyelitis and septic arthritis were methicillin resistant (MRSA).³⁶ Another study of osteomyelitis in pediatric patients showed that 44% of *S. aureus* isolates were MRSA.¹⁴⁴ Resistant bacteria such as MRSA are becoming increasingly problematic for hospitals due to the limited number of antibiotics that are effective against these strains. Vancomycin, a glycopeptide antibiotic, is one of the few drugs effective against MRSA as well as other Gram positive bacteria.

Bacteria can inoculate bone by various routes. One route is through open fractures, such as those sustained on the battlefield. Shrapnel and bone fragments present surfaces that can harbor the growth of biofilms. Osteomyelitis can also be caused by the spread of bacteria from a neighboring infection. Diabetic ulcers are a major cause of osteomyelitis for this reason. Vascularity and immune response are typically compromised in these cases, which renders systemic antibiotic therapy ineffective. Antibiotics must therefore be applied directly to the site of the infection to achieve a local concentration high enough to kill the biofilm.

Buchholz¹⁰⁰ introduced the concept of mixing antibiotics into PMMA bone cements in 1970. While these monolithic cements filled the void space in the bone, they were difficult to remove and did not allow for adequate drainage. Klemm⁹⁹ addressed these issues in 1976 by stringing drug-loaded PMMA beads onto surgical wire which was packed into the infected site. This allowed the PMMA to be removed in a second surgery. It has been estimated that approximately 90% of infections are cleared using this approach.⁹⁹ The most common antibiotics delivered by PMMA beads are gentamicin, tobramycin, and vancomycin because they are resistant to heat given off from the polymerization of PMMA (up to 100 °C).

The relative success of PMMA beads is attributed to the high concentration achieved at the site of the infection. Systemic buildup of antibiotics as measured in serum or urine does not occur with this local therapy.¹⁴⁵ However, PMMA has disadvantages as a drug delivery material. PMMA beads must be removed within approximately 4 weeks to prevent fibrous encapsulation caused by a foreign body response.¹⁰⁰ PMMA has also been reported to release only 25-50% of the loaded drug.^{146,147} This is a wasteful use of expensive antibiotics. Finally, PMMA does not encourage bone ingrowth into the dead area. A bone graft must be implanted in a second surgery to restore the bone tissue. Therefore, drug-loaded PMMA beads are not the ideal material for treating osteomyelitis.

Resorbable polymers have also been investigated for drug delivery to bone. Poly(lactic-co-glycolic acid) (PLGA) copolymers can exhibit drug release above the minimum inhibitory concentration (MIC) for up to 5 weeks.^{101,148} However, the PLGA family of copolymers lowers the local pH and can induce a late immune response.¹⁴⁹

Collagen sponges have the advantage of being a naturally derived material that is remodeled during the bone healing process. Yet, water soluble drugs tend to exhibit a burst release from these sponges.^{150,151} Chitosan is a naturally-derived polysaccharide that has been used in many biomedical and pharmaceutical applications. Chitosan microspheres loaded with vancomycin showed complete drug release within 2 weeks.¹⁵² Dissolution of these materials helps prevent fibrous encapsulation. However, no structural support is offered after these materials dissolves because bone growth is not typically encouraged.

Calcium phosphate cements (CPCs) can offer more long-term structural support. CPCs form either an apatite or brushite ceramic by a rapid acid-base reaction of an amorphous calcium phosphate. These cements are attractive in space-filling applications because they set to form a hard material within approximately 15 mins.¹⁵³ Stallman, et al.¹⁵⁴ demonstrated that mixing gentamicin with the precursors of the CPC causes a slower release than adsorbing the drug onto the CPC once it has been set. Hamanishi¹⁵⁵ showed that vancomycin could be released above the MIC for periods of 2 to 9 weeks *in vivo*, depending on the amount of drug incorporated into the cement. Some CPC compositions exhibited fibrous encapsulation 3 weeks. CPCs undergo limited dissolution and remodeling *in vivo*, which causes the fibrous encapsulation observed by Hamanishi.¹⁵⁵

Silicate glasses slowly dissolve *in vivo* – particularly when the glass contains ions such as Na⁺, Ca²⁺, P³⁻, Mg²⁺, and K⁺. As discussed in chapter 3, mesoporosity can be introduced into glasses to increase the surface area available for the adsorption of

drugs.¹⁰⁷⁻¹¹⁰ Drugs such as vancomycin can also be directly encapsulated in sol-gel matrices.⁹³

Aughenbaugh, et al.⁹² demonstrated that vancomycin could be encapsulated in silica xerogels in concentrations up to 30 mg/g. These xerogels were produced at H₂O:alkoxysilane (R) ratios of 6 and 10. Radin, et al.⁹⁴ extended this work by making microspheres (100-700 μm diameter) of vancomycin-loaded silica. The microspheres were made by emulsifying the silica/vancomycin sols in vegetable oil. The amount of water in the sol was crucial to be able to dissolve the vancomycin. Vancomycin was only soluble up to 6 mg/ml in sols with H₂O:alkoxysilane molar ratio of 4. This is far lower than the solubility of vancomycin in water (200 mg/ml)¹⁵⁶, which indicates poor solubility of vancomycin in the sol. The poor solubility is likely due to ethanol, which is a byproduct of the TEOS hydrolysis. Ethanol is a non-solvent for vancomycin. This explains why more water was needed to dissolve vancomycin in the sol.

The microspheres described in previous chapters were made by interfacial hydrolysis and condensation of TEOS. The initial aqueous droplets contain calcium nitrate and PVP. Alcohol is generated when TEOS hydrolyzed at the oil/water interface, although most is likely carried away into the oil phase. Forming microspheres around aqueous droplets that contain a high concentration of vancomycin may produce microspheres with greater drug loading than described previously.

The goals of this chapter are to demonstrate that vancomycin encapsulated in composite microspheres can be released over a period of one week and that the drug remains effective its effectiveness against *Staphylococcus aureus*. Release was measured by UV absorption over a two week period from various microsphere

compositions. A bacterial inhibition assay was used to ensure that vancomycin remained effective after the encapsulation process.

Materials and Methods

Microsphere Synthesis

Vancomycin was loaded into bioactive glass microspheres that were prepared by acid catalysis, similar to the method described in chapter 4. Hydrochloric acid was used as the catalyst, rather than nitric acid, because vancomycin is provided as a hydrochloride salt. The final hydrochloric acid concentration in the aqueous phase was 0.02 M. Microspheres were made in emulsions half the volume described in chapter 4. This was done in an effort to conserve vancomycin. All other reagents were scaled accordingly. The molar ratio of components used to create the microspheres (Table 5-1) was the same as in chapter 4.

Table 5-1. Molar ratio of components (relative to TEOS) used to make vancomycin-loaded microspheres. The concentration of PVP was 10 wt% in the initial aqueous solution for all samples.

| Glass composition | PVP molecular weight (kg/mol) | TEOS | CNT | TEP | H ₂ O | HCl | Vancomycin |
|-------------------|-------------------------------|------|------|------|------------------|----------------------|----------------------|
| 77S | 10 | 1 | 0.20 | 0.10 | 4 | 1.4×10^{-3} | 2.4×10^{-3} |
| 77S | 40 | 1 | 0.20 | 0.10 | 4 | 1.4×10^{-3} | 2.4×10^{-3} |
| 77S | 1,000 | 1 | 0.20 | 0.10 | 4 | 1.4×10^{-3} | 2.4×10^{-3} |
| 86S | 1,000 | 1 | 0.07 | 0.09 | 4 | 1.4×10^{-3} | 2.4×10^{-3} |
| 100S | 1,000 | 1 | 0 | 0 | 4 | 1.4×10^{-3} | 2.4×10^{-3} |

Vancomycin was added to aqueous solutions containing of calcium nitrate and 10 wt% PVP to achieve a concentration of 36 mg/ml. These solutions were stirred overnight at room temperature to allow the vancomycin to dissolve. Approximately 3 ml of the aqueous phase was added to 22 g of the oil phase while stirring at 500 rpm.

TEOS and TEP were added and the emulsion and stirred for 24 hrs. The microspheres were washed three times with 200 proof ethanol. The samples were centrifuged at 1700 rpm and vortexed to resuspend the particles. The samples were dried as described in previous chapters.

UV Absorption

UV absorption spectra were measured on a Shimadzu UV 2410-PC UV-Vis spectrophotometer. Solutions were measured in quartz cuvettes. Spectra were collected using the following parameters: 1.0 slit width, fast scan speed, and 0.5 nm interval. Vancomycin concentration was measured by absorption of the SBF solution at 280 nm. Samples (180 μ L) were measured in UV-transparent 96 well plate (Corning 3635) on a Molecular Devices plate reader. All SBF solutions were centrifuged prior to analysis. Standard solutions of vancomycin in SBF (0.1, 1, 5, 10, 50, 100 μ g/ml) were prepared by serial dilution in volumetric flasks.

Thermal Analysis

Thermogravimetric analysis was performed on vancomycin-loaded microspheres using the following temperature profile: heating from 30-100 $^{\circ}$ C (at 10 $^{\circ}$ C/min), holding at 100 $^{\circ}$ C for 2 hrs, then heating to 800 $^{\circ}$ C (at 10 $^{\circ}$ C/min). The hold at 100 $^{\circ}$ C was performed to determine how long the powder should be dried at this temperature for future experiments. The samples were purged with air at 100 ml/min during all stages of heating.

SEM

Samples were prepared for SEM as described in previous chapters. The microscope was operated in secondary electron mode at 15 kV accelerating voltage and 16-17 mm working distance for the images presented in this chapter.

Drug Release Study

Samples were immersed in tris(hydroxymethyl)aminomethane (Tris)-buffered SBF which was prepared in the same manner as described in previous chapters. 25 mg of vancomycin-loaded microspheres were immersed in 5 ml of SBF (5 mg/ml concentration). The samples were immersed in a shaker bath at 37 °C for the duration of the study. SBF was replaced at daily intervals by centrifuging the samples at 1000 rpm, removing 4 ml of the supernatant by pipette, and replenishing with 4 ml of pre-warmed SBF. The solutions were then vortexed for 5 seconds to resuspend the particles. The supernatant solutions were stored at -70 °C and thawed prior to measuring absorbance.

The calculations for cumulative release took into account the 1 ml of SBF that was not replaced each day. Release on the first day was calculated by multiplying the measured concentration ($\mu\text{g/ml}$) by the volume drawn off (4 ml). The amount of vancomycin in the 1 remaining ml was subtracted from the concentration measured on the following day.

Bacterial Inhibition Study

The SBF used in the bacterial inhibition study was not buffered with Tris. This is because some studies have indicated that bioactive glasses have a bactericidal effect which is claimed to be caused by an increase in pH caused by the dissolution of the glass¹⁵⁷. Tris was not used in the SBF to capture this potential effect. The pH of the SBF was adjusted to 7.5 with sodium hydroxide. The unbuffered SBF was autoclaved to maintain sterility.

Prior to immersing in SBF, 25 mg of microspheres (77S; 40 kg/mol PVP) were heated at 100 °C for 2 hrs to remove any residual alcohol. 5 ml of SBF was added to

the microspheres to achieve a final concentration of 5 mg/ml. The solutions were incubated at 37 °C and 5% CO₂ during the experiment. 1 ml SBF was drawn off and replaced at 0.5, 1, 2, 4, and 24 hrs and at daily intervals thereafter. The solutions drawn off of the microspheres were stored at room temperature until the bacterial assay could be performed.

Inhibition of *S. aureus* (ATCC # 25923) was measured using a disk diffusion test. Bacteria were grown at 37 °C in tryptic soy broth to an optical density of 0.2, corresponding to a cell density of ~10⁶ CFU/ml. The bacteria were streaked onto 150 mm Petri dishes containing Mueller-Hinton agar. Paper disks (6 mm diameter) were immersed in SBF that had been drawn off from the microspheres at certain time intervals. The SBF was centrifuged at 1000 rpm prior to immersing paper disks. Three disks were placed onto each agar plate in a randomized order. The plates were incubated overnight at 37 °C. Bacterial inhibition was observed as transparent rings surrounding the paper disks. The distance from the center of the disk to the edge of the transparent ring was measured using digital calipers. This distance was measured in four orthogonal directions per disk for three replicate disks (n = 12).

Results

Microsphere Synthesis

Microspheres containing vancomycin appeared morphologically similar to those presented in chapter 4 (Figure 5-1). The particles appear ~2-50 μm by visual inspection of the micrographs. The 77S; 1,000 kg/mol PVP particles appear larger (50 μm) than other compositions and have internal “foam like” morphology. These characteristics were consistent with the microspheres with the same composition prepared in chapter

4. The 77S; 10 kg/mol PVP composition did not appear to have the “core-shell” morphology that was observed in chapter 4.

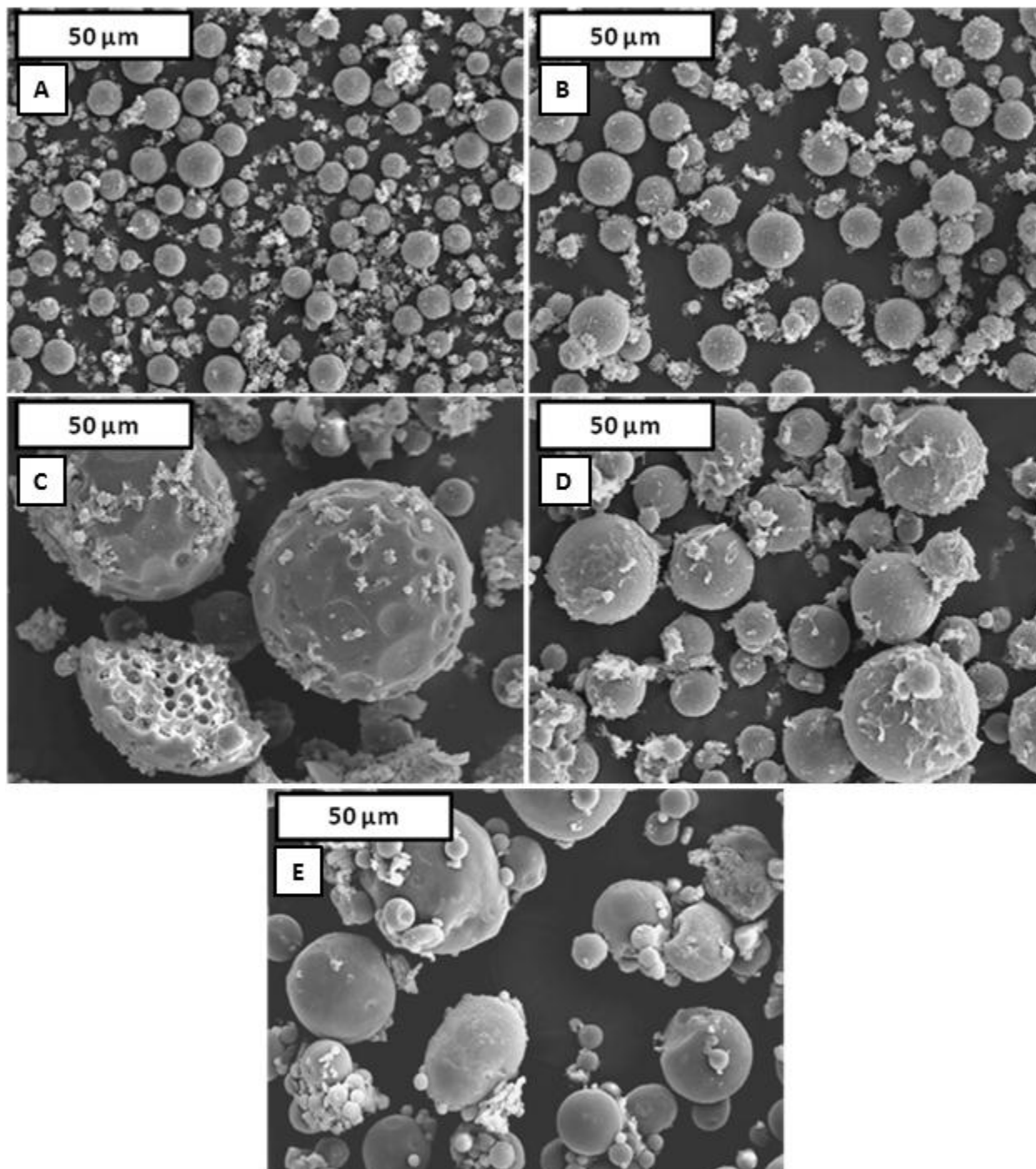


Figure 5-1. SEM images of vancomycin-loaded microspheres prior to soaking in SBF. (A) 77S; 10 kg/mol PVP. (B) 77S; 40 kg/mol PVP. (C) 77S; 1,000 kg/mol PVP. (D) 86S; 1,000 kg/mol PVP. (E) 100S; 1,000 kg/mol PVP.

Microsphere yield directly correlated to the calcium concentration in the aqueous solutions (Table 5-2). Yield was calculated by assuming no loss of PVP or vancomycin and complete conversion of TEOS, Ca(NO₃)₂, and TEP into SiO₂, CaO, and P₂O₅, respectively. Compositions with the highest calcium concentration (77S) yielded 86-92% of the theoretical maximum. This was significantly higher than the 16% yield of microspheres made without calcium (100S).

Table 5-2. Physical properties of vancomycin-loaded microspheres.

| Glass composition | PVP molecular weight (kg/mol) | Microsphere yield (%) | Mass loss after 2 hr, 100 °C heat treatment (%) | Mass loss between 150-800 °C (%) |
|-------------------|-------------------------------|-----------------------|---|----------------------------------|
| 77S | 10 | 86 | 8.1 | 45 |
| 77S | 40 | 88 | 8.5 | 44 |
| 77S | 1,000 | 92 | 12 | 56 |
| 86S | 1,000 | 68 | 7.8 | 48 |
| 100S | 1,000 | 16 | 5.8 | 87 |

Thermogravimetric analysis demonstrated that the 100S; 1,000 kg/mol PVP composition had the highest organic content of all the compositions (Figure 5-2A). This composition lost ~87 % of its mass between 150-800 °C. The other compositions lost 44-56 wt% of their mass in this temperature range (Table 5-2). Microspheres lost approximately 6-12% of their initial mass after heating to 100 °C for 2 hrs. The masses appeared to reach an equilibrium value at the end of this heat treatment (Figure 5-2B). This indicates heating at 100 °C for 2 hours should be sufficient to dry the microspheres of any remaining water or alcohol. Microspheres were given this heat treatment prior to being exposed to bacteria.

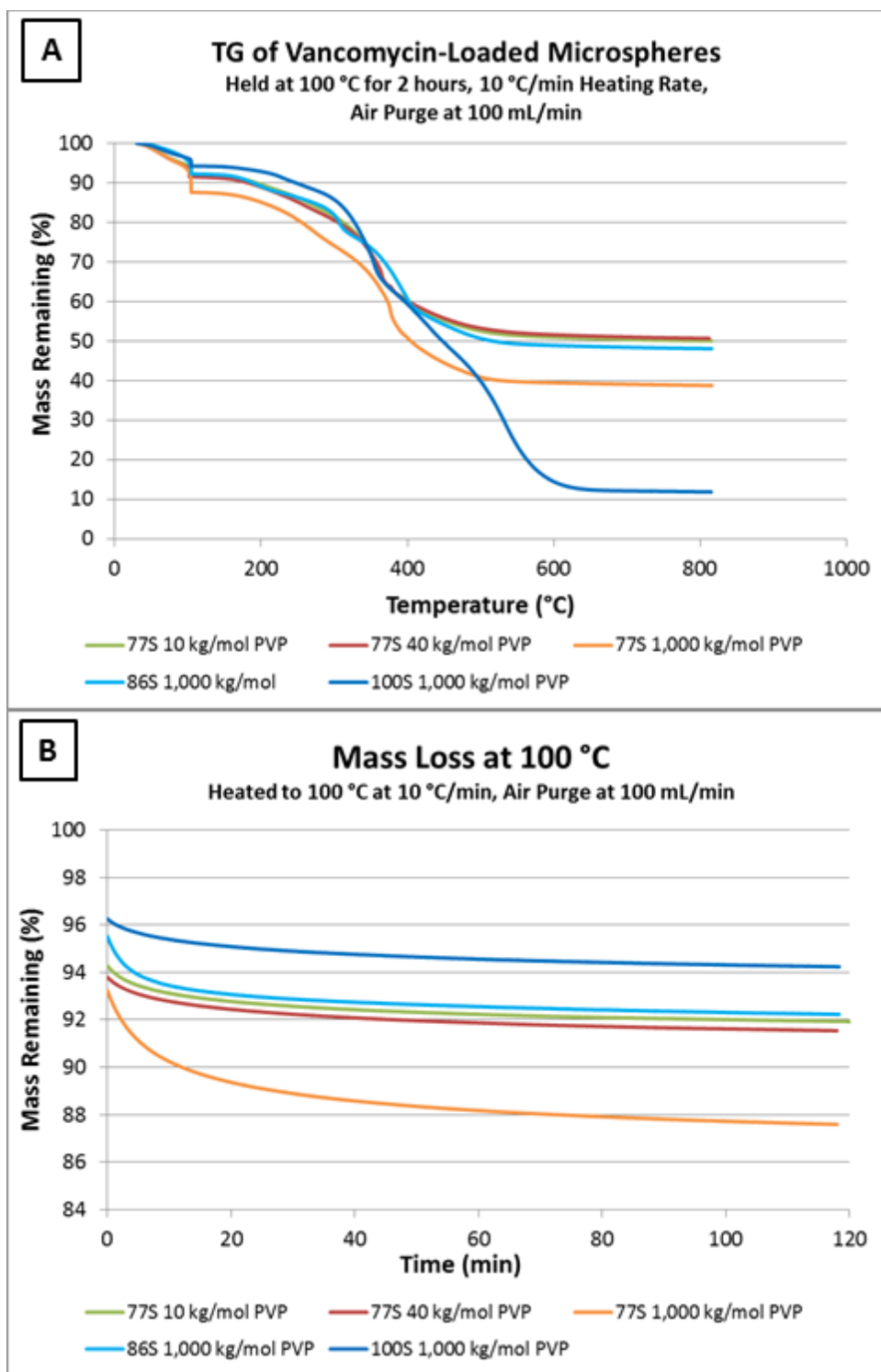


Figure 5-2. Thermogravimetric analysis of vancomycin-loaded microspheres. (A) Heating to 800 °C. The sudden drop in mass at 100 °C is caused by the 2 hr hold at this temperature. (B) Change in mass over 2 hrs at 100 °C for vancomycin loaded microspheres.

Vancomycin Release Study

UV absorption is a commonly used method to detect vancomycin in solution. Vancomycin is typically measured by absorption at 280 nm. However, it is important to ensure that any other compounds that may be released from the microspheres do not absorb at this wavelength. Vancomycin and PVP both show high absorbance in SBF at 220 nm (Figure 5-3). The SBF drawn from microspheres without vancomycin (77S; 40 kg/mol PVP; 10 wt%) also showed high absorbance at 220 nm. This may have been caused by PVP released from the sample.

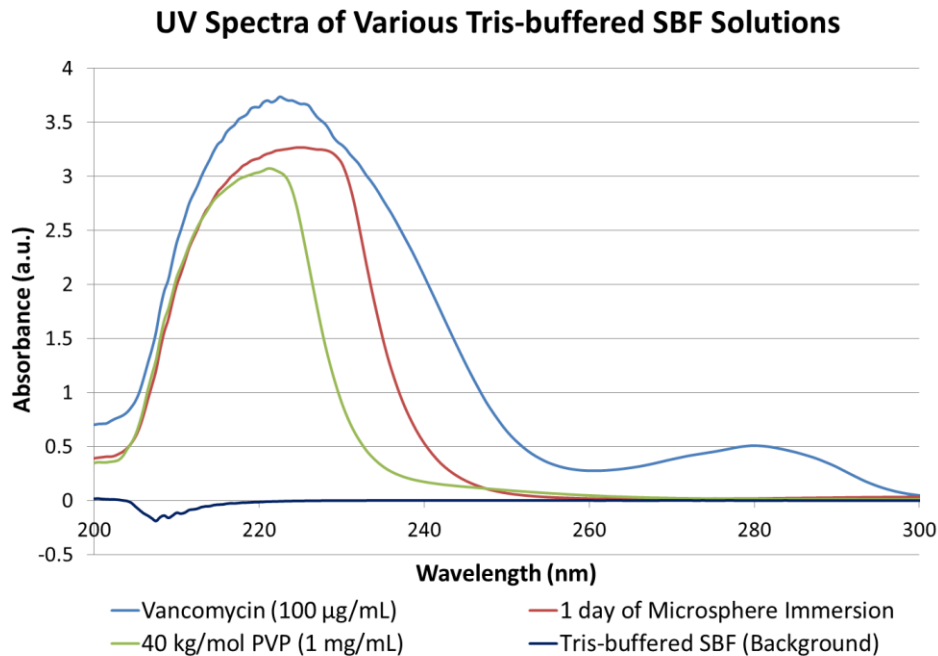


Figure 5-3. Absorbance of SBF solutions containing various compounds. “1 day microsphere immersion” refers to the SBF that was collected from immersing microspheres (77S, 40 kg/mol PVP, 10 wt%) that did not contain vancomycin. SBF was used as the background prior to measurements being taken.

Absorbance at 280 nm correlated strongly ($r^2 > 0.99$) to a standard series of vancomycin solutions (Figure 5-4). SBF containing PVP or microspheres had weak

absorbance at this wavelength, corresponding to $\sim 3 \mu\text{g/ml}$ of vancomycin. Therefore, the error for measuring vancomycin by UV absorption was assumed to be $3 \mu\text{g/ml}$.

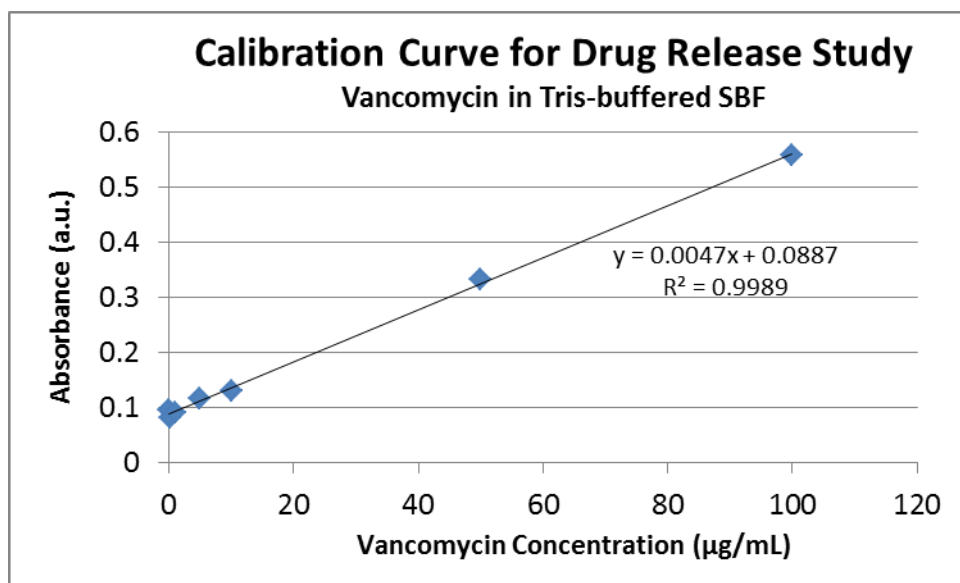


Figure 5-4. Calibration curve for vancomycin in Tris-buffered SBF. Absorbance was measured at 280 nm on a plate reader.

Vancomycin release was monitored by absorbance for up to two weeks in Tris-buffered SBF (Figure 5-5). The highest concentration was detected on the first day for all samples. 100S; 1,000 kg/mol PVP microspheres exhibited a vancomycin concentration of $\sim 600 \mu\text{g/ml}$ on the first day. This was the highest concentration for all the compositions. This composition released vancomycin at concentrations $>100 \mu\text{g/ml}$ during the first three days of the experiment. Other compositions released $\sim 100 \mu\text{g/ml}$ of vancomycin on the first day.

The end of the release was determined by testing whether the vancomycin concentration was statistically different from the error ($3 \mu\text{g/ml}$). A single-tailed t-test ($\alpha = 0.05$, $df = 2$) was used as the statistical test. The release was considered insignificant on the first day that the measured concentration failed this test. The release lasted 5-7 days for all samples using this criterion (Table 5-3).

Daily Release of Vancomycin from Hybrid Bioactive Glass Microspheres

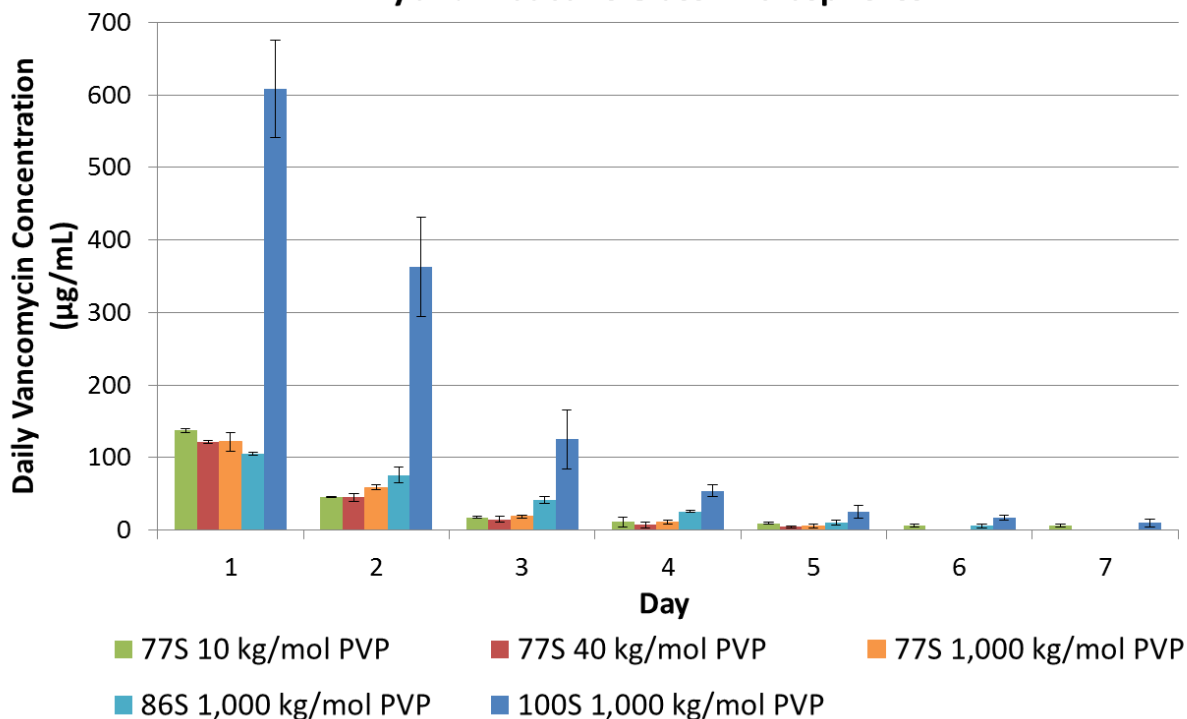


Figure 5-5. Vancomycin release from various microsphere compositions measured by absorbance at 280 nm. Error bars indicate 95% confidence intervals.

Table 5-3. Drug release properties of vancomycin-loaded microspheres.

| Glass composition | PVP molecular weight (kg/mol) | Vancomycin concentration in microspheres (mg/g) | Days of vancomycin concentration >3 µg/ml | Cumulative vancomycin release (µg) | Cumulative vancomycin release (%) |
|-------------------|-------------------------------|---|---|------------------------------------|-----------------------------------|
| 77S | 10 | 31 | 7 | 700 | 92 |
| 77S | 40 | 33 | 5 | 630 | 77 |
| 77S | 1,000 | 29 | 5 | 650 | 91 |
| 86S | 1,000 | 43 | 6 | 790 | 74 |
| 100S | 1,000 | 220 | 7 | 3600 | 65 |

The greatest quantity of vancomycin was released from the 100S; 1,000 kg/mol composition. 3600 µg was released from this composition over a period of 7 days (Figure 5-6A). 86S and 77S compositions released approximately 5 times less (Table 5-3). While the 100S composition released the greatest quantity of vancomycin, this

corresponded to only 65% of the initial drug loaded into the samples. The release was more complete (74-92%) from 86S and 77S microspheres containing calcium (Figure 5-6B).

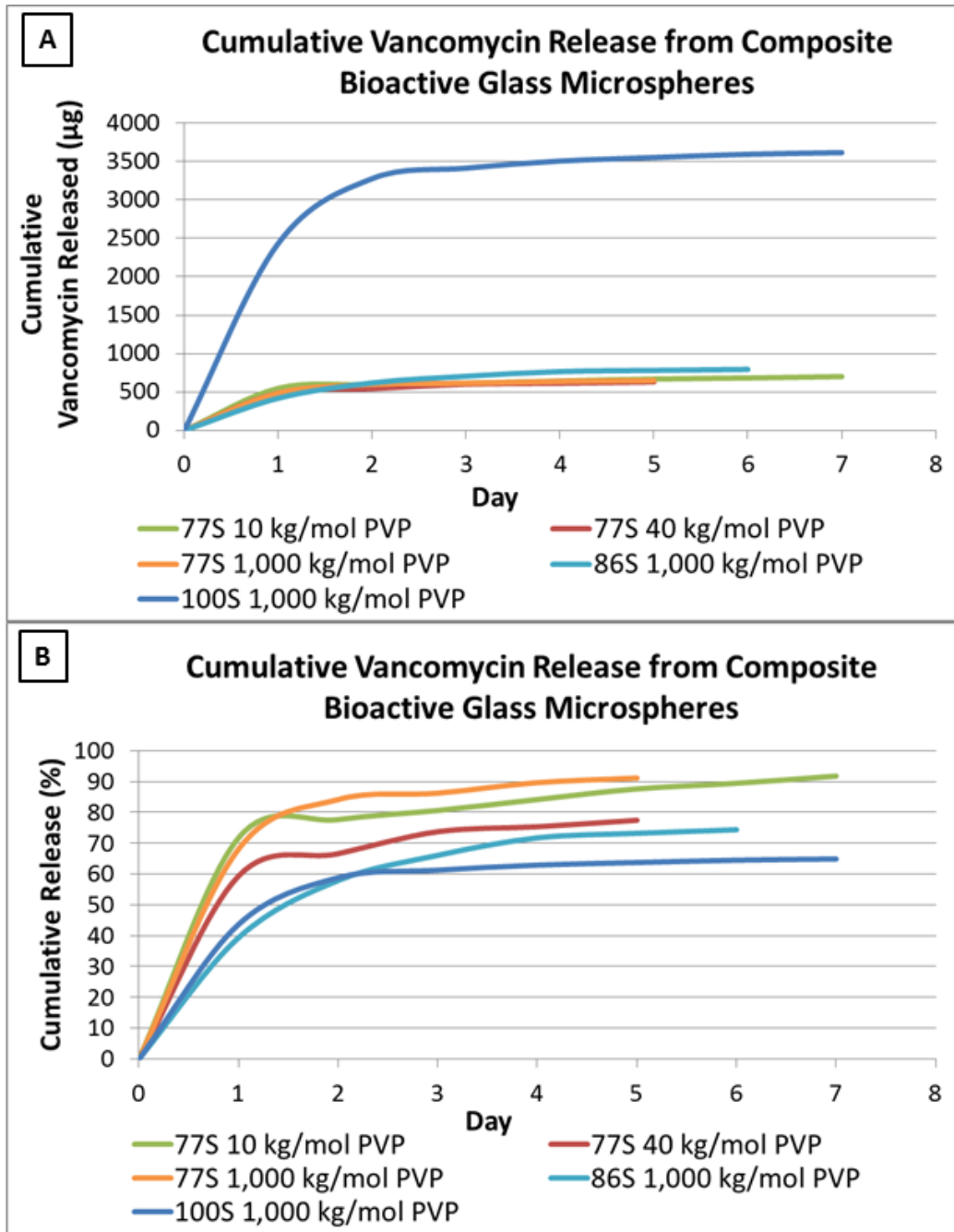


Figure 5-6. Cumulative vancomycin release from composite bioactive glass microspheres. Release expressed as (A) mass and (B) percent vancomycin released.

Microscopic imaging of the particles after soaking in SBF revealed that the 77S compositions made with 10 and 40 kg/mol PVP appeared hollow and broken (Figure 5-7). These compositions did not appear to be hollow prior to soaking in SBF (Figure 5-1). The 100S; 1,000 kg/mol PVP microspheres had completely dissolved after 7 days in SBF.

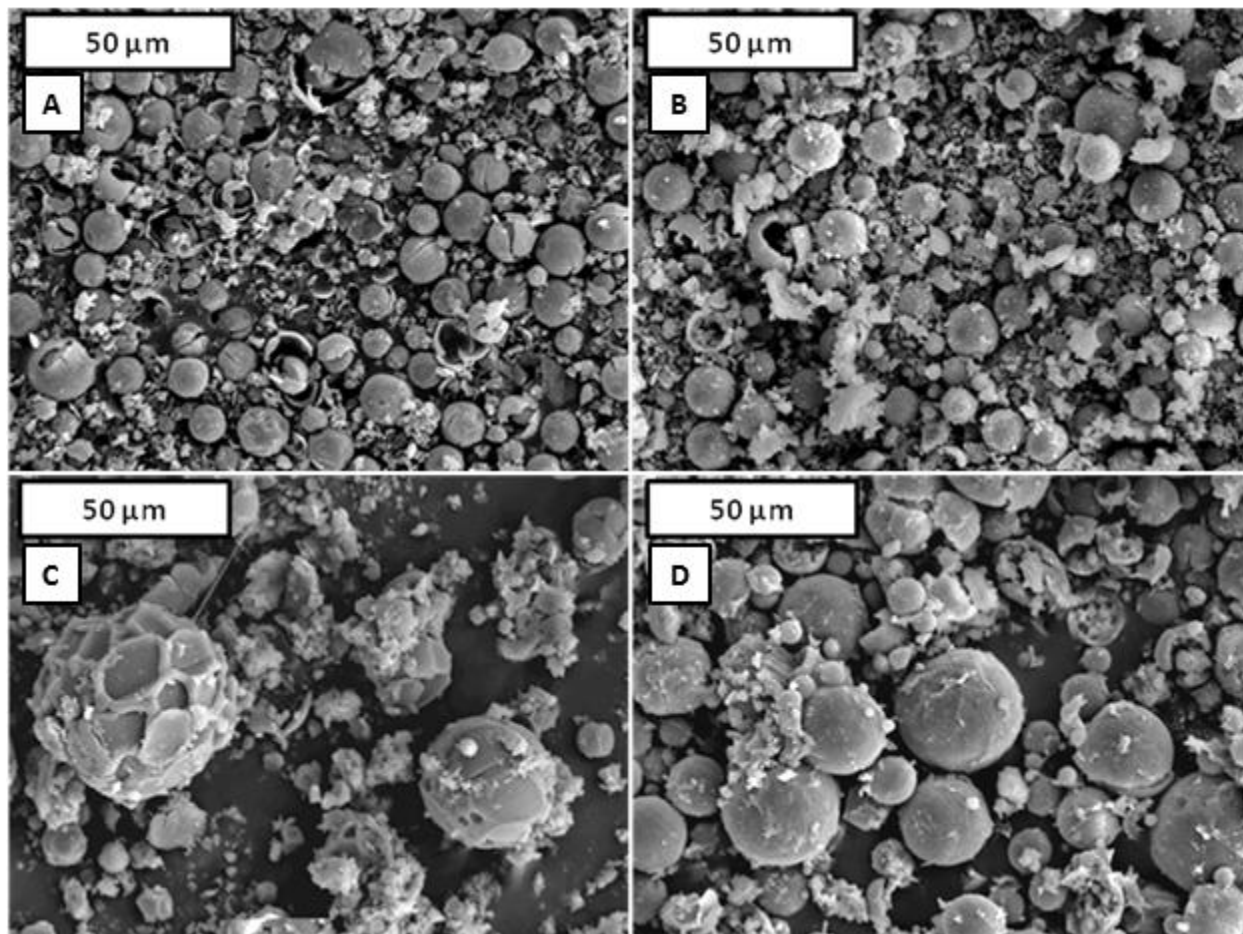


Figure 5-7. SEM images of vancomycin-loaded microspheres after 7 days in SBF. (A) 77S; 10 kg/mol PVP. (B) 77S; 40 kg/mol PVP. (C) 77S; 1,000 kg/mol PVP. (D) 86S; 1,000 kg/mol PVP. The 100S; 1,000 kg/mol PVP composition is not shown because it completely dissolved after 7 days.

Bacterial Inhibition Study

The SBF drawn from the vancomycin-loaded 77S; 40 kg/mol PVP microspheres was tested against *S. aureus*. Bacteria were inhibited for up to 5 days (Figure 5-8).

SBF drawn from microspheres that did not contain vancomycin served as a negative control. No inhibition was observed from these microspheres at either 0.5 or 24 hrs.

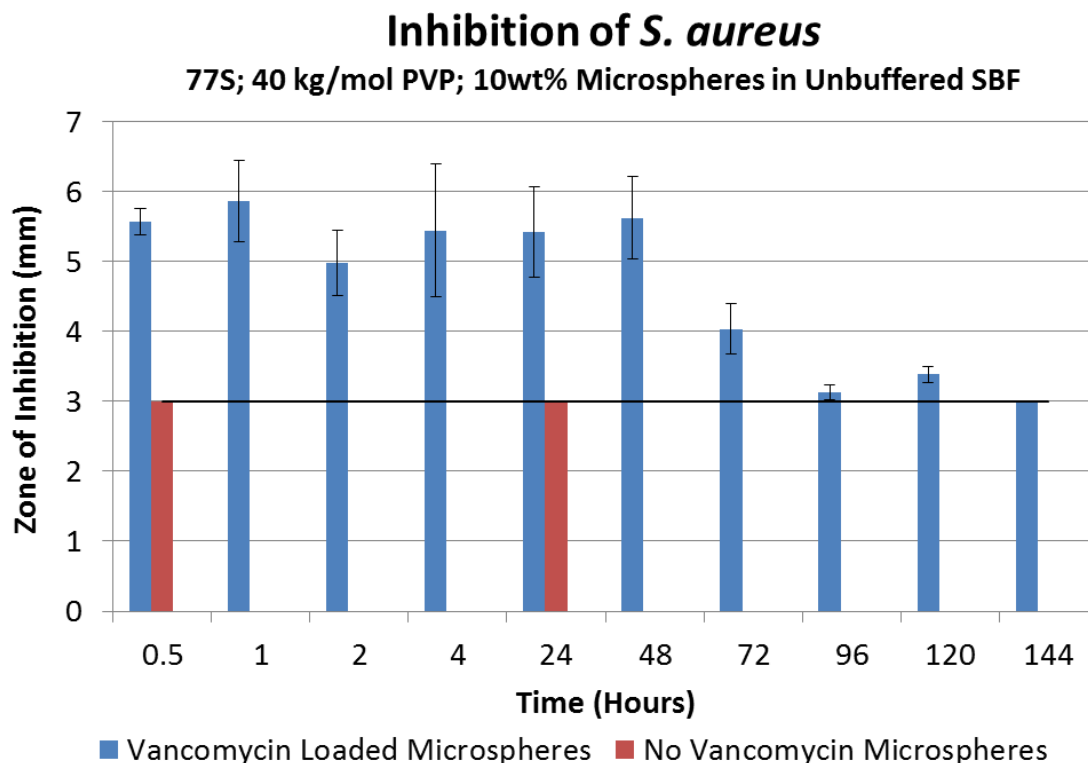


Figure 5-8. Zone of inhibition for *S. aureus* measured around paper disks containing the SBF drawn from a solution of vancomycin-encapsulated microspheres. A 3 mm zone corresponds to the radius of the disk and hence zero inhibition. Error bars indicate 95% confidence intervals.

Vancomycin concentration was calculated from the zone of inhibition data. This was done by establishing a calibration curve by for the zone of inhibition to standard vancomycin solutions (Figure 5-9B). The concentration was also measured by absorbance at 280 nm for comparison (Figure 5-9A). Both techniques yielded similar average concentrations up to 48 hrs. Bacterial inhibition diminished after this time while UV absorbance still indicated the presence of vancomycin.

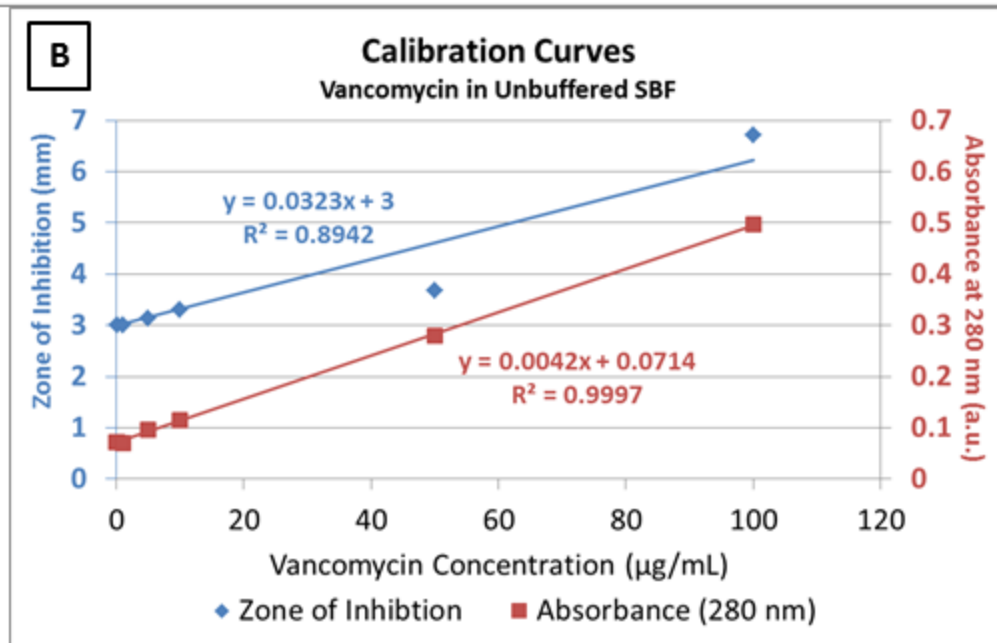
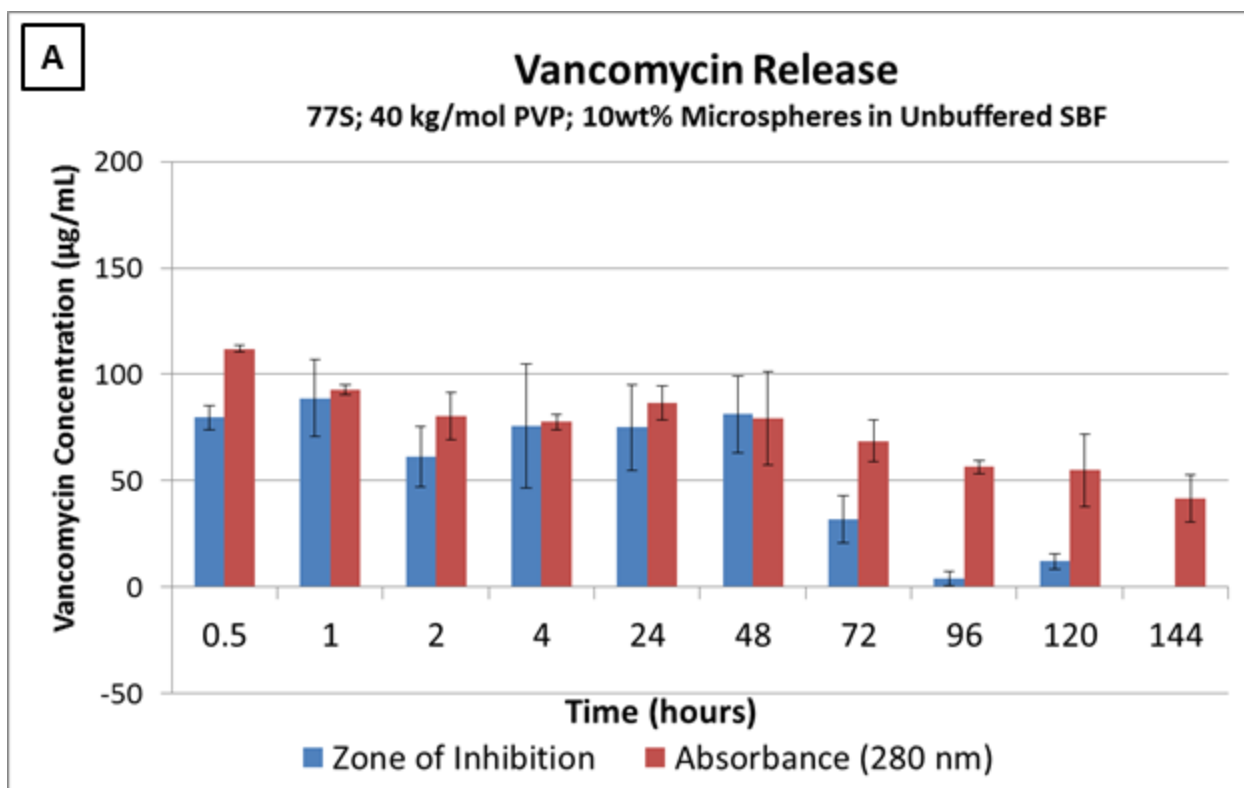


Figure 5-9. Vancomycin release in the bacterial inhibition study. (A) Zone of inhibition and UV absorbance were both used to measure the concentration of vancomycin. (B) Calibration curves used for calculating vancomycin concentration by both zone of inhibition and UV absorbance.

Discussion

Adding vancomycin to the aqueous phase of the emulsion did not appear to significantly affect the formation of microspheres. Vancomycin-loaded microspheres appear similar to those produced in chapter 4. Some compositions appeared hollow and fractured after soaking in SBF (Figure 5-7). This may have been caused by the vortexing that was performed each day after replacing SBF. Yet microspheres did not appear fractured after vortexing three times during the washing procedure. It is possible that PVP leaches out of the microsphere; leaving it more brittle.

Mass loss upon heating to 100 °C is partially attributed to the removal of residual water and alcohol in the particle. The residual solvent in the microspheres directly correlated to both calcium concentration and molecular weight of PVP. The 77S; 1,000 kg/mol PVP composition lost the most weight (12%) after 2 hrs at 100 °C. This was approximately 4% more than any other composition. This partially accounts for the lower final mass than the other 77S compositions. However, this composition had approximately 10 wt% more organic material than the other particles, as indicated by the mass loss between 150-800 °C (Table 5-2).

Microsphere yield was directly correlated with calcium concentration (Table 5-2). This can be attributed to the faster condensation rate of silicate species in the presence of salts, as discussed in chapter 4. The impact of yield was that it changed the effective loading rate of vancomycin in the microspheres. This effect was most dramatic for the 100S composition, which had the lowest yield (16%) and the highest loading rate (220 mg/g). This was calculated under the assumption that no vancomycin was lost during in the process of forming the microspheres.

Cumulative percent release also directly correlated to calcium concentration (Table 5-3). The 77S compositions released 93-95% of their initial vancomycin. The 100S composition released only 65%. The disparity in percent release does not correspond to the dissolution of the microspheres. The 100S compositions completely dissolve after 7 days in SBF while the 77S particles were still intact at this time.

The calculation for percent release assumes that no vancomycin is lost during the process of forming the microspheres. Gupta, et al.¹⁵⁸ showed that vancomycin partially diffuses into the oil phase of a two-part octanol/water mixture. The partition coefficient was measured as 0.2:1 (octanol:water). It is conceivable that surfactants may increase the solubility of vancomycin in octanol. Diffusion of vancomycin out of the aqueous droplets may account for the low cumulative release observed for the 100S samples. Calcium in the aqueous phase may affect this partitioning process.

Calcium has been shown to change the partitioning of vancomycin aqueous two-phase systems¹⁵⁹. This is typically done with two incompatible polymers such as PEG and dextran which form a two-phase solution. Lee, et al.¹⁶⁰ found that 2 M NaCl greatly increased the partitioning of vancomycin into the PEG phase. The authors claim that the salt reduced the activity of water in solution, resulting in increased hydrophobic interactions between vancomycin and PEG. A similar hydrophobic interaction between PVP and vancomycin may also occur in this study in the presence of calcium. Calcium also accelerates the condensation of silicate species, which may also slow the diffusion of vancomycin out of the droplet.

Vancomycin can be dissolved at a higher concentration in an aqueous solution than a silica sol. This allowed the microspheres to attain a higher concentration of

vancomycin (up to 220 mg/g) than reported for xerogels in previous studies (up to 30 mg/g).^{92,161} Microspheres made by this study released a greater quantity of vancomycin (680-3600 µg) than microspheres made by emulsification of the sol (35-200 µg) under the same immersion conditions.⁹⁴ The release was also more complete (65-95%) from these microspheres than those made in previous studies (6-36%).

S. aureus was inhibited for up to 5 days by the vancomycin released from the microspheres. This indicates that the process of encapsulating the drug does not compromise its viability. The efficacy of the drug was diminished at days 4 and 5. This may be have been caused by degradation of the vancomycin molecule. Vancomycin has been shown to degrade at 37 °C in solution with a half -life of 29 days.¹⁶² It is possible that the salts in the SBF accelerate the degradation of vancomycin. The degraded vancomycin molecule may still absorb in the UV. This would account for the difference in concentration at times >3 days between bacterial inhibition and UV absorption (Figure 5-9).

Summary

This study has demonstrated that vancomycin maintains its bactericidal activity upon encapsulation in a calcium silicate composite. Calcium played an important role in the encapsulation process. Calcium increased the yield of the microspheres, the inorganic content, and aided in the retention of vancomycin. The high yield of microspheres containing calcium led to less vancomycin per gram of microspheres. A high loading capacity (up to 220 mg/g) was achieved by calcium-deficient microspheres. The highest release occurred on the first day for all compositions and continued for 4-6 days under the fluid exchange conditions tested. Future work should focus on ways to

extend the release kinetics so that the drug can be released over a period of several weeks.

CHAPTER 6¹
KINETIC ANALYSIS OF THE ATTACHMENT OF ZOOSPORES OF THE GREEN
ALGA *ULVA* TO SILICONE ELASTOMERS

Introductory Remarks

Marine biofouling is a costly, complex and environmentally harmful phenomenon. Biofouling on ship hulls increases fuel consumption and necessitates regular hull cleaning. A recent estimate by Schultz et al.⁵ put the cost of biofouling at \$1 billion over 15 years for the US Navy *Arleigh Burke* (DDG) class of destroyers. Hull fouling is also a primary vector for the introduction of invasive species.^{19,163} The majority of antifouling coatings contain biocides^{40,164}, but environmental issues have increased the interest in the development of non-toxic, antifouling coatings, which encompass a wide range of technologies.¹⁶⁵⁻¹⁷⁰

Polydimethylsiloxane elastomers (PDMS_e) are non-toxic materials that exhibit characteristically low adhesion to fouling organisms. Native, cross-linked PDMS is soft and not durable enough to function as a marine coating. Silica fillers are commonly added to increase the strength and modulus of the material. These materials have a nanocomposite structure, with silica particles forming aggregates which increases the modulus of the rubber. Increasing the elastic modulus, however, has been shown to increase the retention of fouling organisms. Imparting a topography on the surface of reinforced PDMS_e is one route to preventing the attachment of fouling organisms.

Many antifouling topographies are inspired by marine organisms that naturally exhibit low fouling such as crabs, mussels and sharks^{3,64,171}. Our group has developed an antifouling topography inspired by the skin of a shark, called Sharklet. This

¹ Portions of this chapter have been published in *Biofouling*. 27(8):881-892. Reprinted with permission from Taylor and Francis.

topography has been shown to inhibit attachment of zoospores of *Ulva*^{65,66,68,82,172}, cyprids of *Balanus amphitrite*⁶⁶; and cells of the bacteria *Cobetia marina*⁵⁷ and *Staphylococcus aureus*⁶⁷. In a kinetic study, the Sharklet pattern inhibited biofilm formation of non-motile *S. aureus* cells for up to 21 days.⁶⁷ However, no kinetic analysis of attachment rates for the motile zoospores of *Ulva*, which is a common fouling alga in the marine environment, has been performed on microtopographies.

The purpose of this study was to measure the initial attachment kinetics of the zoospores of *Ulva* on Sharklet patterned and smooth PDMS. This should provide insight into how topography functions as an antifouling surface. Observations of zoospores of *Ulva* reveal that the cells do not necessarily adhere to a surface on first contact. Rather, through temporary and therefore reversible contacts (previously referred to as ‘first kiss’ adhesion¹⁷³, they ‘probe’ a surface numerous times before committing themselves to a permanent, irreversible adhesion involving the secretion of an adhesive pad.^{23,24} The ‘first kiss’ phase of adhesion allows spores to respond to a range of surface cues or features, potentially resulting in preferential attachment to specific locations rather than being randomly distributed over the surface. For example, spores may attach in close vicinity to previously attached spores, i.e. gregarious attachment.²⁴

In the context of the present paper, attachment of single spores to specific topographical elements has been observed on Sharklet over a 45 min assay.¹⁷⁴ Yet, it is unknown whether preferential attachment occurs only during the early stages of fouling or spores become less selective with time, leading to the topography becoming a less effective fouling deterrent. In the present study, the distributions of spores, which

are attached either as individuals or in groups, on the topography are mapped versus time in order to address this question.

The experiment was also designed to test whether the spores would ‘choose’ to settle on a smooth surface rather than the Sharklet pattern if given a choice. Test slides (19.4 cm²) were prepared with various areal coverage of the Sharklet pattern (Figure 6-1 A-C) to examine this issue of “choice” by the zoospores. Slides with partial patterning were made by covering a 6.5 cm² area with the Sharklet pattern (Figure 6-1B). The ability of the spore to preferentially ‘choose’ a surface was tested by comparing the attachment kinetics among different sample geometries (Figure 6-1).

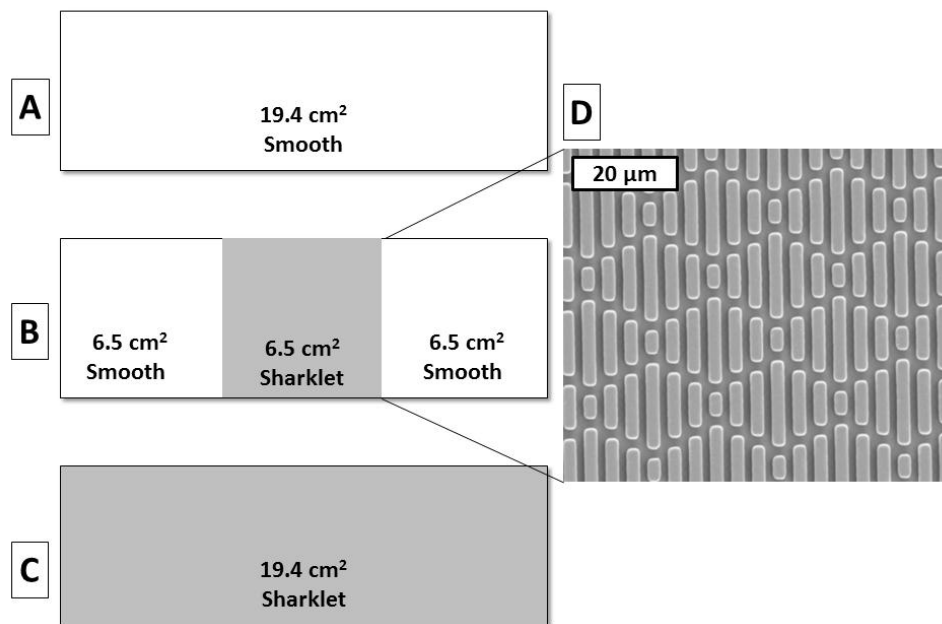


Figure 6-1. Schematic of sample arrangements on 2.54 cm x 7.62 cm glass slides. (A) 19.4 cm² area of smooth PDMS coating on glass slide. (B) 6.5 cm² area of Sharklet micropatterned (+2.5SK2x2) PDMS on glass slide adjacent to two 6.5 cm² areas of smooth PDMS. (C) 19.4 cm² area Sharklet micropatterned (+2.5SK2x2) PDMS on glass slide. (D) Scanning electron microscope image of +2.5SK2x2 topography.

Materials and Methods

Sample Preparation

All test surfaces were fabricated with polydimethylsiloxane elastomer (PDMS_e, Dow Corning Silastic® T2). The PDMS_e surfaces were attached to glass slides 2.54 cm x 7.62 cm (total area 19.4 cm²) for all experiments. All PDMS_e surfaces were prepared by mixing T2 base and curing agent at a 10:1 weight ratio for 5 mins. The T2 was degassed for 30 mins under vacuum and cured for 24 hrs at ~22 °C.

To create smooth surfaces, T2 was cast against glass with a vapor-deposited coating of hexamethyldisilazane. PDMS_e surfaces with the Sharklet topography were made by casting against etched silicon wafers. The silicon wafer molds were prepared by photolithography and deep reactive ion etching as previously described.¹⁷⁴ Silicon wafers were vapor deposited with HMDS to prevent adhesion of cured PDMS_e. All samples were rinsed with 95% ethanol for approximately 10 seconds and blown with nitrogen prior to shipping to Birmingham, UK. As noted previously¹⁷², the topography on the Sharklet samples (e.g., +2.8SK2x2) is designated as:

(feature height in μm) SK (feature width in μm) x (feature spacing in μm)

Attachment Assay for Zoospores

Two kinetic attachment assays were performed on different dates. Assay 1 was performed in October, 2009 and tested sample arrangements A and B in Figure 6-1. Assay 2 was performed in April, 2010 and tested sample arrangements A, B, and C in Figure 6-1.

Samples were shipped dry to the University of Birmingham. Each test surface was placed in an individual compartment (83 x 30 mm) of a Quadriperm dish (Greiner Bio-one Ltd). Test surfaces were immersed in 0.22μm filtered artificial seawater (ASW)

(Tropic Marin, Aquarientechnik GmbH) for 24 h prior to the experiment. Any air visibly trapped in the features was dispersed using a stream of seawater from a pipette.

Zoospores were released from fertile tips of mature plants of *Ulva linza* into 0.22 µm filtered artificial seawater (ASW; 'Tropic Marin', Aquarientechnik GmbH), as described in by Schumacher, et al.⁶⁸. After filtering through 3 layers of nylon plankton net of decreasing pore size (100, 35 and 20 µm) into a glass beaker, the spore suspension was concentrated by plunging the beaker into crushed ice (spores rapidly swim towards the bottom of the beaker). The concentrated suspension of spores was pipetted into a clean beaker and the procedure was repeated. The spore suspension was diluted with filtered ASW to give an absorbance of 0.15 at 660 nm, equivalent to 1×10^6 spores/ml. The suspension was kept on a magnetic stirrer to ensure the spores did not attach to the container. Ten ml of the spore suspension were added to each compartment of the dishes containing the test slides. The dishes were incubated at room temperature (~20 °C) in darkness for periods up to 4 hrs. Three replicates (slides) were analyzed at each time point. At each time point the slides were washed to remove unattached (i.e. still swimming spores) by passing the slides 10 times through a beaker of ASW. Slides were subsequently fixed with 2.5% glutaraldehyde in ASW for 15 min before washing sequentially in ASW, 50% ASW and distilled water, then dried.

The density of zoospores attached to the surface was determined using a Zeiss Kontron 3000 image analysis system attached to a Zeiss Axioplan fluorescence microscope as described by Callow, et al.²⁵. Spores were visualized by autofluorescence of chlorophyll. Spore densities on slides A and C (Figure 6-1) were counted in a line across the middle of the slide at 1-2 mm intervals, 30 counts per

replicate slide (each 0.17 mm²). Spores in the 6.5 cm² smooth areas adjacent to the topography (slide B, Figure 6-1) were counted in the same way with 15 fields of view on either side of the Sharklet pattern. Counts on the 6.5 cm² Sharklet pattern (slide B, Figure 6-1) were taken with 15 counts horizontal and 15 counts vertical to the approximate midpoint of the patterned area.

Zoospore Mapping and Grouping Distribution

Attachment maps were created as described previously^{174,175} to show the preferred attachment locations of zoospores on the topography. Thirty-six transmitted light micrographs (186 μm x 138 μm) of the Sharklet pattern (6.5 cm²) per time point were used from the October 2009 assay for attachment maps and spore grouping analysis. These images were selected because they contained spores. The center of each spore was identified using Image J (US National Institute of Health) by overlaying the spore body with a black ellipse and subsequently using the threshold and particle measurement functions of the software. The coordinates for the center of the spore were transformed to correct for the orientation of the topography in the image. The resulting coordinates of each spore location were graphed on a unit cell of the topography and the spore location was individually checked against the original image for accuracy. The coordinates for the spores were processed with a Kernel smoothing algorithm in Matlab (The MathWorks, Inc). This algorithm creates a smooth probability density function from a two-dimensional histogram. Warm colors on the map indicate a high probability of attachment at the given time point. During the mapping process, each individual zoospore was identified as having attached in a group of 1, 2, 3, or >3 spores. The group size was determined by the number of spores visually touching in the micrographs. This data were used in the analysis of spore grouping. Attachment

maps for groups of 2, 3, or >3 spores represent the location of each individual spore within the group.

Statistical Analysis

Attachment densities were counted as the average over 90 fields of view (3 replicates, 30 fields of view per replicate). 95% confidence intervals for reduction of attachment density were calculated by an arcsine transformation. SigmaStat 3.1 (Systat Software, Inc.) was used to perform analysis of variance (ANOVA), Tukey, and chi-squared tests. Fitting of the kinetic response was performed by a least squares fit algorithm in Matlab with the EzyFit package (Université Paris-Sud).

Results

Kinetic Attachment Assays

Zoospores attached at a higher density on smooth surfaces than on Sharklet surfaces for every time point during the 4-hr experiment (Figure 6-2). The attachment response was the same for the smooth surface regardless of whether it completely covered the slide or was adjacent to the Sharklet topography. Spores were inhibited by the Sharklet topography regardless of the areal coverage on the test slide (6.5 cm² or 19.4 cm²).

This kinetic attachment assay was conducted twice to ensure reproducibility (Figure 6-3). The zoospores responded to the surfaces in the same manner for both tests. The first assay, performed in October 2009, had lower zoospore attachment densities than the assay performed in April 2010. However, previous studies show that there is natural variability in the absolute numbers of attached spores from one experiment to another.²⁴

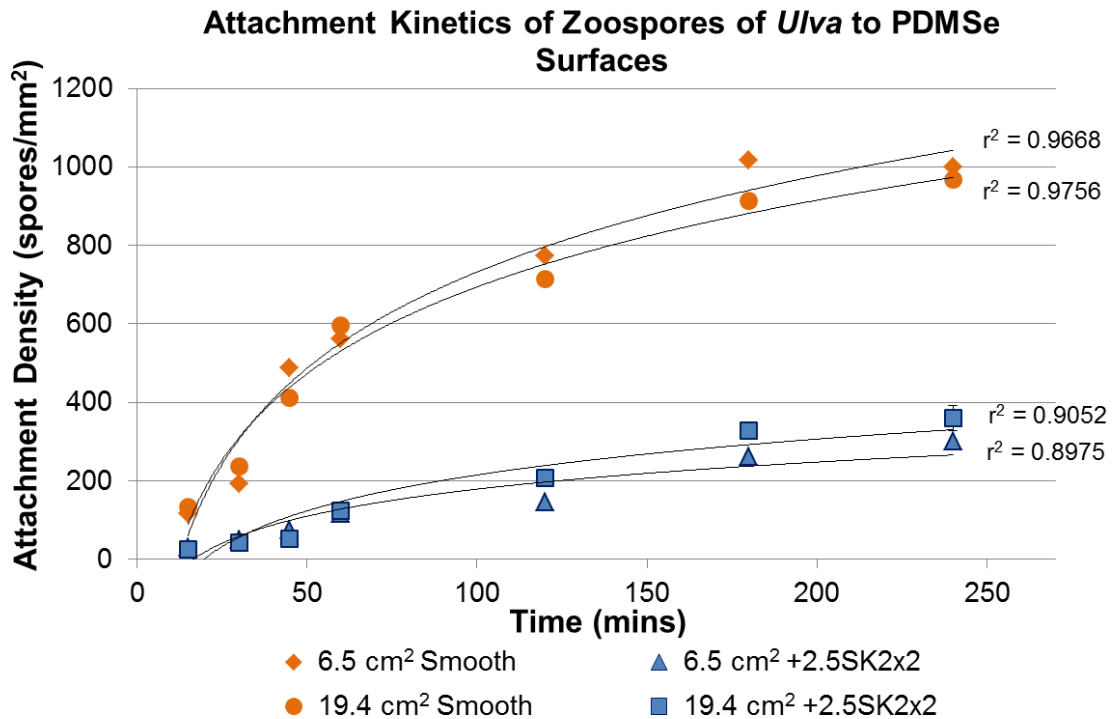


Figure 6-2. Kinetic response of zoospore of *Ulva* to smooth and Sharklet PDMS_e surfaces. Error bars indicate 95% confidence intervals. Correlation coefficients are for the fit of equation (6-1) to the attachment data.

Despite the variability in absolute settled spore density, a one-way ANOVA (df = 12, F = 14.065, p < 0.001) with a Tukey test (p < 0.05) showed that the reduction in zoospore density on the Sharklet surfaces is constant at 80% for up to 2 hrs (Figure 6-3). The attachment reduction is lower at 70% for the 180 and 240 min time points. These results were consistent between the two assays with the exception of assay 1 at 45 mins. The percent reduction in spore density is comparable to previous studies^{65,66,68,82,172} in which the positive SK2x2 surface reduced attachment of spores by 63-86% over a 45 min assay.

Mapping Spore Attachment

Mapping the attachment of zoospores on the Sharklet topography qualitatively illustrates the kinetic fouling process. The maps for all spores attached to the Sharklet

topography (Figure 6-4) reveal that zoospores prefer to attach in the depressed areas between features, rather than on top of them. The spores exhibit a higher selectivity for three particular sites on the Sharklet topography, as noted in a previous publication.¹⁷⁴ Two of these sites are located at the ends of the features and a third site adjacent to midpoint of the longest feature. Fifty percent of the spores attach in these three sites, which account for only 31% of the total surface. The spores' selectivity appears to favor site 1 relative to site 3 for all times other than 15 mins. There also appears to be a decreasing selectivity for site 3 beyond 45 mins. Site 1 and site 2 appear to be equivalent in terms of spore selectivity.

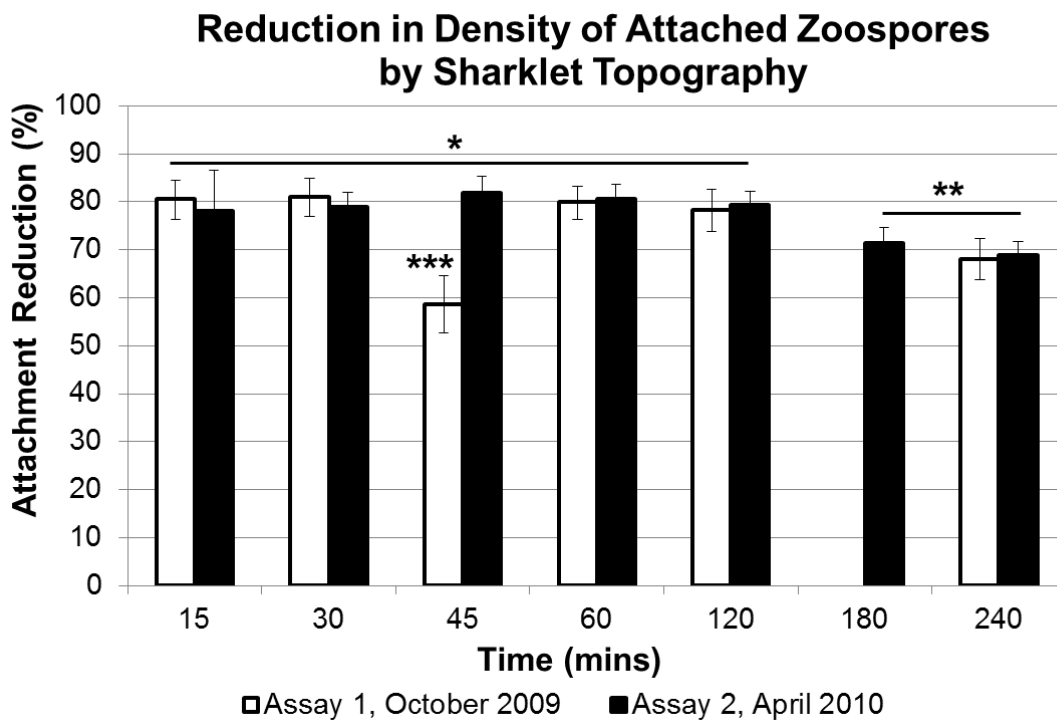


Figure 6-3. Reduction in zoospore attachment density on Sharklet microtopography versus smooth PDMSe (6.5 cm² areas). Results are shown for two assays. Groups indicated by asterisks were shown to be similar ($p < 0.05$) by a Tukey test. Error bars indicate 95% confidence intervals.

All Spores (1 + 2 + 3 + >3)

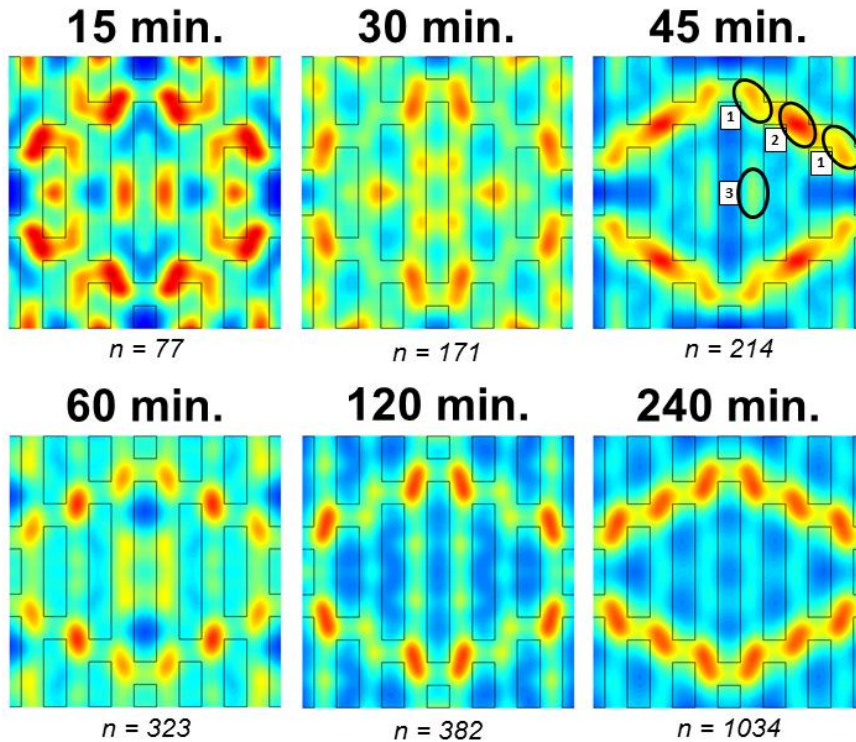


Figure 6-4. Maps of all zoospores attached to the Sharklet topography during the kinetic study. The map at 45 mins indicates the sites of high preferential settlement that were originally described by Long et al. (2010a). Warm colors indicate high attachment density for that time point. Colors cannot be compared between time points.

Breaking down the attachment maps for all spores (Figure 6-4) into substituent groups (Figures 6-5 through 6-8) provided additional insight. Most of the spores attach to the Sharklet topography as single organisms. As a result, the attachment map for single spores (Figure 6-5) most closely represents the behavior of all spores attaching to the surface. The preference for attaching at the edge of the diamond pattern is maintained as the size of the settlement group increases to two and three spores (Figure 6-6 and 6-7). It also appears that as the size of the group increases, the attachment spreads out from the preferential sites observed for single spores. This

indicates that additional spores attach on the surface next to a spore that has already settled. Large groups (>3 spores) were not as selective, especially after 120 mins (Figure 6-8). Large rafts of cells were occasionally seen on the surface at these later times which reflects the lack of preference in the settlement maps at these time points.

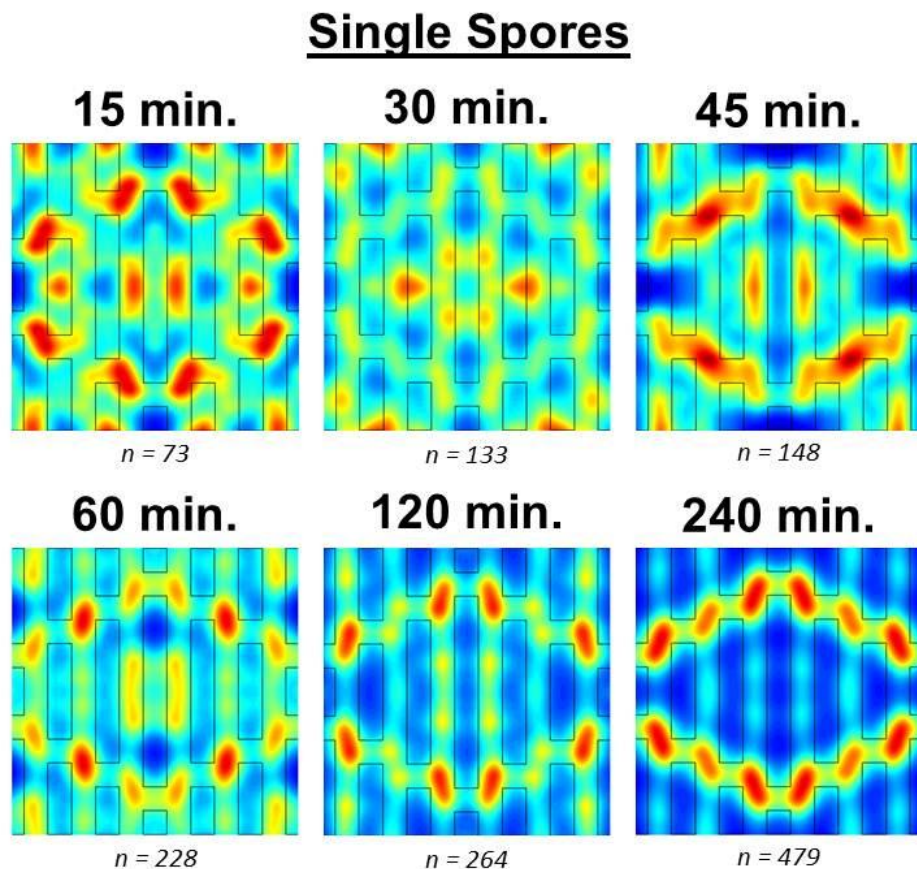


Figure 6-5. Settlement maps of individual spores on the Sharklet topography. Colors cannot be compared between time points.

Spore Grouping

The attachment of spores of *Ulva* on smooth surfaces shows the characteristics of ‘gregariousness’, i.e. depending on the initial spore density, the attachment of one spore appears to promote the attachment of additional spores in the same vicinity resulting in groups attached to the surface.²⁴ The grouping of spores was compared between

Sharklet and smooth surfaces to test whether the topography influenced gregariousness (Figure 6-9). The Sharklet topography inhibited the ability of spores to form groups of more than three spores. Chi-squared tests revealed that the distributions of spore groups was statistically different between Sharklet and smooth surface at both early (Figure 6-9A, $\chi^2 = 371$, $df = 3$, $p < 0.001$) and late (Figure 6-9B, $\chi^2 = 1143$, $df = 3$, $p < 0.001$) time points. Seven percent of spores attached on smooth PDMS as single spores after 240 mins compared to 46% of the on the Sharklet microtopography (Figure 6-9B).

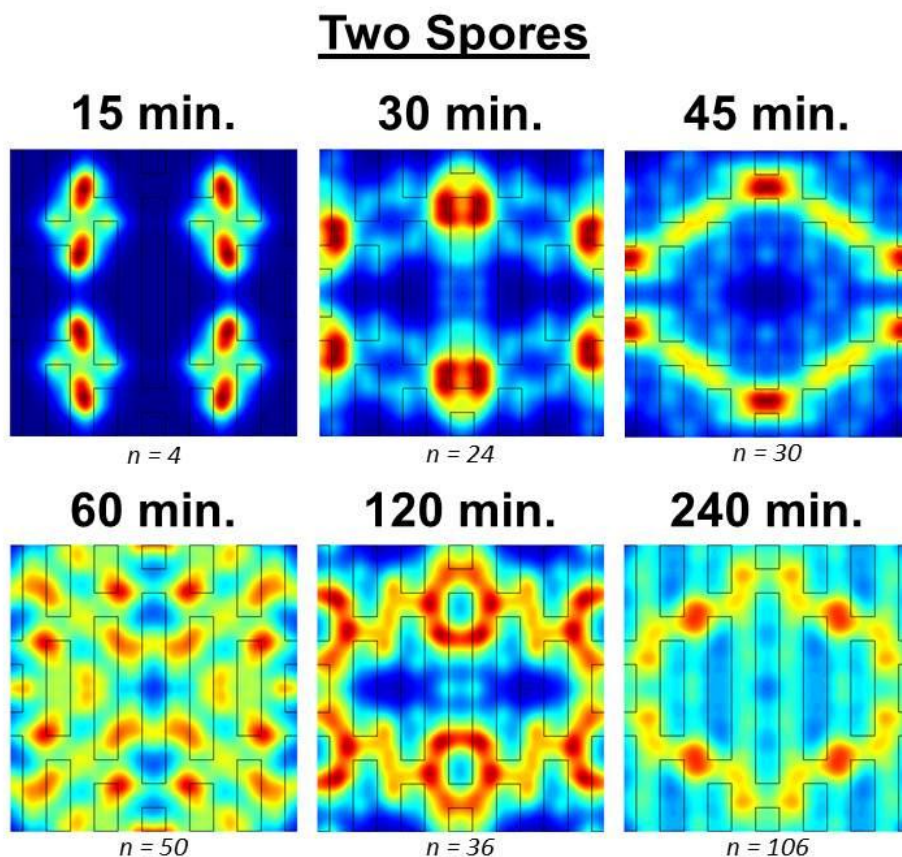


Figure 6-6. Settlement maps of spores in groups of 2 on the Sharklet topography. Sharp color contrast at early time points arises from low numbers of spores observed on the surface (less than approximately 50 spores). Colors cannot be compared between time points.

Three Spores

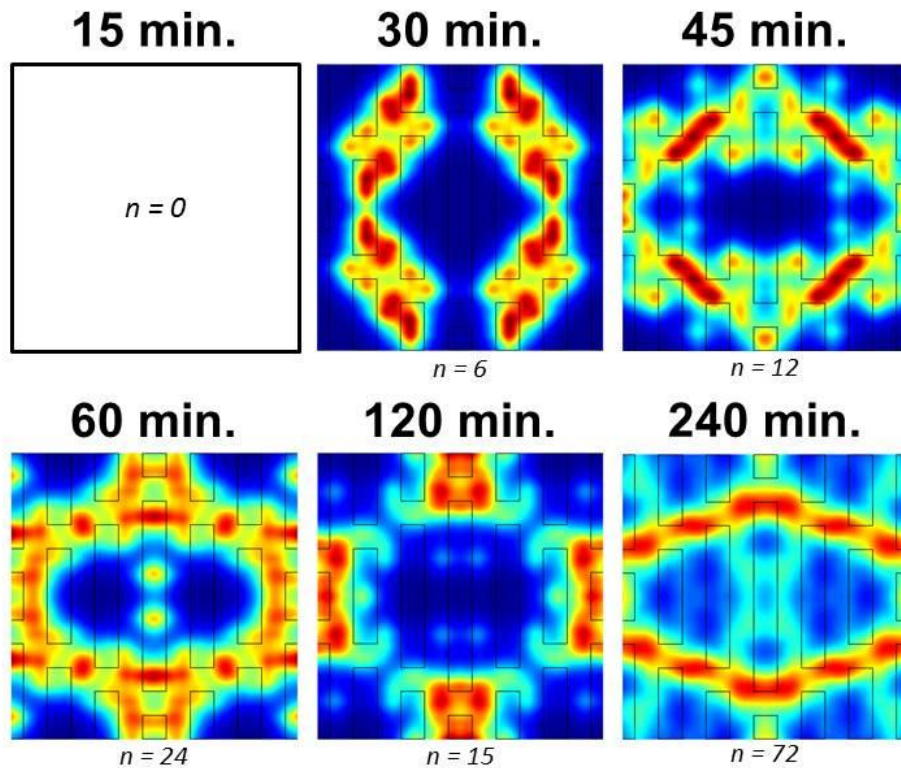


Figure 6-7. Settlement maps of spores in groups of 3 on the Sharklet topography. No groups of 3 spores were observed after 15 mins. Sharp color contrast on some images arises from low numbers of spores observed on the surface (less than approximately 50 spores). Colors cannot be compared between time points.

To ensure that the results of this analysis were not caused by a lower density of spores on the Sharklet surface, the spore density after 30 mins on smooth (236 spores/mm²) and 120 mins on Sharklet (207 spores/mm²) were chosen to compare grouping at the same approximate spore density. The distribution of spore groupings is significantly different for the two surfaces (Figure 6-9C, $\chi^2 = 446$, $df = 3$, $p < 0.001$). Sixty-nine percent of the spores attached as single cells on the Sharklet topography compared to only 14% on the smooth surface. Chi-squared tests confirmed that the

distributions of spore groupings are statistically different ($p < 0.001$) for Sharklet and smooth (Figure 6-9 A-C).

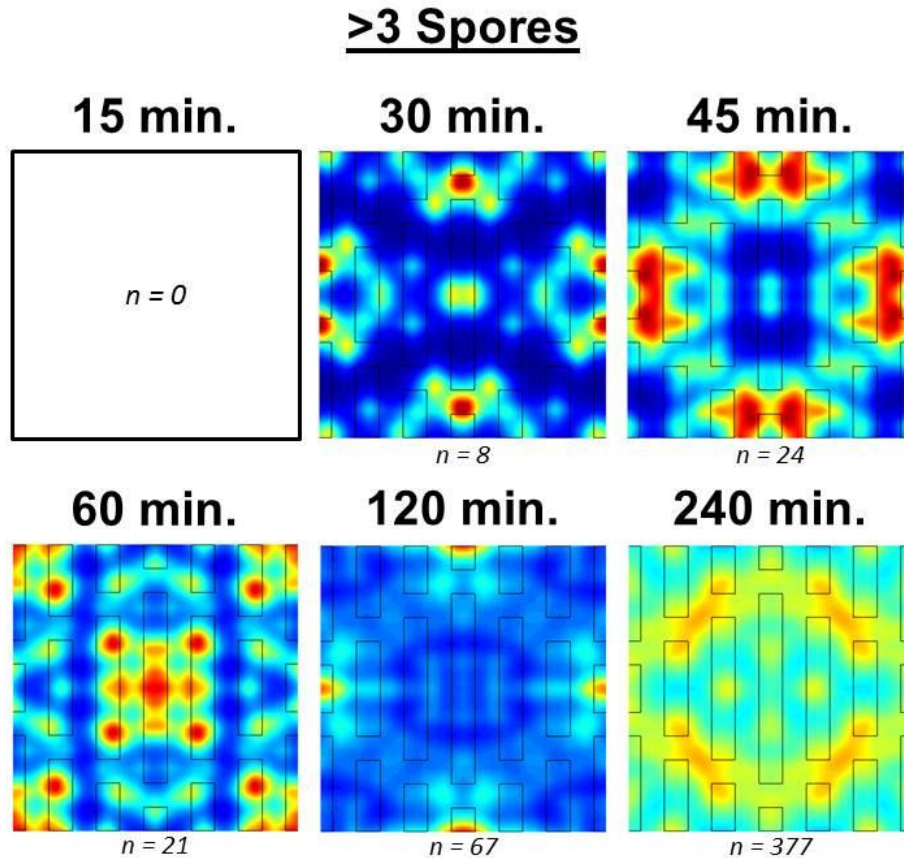


Figure 6-8. Settlement maps of spores in groups of more than 3 on the Sharklet topography. No groups of more than 3 spores were observed after 15 mins. Sharp color contrast on some images arises from low numbers of spores observed on the surface (less than approximately 50 spores). Colors cannot be compared between time points.

Discussion

The kinetics of spore attachment on smooth surfaces over a 4 hr period reveal an approximately linear rate over the first 60 mins, but thereafter the attachment rate progressively decreases. Similar kinetics were reported by Callow, et al.²⁴ and were ascribed to reduced competence of the zoospore population to attach with time under the assay conditions (i.e. within a population of 'wild' spores, there is a range of

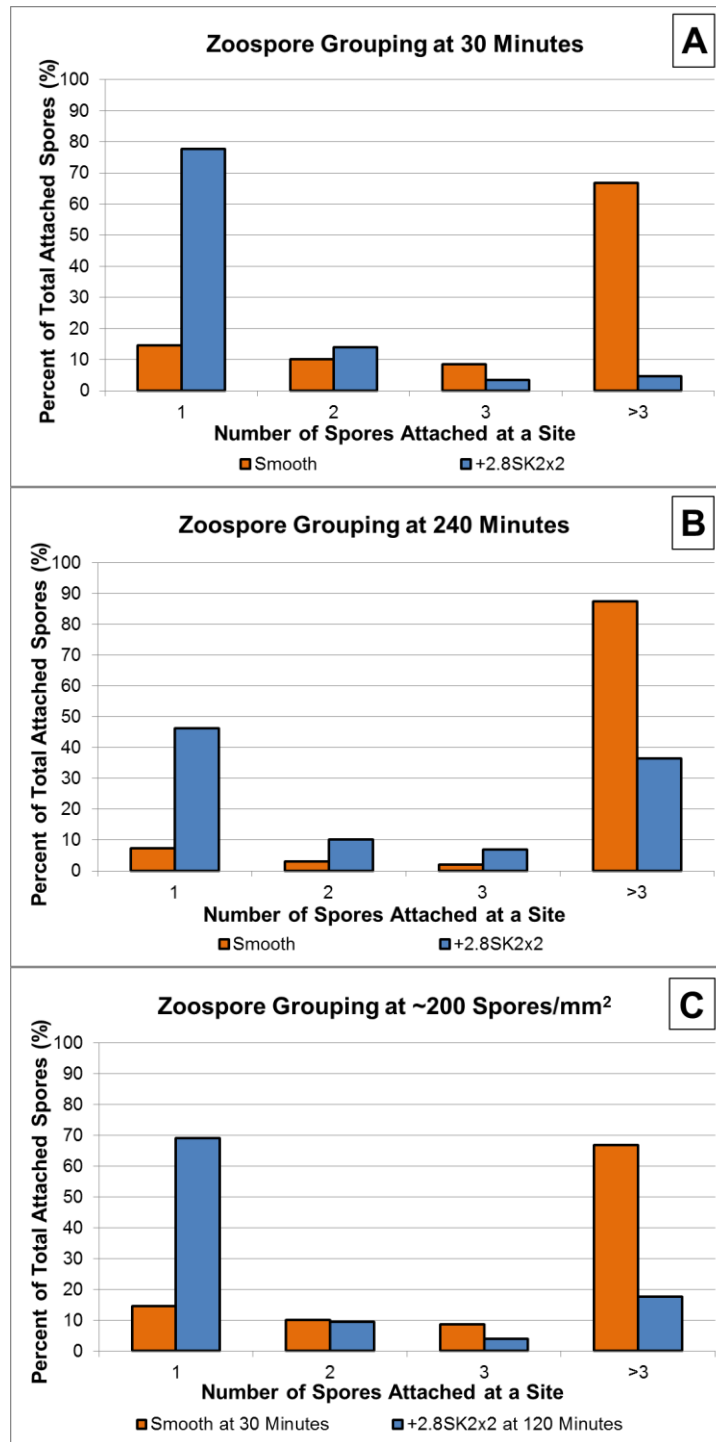


Figure 6-9. Distribution of zoospores in groups of 1, 2, 3, or more than 3 (as determined microscopically by spores touching) at (A) 30 mins, (B) 240 mins, and (C) a spore density of approximately 200 spores/mm². A chi-squared test for each condition (A-C) showed that the Sharklet surface has a statistically different distribution from the smooth surface ($p < 0.001$). These samples were taken from the smooth and 6.5 cm² Sharklet surface (Fig. 1A and B).

propensity for settlement so that with time the population of spores in the assay becomes biased towards those with reduced propensity to settle). In the context of these experiments, two other causes of progressively reduced attachment rates may be operating beyond reduced competence. First, it is likely that with time the surface became progressively conditioned by organic materials either present in the water in which the spores were released, or which was secreted by the swimming spores. Such conditioning materials could make surfaces less attractive for attachment. Second, the number of swimming spores in solution was reduced over time by attachment to both the test surfaces and especially those of the container in which the test slides are immersed.

The spore attachment density on Sharklet topographies was nearly linear with time and was significantly lower at each time point compared to smooth PDMS_e (70-80% reduction). These results are consistent with previous assays^{65,66,68,82,172} in which the microtopography reduced attachment densities from 63 to 86% over 45 mins.

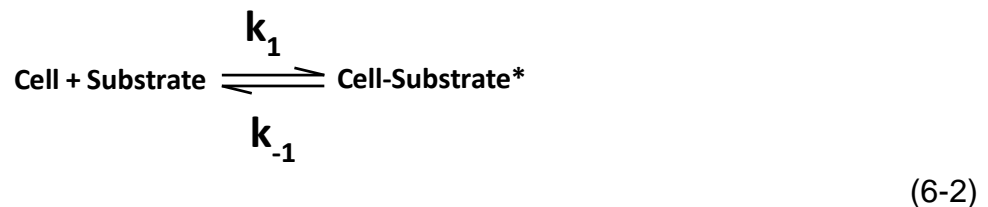
Mapping the spore attachment sites on the Sharklet microtopography showed that the zoospores preferentially attach in the recessed areas. This is consistent with previous results showing that spores attach preferentially in the recessed channels of PDMS_e patterned surfaces²⁵, specifically at the long ends of the features.¹⁷⁴ The maps generated in this study capture the attachment at various time points and also categorize the spores as individuals or part of a group of spores. This was done to identify any cooperative behavior. It appears from the maps that attachment of single spores occurs at preferential sites along the edge of the diamond pattern, with attachment becoming more diffuse along the edge as the size of the group increases.

This indicates that additional spores are settling adjacent to the first spore during the initial colonization of the surface. It is worth noting that the results of mapping all spores (Figure 6-4) represent a weighted-average map for spore groups of 1, 2, 3 and >3 cells. The attachment maps for all cells most closely resemble the map for single spores because spores predominantly attach as individuals.

The kinetic attachment curve can be fitted to the asymptotic exponential function in Equation (6-1) to provide a quantitative measure of the rate of adhesion. This function was used to describe attachment kinetics of bacteria to surfaces:¹⁷⁶⁻¹⁸⁰

$$A(t) = A_e(1 - e^{-\beta t}) \quad (6-1)$$

where $A(t)$ is the number of attached organisms at time t , A_e is the equilibrium density of attached cells, and β is a characteristic time constant. This equation describes the reversible process:



in which k_1 and k_{-1} are the rates of attachment and detachment from the surface, respectively. In the case of *Ulva*, experimental observations of a reversible ‘first kiss’ contact with the surface warrant a model such as that in Equation (6-2).²⁴ Since these experiments were not performed *in situ*, a direct measure of the adsorption (k_1) and desorption (k_{-1}) cannot be obtained. Equation 6-1 is fit to the data as an estimation of the kinetic response. A least-squares fit of this equation provides values for β . Using

this time characteristic time constant, the initial flux of spores at the surface can be approximated by the quantity J_o :

$$J_o = A_e \times \beta \quad (6-3)$$

in which J_o has equivalent units of flux (spores·mm⁻²·min⁻¹).

Table 6-1. Parameters A_e and β generated by the least squares fit of Equation (6-1). A_e is the anticipated density of spores at equilibrium ($t \rightarrow \infty$). β is the characteristic time constant and J_o is the flux of spores at the surface.

| Assay | Test area (cm ²) | Surface | A_e (spores·mm ⁻²) | $\beta \times 10^3$ (mins ⁻¹) | J_o (spores·mm ⁻² ·min ⁻¹) | r^2 |
|--------------|------------------------------|-----------|----------------------------------|---|---|-------|
| October 2009 | 19.4 | Smooth | 748 | 9.2 | 6.9 | 0.924 |
| | 13 | Flat Area | 639 | 11 | 7.0 | 0.960 |
| | 6.5 | +2.8SK2x2 | 371 | 3.4 | 1.3 | 0.979 |
| | 19.4 | Smooth | 1042 | 11 | 11.5 | 0.975 |
| April 2010 | 13 | Flat Area | 1135 | 10 | 11.4 | 0.963 |
| | 6.5 | +2.5SK2x2 | 639 | 2.7 | 1.7 | 0.978 |
| | 19.4 | +2.5SK2x2 | 1046 | 1.9 | 2.0 | 0.988 |

Fitting Equation 6-1 to the kinetic data show that the characteristic time constant (β) is distinctly lower on Sharklet surfaces (1.9-3.4 mins⁻¹) than on smooth surfaces (9.2-11 mins⁻¹, Table 6-1). The projected flux, J_o , offers a more physically intuitive sense of the early-stage response of the spores to the surface. J_o for Sharklet was consistently lower (1.3-2.0 spores·mm⁻²·min⁻¹) than J_o for smooth surfaces (6.9-11.5 spores·mm⁻²·min⁻¹). The value of J_o was approximately 80% lower on Sharklet than on smooth surfaces within the same assay. This fitted value for the initial flux at the surface correlates well with the observed 80% reduction in spore density on Sharklet surfaces during the first 2 hrs of the assays.

The parameter β has been associated with numerous cell-surface phenomena in bacteria including the synthesis of extracellular matrix and the exclusion of bacteria from settling next to neighbors.^{176,180,181} While Equation 6-1 has been effective in describing

adhesion of non-motile bacteria, it was unknown whether this Langmuir-type adsorption process would effectively describe the attachment of motile spores. Indeed, the surface is far from saturated with spores. The surface area coverage is only 6.4% if two assumptions are made, i.e., area of an attached spore with its halo of adhesive on PDMS_e is $64 \mu\text{m}^2$ ¹⁸² and density of spores is 1000 spores/mm² (maximum on the smooth PDMS_e). The assay only captures the response of the zoospores which have strongly committed to adhesion – a process that is fundamentally different to the dynamic adhesion/detachment (or adsorption/desorption) observed for bacterial adhesion. Yet Equation (6-1) fit with high correlation ($r^2 > 0.9$) and J_0 accurately reflected the observed 80% reduction in attachment rate. The lower values for β on the Sharklet topography may reflect a reduced ability for attached spores to cooperatively recruit other spores to the surface. Additional evidence to this end is provided by comparing the grouping of spores on the smooth and Sharklet surfaces.

Spores attach as larger groups on smooth PDMS_e (Figure 6-9). After 45 mins, the percentage of spores attached as individuals on smooth PDMS_e (contact angle 113°) was 19%. This correlated well with a previously published value of ~22% spores attached as singles on flat SAMs with a similar contact angle (110°) after 1 hr.⁵⁵ In contrast, a majority of spores (69%) on the Sharklet surface were attached as singles after 45 mins. It seems that zoospores were not able to form gregarious communities on the Sharklet pattern. This may be simply due to the fact that the early colonizing spores physically occupy those sites on the Sharklet surface that are topographically the most attractive for attachment (i.e. a form of 'niche exclusion'). Alternatively more complex mechanisms may be at work whereby the Sharklet surface inhibits the ability of

attached zoospores to recruit neighboring spores to attach. Future quantitative analysis of spore behavior on Sharklet topographies by digital holographic microscopy^{23,183} may provide further insight into the mechanism(s) involved.

Cooperative behavior has been observed for the attachment of *Ulva* to surfaces.²⁴ A Scatchard plot of zoospores binding to glass showed a positive slope at densities below approximately 1,000 spores/mm². This means that at low coverage, the attached cells recruited other cells to the surface. This positively cooperative behavior has also been shown for bacteria binding to surfaces^{181,184,185} and aggregating in suspension.¹⁸⁶ However, at high densities of attached spores, a different behavior has been observed. The Scatchard analysis showed a negative slope, indicating that the attached spores deterred swimming spores from settling.²⁴

The communication mechanisms underlying cooperative effects between zoospores of *Ulva* are essentially unknown but may include both diffusible (chemical) cues or physical, topographical cues presented by previously attached spores. It is possible that the inhibitory nature of the Sharklet topography is due to interference in the dynamics of such cooperative effects. For example, the Sharklet topography may simulate a high density of attached spores leading to negative cooperativity, a slower rate of attachment (k_1) and a smaller characteristic time constant (β). While these experiments do not identify the individual rate constants (k_1 and k_{-1}), future experiments such as Scatchard analyses may be able to identify any cooperative behavior on the Sharklet surface.

CHAPTER 7 CONCLUSIONS AND FUTURE WORK

Introductory Remarks

Microbial biofilms were the first form of life that existed on earth. Their long history has given rise to diverse, complex organisms from several kingdoms of life. Biofilms protect microorganisms from the environment, ensuring the survival of the species from one generation to the next. As a result, biofilms are difficult to eradicate when they threaten human health and productivity.

Organic/inorganic nanocomposites were implemented in this work to address the issue of biofouling. These composites took two forms: polymer-bioactive glass microspheres and antifouling topographies in silica-reinforced PDMS. Both approaches aimed to understand how surface structure correlates to the prevention of biofilms.

Composite Bioactive Glass Microspheres

Organic/inorganic microspheres were created to eliminate biofilms and restore the function of bone tissue. Microspheres encapsulated vancomycin, an antibiotic that has semi-specific toxicity to Gram-positive bacteria. The inorganic phase dissolved to produce calcium and silicate ions, which have been shown to stimulate bone growth.¹⁸⁷ When the inorganic phase is formed by acid catalysis, the microspheres were stable over a period of 1 week. The organic phase acted to bind the microspheres together and played a key role in determining the final morphology.

The pH of the sol influenced the composition of the microspheres. 77S microspheres prepared at pH ~10.5 were 65-85 wt% organic, while 77S microspheres at pH ~2 were 38-48 wt% organic. This can be attributed to the higher rate of hydrolysis

of TEOS under acidic conditions. The resulting microspheres were more stable in SBF when produced by acid catalysis. This may be attributed to the greater inorganic content or the structure of the gel.

Calcium-silicate glasses have been previously shown to stimulate osteogenic differentiation of osteoblasts.^{104,187,188} However, this was not tested in this work. Alkaline phosphatase¹⁸⁸, osteocalcin¹⁰⁴, and collagen production¹⁰⁵ are osteogenic indicators that can be measured *in vitro* in future experiments. *In vivo* studies should be performed if these assays indicate that the microspheres encourage bone formation. One *in vivo* study has shown that vancomycin-loaded xerogels cause a mild inflammatory response and fibrous encapsulation.¹⁶¹ This may have been due to slow dissolution of the calcium-deficient xerogel. The microspheres presented in this work may dissolve more quickly because they contain a water-soluble organic component.

Future work should also focus on extending the release of vancomycin. Linear drug release over 2-3 weeks is ideal for treating osteomyelitis.¹⁰¹ Several approaches can be used to extend the release. Soaking the microspheres in an alkaline solution after forming them by acid catalysis should reduce the pore size by driving condensation of any remaining silanol or alkoxy groups. Another approach is to covalently attach vancomycin to the polymer present in the aqueous phase. Carbodiimide chemistry could be used to perform this covalent attachment.¹⁸⁹ This could also crosslink the polymer, which may slow the drug release even further.

Bone morphogenic proteins (BMPs) could also be delivered using these microspheres. BMPs have been approved by the FDA for in both spinal fusion and long bone defects. While BMPs are very effective at causing bone growth, there have been

some issues related to ectopic bone formation.¹⁹⁰ BMPs are typically delivered by a collagen sponge, which is soaked in a solution of the protein. This method of drug loading is dependent on handling by the surgeon – which could be highly variable. Incorporating the BMPs into microspheres may provide a more accurate way to dose the drug.

These microspheres should be incorporated into a paste or gel that can be easily applied by the surgeon. Ideally this paste or gel would harden to provide some mechanical stability. This may also slow the release of the encapsulated drug.

The current method for creating microspheres can only be used to encapsulate water-soluble drugs. This work could be extended by identifying a way to encapsulate oil-soluble drugs into these microspheres. One approach is to create a double emulsion (oil-in-water-in-oil) in which the drug is dissolved in the innermost oil phase.

Antifouling Topographies on Elastomeric Films

The surface topography of a silica-filled PDMS elastomer was used to deter the settlement of marine algae. The organic phase, PDMS, has a surface energy of ~22 mN/m, which forms a weak adhesion to a variety of fouling organisms.⁴⁸ The nanometer-sized silica particles increase the toughness and durability to the coating, which is important for long-term performance in marine applications.

The long-term performance was examined in an extended laboratory. The surface texture consistently inhibited marine algae by 70-80% over a 4 hr period. Image analysis showed that algal zoospores cannot easily form groups on the micro-textured surface. Conversely, the organisms form clusters on smooth surfaces. This indicates that topography may prevent the early stage of biofouling by preventing the aggregation

of individual cells. However, future work is needed to fully understand how microtopographies inhibit biofilm formation.

A Scatchard analysis is one experiment that will provide additional insight into the behavior of zoospores attaching to topographies.¹⁸¹ This experiment will show whether the zoospores act cooperatively, i.e., whether the attachment of one zoospore facilitates the attachment of a second. A previous study with zoospores of *Ulva* showed positive cooperativity at low cell densities and negative cooperativity at high cell densities.²⁴ If topography mimics cells already attached to the surface, negative cooperativity would be observed by a negative slope on a Scatchard plot.

The results in chapter 6 showed that equations derived from Langmuir-type adsorption fit kinetic attachment of zoospores. This suggests that the attachment process is driven largely by physical phenomena. The Brennan Research Group has developed a model called the engineered roughness index (ERI) as a way to quantify the physical structure of the surface. The ERI model has the ability to predict the relative attachment for a variety of species to textured surfaces.^{57,172} The ERI was derived from steady state (45 min) adhesion assays. A logical extension of this work would be to combine the kinetic parameters identified in chapter 6 (β and A_e) with the ERI to create a model that can predict settlement over longer periods of time.

Amphiphilic, Nanocomposite Hydrogels as Fouling-Release Coatings

Amphiphilic surfaces have garnered recent interest as fouling-release (FR) coatings. These materials contain both hydrophobic and hydrophilic chemical groups dispersed on the nanoscale. This chemical heterogeneity is believed to weaken the protein interaction with the surface, resulting in FR behavior.

Amphiphilic coatings in the literature typically use fluoropolymer and PEG as the hydrophobic and hydrophilic constituents, respectively. These chemical groups have been implemented as pendant chains of a polymer⁶⁰, in cross-linked diacrylate gels^{188,189}, or as hybranched networks.⁶² Wang, et al.¹⁸⁸ have created perfluoropolyether/PEG gels that that have high (~60°) contact angle hysteresis, which is indicative of chemical or topographical heterogeneity. The contact angle hysteresis was inversely proportional to fibrinogen adsorption.

Nanocomposites have not been extensively investigated as a way of creating amphiphilic chemistries. Detty's group has explored this idea by using sol-gel chemistry to create xerogels which contain alkyl, fluoroalkyl, and aminoalkyl groups.^{83,85} Trialkoxy(silanes) were used to introduce these various organic groups. Xerogels with a wide range of surface energies have been created using this method. Relationships have been established for the surface energy of these materials and the attachment of barnacles⁸⁴ and zoospore of *Ulva*⁸⁷. However, only a few xerogel compositions have shown to have discontinuous or dispersed phases with a nanoscale domain size.⁸⁵ Most of the xerogels appear to be a single, mixed phase.

Preliminary work has been done to create amphiphilic nanocomposites based on poly(ethylene glycol) methacrylate (PEGMA) and fluorocarbon-functionalized silica particles. The intent is to co-functionalize silica nanoparticles with methacryloxypropyl (MAP) and nonahexylfluorocarbon (NHF) groups. These particles then act as the crosslinking agents in PEGMA gels. The MAP groups allow the particles to react with the PEGMA polymer. Fluorocarbon groups impart nanoscale hydrophobicity to the gel. The preliminary results are shown below.

Silica nanoparticles were made by a Stöber-type process. These multi-functional particles were mixed with PEGMA at various concentrations and photopolymerized with Irgacure 2959 (Appendix E). Dynamic light scattering was performed on solutions of both methacrylate-functionalized silica particles (MAP-SiO₂) and fluorocarbon/methacrylate-functionalized silica particles (NHF/MAP-SiO₂). The particle diameters calculated from this technique were 13 nm and 7 nm for MAP-SiO₂ and NHF/MAP-SiO₂, respectively. This assumed that the refractive index of the particles was $n_{\text{real}} = 1.420$ and $n_{\text{imaginary}} = 0.001$ and that the solvent was 190 proof alcohol. The measured diameters were smaller than the anticipated size (>50 nm) based on previous reports of this process.^{190,191}

When these particles were photopolymerized with PEGMA, gels were created that swelled 600-1,000 wt% in water (Table 7-1). Gels containing 25 wt% NHF/MAP-SiO₂ appeared more opaque than gels containing 25 wt% MAP-SiO₂. Fluorocarbon functionalized nanoparticles did not influence the final water content of the gels (Table 7-1), but did appear to slow the initial swelling of the gel (Figure 7-1).

Table 7-1. Swelling ratio of nanocomposite hydrogels after 48 hrs in DI water. Error values represent 95% confidence intervals

| Particle Type | Particle concentration in dry gel (wt%) | Swelling ratio, Q $Q = (\text{mass}_{\text{wet}} - \text{mass}_{\text{dry}}) / \text{mass}_{\text{dry}}$ |
|--------------------------|---|---|
| MAP-SiO ₂ | 1 | 15 ± 1.7 |
| MAP-SiO ₂ | 10 | 14 ± 1.1 |
| MAP-SiO ₂ | 25 | 6.2 ± 1.3 |
| NHF/MAP-SiO ₂ | 25 | 6.2 ± 0.4 |

The captive air bubble contact angle for gels with and without fluorocarbon groups was approximately 30° (Figure 7-2). This indicates that PEG dominated the surface

when immersed in water. The contact angle was only 2° higher for gels containing fluorocarbon groups ($p = 0.039$, $n = 20$ measurements).

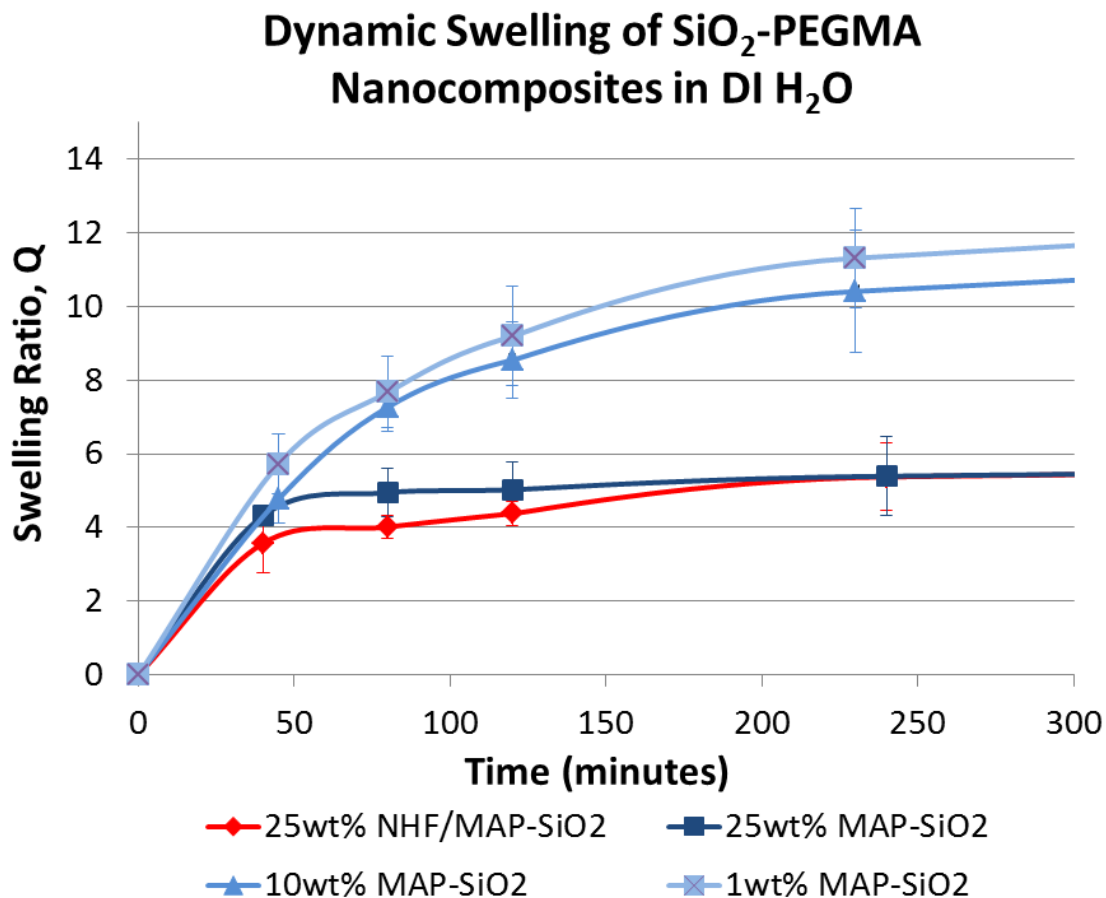


Figure 7-1. Dynamic swelling of PEGMA gels containing various concentrations of functionalized SiO₂ nanoparticles. Error bars indicate 95% confidence intervals.

FESEM indicated that the material that is in contact with the gel as it was polymerized influence the gel’s structure and composition. Surfaces polymerized against PDMS_e appeared “rougher” than gels polymerized against quartz (Figure 7-3). EDS showed that surfaces polymerized against PDMS_e had a very small fluorine peak. The fluorine peak was not apparent on surfaces polymerized against quartz (Figure 7-3). This indicated that NHF/MAP-SiO₂ nanoparticles may have selectively adsorbed

on the hydrophobic PDMS surface, increasing the concentration of particles near this surface.

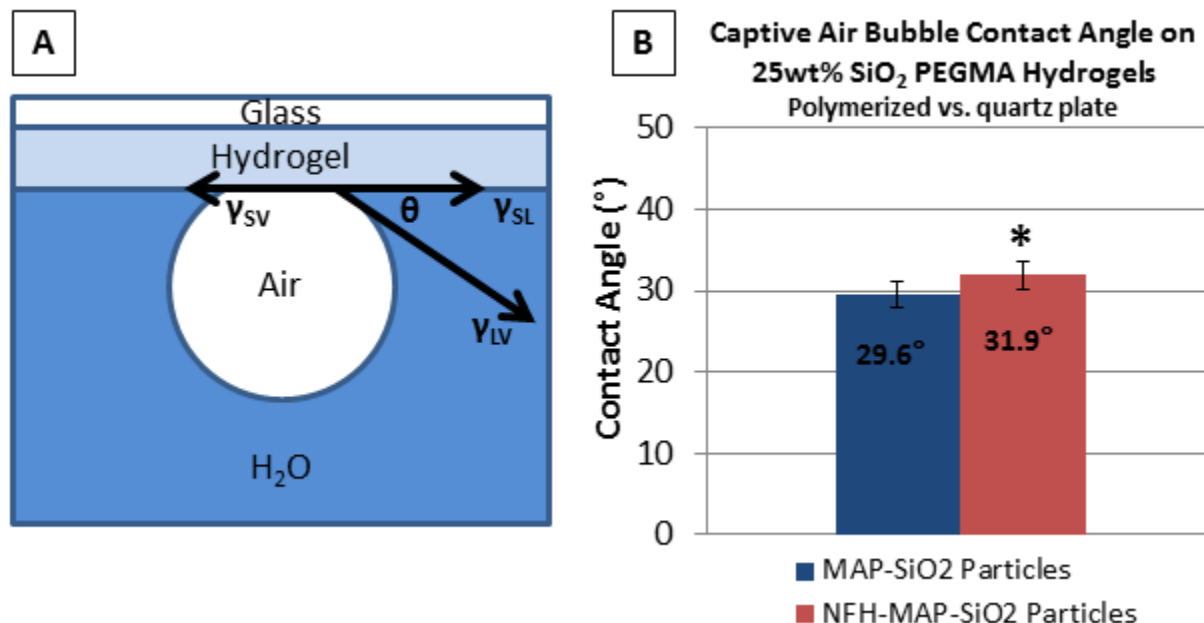


Figure 7-2. Contact angle on nanocomposite gels. (A) The samples are inverted and a 10 μ L captive air bubble is placed in contact with the gel surface. The contact angle is shown as θ . (B) Contact angle measurements for 25 wt% MAP-SiO₂-PEGMA gels and 25 wt% NHF/MAP-SiO₂-PEGMA gels. Contact angle was measured for surfaces polymerized versus quartz.

The results suggest that gels produced by this method may not be covalently cross-linked. Rather, the gels may be physically entangled. The particle diameters measured by dynamic light scattering are likely too small to have the numerous methacrylate groups required to crosslink the system. This would explain why there no apparent difference in swelling ratio between gels made with 1 or 10 wt% MAP-SiO₂ particles. The surfaces appear to be largely dominated by PEGMA. Dynamic swelling and EDS measurements indicate that fluorocarbon is incorporated into the material, although the effect appears to be very weak.

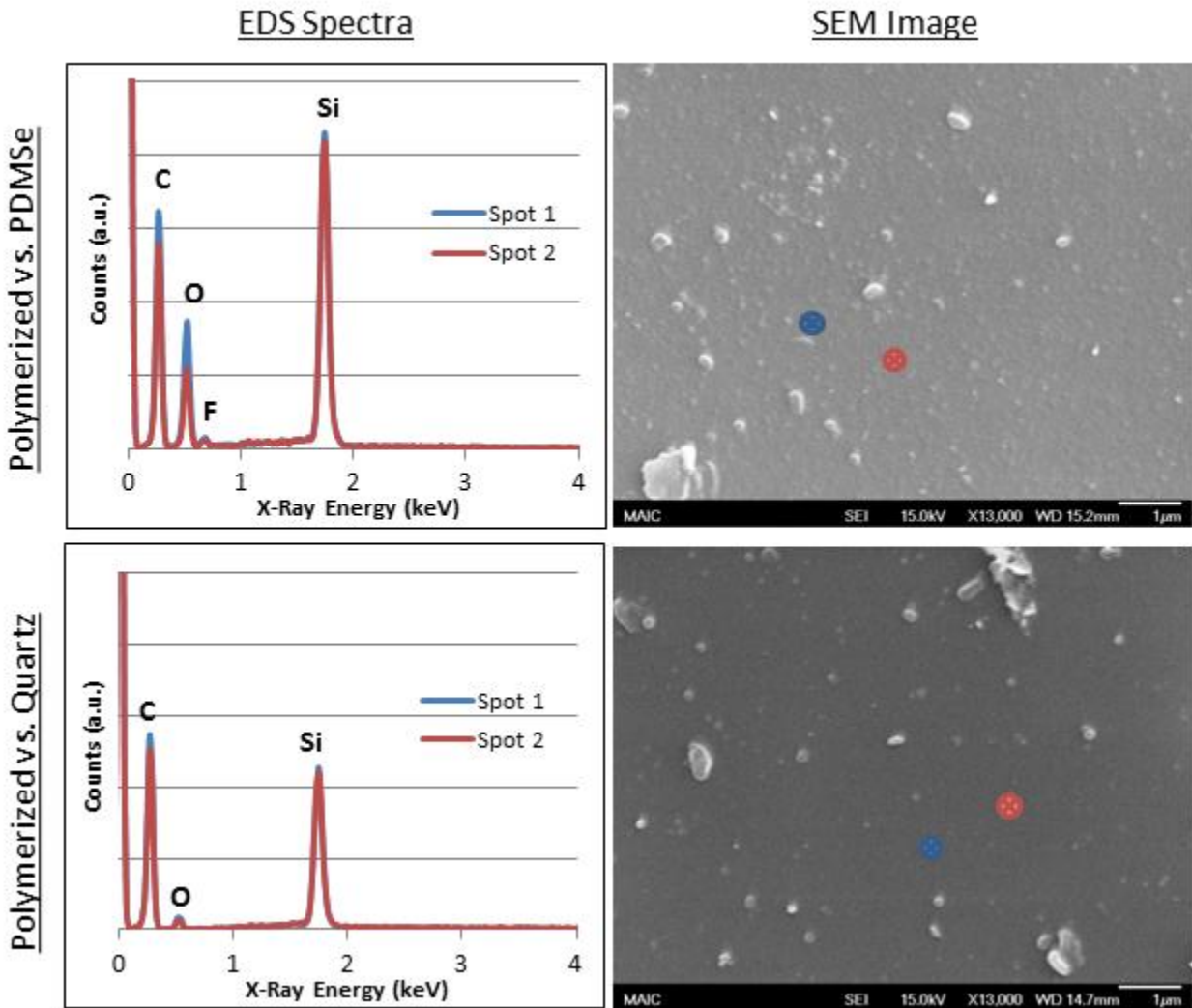


Figure 7-3. SEM/EDS analysis of gels containing 25 wt% NHF/MAP-SiO₂ particles. The surface polymerized against PDMSe (top row) appears to have a “rougher” texture than gels polymerized against quartz (bottom row). Surfaces polymerized against PDMSe have a very small fluorine peak, which is not apparent when the surface is polymerized against quartz.

Future work on these amphiphilic nanocomposites should use larger particles to increase the number of methacrylate groups on the particles. Increasing the crosslink density of the gels should restrict the ability of the network to rearrange and bury the hydrophobic particles. This could be accomplished by incorporating PEG-dimethacrylate or increasing the number of particles in the nanocomposite.

Fluorocarbon groups with higher molecular weights could also be used to increase the hydrophobicity of the particles

APPENDIX A
CALCULATION OF CRITICAL MOLECULAR WEIGHT OF ENTANGLEMENT FOR
PVP IN SOLUTION

The molecular weight of entanglement (M_e) can be calculated from the principles of chain dimensions according to the paper by Fetters.¹⁹² This calculation is based on the pervaded volume of the chain (Figure A-1). This pervaded volume is approximated as the smallest sphere which can encompass the chain (V_{sp}), which is expressed as:

$$V_{sp} = A \langle R_g^2 \rangle_o^{3/2}$$

in which A is a constant on the order of 1 and $\langle R_g^2 \rangle_o$ is the unperturbed mean-square radius of gyration.

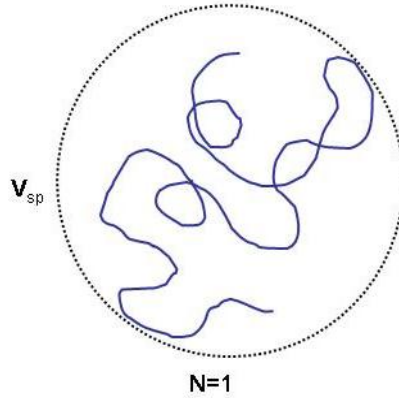


Figure A-1. Spherical pervaded volume of a polymer chain (V_{sp}).

The radius of gyration can also be written as:

$$\langle R_g^2 \rangle_o = \frac{C_\infty M l_o^2}{m_o \phi}$$

in which C_∞ is the characteristic ratio, M is the molecular weight of the entire chain, l_o is the length of each repeat unit, and m_o is the molecular weight of each repeat unit.

Substituting this expression into the equation for pervaded volume:

$$V_{sp} = A C_\infty^{3/2} M^{3/2} l_o^3 m_o^{-3/2} \phi^{-3/2}$$

Now consider the number of chains (N) which completely fill the volume V_{sp} . This number of chains is calculated as:

$$N = \frac{V_{sp} \rho N_A}{M}$$

in which ρ is the polymer density and N_A is Avogadro's number. Substituting the expression for V_{sp} from above into this equation, N is given as:

$$N = AC_{\infty}^{3/2} M^{1/2} l_o^3 m_o^{-3/2} 6^{-3/2} \rho N_A$$

It can be assumed that the number of chains with which a given chain is entangled is N-1. The condition for entanglement can be considered as when $N = 2$. This condition is shown in Figure A-2. In this case, there are two chains present in the pervaded volume of a single chain. This means that the primary chain (in blue) is entangled with another chain (shown in red).

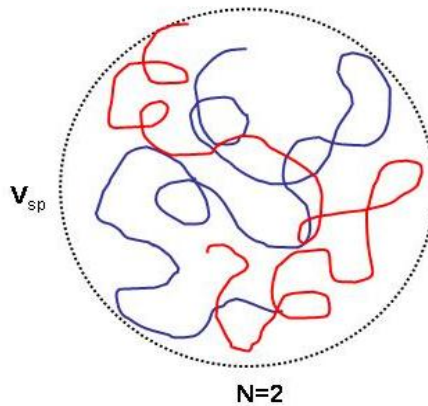


Figure A-2. The condition of entanglement, in which two chains are present in the pervaded volume of a single chain ($N=2$).

The equation above can be expressed for the entanglement condition. In this case, N is replaced with 2 and M is replaced with M_e , or the critical molecular weight of entanglement.

$$2 = AC_{\infty}^{3/2} M_e^{1/2} l_o^3 m_o^{-3/2} 6^{-3/2} \rho N_A$$

Solving this equation for M_e yields:

$$M_e = B^{-2} C_\infty^{-3} l_o^{-6} m_o^3 \rho^{-2} N_A^{-2}$$

in which B is a constant which is:

$$B = \frac{A}{2 \times 6^{3/2}}.$$

This equation can be used to calculate the critical molecular weight of entanglement for PVP. Shenoy¹⁹³ used this equation to estimate the M_e for PVP in ethanol (16.8 kg/mol). In this calculation, polystyrene (PS) was used to approximate the values of B and l_o for PVP in the equation above.. However, M_e for PVP in water will be different than described by Shenoy. To calculate M_e of PVP, a simple ratio is set up using PS as a model:

$$M_e(PVP) = \frac{M_e(PS) C_\infty(PVP)^{-3} m_o(PVP)^3 \rho(PVP)^{-2}}{C_\infty(PS)^{-3} m_o(PS)^3 \rho(PS)^{-2}}$$

Using the values for PVP and PS given by Shenoy:¹⁹³

- $M_e(PS) = 16.6 \times 10^3$ g/mol
- $C_\infty(\text{PVP in H}_2\text{O}) = 14$
- $m_o(\text{PVP}) = 111$ g/mol
- $\rho(\text{PVP}) = 1.13$ g/cm³
- $C_\infty(PS) = 10.8$
- $m_o(PS) = 104$ g/mol
- $\rho(PS) = 1.06$ g/cm³

The value of M_e for PVP in water is 8.15×10^3 g/mol.

APPENDIX B
REAGENTS USED IN SIZE AND MORPHOLOGY STUDY OF ACID-CATALYZED
MICROSPHERES

The reactants used in the synthesis of microspheres for the size/morphology study in chapter 4 are listed as moles (Table B-1) and moles relative to TEOS (Table B-2).

Note that the same oil phase was used for all samples, which consisted of (in moles):

0.3 1-octanol, 3.1×10^{-3} Span 80, and 1.7×10^{-6} hydroxypropylcellulose.

Table B-1. Moles of reagents used in synthesizing acid-catalyzed microspheres for size/morphology study in chapter 4.

| PVP molecular weight (kg/mol) | PVP in aqueous phase (wt%) | Glass | TEOS (moles $\times 10^{-3}$) | CNT (moles $\times 10^{-3}$) | TEP (moles $\times 10^{-3}$) | H ₂ O (moles) | HNO ₃ (moles $\times 10^{-3}$) | PVP (moles $\times 10^{-6}$) | |
|-------------------------------|----------------------------|-------|--------------------------------|-------------------------------|-------------------------------|--------------------------|--|-------------------------------|-----|
| 1,000 | 2 | 77S | 85 | 17 | 8.4 | 0.3 | 0.1 | 0.2 | |
| | | 86S | 85 | 5.6 | 7.5 | 0.3 | 0.1 | 0.1 | |
| | | 100S | 85 | 0.0 | 0.0 | 0.3 | 0.1 | 0.1 | |
| | 6 | 77S | 85 | 17 | 8.4 | 0.3 | 0.1 | 0.6 | |
| | | 86S | 85 | 5.6 | 7.5 | 0.3 | 0.1 | 0.5 | |
| | | 100S | 85 | 0.0 | 0.0 | 0.3 | 0.1 | 0.4 | |
| | | 77S | 85 | 17 | 8.4 | 0.3 | 0.1 | 1.0 | |
| | | 10 | 86S | 85 | 5.6 | 7.5 | 0.3 | 0.1 | 0.8 |
| | | | 100S | 85 | 0.0 | 0.0 | 0.3 | 0.1 | 0.7 |
| 40 | 2 | 77S | 85 | 17 | 8.4 | 0.3 | 0.1 | 4.5 | |
| | | 86S | 85 | 5.6 | 7.5 | 0.3 | 0.1 | 3.6 | |
| | | 100S | 85 | 0.0 | 0.0 | 0.3 | 0.1 | 3.1 | |
| | 6 | 77S | 85 | 17 | 8.4 | 0.3 | 0.1 | 14 | |
| | | 86S | 85 | 5.6 | 7.5 | 0.3 | 0.1 | 11 | |
| | | 100S | 85 | 0.0 | 0.0 | 0.3 | 0.1 | 9.7 | |
| | | 77S | 85 | 17 | 8.4 | 0.3 | 0.1 | 25 | |
| | | 10 | 86S | 85 | 5.6 | 7.5 | 0.3 | 0.1 | 20 |
| | | | 100S | 85 | 0.0 | 0.0 | 0.3 | 0.1 | 17 |
| 10 | 2 | 77S | 85 | 17 | 8.4 | 0.3 | 0.1 | 18 | |
| | | 86S | 85 | 5.6 | 7.5 | 0.3 | 0.1 | 14 | |
| | | 100S | 85 | 0.0 | 0.0 | 0.3 | 0.1 | 12 | |
| | 6 | 77S | 85 | 17 | 8.4 | 0.3 | 0.1 | 57 | |
| | | 86S | 85 | 5.6 | 7.5 | 0.3 | 0.1 | 45 | |
| | | 100S | 85 | 0.0 | 0.0 | 0.3 | 0.1 | 39 | |
| | | 77S | 85 | 17 | 8.4 | 0.3 | 0.1 | 98 | |
| | | 10 | 86S | 85 | 5.6 | 7.5 | 0.3 | 0.1 | 78 |
| | | | 100S | 85 | 0.0 | 0.0 | 0.3 | 0.1 | 68 |

Table B-2. Relative moles of reagents (to TEOS) used in synthesizing acid-catalyzed microspheres for size/morphology study in chapter 4.

| PVP molecular weight (kg/mol) | PVP in aqueous phase (wt%) | Glass | TEOS | CNT | TEP | H ₂ O | HNO ₃ (x 10 ⁻³) | PVP |
|-------------------------------|----------------------------|-------|------|------|------|------------------|--|------------------------|
| 1,000 | 2 | 77S | 1 | 0.20 | 0.10 | 4 | 1.44 | 2.1 x 10 ⁻⁶ |
| | | 86S | 1 | 0.07 | 0.09 | 4 | 1.44 | 1.7 x 10 ⁻⁶ |
| | | 100S | 1 | 0.00 | 0.00 | 4 | 1.44 | 1.5 x 10 ⁻⁶ |
| | 6 | 77S | 1 | 0.20 | 0.10 | 4 | 1.44 | 6.7 x 10 ⁻⁶ |
| | | 86S | 1 | 0.07 | 0.09 | 4 | 1.44 | 5.3 x 10 ⁻⁶ |
| | | 100S | 1 | 0.00 | 0.00 | 4 | 1.44 | 4.6 x 10 ⁻⁶ |
| | 10 | 77S | 1 | 0.20 | 0.10 | 4 | 1.44 | 1.2 x 10 ⁻⁵ |
| | | 86S | 1 | 0.07 | 0.09 | 4 | 1.44 | 9.2 x 10 ⁻⁶ |
| | | 100S | 1 | 0.00 | 0.00 | 4 | 1.44 | 8.0 x 10 ⁻⁶ |
| 40 | 2 | 77S | 1 | 0.37 | 0.11 | 4 | 1.44 | 6.8 x 10 ⁻⁵ |
| | | 86S | 1 | 0.20 | 0.10 | 4 | 1.44 | 5.4 x 10 ⁻⁵ |
| | | 100S | 1 | 0.07 | 0.09 | 4 | 1.44 | 4.2 x 10 ⁻⁵ |
| | 6 | 77S | 1 | 0.00 | 0.00 | 4 | 1.44 | 3.7 x 10 ⁻⁵ |
| | | 86S | 1 | 0.37 | 0.11 | 4 | 1.44 | 2.1 x 10 ⁻⁴ |
| | | 100S | 1 | 0.20 | 0.10 | 4 | 1.44 | 1.7 x 10 ⁻⁴ |
| | 10 | 77S | 1 | 0.07 | 0.09 | 4 | 1.44 | 1.3 x 10 ⁻⁴ |
| | | 86S | 1 | 0.00 | 0.00 | 4 | 1.44 | 1.2 x 10 ⁻⁴ |
| | | 100S | 1 | 0.37 | 0.11 | 4 | 1.44 | 3.7 x 10 ⁻⁴ |
| 10 | 2 | 77S | 1 | 0.20 | 0.10 | 4 | 1.44 | 2.9 x 10 ⁻⁴ |
| | | 86S | 1 | 0.07 | 0.09 | 4 | 1.44 | 2.3 x 10 ⁻⁴ |
| | | 100S | 1 | 0.00 | 0.00 | 4 | 1.44 | 2.0 x 10 ⁻⁴ |
| | 6 | 77S | 1 | 0.37 | 0.11 | 4 | 1.44 | 2.7 x 10 ⁻⁴ |
| | | 86S | 1 | 0.20 | 0.10 | 4 | 1.44 | 2.1 x 10 ⁻⁴ |
| | | 100S | 1 | 0.07 | 0.09 | 4 | 1.44 | 1.7 x 10 ⁻⁴ |
| | 10 | 77S | 1 | 0.00 | 0.00 | 4 | 1.44 | 1.5 x 10 ⁻⁴ |
| | | 86S | 1 | 0.37 | 0.11 | 4 | 1.44 | 8.5 x 10 ⁻⁴ |
| | | 100S | 1 | 0.20 | 0.10 | 4 | 1.44 | 6.7 x 10 ⁻⁴ |

APPENDIX C
 VISCOSITIES AND WEBER NUMBERS OF ACID-CATALYZED EMULSIONS

The Weber number (We) for each microsphere composition was calculated as:

$$We = \frac{\text{viscous forces}}{\text{interfacial forces}} = \frac{d\dot{\epsilon}\eta_c}{2\gamma_{int}}$$

in which d is the median, volume-weighted particle diameter measured by light scattering (Table C-1), $\dot{\epsilon}$ is the shear rate (83 s^{-1}), η_c is the viscosity of the continuous phase (557 cP), and γ_{int} is the interfacial tension (4 mN/m as measured by Xu, et al.¹³³).

Table C-1. Viscosity, diameter, and Weber number of acid-catalyzed emulsions.

| PVP molecular weight (kg/mol) | PVP in aqueous phase (wt%) | Glass composition | Viscosity, η_d (cP) | Particle diameter, d (μm) | Weber number, $We \times 10^{-2}$ |
|-------------------------------|----------------------------|-------------------|--------------------------|--|-----------------------------------|
| 1,000 | 2 | 77S | 9.10 | 30.9 | 18 |
| | | 86S | 6.11 | 12.6 | 7.3 |
| | | 100S | 4.68 | 12.5 | 7.3 |
| | 6 | 77S | 67.85 | 23.2 | 13 |
| | | 86S | 43.5 | 12.1 | 7.0 |
| | | 100S | 27.6 | 7.94 | 4.6 |
| | 10 | 77S | 432 | 30.2 | 18 |
| | | 86S | 178 | 8.67 | 5.0 |
| | | 100S | 93.8 | 6.39 | 3.7 |
| 40 | 2 | 77S | 4.02 | 15.0 | 8.7 |
| | | 86S | 1.99 | 19.0 | 11 |
| | | 100S | 1.5 | 9.57 | 5.6 |
| | 6 | 77S | 10.9 | 18.9 | 11 |
| | | 86S | 4.52 | 11.2 | 6.5 |
| | | 100S | 3.54 | 16.8 | 9.7 |
| | 10 | 77S | 28.2 | 15.2 | 8.8 |
| | | 86S | 9.72 | 9.72 | 5.6 |
| | | 100S | 6.81 | 16.4 | 9.5 |
| 10 | 2 | 77S | 3.17 | 11.1 | 6.5 |
| | | 86S | 1.47 | 16.2 | 9.4 |
| | | 100S | 1.12 | 23.4 | 14 |
| | 6 | 77S | 5.62 | 13.2 | 7.6 |
| | | 86S | 2.38 | 12.0 | 7.0 |
| | | 100S | 1.67 | 30.2 | 18 |
| | 10 | 77S | 10.3 | 11.2 | 6.5 |
| | | 86S | 3.85 | 7.81 | 4.5 |
| | | 100S | 2.45 | 16.8 | 9.8 |

APPENDIX D
IMAGES OF EXTERNAL AND INTERNAL MORPHOLOGY OF BIOACTIVE GLASS
MICROSPHERES

Bioactive glass microspheres were created by an acid catalyzed process over a wide range of compositions. These microspheres were imaged externally and in cross-section by SEM. This appendix is a complete listing of these images. Each composition is accompanied by a ternary phase diagram for reference (Figure D-1).

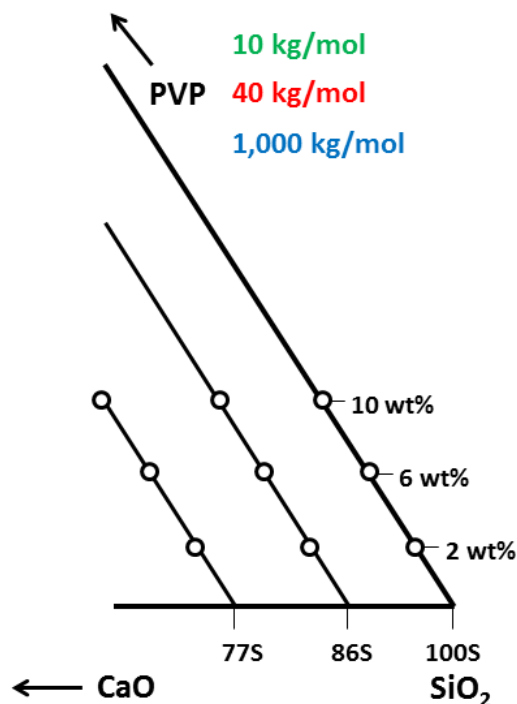


Figure D-1. Example of ternary phase diagram that is used as a guide throughout this appendix. Molecular weight of PVP is indicated by the color of the diagram: green= 10 kg/mol, red = 40 kg/mol, and blue = 1,000 kg/mol.

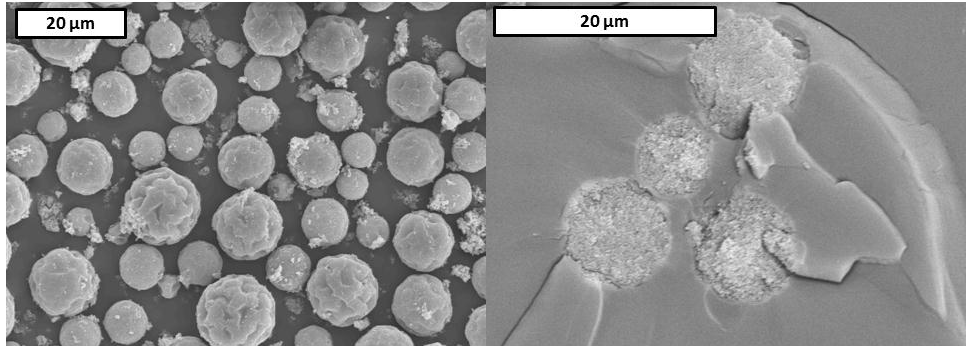
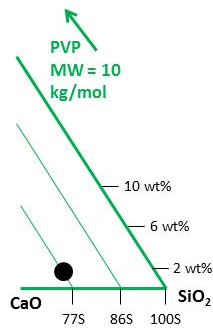


Figure D-2. 10 kg/mol, 77S, 2 wt% bioactive glass microspheres external morphology (left, secondary electron image) and in cross-section (right, backscattered electron image).

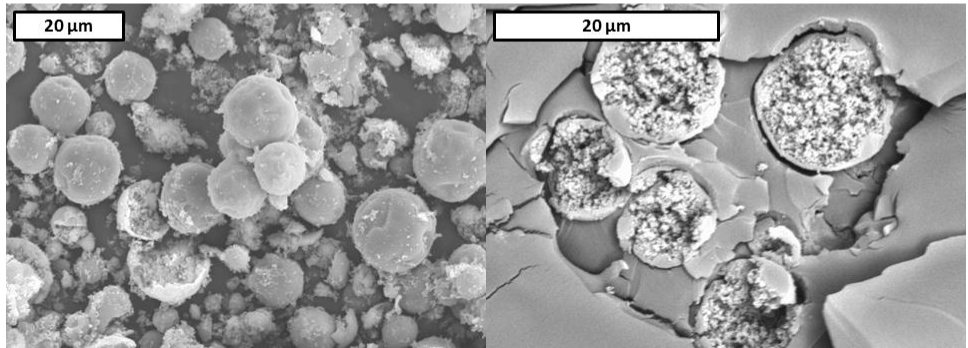
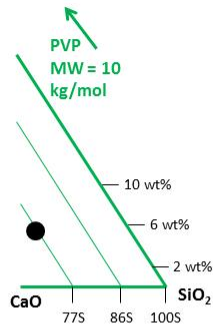


Figure D-3. 10 kg/mol, 77S, 6 wt% bioactive glass microspheres external morphology (left, secondary electron image) and in cross-section (right, backscattered electron image).

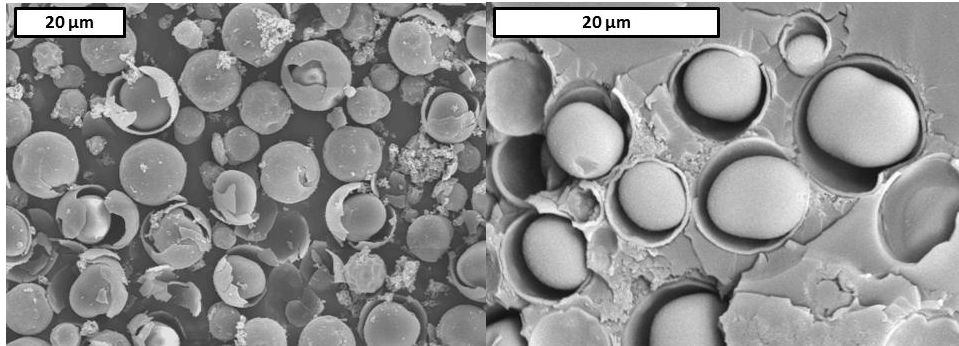
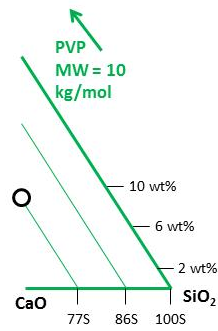


Figure D-4. 10 kg/mol, 77S, 10 wt% bioactive glass microspheres external morphology (left, secondary electron image) and in cross-section (right, backscattered electron image).

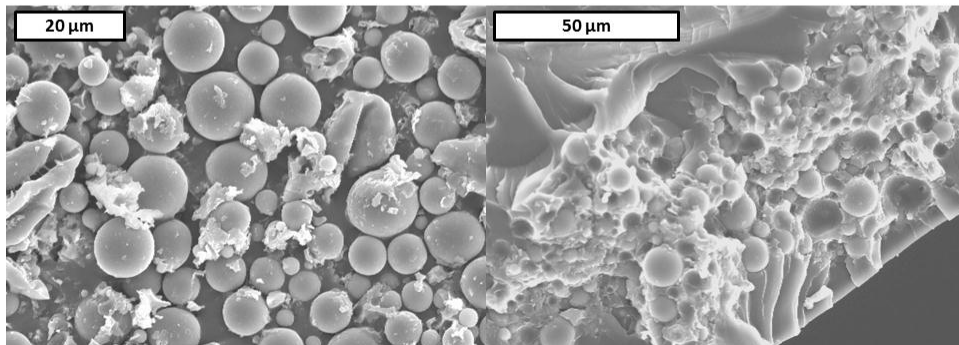
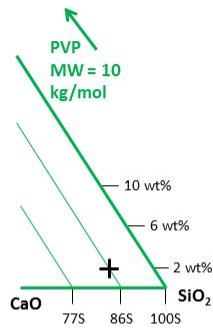


Figure D-5. 10 kg/mol, 86S, 2 wt% bioactive glass microspheres external morphology (left, secondary electron image) and in cross-section (right, secondary electron image).

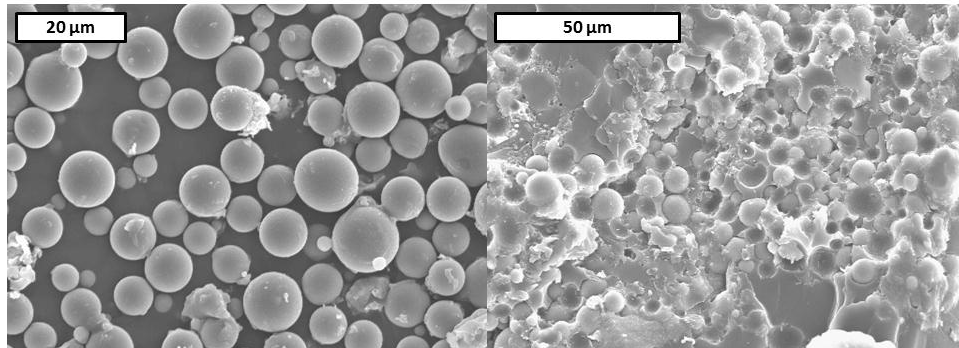
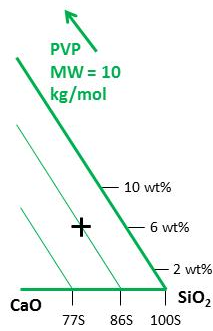


Figure D-6. 10 kg/mol, 86S, 6 wt% bioactive glass microspheres external morphology (left, secondary electron image) and in cross-section (right, secondary electron image).

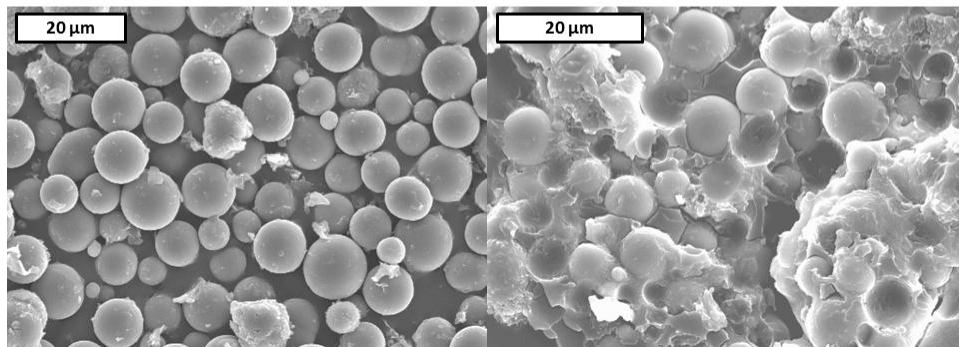
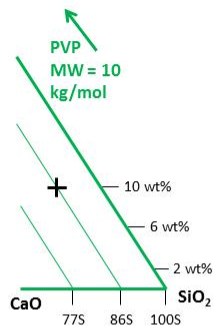


Figure D-7. 10 kg/mol, 86S, 10 wt% bioactive glass microspheres external morphology (left, secondary electron image) and in cross-section (right, secondary electron image).

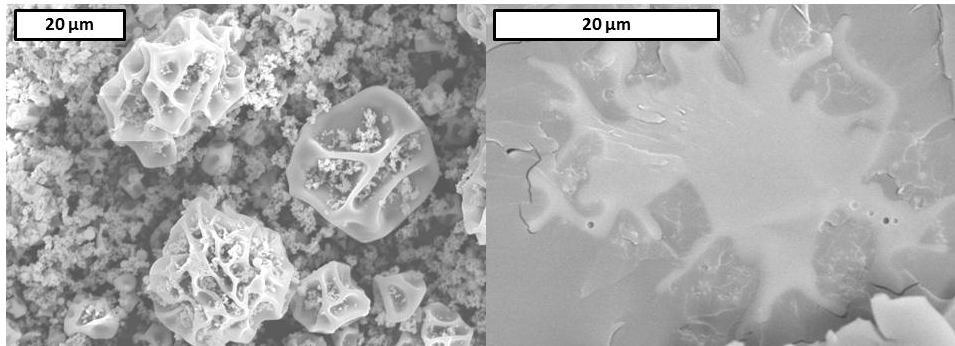
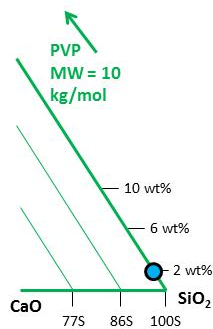


Figure D-8. 10 kg/mol, 100S, 2 wt% bioactive glass microspheres external morphology (left, secondary electron image) and in cross-section (right, backscattered electron image).

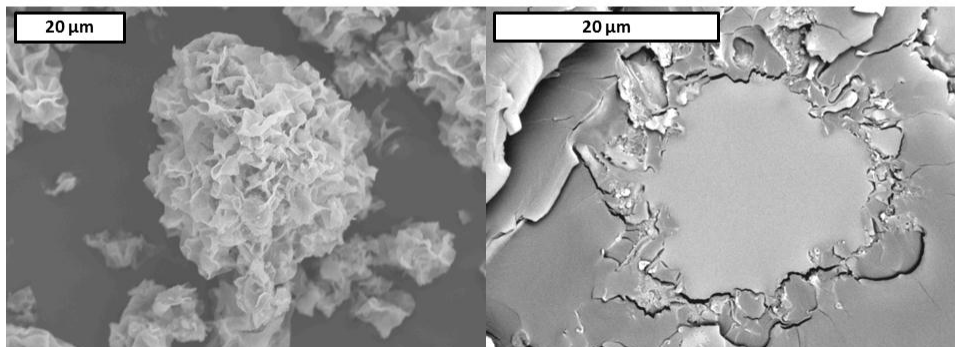
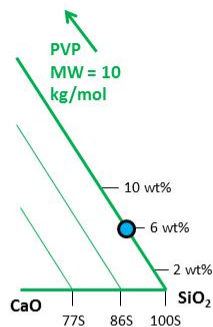


Figure D-9. 10 kg/mol, 100S, 6 wt% bioactive glass microspheres external morphology (left, secondary electron image) and in cross-section (right, backscattered electron image).

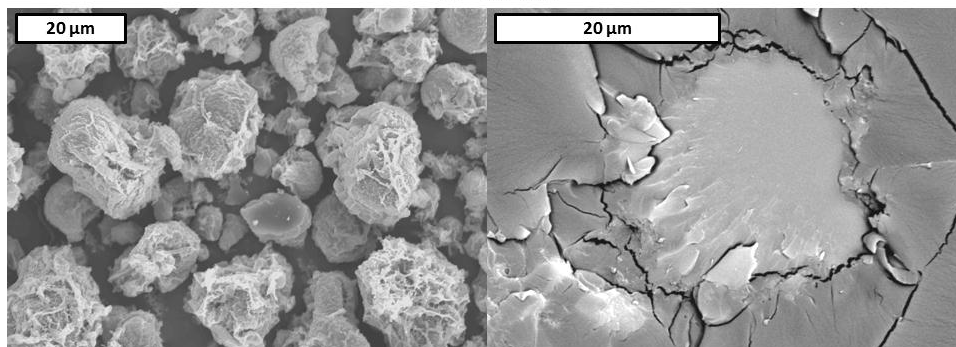
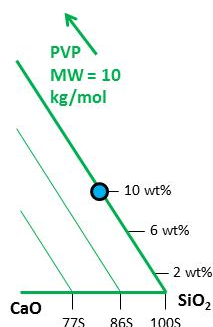


Figure D-10. 10 kg/mol, 100S, 10 wt% bioactive glass microspheres external morphology (left, secondary electron image) and in cross-section (right, backscattered electron image).

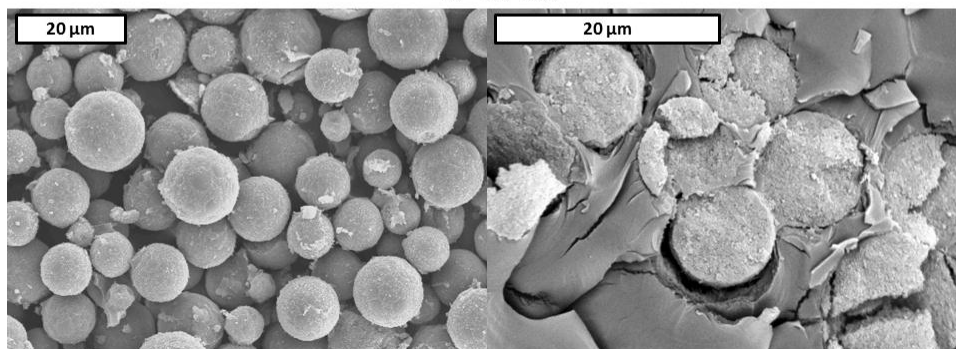
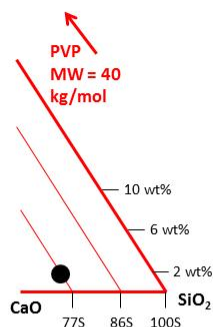


Figure D-11. 40 kg/mol, 77S, 2 wt% bioactive glass microspheres external morphology (left, secondary electron image) and in cross-section (right, backscattered electron image).

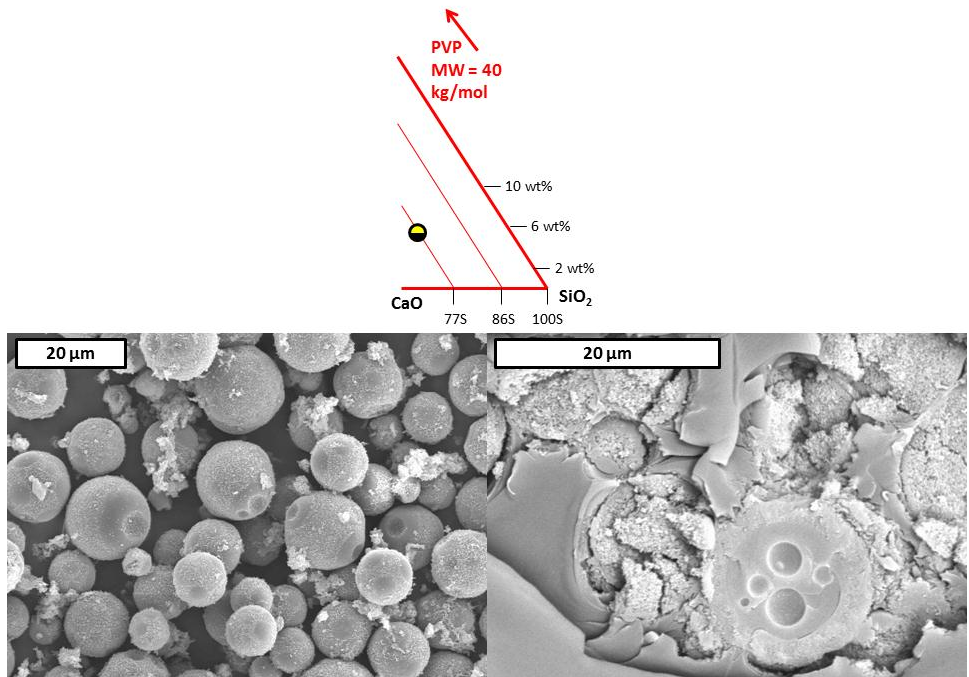


Figure D-12. 40 kg/mol, 77S, 6 wt% bioactive glass microspheres external morphology (left, secondary electron image) and in cross-section (right, backscattered electron image).

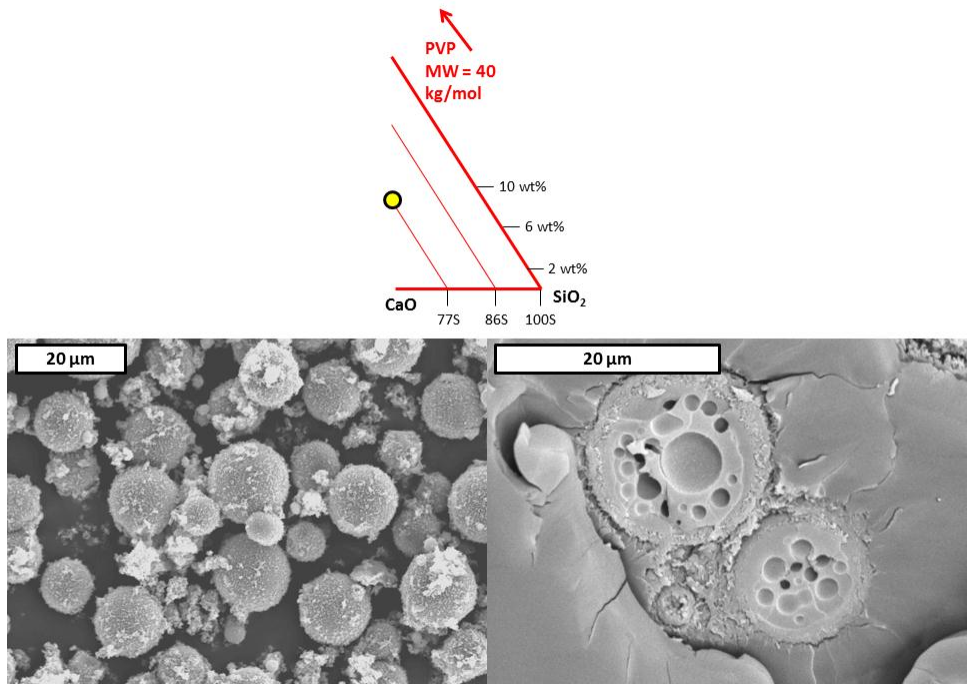


Figure D-13. 40 kg/mol, 77S, 10 wt% bioactive glass microspheres external morphology (left, secondary electron image) and in cross-section (right, backscattered electron image).

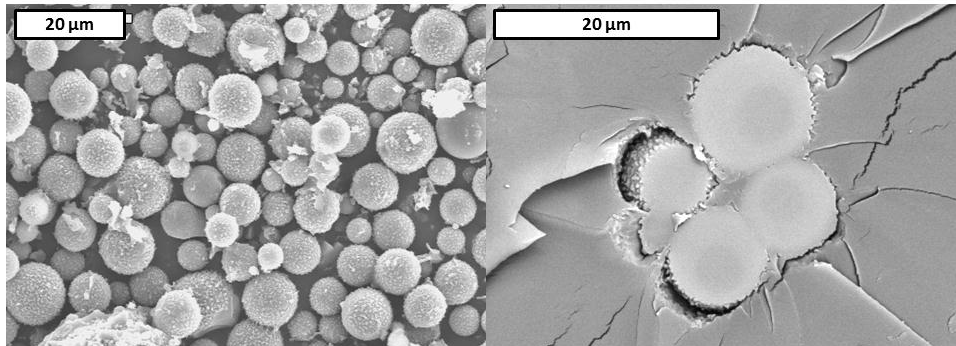
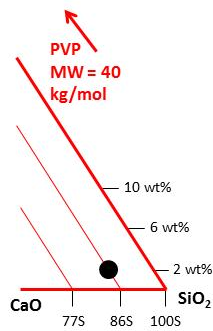


Figure D-14. 40 kg/mol, 86S, 2 wt% bioactive glass microspheres external morphology (left, secondary electron image) and in cross-section (right, backscattered electron image).

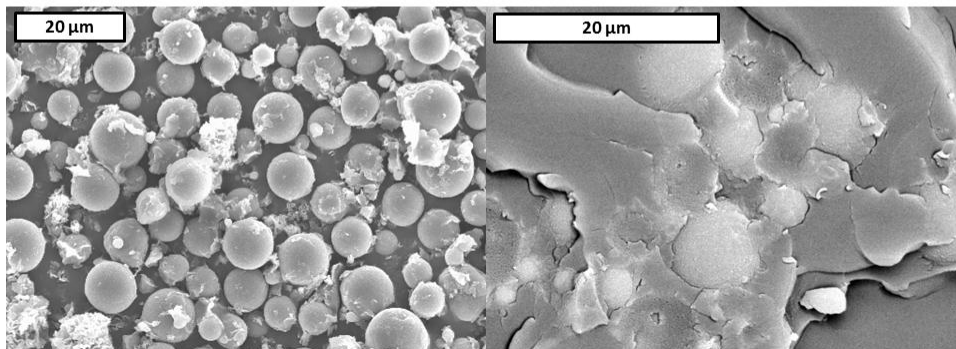
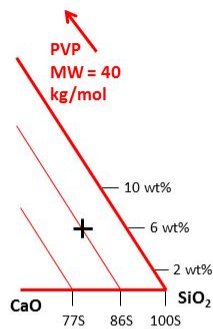


Figure D-15. 40 kg/mol, 86S, 6 wt% bioactive glass microspheres external morphology (left, secondary electron image) and in cross-section (right, backscattered electron image).

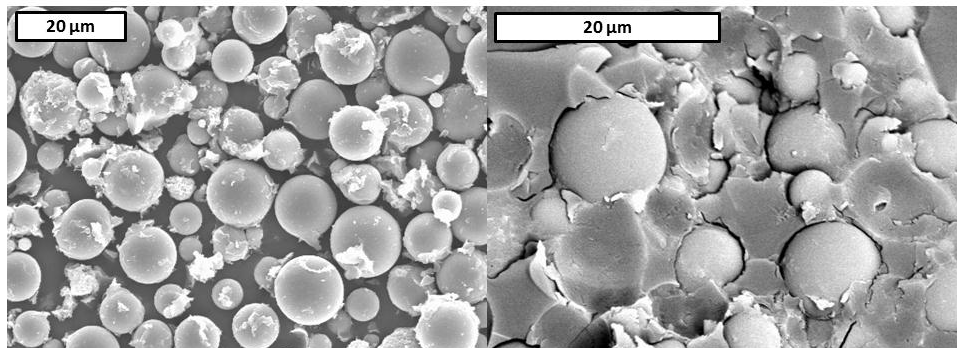
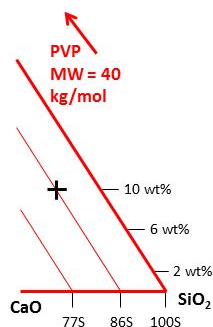


Figure D-16. 40 kg/mol, 86S, 10 wt% bioactive glass microspheres external morphology (left, secondary electron image) and in cross-section (right, backscattered electron image).

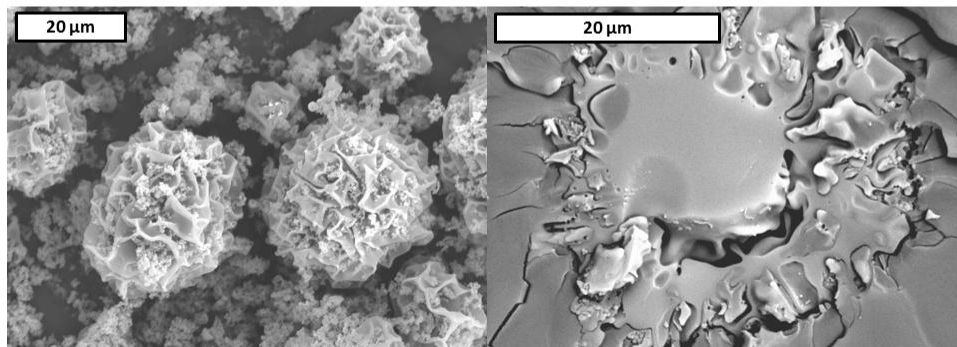
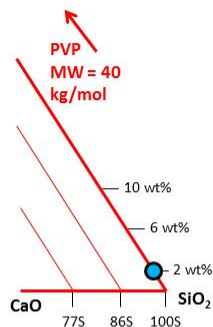


Figure D-17. 40 kg/mol, 100S, 2 wt% bioactive glass microspheres external morphology (left, secondary electron image) and in cross-section (right, backscattered electron image).

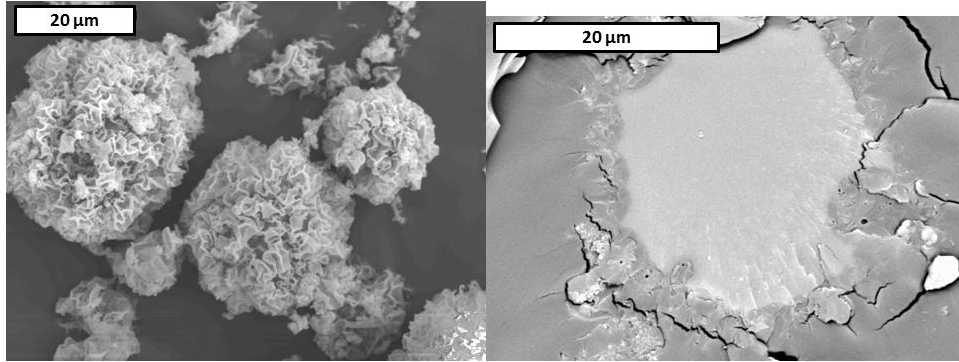
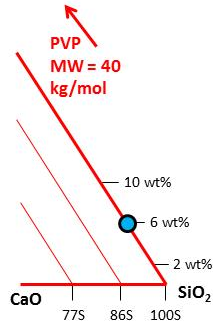


Figure D-18. 40 kg/mol, 100S, 6 wt% bioactive glass microspheres external morphology (left, secondary electron image) and in cross-section (right, backscattered electron image).

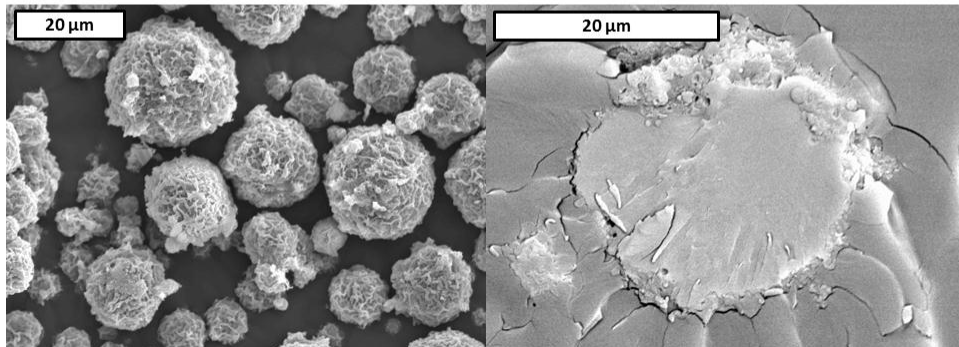
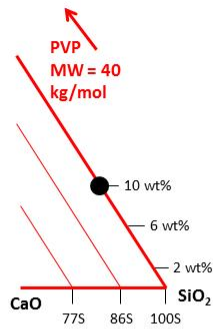


Figure D-19. 40 kg/mol, 100S, 10 wt% bioactive glass microspheres external morphology (left, secondary electron image) and in cross-section (right, backscattered electron image).

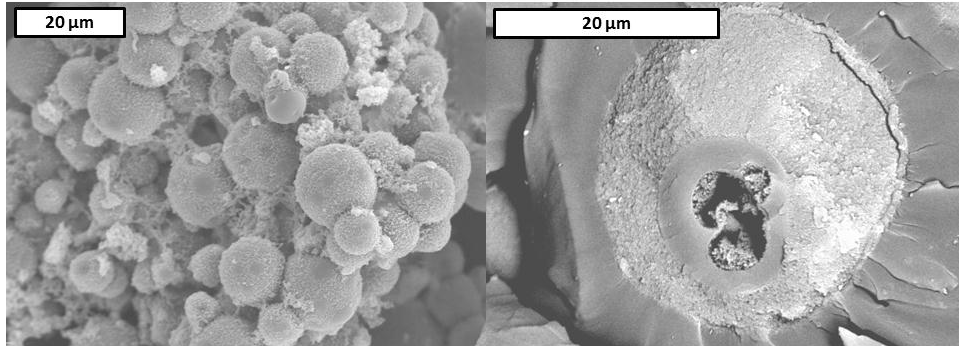
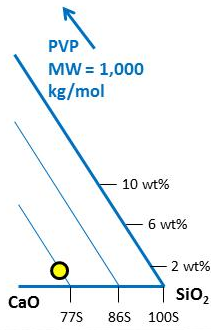


Figure D-20. 1,000 kg/mol, 77S, 2 wt% bioactive glass microspheres external morphology (left, secondary electron image) and in cross-section (right, backscattered electron image).

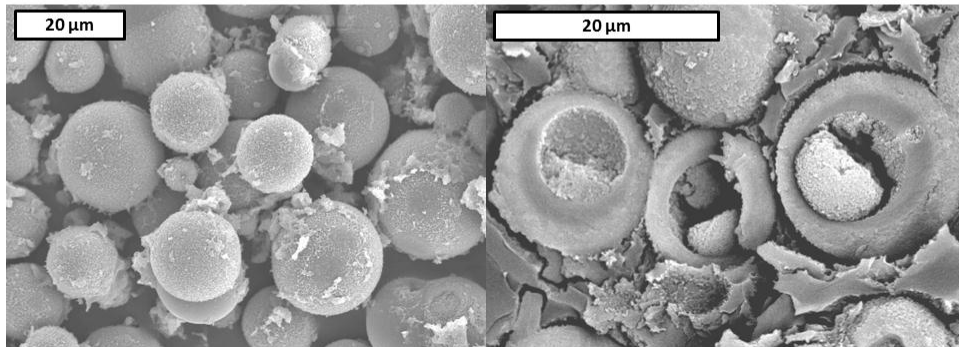
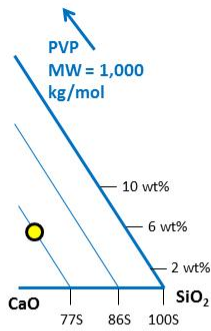


Figure D-21. 1,000 kg/mol, 77S, 6 wt% bioactive glass microspheres external morphology (left, secondary electron image) and in cross-section (right, backscattered electron image).

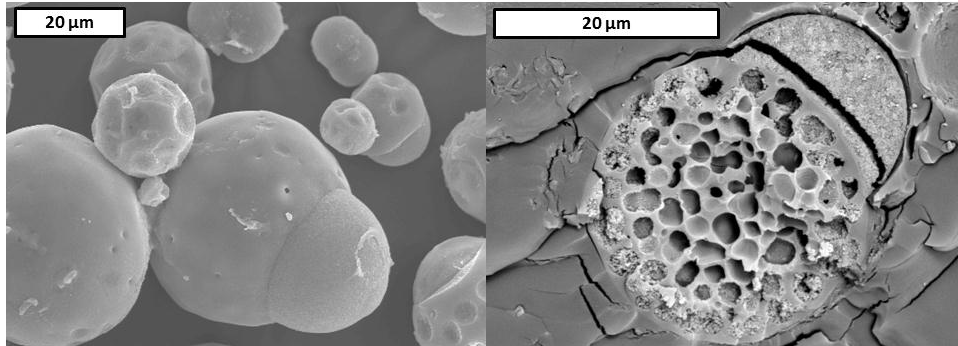
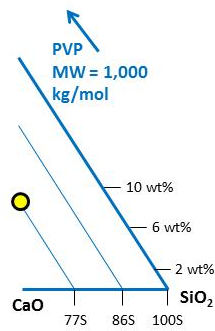


Figure D-22. 1,000 kg/mol, 77S, 10 wt% bioactive glass microspheres external morphology (left, secondary electron image) and in cross-section (right, backscattered electron image).

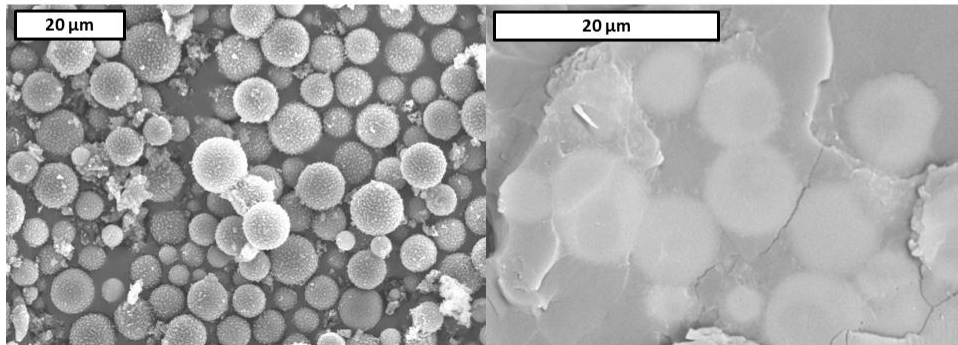
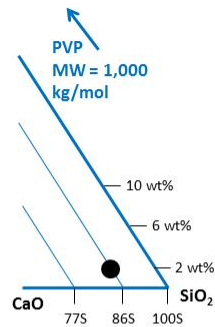


Figure D-23. 1,000 kg/mol, 86S, 2 wt% bioactive glass microspheres external morphology (left, secondary electron image) and in cross-section (right, backscattered electron image).

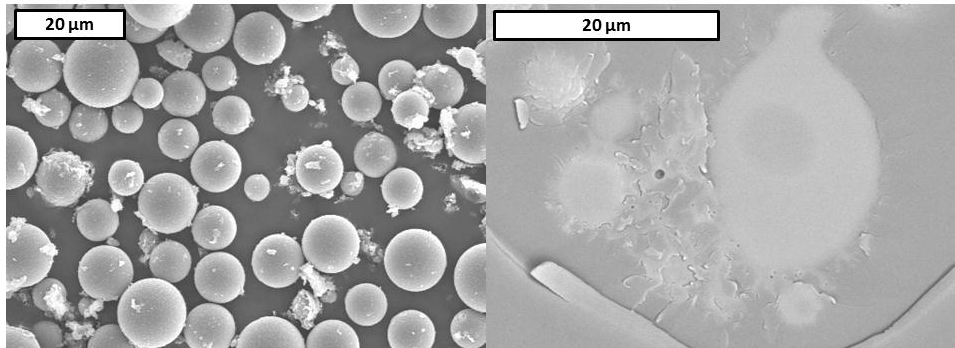
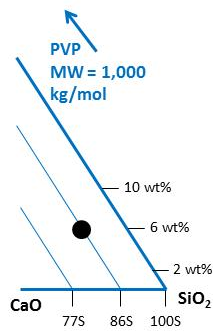


Figure D-24. 1,000 kg/mol, 86S, 6 wt% bioactive glass microspheres external morphology (left, secondary electron image) and in cross-section (right, backscattered electron image).

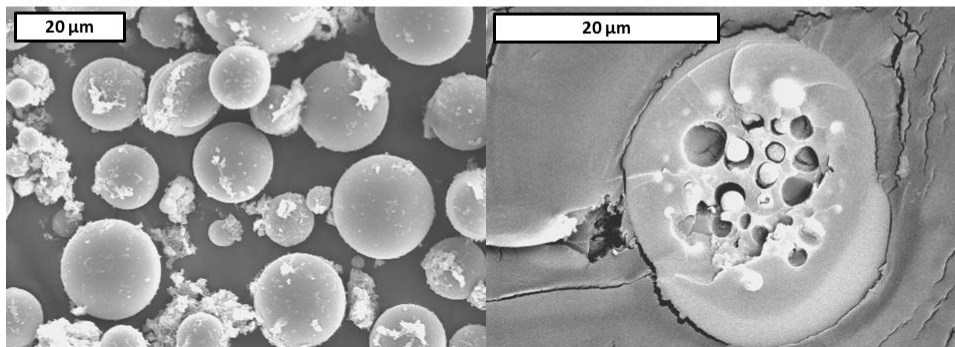
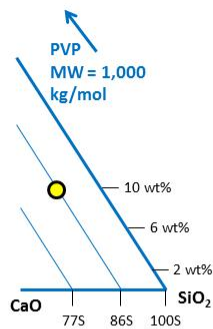


Figure D-25. 1,000 kg/mol, 86S, 10 wt% bioactive glass microspheres external morphology (left, secondary electron image) and in cross-section (right, backscattered electron image).

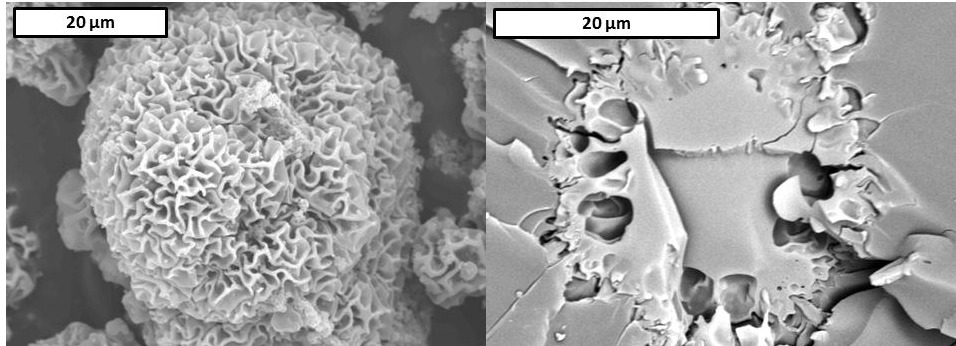
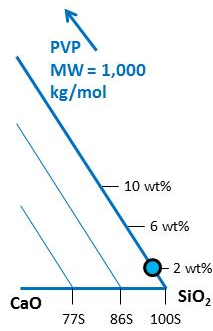


Figure D-26. 1,000 kg/mol, 100S, 2 wt% bioactive glass microspheres external morphology (left, secondary electron image) and in cross-section (right, backscattered electron image).

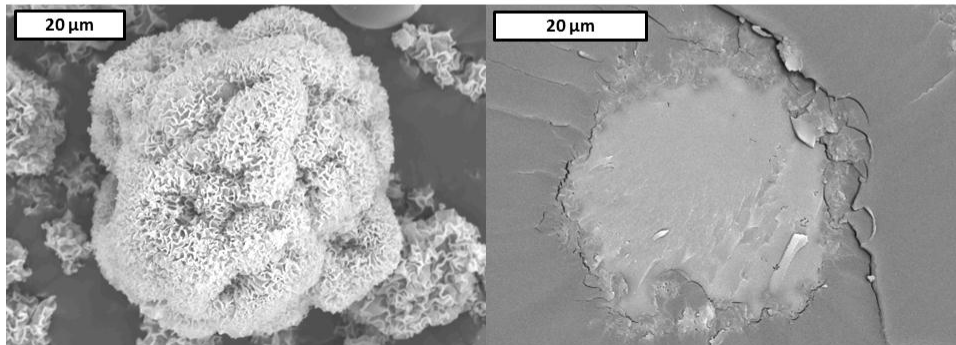
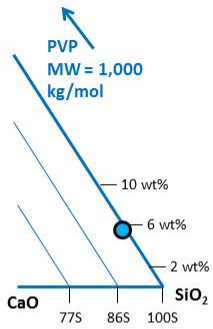


Figure D-27. 1,000 kg/mol, 100S, 6 wt% bioactive glass microspheres external morphology (left, secondary electron image) and in cross-section (right, backscattered electron image).

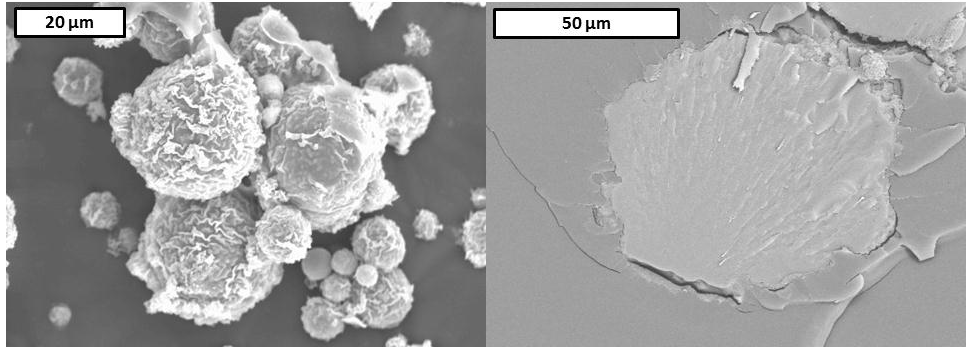
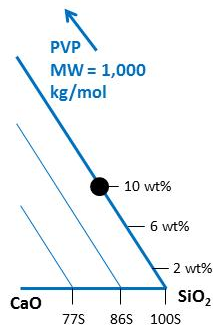


Figure D-28. 1,000 kg/mol, 100S, 10 wt% bioactive glass microspheres external morphology (left, secondary electron image) and in cross-section (right, backscattered electron image).

APPENDIX E
PROCESS FOR CREATING NANOCOMPOSITE HYDROGELS

Silica nanoparticles were created using a process similar to that described by Stöber, Fink, and Bohn.¹⁹⁴ First, 775 ml of 200 proof ethanol and 62 ml of a 0.8 M aqueous ammonia solution were added to a 1000 ml round bottom flask. A second solution was prepared that contained 132 ml of 200 proof ethanol and 31 ml of TEOS. Both solutions were heated in separate water baths at 60 °C for at least 1 hr. The solution containing TEOS was then added to the round bottom flask and the mixture was stirred at 60 °C for 24 hrs.

After stirring for 24 hrs, the silane coupling agents 3-methacryloxypropyltriethoxysilane (MAP) and/or nonahexylfluorotriethoxysilane (NHF) were added to the solution to at the concentrations indicated in Table D-1. The nanoparticle solutions were stirred for another 24 hrs at 60 °C. The solutions were then boiled at 80 °C to increase the concentration 10 fold. The solutions were then cooled and stored at approximately 4 °C.

Table E-1. Concentrations of reagents (M) used in making multi-functional silica nanoparticles.

| Particle designation | H ₂ O | TEOS | NH ₃ | MAP (x 10 ⁻³) | NHF (x 10 ⁻³) |
|--------------------------|------------------|------|-----------------|---------------------------|---------------------------|
| SiO ₂ | 3.47 | 0.14 | 0.05 | 0.0 | 0.0 |
| MAP-SiO ₂ | 3.47 | 0.14 | 0.05 | 6.5 | 0.0 |
| MAP/NHF-SiO ₂ | 3.47 | 0.14 | 0.05 | 3.2 | 3.2 |

The nanoparticle solutions were diluted with 190 proof ethanol. PEGMA was added by to achieve a concentration of 0.41 M, or 25 wt% of the prepolymerization mixture. Irgacure 29959 was then added by mass to a concentration of 0.01 M. The solution was stirred with a magnetic stir bar until visibly homogenous. The

prepolymerization mixture was then placed in a glass test tube and degassed in a sonicator for 5 mins. The mold assembly (Figure E-1) was cleaned with 190 proof ethanol between uses and purged nitrogen gas for 5 mins immediately before adding the prepolymerization mixture. The samples were set inside a box 3 inches below a Blak-Ray UVL-56 lamp (366 nm) and exposed to UV light for 2 hrs. A slight nitrogen purge was kept flowing during the polymerization.

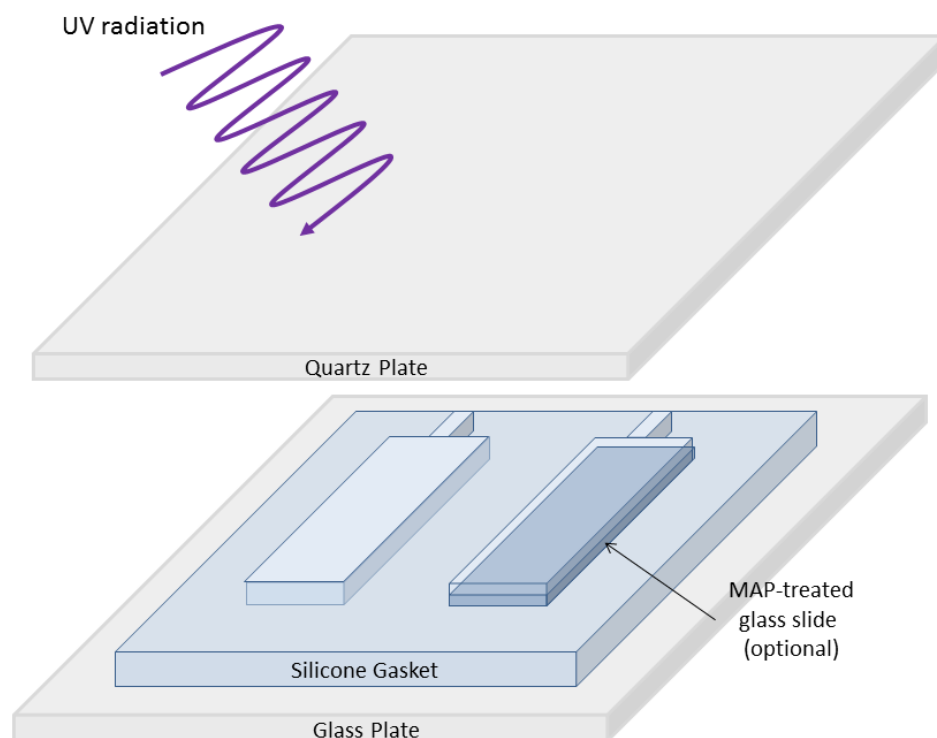


Figure E-1. Mold assembly for polymerizing nanocomposite hydrogels.

After polymerization, the samples were removed from the mold and swollen in approximately 25 ml of deionized water. The water was exchanged three times over a 24-hr period before any further analysis was done. The gels were cut into 6 mm discs and dried under vacuum to perform swelling experiments. Gels were frozen in liquid nitrogen and freeze dried prior to SEM/EDS analysis.

LIST OF REFERENCES

1. Riding R. Microbial carbonates: the geological record of calcified bacterial–algal mats and biofilms. *Sedimentology* 2000;47:179-214.
2. Nicolaus B, Kambourova M, Oner ET. Exopolysaccharides from extremophiles: from fundamentals to biotechnology. *Environ Technol* 2010;31(10):1145-1158.
3. Magin CM, Cooper SP, Brennan AB. Non-toxic antifouling strategies. *Mater Today* 2010;13(4):36-44.
4. Schultz MP. Effects of coating roughness and biofouling on ship resistance and powering. *Biofouling* 2007;23(5):331-341.
5. Schultz MP, Bendick JA, Holm ER, Hertel WM. Economic impact of biofouling on a naval surface ship. *Biofouling* 2011;27(1):87-98.
6. Hewitt CL, Gollasch S, Minchin D. Chapter 6: The vessel as a vector - biofouling, ballast water, and sediments. In: Rilov G, Crooks JA, editors. *Biological Invasions in Marine Ecosystems*. Berlin: Springer-Verlag; 2009. p 117-131.
7. Hench LL. Bioceramics - from concept to clinic. *J Am Ceram Soc* 1991;74(7):1487-1510.
8. Epstein AK, Pokroy B, Seminara A, Aizenberg J. Bacterial biofilm shows persistent resistance to liquid wetting and gas penetration. *Proc Natl Acad Sci U S A* 2011;108(3):995-1000.
9. Costerton JW, Cheng KJ, Geesey GG, Ladd TI, Nickel JC, Dasgupta M, Marrie TJ. Bacterial Biofilms in Nature and Disease. *Ann Rev Microbiol* 1987;41(1):435-464.
10. Costerton JW, Stewart PS, Greenberg EP. Bacterial biofilms: a common cause of persistent infections. *Science* 1999;284(5418):1318-1322.
11. Lamont RJ, Burne RA, Lantz MS, LeBlanc DJ, editors. *Oral Microbiology and Immunology*. Washington, DC: American Society for Microbiology; 2006.
12. National Health and Nutrition Examination Survey, Dental Caries (Tooth Decay) in Adults (Age 20 to 64). Bethesda, MD: National Institute of Dental and Craniofacial Research, National Institute of Health; 1999-2004.
13. Beazoglou T, Eklund S, Heffley D, Meiers J, Brown LJ, Bailit H. Economic impact of regulating the use of amalgam restorations. *Public Health Rep* 2007;122(5):657-63.

14. Garret-Price B. Fouling of heat exchangers: characteristics, cost, prevention, control and removal. Park Ridge, NJ: Noyes Publications; 1985. 417 p.
15. Plutarch. Book II, Question 7. In: Goodwin WW, editor. Plutarch's Miscellanies and Essays. 6th edition ed. Volume 3. Boston: Little, Brown, and Company.
16. Marine Fouling and its Prevention. Woods Hole Oceanographic Institution. Menasha, WI: George Banta Publishing Co.; 1952.
17. US Navy. Status of the Navy. Volume 2011:
http://www.navy.mil/navydata/navy_legacy_hr.asp?id=146; 2011.
18. International Chamber of Shipping. Shipping and World Trade. Volume 2011:
<http://www.marisec.org/shippingfacts/worldtrade/number-of-ships.php>; 2010.
19. Drake JM, Lodge DM. Hull fouling is a risk factor for intercontinental species exchange in aquatic ecosystems. *Aquatic Invasions* 2007;2(2):121-131.
20. Minchin D, Floerl O, Savini D, Occhipinti-Ambrogi A. Small craft and the spread of exotic species. In: Davenport J, Davenport JL, editors. *The Ecology of Transportation: Managing Mobility for the Environment*: Springer Netherlands; 2006. p 99-118.
21. Colautti R, Bailey S, Overdijk C, Amundsen K, MacIsaac H. Characterised and projected costs of nonindigenous species in Canada. *Biol Invasions* 2006;8(1):45-59.
22. Callow ME. Chapter 1: A world-wide survey of slime formation on anti-fouling paints. In: Evans LV, Hoagland KD, editors. *Algal Biofouling*. Amsterdam: Elsevier; 1986. p 1-20.
23. Heydt M, Divós P, Grunze M, Rosenhahn A. Analysis of holographic microscopy data to quantitatively investigate three-dimensional settlement dynamics of algal zoospores in the vicinity of surfaces. *Eur Phys J E* 2009;30(2):141-148.
24. Callow ME, Callow JA, Pickett-Heaps JD, Wetherbee R. Primary adhesion of *Enteromorpha* (Chlorophyta, Ulvales) propagules: quantitative settlement studies and video microscopy. *J Phycol* 1997;33(6):938-947.
25. Callow ME, Jennings AR, Brennan AB, Seegert CE, Gibson A, Wilson L, Feinberg A, Baney R, Callow JA. Microtopographic cues for settlement of zoospores of the green fouling alga *Enteromorpha*. *Biofouling* 2002;18(3):237-245.
26. Biofilms: The Hypertextbook. In: Cunningham AB, Lennox JE, Ross RJ, editors: Montana State University; 2011.

27. Brock TD. Robert Koch: A Life in Medicine and Bacteriology. Washington, DC: ASM Press; 1988.
28. Henrici AT. Studies of freshwater bacteria: I. a direct microscopic technique. *J. Bacteriol.* 1933;25(3):277-287.
29. Zobell CE. The effect of solid surfaces upon bacterial activity. *J Bacteriol* 1943;46(1):39-56.
30. Hall-Stoodley L, Costerton JW, Stoodley P. Bacterial biofilms: from the natural environment to infectious diseases. *Nat Rev Micro* 2004;2(2):95-108.
31. Spratt DA, Ready D, Pratten J. Chapter 11: Biofilms in medicine. In: Dürr S, Thomason JC, editors. *Biofouling*. Chichester, United Kingdom: Wiley-Blackwell; 2010. p 154-164.
32. Potera C. Forging a link between biofilms and disease. *Science* 1999;283(5409):1837-1839.
33. Klevens RM, Edwards JR, Richards CL, Jr., Horan TC, Gaynes RP, Pollock DA, Cardo DM. Estimating health care-associated infections and deaths in U.S. hospitals, 2002. *Public Health Rep* 2007;122(2):160-6.
34. Weinstein RA. Nosocomial infection update. *Emerg Infect Dis* 1998;4(3):416-20.
35. Edwards R, Harding KG. Bacteria and wound healing. *Curr Opin Infect Dis* 2004;17(2):91-6.
36. Lipsky BA, Weigelt JA, Gupta V, Killian A, Peng MM. Skin, soft tissue, bone, and joint infections in hospitalized patients: epidemiology and microbiological, clinical, and economic outcomes. *Infect Control Hosp Epidemiol* 2007;28(11):1290-8.
37. Waldvogel F. Osteomyelitis. In: Gorbach S, Bartlett J, Blacklow N, editors. *Infectious Diseases*. Philadelphia: W.B. Saunders Company; 1998. p 1339-1343.
38. Simmen H-P, Blaser J. Analysis of pH and pO₂ in abscesses, peritoneal fluid, and drainage fluid in the presence or absence of bacterial infection during and after abdominal surgery. *Am J Surg* 1993;166(1):24-27.
39. Yebra DM, Kiil S, Dam-Johansen K. Antifouling technology--past, present and future steps towards efficient and environmentally friendly antifouling coatings. *Prog Org Coat* 2004;50(2):75-104.
40. Finnie AA, Williams DN. Paint and coatings technology for the control of marine fouling. In: Dürr S, Thomason JC, editors. *Biofouling*. Oxford (UK): Wiley-Blackwell; 2010. p 185-206.

41. Howell D, Behrends B. Consequences of antifouling coatings -- the chemist's perspective. In: Dürr S, Thomason JC, editors. Biofouling. Oxford (UK): Wiley-Blackwell; 2010. p 227-242.
42. Walker EB. Quaternary ammonium compounds. In: Paulson DS, editor. Handbook of Topical Antimicrobials: Industrial Applications in Consumer Products and Pharmaceuticals. New York: Marcel Dekker; 2003. p 99-116.
43. MacGregor DR, Elliker PR. A comparison of some properties of strains of *Pseudomonas aeruginosa* sensitive and resistant to quaternary ammonium compounds. Can J Microbiol 1958;4(5):499-503.
44. Kenawy E-R, Worley SD, Broughton R. The chemistry and applications of antimicrobial polymers: a state-of-the-art review. Biomacromolecules 2007;8(5):1359-1384.
45. Majumdar P, Lee E, Patel N, Ward K, Stafslie SJ, Daniels J, Chisholm BJ, Boudjouk P, Callow ME, Callow JA and others. Combinatorial materials research applied to the development of new surface coatings IX: An investigation of novel antifouling/fouling-release coatings containing quaternary ammonium salt groups. Biofouling 2008;24(3):185-200.
46. Alberts B, Johnson A, Lewis J, Raff M, Roberts K, Walter P. Molecular Biology of the Cell New York: Garland Science; 2002.
47. Arias CA, Murray BE. Antibiotic-resistant bugs in the 21st Century — a clinical super-challenge. N Engl J Med 2009;360(5):439-443.
48. Baier RE. Surface behaviour of biomaterials: the theta surface for biocompatibility. J Mater Sci Mater Med 2006;17(11):1057-62.
49. Zisman W. Relation of the equilibrium contact angle to liquid and solid constitution. Contact Angle, Wettability, and Adhesion. Washington, D.C.: American Chemical Society; 2009. p 1-51.
50. . In: Harris J, Zalipsky S, editors. Poly(ethylene glycol): Chemistry and Biological Applications. Washington, DC: American Chemical Society; 1997.
51. Jeon SI, Lee JH, Andrade JD, De Gennes PG. Protein--surface interactions in the presence of polyethylene oxide: I. simplified theory. J Colloid Interface Sci 1991;142(1):149-158.
52. Szleifer I. Polymers and proteins: interactions at interfaces. Curr Opin Solid State Mater Sci 1997;2(3):337-344.

53. Prime KL, Whitesides GM. Adsorption of proteins onto surfaces containing end-attached oligo(ethylene oxide): a model system using self-assembled monolayers. *J Am Chem Soc* 1993;115(23):10714-10721.
54. Harder P, Grunze M, Dahint R, Whitesides GM, Laibinis PE. Molecular conformation in oligo(ethylene glycol)-terminated self-assembled monolayers on gold and silver surfaces determines their ability to resist protein adsorption. *J Phys Chem B* 1998;102(2):426-436.
55. Callow ME, Callow JA, Ista LK, Coleman SE, Nolasco AC, Lopez GP. Use of self-assembled monolayers of different wettabilities to study surface selection and primary adhesion processes of green algal (*Enteromorpha*) zoospores. *Appl Environ Microb* 2000;66(8):3249-3254.
56. Schilp S, Rosenhahn A, Pettitt ME, Bowen J, Callow ME, Callow JA, Grunze M. Physicochemical properties of (ethylene glycol)-containing self-assembled monolayers relevant for protein and algal cell resistance. *Langmuir* 2009;25(17):10077-10082.
57. Magin CM, Long CJ, Cooper SP, Ista LK, Lopez GP, Brennan AB. Engineered antifouling microtopographies: the role of Reynolds number in a model that predicts attachment of zoospores of *Ulva* and cells of *Cobetia marina*. *Biofouling* 2010;26(6):719-727.
58. Lundberg P, Bruin A, Klijnstra JW, Nyström AM, Johansson M, Malkoch M, Hult A. Poly(ethylene glycol)-based thiol-ene hydrogel coatings—curing chemistry, aqueous stability, and potential marine antifouling applications. *ACS Appl Mater Interfaces* 2010;2(3):903-912.
59. Krishnan S, Weinman CJ, Ober CK. Advances in polymers for anti-biofouling surfaces. *J Mater Chem* 2008;18(29):3405-3413.
60. Krishnan S, Ayothi R, Hexemer A, Finlay JA, Sohn KE, Perry R, Ober CK, Kramer EJ, Callow ME, Callow JA and others. Anti-biofouling properties of comblike block copolymers with amphiphilic side chains. *Langmuir* 2006;22(11):5075-5086.
61. Gan D, Mueller A, Wooley KL. Amphiphilic and hydrophobic surface patterns generated from hyperbranched fluoropolymer/linear polymer networks: minimally adhesive coatings via the crosslinking of hyperbranched fluoropolymers. *J Polym Sci, Part A: Polym Chem* 2003;41(22):3531-3540.

62. Gudipati CS, Finlay JA, Callow JA, Callow ME, Wooley KL. The antifouling and fouling-release performance of hyperbranched fluoropolymer (HBFP)-poly(ethylene glycol) (PEG) composite coatings evaluated by adsorption of biomacromolecules and the green fouling alga *Ulva*. *Langmuir* 2005;21(7):3044-3053.
63. Salta M, Wharton JA, Stoodley P, Dennington SP, Goodes LR, Werwinski S, Mart U, Wood RJ, Stokes KR. Designing biomimetic antifouling surfaces. *Philos Transact A Math Phys Eng Sci* 2010;368(1929):4729-54.
64. Scardino AJ, de Nys R. Mini review: Biomimetic models and bioinspired surfaces for fouling control. *Biofouling* 2011;27(1):73-86.
65. Carman M, Estes T, Feinberg A, Schumacher J, Wilkerson W, Wilson L, Callow M, Callow J, Brennan A. Engineered antifouling microtopographies – correlating wettability with cell attachment. *Biofouling* 2006;22(1):11-21.
66. Schumacher JF, Aldred N, Callow ME, Finlay JA, Callow JA, Clare AG, Brennan AB. Species-specific engineered antifouling topographies: correlations between the settlement of algal zoospores and barnacle cyprids. *Biofouling* 2007;23(5-6):307-317.
67. Chung KK, Schumacher JF, Sampson EM, Burne RA, Antonelli PJ, Brennan AB. Impact of engineered surface microtopography on biofilm formation of *Staphylococcus aureus*. *Biointerphases* 2007;2(2):89-94.
68. Schumacher JF, Carman ML, Estes TG, Feinberg AW, Wilson LH, Callow ME, Callow JA, Finlay JA, Brennan AB. Engineered antifouling microtopographies - effect of feature size, geometry, and roughness on settlement of zoospores of the green alga *Ulva*. *Biofouling* 2007;23(1):55-62.
69. Scardino AJ, Harvey E, De Nys R. Testing attachment point theory: diatom attachment on microtextured polyimide biomimics. *Biofouling* 2006;22(1):55-60.
70. Thula TT, Rodriguez DE, Lee MH, Pendi L, Podschun J, Gower LB. In vitro mineralization of dense collagen substrates: A biomimetic approach toward the development of bone-graft materials. *Acta Biomaterialia* 2011;7(8):3158-3169.
71. Friess W. Collagen - biomaterial for drug delivery. *Eur J Pharm Biopharm* 1998;45(2):113-136.
72. Weiner S, Traub W. Bone structure: from angstroms to microns. *FASEB J* 1992;6(3):879-885.
73. Wen JY, Wilkes GL. Organic/inorganic hybrid network materials by the sol-gel approach. *Chem Mater* 1996;8(8):1667-1681.

74. Landry CJT, Coltrain BK, Wesson JA, Zumbulyadis N, Lippert JL. In situ polymerization of tetraethoxysilane in polymers: chemical nature of the interactions. *Polymer* 1992;33(7):1496-1506.
75. Brennan AB, Miller TM, Vinocur RB. Hybrid organic-inorganic interpenetrating networks. In: Mark JE, Lee CY-C, Bianconi PA, editors. *Hybrid Organic-Inorganic Composites*. Washington, D C: American Chemical Society; 1995. p 142-162.
76. Brinker C, Sherer G. *Sol-gel Science: The Physics and Chemistry of Sol-Gel Processing*. San Diego, CA: Academic Press, Inc; 1990. 908 p.
77. Iler R. *The Chemistry of Silica*. New York: John Wiley & Sons; 1979. 866 p.
78. Lewis F. The Science and Technology of Silicone Rubber. *Rubber Chem. Technol.* 1962;35(5):1222.
79. Stein J, Truby K, Darkangelo Wood C, Takemori M, Vallance M, Swain G, Kavanagh C, Kovach B, Schultz M, Wiebe D and others. Structure-Property Relationships of Silicone Biofouling-Release Coatings: Effect of Silicone Network Architecture on Pseudobarnacle Attachment Strengths. *Biofouling* 2003;19(2):87-94.
80. Brady R. A fracture mechanical analysis of fouling release from nontoxic antifouling coatings. *Progress in Organic Coatings* 2001;43:188-192.
81. Chaudhury M, Finlay JA, Chung JY, Callow ME, Callow JA. The influence of elastic modulus and thickness on the release of the soft-fouling green alga *Ulva linza* (syn. *Enteromorpha linza*) from poly(dimethylsiloxane) (PDMS) model networks. *Biofouling* 2005;21:41-48.
82. Schumacher JF, Long CJ, Callow ME, Finlay JA, Callow JA, Brennan AB. Engineered nanoforce gradients for inhibition of settlement (attachment) of swimming algal spores. *Langmuir* 2008;24(9):4931-4937.
83. Tang Y, Finlay JA, Kowalke GL, Meyer AE, Bright FV, Callow ME, Callow JA, Wendt DE, Detty MR. Hybrid xerogel films as novel coatings for antifouling and fouling release. *Biofouling* 2005;21(1):59-71.
84. Finlay JA, Bennett SM, Brewer LH, Sokolova A, Clay G, Gunari N, Meyer AE, Walker GC, Wendt DE, Callow ME and others. Barnacle settlement and the adhesion of protein and diatom microfouling to xerogel films with varying surface energy and water wettability. *Biofouling* 2010;26(6):657-66.

85. Gunari N, Brewer LH, Bennett SM, Sokolova A, Kraut ND, Finlay JA, Meyer AE, Walker GC, Wendt DE, Callow ME and others. The control of marine biofouling on xerogel surfaces with nanometer-scale topography. *Biofouling* 2011;27(2):137-149.
86. Liu C, Zhao Q. Influence of surface-energy components of Ni–P–TiO₂–PTFE nanocomposite coatings on bacterial adhesion. *Langmuir* 2011;27(15):9512-9519.
87. Bennett SM, Finlay JA, Gunari N, Wells DD, Meyer AE, Walker GC, Callow ME, Callow JA, Bright FV, Dettly MR. The role of surface energy and water wettability in aminoalkyl/fluorocarbon/hydrocarbon-modified xerogel surfaces in the control of marine biofouling. *Biofouling* 2010;26(2):235-246.
88. Olsen SM, Pedersen LT, Laursen MH, Kiil S, Dam-Johansen K. Enzyme-based antifouling coatings: a review. *Biofouling* 2007;23(5):369-383.
89. Luckarift HR, Dickerson MB, Sandhage KH, Spain JC. Rapid, room-temperature synthesis of antibacterial bionanocomposites of lysozyme with amorphous silica or titania. *Small* 2006;2(5):640-643.
90. Kim J, Delio R, Dordick JS. Protease-containing silicates as active antifouling materials. *Biotechnol Progr* 2002;18(3):551-555.
91. Jin W, Brennan JD. Properties and applications of proteins encapsulated within sol-gel derived materials. *Anal Chim Acta* 2002;461(1):1-36.
92. Aughenbaugh W, Radin S, Ducheyne P. Silica sol-gel for the controlled release of antibiotics. II. The effect of synthesis parameters on the *in vitro* release kinetics of vancomycin. *J Biomed Mater Res* 2001;57(3):321-326.
93. Radin S, Ducheyne P, Kamplain T, Tan BH. Silica sol-gel for the controlled release of antibiotics. I. Synthesis, characterization, and *in vitro* release. *J Biomed Mater Res* 2001;57(2):313-320.
94. Radin S, Chen T, Ducheyne P. The controlled release of drugs from emulsified, sol gel processed silica microspheres. *Biomaterials* 2009;30(5):850-858.
95. Costache MC, Qu H, Ducheyne P, Devore DI. Polymer-xerogel composites for controlled release wound dressings. *Biomaterials* 2010;31:6336-6343.
96. Ahola M, Korteso P, Kangasniemi I, Kiesvaara J, Yli-Urpo A. Silica xerogel carrier material for controlled release of toremifene citrate. *Int J Pharm* 2000;195(1-2):219-227.

97. Rich J, Kortesus P, Ahola M, Yli-Urpo A, Kiesvaara J, Seppälä J. Effect of the molecular weight of poly(ϵ -caprolactone-co-lactide) on toremifene citrate release from copolymer/silica xerogel composites. *Int J Pharm* 2001;212(1):121-130.
98. Brooks G, Pons V. Osteomyelitis. In: Hoepfich P, Jordan M, Ronald A, editors. *Infectious Diseases: A Treatise of Infectious Processes*. Philadelphia: J.B. Lippincott Company; 1994. p 1390-1391.
99. Klemm K. The use of antibiotic-containing bead chains in the treatment of chronic bone infections. *Clinical Microbiol Infec* 2000;7(1):28-31.
100. Henry SL, Galloway KP. Local antibacterial therapy for the management of orthopaedic infections. Pharmacokinetic considerations. *Clin Pharmacokinet* 1995;29(1):36-45.
101. Kanellakopoulou K, Giamarellos-Bourboulis EJ. Carrier systems for the local delivery of antibiotics in bone infections. *Drugs* 2000;59(6):1223-32.
102. Habraken WJEM, Wolke JGC, Jansen JA. Ceramic composites as matrices and scaffolds for drug delivery in tissue engineering. *Adv Drug Delivery Rev* 2007;59(4-5):234-248.
103. Filgueiras MR, Latorre G, Hench LL. Solution effects on the surface-reactions of a bioactive glass. *J Biomed Mater Res* 1993;27(4):445-453.
104. Xynos ID, Hukkanen MVJ, Batten JJ, Buttery LD, Hench LL, Polak JM. Bioglass®45S5 stimulates osteoblast turnover and enhances bone formation *in vitro*: implications and applications for bone tissue engineering. *Calcified Tissue Int* 2000;67(4):321-329.
105. Bosetti M, Zanardi L, Hench L, Cannas M. Type I collagen production by osteoblast-like cells cultured in contact with different bioactive glasses. *J Biomed Mater Res A* 2003;64A(1):189-195.
106. Kawanabe K, Okada Y, Matsusue Y, Iida H, Nakamura T. Treatment of osteomyelitis with antibiotic-soaked porous glass ceramic. *J Bone Joint Surg Br* 1998;80-B(3):527-530.
107. Vallet-Regi M, Balas F, Colilla M, Manzano M. Bone-regenerative bioceramic implants with drug and protein controlled delivery capability. *Prog Solid State Chem* 2008;36(3):163-191.
108. Vallet-Regi M, Ramila A, del Real RP, Perez-Pariente J. A new property of MCM-41: drug delivery system. *Chem Mater* 2001;13(2):308-311.

109. Cauda V, Fiorilli S, Onida B, Vernè E, Vitale Brovarone C, Viterbo D, Croce G, Milanese M, Garrone E. SBA-15 ordered mesoporous silica inside a bioactive glass–ceramic scaffold for local drug delivery. *J Mater Sci - Mater Med* 2008;19(10):3303-3310.
110. Arcos D, Lopez-Noriega A, Ruiz-Hernandez E, Terasaki O, Vallet-Regi M. Ordered Mesoporous Microspheres for Bone Grafting and Drug Delivery. *Chem Mater* 2009;21(6):1000-1009.
111. Xia W, Chang J, Lin J, Zhu J. The pH-controlled dual-drug release from mesoporous bioactive glass/polypeptide graft copolymer nanomicelle composites. *Eur J Pharm Biopharm* 2008;69(2):546-552.
112. Hatcher B, Seegert C, Brennan A. Polyvinylpyrrolidone modified bioactive glass fibers as tissue constructs: In vitro mesenchymal stem cell response. *J Biomed Mater Res A* 2003;66A(4):840-849.
113. Costa HS, Rocha MF, Andrade GI, Barbosa-Stancioli EF, Pereira MM, Orefice RL, Vasconcelos WL, Mansur HS. Sol-gel derived composite from bioactive glass-polyvinyl alcohol. *J Mater Sci* 2008;43(2):494-502.
114. Li R, Clark AE, Hench LL. An investigation of bioactive glass powders by sol-gel processing. *J Appl Biomater* 1991;2(4):231-239.
115. Park J-H, Oh C, Shin S-I, Moon S-K, Oh S-G. Preparation of hollow silica microspheres in W/O emulsions with polymers. *J Colloid Interface Sci* 2003;266(1):107-114.
116. Park JH, Bae SY, Oh SG. Fabrication of hollow silica microspheres through the self-assembly behavior of polymers in W/O emulsion. *Chem Lett* 2003;32(7):598-599.
117. Leuner C, Dressman J. Improving drug solubility for oral delivery using solid dispersions. *Eur J Pharm Biopharm* 2000;50(1):47-60.
118. Young S, Wong M, Tabata Y, Mikos AG. Gelatin as a delivery vehicle for the controlled release of bioactive molecules. *J Control Release* 2005;109(1-3):256-74.
119. Yan WQ, Oka M, Nakamura T. Bone bonding in bioactive glass ceramics combined with bone matrix gelatin. *J Biomed Mater Res* 1998;42(2):258-65.
120. Kokubo T, Takadama H. How useful is SBF in predicting in vivo bone bioactivity? *Biomaterials* 2006;27(15):2907-2915.

121. Kokubo T, Kushitani H, Sakka S, Kitsugi T, Yamamuro T. Solutions able to reproduce in vivo surface-structure changes in bioactive glass-ceramic A-W. *J Biomed Mater Res* 1990;24(6):721-734.
122. Hench L, Splinter R, Allen W, Greenlee T. Bonding Mechanisms at the Interface of Ceramic Prosthetic Materials. *Journal of Biomedical Materials Research* 1971;5(6):117-141.
123. Nakanishi K. Sol-gel process of oxides accompanied by phase separation. *Bull Chem Soc Jpn* 2006;79(5):673-691.
124. Nakanishi K. Pore Structure Control of Silica Gels Based on Phase Separation. *Journal of Porous Materials* 1997;4(2):67-112.
125. Nakanishi K, Komura H, Takahashi R, Soga N. Phase-separation in silica sol-gel system containing poly(ethylene oxide) 1. phase relation and gel morphology. *Bull Chem Soc Jpn* 1994;67(5):1327-1335.
126. Kim IY, Kawachi G, Kikuta K, Cho SB, Kamitakahara M, Ohtsuki C. Preparation of bioactive spherical particles in the CaO-SiO₂ system through sol-gel processing under coexistence of poly(ethylene glycol). *J Eur Ceram Soc* 2008;28(8):1595-1602.
127. Saravanapavan P, Jones JR, Pryce RS, Hench LL. Bioactivity of gel-glass powders in the CaO-SiO₂ system: A comparison with ternary (CaO-P₂O₅-SiO₂) and quaternary glasses (SiO₂-CaO-P₂O₅-Na₂O). *J Biomed Mater Res A* 2003;66A(1):110-119.
128. Xu Y, Wu D, Sun Y, Chen W, Yuan H, Deng F, Wu Z. Effect of polyvinylpyrrolidone on the ammonia-catalyzed sol-gel process of TEOS: Study by in situ ²⁹Si NMR, scattering, and rheology. *Colloids Surf, A* 2007;305(1-3):97-104.
129. Gun'ko VM, Voronin EF, Nosach LV, Pakhlov EM, Voronina OE, Guzenko NV, Kazakova OA, Leboda R, Skubiszewska-Zieba J. Nanocomposites with fumed silica/poly(vinyl pyrrolidone) prepared at a low content of solvents. *Applied Surface Science* 2006;253(5):2801-2811.
130. Pattanayek SK, Juvekar VA. Prediction of adsorption of nonionic polymers from aqueous solutions to solid surfaces. *Macromolecules* 2002;35(25):9574-9585.
131. Grace HP. Dispersion phenomena in high viscosity immiscible fluid systems and application of static mixers as dispersion devices in such systems. *Chem Eng Commun* 1982;14(3-6):225-277.

132. Stegeman YW, Vosse FNVD, Meijer HEH. On the applicability of the grace curve in practical mixing operations. *Can J Chem Eng* 2002;80(4):1-6.
133. Xu JH, Li SW, Lan WJ, Luo GS. Microfluidic approach for rapid interfacial tension measurement. *Langmuir* 2008;24(19):11287-11292.
134. Jansseune T, Mewis J, Moldenaers P, Minale M, Maffettone PL. Rheology and rheological morphology determination in immiscible two-phase polymer model blends. *J Non-Newtonian Fluid Mech* 2000;93(1):153-165.
135. Adelman RL. Studies on the base strengths of n,n-disubstituted amides. *J Org Chem* 1964;29(7):1837-1844.
136. Li PJ, Ohtsuki C, Kokubo T, Nakanishi K, Soga N, Nakamura T, Yamamuro T. Apatite formation induced by silica-gel in a simulated body-fluid. *J Am Ceram Soc* 1992;75(8):2094-2097.
137. Walstra P, Smulders PEA. Emulsion Formation. In: Brinks BP, editor. *Modern Aspects of Emulsion Science*. Cambridge, UK: The Royal Society of Chemistry; 1998. p 56-114.
138. Walstra P. *Physical Chemistry of Foods*. New York: Marcel Dekker, Inc.; 2003.
139. Chan C-K, Chu IM, Ou C-F, Lin Y-W. Interfacial interactions and their influence to phase behavior in poly(vinyl pyrrolidone)/silica hybrid materials prepared by sol-gel process. *Mater Lett* 2004;58(17-18):2243-2247.
140. Zhao T, Qiu D. One-Pot Synthesis of Highly Folded Microparticles by Suspension Polymerization. *Langmuir* 2011.
141. Sundberg DC, Durant YG. Latex particle morphology, fundamental aspects: A review. *Polym React Eng* 2003;11(3):379-432.
142. Stubbs JM, Sundberg DC. The dynamics of morphology development in multiphase latex particles. *Prog Org Coat* 2008;61(2-4):156-165.
143. Smeltzer M, Nelson C. Osteomyelitis and septic arthritis. In: Honeyman A, Friedman H, Bendinelli M, editors. *Staphylococcus Aureus Infection and Disease*. New York: Kluwer Academic Publishers; 2002. p 213-246.
144. Hawkshead JJ, 3rd, Patel NB, Steele RW, Heinrich SD. Comparative severity of pediatric osteomyelitis attributable to methicillin-resistant versus methicillin-sensitive *Staphylococcus aureus*. *J Pediatr Orthop* 2009;29(1):85-90.

145. Wahlig H, Dingeldein E, Bergmann R, Reuss K. The release of gentamicin from polymethylmethacrylate beads. An experimental and pharmacokinetic study. *J Bone Joint Surg Br* 1978;60-B(2):270-275.
146. Rushton N. Applications of local antibiotic therapy. *Eur J Surg Suppl* 1997(578):27-30.
147. Kent ME, Rapp RP, Smith KM. Antibiotic beads and osteomyelitis: here today, what's coming tomorrow? *Orthopedics* 2006;29(7):599-603.
148. Liu SJ, Ueng SWN, Lin SS, Chan EC. In vivo release of vancomycin from biodegradable beads. *J Biomed Mater Res* 2002;63(6):807-813.
149. Athanasiou KA, Agrawal CM, Barber FA, Burkhart SS. Orthopaedic applications for PLA-PGA biodegradable polymers. *Arthroscopy* 1998;14(7):726-737.
150. Stemberger A, Grimm H, Bader F, Rahn HD, Ascherl R. Local treatment of bone and soft tissue infections with the collagen-gentamicin sponge. *Eur J Surg Suppl* 1997(578):17-26.
151. Drognitz O, Thorn D, Kruger T, Gatermann SG, Iven H, Bruch HP, Muhl E. Release of vancomycin and teicoplanin from a plasticized and resorbable gelatin sponge: in vitro investigation of a new antibiotic delivery system with glycopeptides. *Infection* 2006;34(1):29-34.
152. Cevher E, Orhan Z, Mulazimoglu L, Sensoy D, Alper M, Yildiz A, Ozsoy Y. Characterization of biodegradable chitosan microspheres containing vancomycin and treatment of experimental osteomyelitis caused by methicillin-resistant *Staphylococcus aureus* with prepared microspheres. *Int J Pharm* 2006;317(2):127-135.
153. Bohner M, Gbureck U, Barralet JE. Technological issues for the development of more efficient calcium phosphate bone cements: a critical assessment. *Biomaterials* 2005;26(33):6423-6429.
154. Stallmann HP, Faber C, Bronckers AL, Nieuw Amerongen AV, Wuisman PI. In vitro gentamicin release from commercially available calcium-phosphate bone substitutes influence of carrier type on duration of the release profile. *BMC Musculoskelet Disord* 2006;7:18.
155. Hamanishi C, Kitamoto K, Tanaka S, Otsuka M, Doi Y, Kitahashi T. A self-setting TTCP-DCPD apatite cement for release of vancomycin. *J Biomed Mater Res* 1996;33(3):139-143.
156. Robison RL; Eli Lilly and Company, assignee. Vancomycin-HCL solutions and the lyophilization thereof. United States patent 4885275. 1989.

157. Stoor P, Soderling E, Salonen JI. Antibacterial effects of a bioactive glass paste on oral microorganisms. *Acta Odontologica Scandinavica* 1998;56(3):161-165.
158. Gupta MM, Saini TR. Preformulation parameters characterization to design, development and formulation of vancomycin hydrochloride tablets for pseudomembranous colitis (sic). *International Journal of Pharmaceutical Research and Development* 2009;1(9).
159. Godbole PP, Tsai R-S, Clark WM. Affinity partitioning of vancomycin. *Biotechnol Bioeng* 1991;38(5):535-544.
160. Lee C-K, Sandler SI. Vancomycin partitioning in aqueous two-phase systems: Effects of pH, salts, and an affinity ligand. *Biotechnol Bioeng* 1990;35(4):408-416.
161. Radin S, El-Bassyouni G, Vresilovic EJ, Schepers E, Ducheyne P. In vivo tissue response to resorbable silica xerogels as controlled-release materials. *Biomaterials* 2005;26(9):1043-1052.
162. Claudius JS, Neau SH. The solution stability of vancomycin in the presence and absence of sodium carboxymethyl starch. *Int J Pharm* 1998;168(1):41-48.
163. Piola RF, Dafforn KA, Johnston EL. The influence of antifouling practices on marine invasions. *Biofouling* 2009;25(7):633-644.
164. Thomas KV, Brooks S. The environmental fate and effects of antifouling paint biocides. *Biofouling* 2010;26(1):73-88.
165. Lindgren JF, Haeffner M, Ericsson CT, Jonsson PR. Oxygen-depleted surfaces: a new antifouling technology. *Biofouling* 2009;25(5):455-461.
166. McMaster D, Bennett S, Tang Y, Finlay JA, Kowalke GL, Nedved B, Bright FV, Callow ME, Callow JA, Wendt DE and others. Antifouling character of 'active' hybrid xerogel coatings with sequestered catalysts for the activation of hydrogen peroxide. *Biofouling* 2009;25(1):21-33.
167. Tasso M, Pettitt ME, Cordeiro AL, Callow ME, Callow JA, Werner C. Antifouling potential of Subtilisin A immobilized onto maleic anhydride copolymer thin films. *Biofouling* 2009;25(6):505-516.
168. Bressy C, Hellio C, Maréchal JP, Tanguy B, Margailan A. Bioassays and field immersion tests: a comparison of the antifouling activity of copper-free poly(methacrylic)-based coatings containing tertiary amines and ammonium salt groups. *Biofouling* 2010;26(7):769-777.

169. Kristensen JB, Olsen SM, Laursen BS, Kragh KM, Poulsen CH, Besenbacher F, Meyer RL. Enzymatic generation of hydrogen peroxide shows promising antifouling effect. *Biofouling* 2010;26(2):141-153.
170. Sommer S, Ekin A, Webster DC, Stafslie SJ, Daniels J, Van der Wal LJ, Thompson SEM, Callow ME, Callow JA. A preliminary study on the properties and fouling-release performance of siloxane–polyurethane coatings prepared from poly(dimethylsiloxane) (PDMS) macromers. *Biofouling* 2010;26(8):961-972.
171. Scardino AJ, Hudleston D, Peng Z, Paul NA, de Nys R. Biomimetic characterisation of key surface parameters for the development of fouling resistant materials. *Biofouling* 2009;25(1):83-93.
172. Long CJ, Schumacher JF, Robinson PAC, Finlay JA, Callow ME, Callow JA, Brennan AB. A model that predicts the attachment behavior of *Ulva linza* zoospores on surface topography. *Biofouling* 2010;26(4):411-419.
173. Callow ME, Callow JA. Marine biofouling: A sticky problem. *Biologist* 2002;49:10-14.
174. Long CJ, Finlay JA, Callow ME, Callow JA, Brennan AB. Engineered antifouling microtopographies: mapping preferential and inhibitory microenvironments for zoospore attachment. *Biofouling* 2010;26(8):941-952.
175. Long CJ. Analytical methods for predicting bio-settlement on patterned surfaces [Dissertation]. Gainesville (FL): University of Florida; 2009. 134 p.
176. Dabros T, Van De Ven TGM. Kinetics of coating by colloidal particles. *J Colloid Interf Sci* 1982;89(1):232-244.
177. Cowan MM, Taylor KG, Doyle RJ. Kinetic analysis of *Streptococcus sanguis* adhesion to artificial pellicle. *J Dent Res* 1986;65(10):1278-1283.
178. Pratt-Terpstra IH, Weerkamp AH, Busscher HJ. Microbial factors in a thermodynamic approach of oral streptococcal adhesion to solid substrata. *Journal of Colloid Interf Sci* 1988;129(2):568-574.
179. Sjollema J, Busscher HJ, Weerkamp AH. Experimental approaches to studying adhesion of microorganisms to solid substrata: applications and mass transport. *Journal of Microbiol Meth* 1989;9:79-90.
180. Busscher HJ, Sjollema J, van der Mei HC. Relative importance of surface free energy as a measure of hydrophobicity in bacterial adhesion to solid surfaces. In: Doyle RJ, Rosenberg M, editors. *Microbial cell surface hydrophobicity*. Washington (DC): American Society for Microbiology; 1990. p 335-359.

181. Van der Mei HC, Cox SD, Geertsema-Doornbusch GI, Doyle RJ, Busscher HJ. A critical appraisal of positive cooperativity in oral streptococcal adhesion: scatchard analyses of adhesion data versus analyses of the spatial arrangement of adhering bacteria. *J Gen Microbiol* 1993;139(5):937-948.
182. Callow JA, Callow ME, Ista LK, Lopez G, Chaudhury MK. The influence of surface energy on the wetting behaviour of the spore adhesive of the marine alga *Ulva linza* (synonym *Enteromorpha linza*). *J R Soc Interface* 2005;2(4):319-325.
183. Heydt M, Rosenhahn A, Grunze M, Pettitt M, Callow JA, Callow ME. Digital in-line holography as a three-dimensional tool to study motile marine organisms during their exploration of surfaces. *J Adhes* 2007;83:417-430.
184. Krishnamurti K, Soman S. Studies in the adsorption of bacteria. *P Indian Acad Sci B* 1951;34(2):81-91.
185. Sjollemma J, van der Mei HC, Uyen HM, Busscher HJ. Direct observations of cooperative effects in oral streptococcal adhesion to glass by analysis of the spatial arrangement of adhering bacteria. *FEMS Microbiol Lett* 1990;69:263-270.
186. Lin L, Rosenberg M, Taylor KG, Doyle RJ. Kinetic analysis of ammonium sulfate dependent aggregation of bacteria. *Colloid Surface B* 1995;5(3-4):127-134.
187. Xynos ID, Edgar AJ, BATTERY LDK, Hench LL, Polak JM. Ionic products of bioactive glass dissolution increase proliferation of human osteoblasts and induce insulin-like growth factor II mRNA expression and protein synthesis. *Biochem Biophys Res Commun* 2000;276(2):461-465.
188. Wang Y, Finlay JA, Betts DE, Merkel TJ, Luft JC, Callow ME, Callow JA, DeSimone JM. Amphiphilic co-networks with moisture-induced surface segregation for high-performance nonfouling coatings. *Langmuir* 2011;10365–10369.
189. Wang Y, Betts DE, Finlay JA, Brewer L, Callow ME, Callow JA, Wendt DE, DeSimone JM. Photocurable amphiphilic perfluoropolyether/poly(ethylene glycol) networks for fouling-release coatings. *Macromolecules* 2011;44(4):878-885.
190. Bogush GH, Tracy MA, Zukoski CF. Preparation of monodisperse silica particles - control of size and mass fraction. *J Non-Cryst Solids* 1988;104(1):95-106.
191. Giesche H. Synthesis of monodispersed silica powders I. Particle properties and reaction kinetics. *J Eur Ceram Soc* 1994;14(3):189-204.
192. Fetters LJ, Lohse DJ, Richter D, Witten TA, Zirkel A. Connection between polymer molecular weight, density, chain dimensions, and melt viscoelastic properties. *Macromolecules* 2002;27(17):4639-4647.

193. Shenoy SL, Bates WD, Frisch HL, Wnek GE. Role of chain entanglements on fiber formation during electrospinning of polymer solutions: good solvent, non-specific polymer-polymer interaction limit. *Polymer* 2005;46(10):3372-3384.
194. Stöber W, Fink A, Bohn E. Controlled growth of monodisperse silica spheres in the micron size range. *J Colloid Interface Sci* 1968;26:62-69.

BIOGRAPHICAL SKETCH

Scott Patrick Cooper was born in Scottsdale, Arizona in 1985 to Pat and Larry Cooper. He grew up in Arizona, Arkansas, Tennessee, and California but calls Phoenix, Arizona home. As a child, Scott enjoyed many activities including: outdoor adventures with his brother, playing golf with his dad, and going on family road trips to North Dakota in the summer. His interest in materials science began when he took a ceramic art class in high school. He later worked for a glass artist producing pieces of fused, dichroic glass. He graduated from Desert Vista High School in Phoenix in 2003.

Scott attended the University of Arizona in Tucson, where he studied materials science and engineering and German studies. Scott traveled during summer breaks, studying at the University of Leipzig, Germany in 2004 and performing undergraduate research at North Dakota State University in 2005. Scott was selected as one of 25 students to take part in Transatlantic Program in 2006, a German business immersion program. As a part of this program, he worked at the Schott glass company in Marienborn, Germany where he characterized the fluorescent properties of glasses and glass-ceramics. For his senior design project, Scott worked on a team with 4 other students to design and build a glassblowing furnace. Scott graduated *summa cum laude* with bachelor's degrees in both materials science and engineering and German studies. He was named an "Outstanding Senior" by the College of Humanities.

Scott received a National Science Foundation Graduate Research Fellowship to attend the University of Florida. He joined the Brennan Research Group in the summer of 2007. Scott married his high school sweetheart in June of 2008. In January 2010, Scott was selected to attend the US-China Winter School on Glass at Zhejiang University in Hangzhou, China. The trip was a learning experience both academically

and culturally. In July 2010, Scott presented his work in Newcastle, England at the International Congress on Marine Corrosion and Fouling, where he received an award for best poster.

While at the University of Florida, Scott was actively involved in the Society for Biomaterials (SFB). He served as treasurer for the UF chapter from 2007-2008 and president from 2008-2009. He is currently serving a term as the president of the national student chapter of SFB. Scott has also written several summaries of research articles for the *MRS Bulletin*. In his free time, Scott enjoys playing golf, homebrewing beer, and traveling with his wife.